

Medium Voltage DC-DC Converter for Power Collection Links - A Multistage Stacked Boost Architecture

THÈSE N° 7361 (2017)

PRÉSENTÉE LE 20 JANVIER 2017

À LA FACULTÉ DES SCIENCES ET TECHNIQUES DE L'INGÉNIEUR
LABORATOIRE D'ÉLECTRONIQUE INDUSTRIELLE
PROGRAMME DOCTORAL EN ENERGIE

ÉCOLE POLYTECHNIQUE FÉDÉRALE DE LAUSANNE

POUR L'OBTENTION DU GRADE DE DOCTEUR ÈS SCIENCES

PAR

Gina Kristin STEINKE

acceptée sur proposition du jury:

Dr S.-R. Cherkaoui, président du jury
Prof. A. Rufer, Prof. M. Paolone, directeurs de thèse
Dr K.-B. Park, rapporteur
Prof. M. Liserre, rapporteur
Prof. D. Dujic, rapporteur



ÉCOLE POLYTECHNIQUE
FÉDÉRALE DE LAUSANNE

Suisse
2017



Acknowledgements

I would like to thank my supervisor Prof. Alfred Rufer for overseeing my thesis at the Laboratory of Industrial Electronics at EPFL. He has shown great interest in my research topic and guided me with his experience whenever needed.

I especially want to thank ABB Switzerland for the financial support of this research work. Many thanks to Drazen Dujic who started the project and was my ABB contact in the beginning. Thanks also go to Ki-Bum Park for taking over as contact after Drazen Dujic became Professor at EPFL.

Thanks are also deserved for Prof. Mario Paolone for being my thesis co-director as well as for Prof. Marco Liserre, Prof. Drazen Dujic, Dr. Ki-Bum Park and Dr. Rachid Cherkaoui for dedicating their time by serving as members of the scientific committee evaluating my thesis.

From the former Laboratory of Industrial Electronics I want to thank Martel for being a enjoyable office partner and for the interesting discussions we had. To more and hopefully regularly lunch meetings. Thank you to Maria, the secretary of the LEI, and to Sophie, the secretary of the DESL, for their help with all the administrative issues. The Imperix team Simon and Nicolas, Philippe, Roberto, Fred, Roland, Michalis, Behrooz, Sébastien and all the scientific and technical LEI staff who were part of the everyday working life at LEI and who deserve thanks for their help on various matters.

In the Power Electronics Laboratory I'd like to thank Yan-Kim, Marco and Emilien for fun and interesting days during conferences and courses as well as them and Alexandre, Uzair and Min for being the new everyday working life in phasing out time of the LEI and afterwards.

Last but not least I'm grateful to my family for their endless support and especially my father Dr. Jürgen Steinke for always being available to discuss work.





Abstract

Nowadays electrical energy generation is an important topic discussed in the society. More and more focus is put onto regenerative and CO₂ friendly generation technologies. Since technologies like wind or solar energy generation are most of the time placed far away from the city centres one point to focus on is the transmission of the energy. Besides having to transmit the renewably generated energy over long distances, another problem of grids with a high content of renewable energy is the issue of stabilizing such grids. In order to evaluate the opportunities of DC-distribution within the energy distribution system there is also need for research in medium voltage DC distribution since this could be an important part of a complete distribution grid. An important component within DC distribution networks are DC-DC converters, especially for connecting low voltage DC sources or loads to the medium voltage DC network.

Before going into possible medium voltage DC-DC converter topologies, it is useful to analyse typical examples for applications where such a converter could be used. Two main applications were considered here. The first one is a microgrid application since nowadays a lot of thought is put into self-supplying industry complexes. Realizing such structure will result in new requirements for the converters on such a facility and is also opening opportunities for new technologies. The second application considered is the regenerative energy generation. Especially solar power plants might prove quite suitable since the electrical power generated by the solar cells is already DC and would not need to be transformed.

Focussing on solar plants as application it became obvious that to achieve high power levels, a huge number of solar panels need to be installed, using a large surface area. Covering such a large area, where the energy is generated, means that the power must be collected over long distances, which leads to a low efficiency if the transmission is done under low voltage conditions. A better efficiency could be expected by increasing the voltage to a medium voltage level using a DC-DC converter resulting into an interest into the research of possible DC-DC configurations for the photovoltaic plant grid.

The introduced converter is based on the current divider topology, which is used to equalize the voltage between different cells, in this case between different series capacitors. To use this topology as a step-up converter a boost stage was added as input stage forming the Multistage Stacked Boost Architecture. To ensure that this topology would be a possible solution for the before mentioned challenges calculations were done to verify a satisfying efficiency of the converter. To understand the elementary properties of Multistage Stacked Boost Architecture the topology was split into its essential stages, an Energetic Macroscopic Representation was done and a control was designed for each. For this a dedicated control structure using the principle of Feed-Forward was studied and simulations showed that even with perturbations the control for the input boost stage is working fine. The elementary MSBA cell in contrast shows resonant phenomenon because of its' LC components, which was also handled by implementing a Feed-Forward control. The dynamic response of the controlled MSBA cell was verified by simulation and is working well for this case. Finally, the boost stage controlled with the LFF control scheme in combination with three MSBA cells, also called a 4-stage MSBA converter, was researched. Simulation



verified that the control is able to provide stable output quantities without resonant oscillations for a four stage MSBA topology.

Since the LFF control relies on the measurement of nine state variables, it was considered important to introduce a second control. This control was an observer control. The first step to achieving that was to introduce a State-Space control, which is based on the description of system with n first-order differential equations. The eigenvalues of the system were then investigated as well as the controllability and observability of the system. After choosing closed-loop poles simulations of the system showed that the State-Space control was working well and that only a small steady state error occurred, which could be adjusted with a precompensation. Therefore, the research continued into a control strategy using an observer. The observer is basically a copy of the state space system; it has the same input and almost the same differential equations. An extra term compares the actual measured output to the estimated output; this will cause the estimated states to approach the values of the actual states. Simulation results were almost identical to the results of the state space simulation without the observer. So the observer was working reliably and fast.

To verify the simulation results and the working of the proposed controls a low voltage prototype was built. The converter was built to work with an input voltage of 100V using a step up ratio of 1:8 using a fast prototyping modular system. To implement the control, the BoomBox was used. The BoomBox has 16 analogue inputs for the voltage and current sensors of the converter. This input is then going through an analogue-to-digital converter so that it can be transferred to the microcontroller of the system. These digital signals can then be used in the control software. The measurements that were conducted all included normal steady-state operation as well as test to verify the correct functioning during perturbations such as variations of the load. All the measurement showed that the controls were able to keep all the capacitor voltages at the same level and that they were able to handle perturbations.

To conclude, the work that has been done for this thesis included considering applications for medium voltage DC-DC converters as well as a case study of a solar plant application case. In addition, the problems of the approach of having huge solar plants use a low voltage distribution inside were shown. A converter that could be used to elevate said voltage to a medium voltage level was introduced. The Multistage Stacked Boost Architecture, which is based on the idea of the current divider. This topology was then investigated in detail and calculations for the efficiency of the topology were conducted. An Energetic Macroscopic Representation of the system was done and the specific resonant phenomena of the converter were considered. Three different dedicated controls were investigated. A control based on the feed forwarding of the output current (LFF), a state-space control and an observer control. All control schemes were first tested with simulations and then verified on a low voltage prototype. The measurement results obtained with the different controls proved satisfactory, showing that the Multistage Stacked Boost Architecture is a reliable and interesting topology.

Keywords: DC-DC converter, Step-up, Medium Voltage, regenerative energies, PV applications, feed-forward, state-space, observer



Zusammenfassung

Heutzutage ist die Erzeugung elektrischer Energie ein wichtiges Thema, das in der Gesellschaft diskutiert wird. Immer mehr Fokus wird auf regenerative und CO₂-freundliche Technologien zur Erzeugung gesetzt. Da Technologien wie Wind- oder Solarenergieerzeugung die meiste Zeit weit weg von den Stadtzentren platziert sind, ist ein wichtiger Punkt die Übertragung der Energie. Nicht nur ist die Übertragung der regenerativ erzeugten Energie über weite Strecken problematisch, es ist auch kritisch, Netze mit einem hohen Anteil an erneuerbaren Energien zu stabilisieren. DC Übertragung und DC Netzwerke können wichtige Beiträge zur Lösung dieser Probleme leisten. Um die Chancen der DC-Netzwerke innerhalb des Energieverteilungssystems zu bewerten, ist es für die Forschung erforderlich sich mit Mittelspannungsgleichstromnetzwerken zu beschäftigen, da diese ein wichtiger Bestandteil eines kompletten Verteilnetzes sein könnten.

Bevor auf mögliche Mittelspannungsstromrichter, insbesondere zur Anpassung verschiedener Gleichspannungsniveaus, eingegangen wird, ist es nützlich, typische Beispiele für Anwendungen zu analysieren, wo ein solcher Stromrichter eingesetzt werden könnte. Zwei Hauptanwendungen wurden hierbei berücksichtigt. Die erste ist eine Microgrid-Anwendung, da heutzutage oft mit dem Gedanken gespielt wird, auf selbstversorgende Industrie-Komplexe zu setzen. Die Realisierung einer solchen Struktur wird für die Stromrichter einer solchen Anlage neue Anforderungen ergeben und eröffnet Möglichkeiten für neue Technologien. Die zweite untersuchte Anwendung ist die regenerative Energieerzeugung. Vor allem Solarkraftwerke könnten durchaus geeignet sein, da die elektrische Leistung, die von den Solarzellen erzeugt wird, bereits Gleichstrom ist und nicht umgewandelt werden müsste.

Fokussiert man sich auf Solaranlagen, ist es offensichtlich, dass, um hohe Leistungen zu erreichen, eine große Anzahl von Sonnenkollektoren installiert werden müssen, wofür eine große Bodenfläche verwendet wird. Die Nutzung einer so großen Fläche, auf der die Energie erzeugt wird, bedeutet, dass die Energie über lange Strecken gesammelt werden muss, was zu einem geringen Wirkungsgrad führt, wenn die Übertragung mit Niederspannung durchgeführt wird. Eine bessere Effizienz kann durch eine Erhöhung der Spannung auf einen mittleren Spannungspegel erwartet werden, wodurch es interessant wird, DC-DC-Stromrichter für Photovoltaik-Anlagen zu erforschen.

Der vorgeschlagene Stromrichter basiert auf der „Current Diverter“ Topologie, die verwendet wird, um die Spannung zwischen verschiedenen Zellen zu egalisieren, in diesem Fall zwischen verschiedenen Reihen-kondensatoren. Um diese Topologie für variable Eingangsgleichspannung verwenden zu können, wurde ein Standard-Hochsetzsteller als Eingangsstufe hinzugefügt, wodurch die „Multistage Stacked Boost Architecture“ entsteht. Um sicherzustellen, dass diese Topologie eine mögliche Lösung für die zuvor genannten Herausforderungen ist, wurden Berechnungen durchgeführt, um sicherzustellen, dass der Stromrichter einen befriedigenden Wirkungsgrad erreichen kann.

Um die elementaren Eigenschaften der „Multistage Stacked Boost Architecture“ zu verstehen, wurde die Topologie in seinen wesentlichen Abschnitte unterteilt, eine „Energetic Macroscopic Representation“



erstellt und dann jeweils eine Steuerung entworfen. Eine spezielle Kontrollstruktur basierend auf dem Rückkopplungs-Prinzip wurde untersucht und Simulationen haben gezeigt, dass auch bei Störungen diese Steuerung für die Eingangsstufe gut funktioniert. Die elementare MSBA Zelle weist Resonanzphänomene auf wegen ihrer LC-Komponenten. Es muss daher eine geeignete Regelung verwendet werden, um diese Resonanzphänomene zu vermeiden. Dies wird durch eine Steuerung nach dem Rückkopplungs-Prinzip erreicht und das dynamische Verhalten der so gesteuerten MSBA Zelle wurde durch Simulation überprüft und funktioniert gut. Schließlich wurden der Hochsetzsteller und die drei MSBA Zellen mit dem LFF Steuerungsschema zum 4-stufigen MSBA Stromrichter zusammengefügt. Simulationsergebnisse verifizierten, dass die Steuerung in der Lage ist, für eine vierstufige MSBA Topologie ohne Resonanzschwingungen eine stabile Ausgangsspannung zu erzeugen.

Da die LFF Regelung auf der Messung von neun Zustandsvariablen beruht, wurde es als wichtig erachtet, eine zweite Regelungsvariante zu untersuchen, eine Regelung mit einem Beobachter. Der erste Schritt, das zu erreichen, war eine Zustandsraumsteuerung einzuführen, die auf der Beschreibung des Systems mit n Differentialgleichungen erster Ordnung basiert. Die Eigenwerte des Systems wurden dann untersucht sowie auch die Steuerbarkeit und Beobachtbarkeit des Systems. Simulationen des Systems nach der Wahl der „Closed-Loop“-Pole zeigten, dass die Steuerung gut funktioniert und dass nur ein kleiner Fehler auftritt, der mit einer Vorsteuerung angepasst werden kann. Daher erfolgte im Weiteren eine Untersuchung einer Steuerungsstrategie mit einem Beobachter. Der Beobachter ist im Grunde eine Kopie des Zustandsraum-System; er hat das gleiche Eingangssignal und fast die gleichen Differentialgleichungen. Eine zusätzliche Gleichung vergleicht den tatsächlich gemessenen Ausgang mit dem geschätzten Ausgang; dies bewirkt, dass sich die geschätzten Zustände den Werten der Ist-Zustände annähern. Die Simulationsergebnisse dieses Regelungssystems waren fast identisch mit den Ergebnissen der Zustandsraum-Simulationen ohne den Beobachter. Das heißt, der Beobachter arbeitet zuverlässig und schnell.

Um die Simulationsergebnisse und die Funktionsweise der vorgeschlagenen Steuerungen zu überprüfen, wurde ein Niederspannungs-Prototyp gebaut. Dieser Stromrichter wurde konzipiert, um mit einer Eingangsspannung von 100 V zu arbeiten und mit einem Spannungsverhältnis von 1:8. Der Prototyp wurde mit Hilfe eines modularen Systems zum schnellen Erstellen von Prototypen aufgebaut. Zur Umsetzung der Steuerung wurde die „BoomBox“ verwendet. Die „BoomBox“ verfügt über 16 analoge Eingänge für die Spannungs- und Stromsensoren des Stromrichters. Diese Eingänge werden dann durch einen Analog-Digital-Wandler übersetzt, so dass sie an den Mikrocontroller des Systems übertragen werden können. Diese digitalen Signale können dann in der Steuerungssoftware verwendet werden. Alle durchgeführten Messungen für die verschiedenen Steuerungen wurden sowohl im normalen stationären Betrieb durchgeführt als auch bei Störungen wie Schwankungen der Belastung oder Änderungen an der Eingangsstufe. Alle Messungen zeigten, dass die verschiedenen Regelungsvarianten in der Lage waren, alle Kondensatorspannungen auf dem gleichen Niveau zu halten, und dass sie in der Lage waren, Störungen zu widerstehen mit nur einem kleinen kurzzeitigen Spannungsabfall in den verschiedenen Kondensatoren.

Zusammenfassend hat sich diese Arbeit mit der Überprüfung von Anwendungen für Mittelspannungs-DC-DC-Stromrichter sowie eine Fallstudie zu einer Solaranlage beschäftigt. Es wurden die Probleme



großer Solaranlagen aufgezeigt, die innerhalb ihres Systems eine Niederspannungsverteilung verwenden. Ein Stromrichter, der verwendet werden könnte, um diese Spannung auf eine Mittelspannungsebene zu erhöhen, wurde eingeführt, nämlich die „Multistage Stacked Boost Architecture“, welche auf der Idee des „Current Diverters“ basiert. Diese Topologie wurde dann im Detail untersucht und Berechnungen zur Effizienz wurden durchgeführt. Eine energetische makroskopische Darstellung des Systems wurde durchgeführt und die spezifischen Resonanzerscheinungen des Stromrichters berücksichtigt. Drei verschiedene Regelungsvarianten wurden untersucht; eine Rückkopplungsregelung, eine Zustandsraumregelung und eine Beobachter-Regelung. Alle Regelungsvarianten wurden zunächst mit Simulationen und dann auf einem Niederspannungs- Prototyp getestet. Die Messergebnisse erwiesen sich als zufriedenstellend und zeigten, dass die „Multistage Stacked Boost Architecture“ eine robuste und interessante Topologie ist.

Stichwörter: DC-DC Stromrichter, Hochsetzsteller, Mittelspannung, Regenerative Energien, PV Anwendungen, Rückkopplungs-Prinzip, State-Space, Beobachter





Content

Acknowledgement	III
Abstract	V
Zusammenfassung	VII
Content	XI
List of Abbreviations	XV
List of Main Symbols	XVII
1. Introduction.....	19
1.1. Motivation	19
1.2. Application Cases.....	20
1.3. Example for an Industrial Microgrid.....	21
1.4. Agua Caliente.....	25
1.5. Transmission Losses in Regards to Solar Plant Size.....	26
1.6. DC-DC Converters.....	34
1.6.1. Non-Isolated DC-DC Converters	35
1.6.2. Isolated DC-DC Converters	38
2. The Multistage Stacked Boost Architecture.....	41
2.1. Current diverter.....	41
2.2. The Elementary MSBA Cell	42
2.3. Duty Cycle Definition.....	43
2.4. Specific Resonance Properties	44
2.4.1. General Description of the Resonance Phenomenon	44
2.4.2. Resonance Excitation of the MSBA Cell due to a Load Change.....	49
2.4.3. The Non-Excited Regime for Load Variation	49
2.4.4. The Non-Excited Regime for an Input Voltage Variation	50
2.5. The Multistage Stacked Boost Architecture Family	52
2.5.1. The Symmetric Step-Up MSBA	52
2.5.2. The Asymmetric Step-Down MSBA	55
2.5.3. The Symmetric MSBA with NPC Inverter	56



2.5.4.	NPC Balanced Capacitive Divider.....	56
3.	The Asymmetric Multistage Stacked Boost Architecture.....	59
3.1.	MSBA Characteristic Equations	59
3.2.	Specific Resonance Phenomena.....	63
3.2.1.	The 4-Stage Asymmetric MSBA	63
3.2.2.	The MSBA Connected to an Inverter.....	64
3.3.	Efficiency and Loss Calculation.....	66
3.3.1.	Asymmetric MSBA with $d=0.5$	67
3.3.2.	Symmetric MSBA with $d=0.5$	70
3.3.3.	Asymmetric MSBA with $d=0.439$	72
3.3.4.	Inductor Losses.....	73
3.3.5.	Comparison of the Losses and the Efficiency.....	74
3.4.	Energetic Macroscopic Representation	76
3.4.1.	Elementary MSBA Cell	77
3.4.2.	Two and Three MSBA Stages.....	80
3.4.3.	Three MSBA Stages with Output Stage	83
3.4.4.	Boost stage	84
3.4.5.	Four Stage MSBA Converter	85
3.4.6.	Simulation.....	86
4.	Control.....	93
4.1.	Linearized Fast Feed-Forward	93
4.1.1.	Introduction.....	93
4.1.2.	The Boost Stage.....	93
4.1.3.	The MSBA cell.....	98
4.1.4.	Controlled Boost Stage with MSBA Cell as “Load”	102
4.1.5.	Multilevel MSBA Converter	107
4.1.6.	Start-Up of the 4-Stage MSBA Converter	118
4.1.7.	Energetic Macroscopic Representation and the LFF Control	120
4.2.	State Space	130
4.2.1.	Description	130
4.2.2.	Mathematical Equations	130
4.2.3.	State Space Approach.....	132



4.2.4.	State Space Computing with MATLAB.....	134
4.2.5.	Root-Locus Method	139
4.3.	Observer Control	145
5.	Prototype and experimental results.....	151
5.1.	The Prototype	151
5.2.	Control Platform.....	154
5.3.	Linearized Fast-Feed Forward Measurements.....	155
5.4.	State-Space measurements.....	158
5.5.	Observer measurements	160
6.	Conclusions and Future Research	163
6.1.	Summary and Conclusion	163
6.2.	Future Prospects.....	165
7.	Appendix.....	167
a)	Safety considerations	167
8.	Bibliography.....	169
8.1.	List of Figures.....	169
8.2.	List of Tables	175
8.3.	References	177
8.4.	Curriculum Vitae.....	183





List of Abbreviations

DAB – Dual Active Bridge

EMR – Energetic Macroscopic Representation

ESS – Energy Storage System

HP – High Power

HVAC – High Voltage Alternating Current

HVDC – High Voltage Direct Current

LFF – Linearized Feed-Forward

LP – Low Power

LQR – Linear Quadratic Regulation

LV – Low Voltage

MFT – Medium Frequency Transformer

MSBA – Multistage Stacked Boost Architecture

MVDC – Medium Voltage Direct Current

PCB – Printed Circuit Boards

PLL – Phase-Locked Loop

PWM – Pulse-Width Modulation

RSC – Resonant Switched-Capacitor

STATCOM – Static Synchronous Compensator

ZCS – Zero Current Switching

ZVS – Zero Voltage Switching





List of Main Symbols

A – area	R_S – capacitor series resistance
A_{cu} – conductor section	R_{SA} – line resistance
d – duty cycle	T_a – non conducting time
D_j – current density	t_f – fall time
D_p – power density	T_{on} – conducting time
E_{off} – turn-off switching energy	T_p – switching period
E_{on} – turn-on switching energy	t_r – rise time
f – switching frequency	u_C – capacitor voltage
i_D – diode current	u_D^* – diode voltage contribution
i_L – inductor current	u_L – inductor voltage
i_T – transistor current	u_T^* – transistor voltage contribution
I_{peak} – maximum current	V_{CEO} – zero current collector emitter voltage
I_R – reverse plateau current	V_{DS} – breakdown voltage
k_1 – inductor core material	V_e – inductor core volume
L – length	V_R – reverse plateau voltage
L_{SA} – subarea line length	V_{to} – diode threshold voltage
R_c – IGBT onstate resistance	ρ – copper resistivity
R_D – dynamic resistance	η – efficiency
$R_{DS(on)}$ – MOSFET onstate resistance	λ – Eigenvalue



1. Introduction

1.1. Motivation

Nowadays electrical energy generation is an important topic discussed in the society. More and more focus is put onto regenerative and CO₂ friendly generation technologies. Since technologies like wind or solar energy generation are most of the time placed far away from the city centres one point to focus on is the transmission of the energy. Balancing electrical energy generation and energy consumption like e.g. between offshore wind farms in the North Sea and industrial centres in southern Germany, using HVDC transmission seems to be the best approach and is under evaluation. Besides having to transmit the renewably generated energy over long distances another problem of grids with a high content of renewable energy is the issue of stabilizing such grids. Traditional grids are stabilized by the inertia of the rotating masses of the generator. Energy sources like solar cells don't have any inertia, i.e. this effect is not available in grids with a large amount of energy generated via solar cells. In order to make stabilization easier, an approach is to split the traditional large grids into smaller portions (*sub-grids*) that are only weakly coupled to each other and stabilize these *sub-grids* individually. Such a *sub-grid* could not only be operated as an AC system, but also as a DC system. In order to evaluate the opportunities of DC-distribution within the energy distribution system there is also need for research in medium voltage DC distribution since this could be an important part of a complete distribution grid.

Within the renewable energy generation, medium voltage collection grids are applied to collect the energy from wind turbines in a wind farm or from the solar cells in a solar farm. Today these medium voltage collection grids are almost exclusively realized as AC-grids as an intermediate level of distribution from low to high voltage. The energy production density per square meter of solar or wind farms is low compared to conventional power plants. The renewable energy resources are scattered in their locations. The collection grids within these farms have to bridge quite long distances and the losses in the internal cabling of such a farm can be quite substantial. This has led to thoughts of realizing local medium voltage distribution as DC. The problem of losses in the AC collection grids becomes even more severe due to the fact that the solar and wind parks are getting bigger in their size with the aim to reduce the investment costs. Background for the aim to reduce investment costs is to be seen in reduced subsidies for renewable energy generation, i.e. a reasonable amortization time for the investment can only be achieved if costs go down. Under the aspect of amortization also the losses become more important, because energy lost before fed into the grid doesn't generate income. Extending the structures proven to be sufficient for small or medium size wind or solar farms to large installations will not improve the conversion efficiency. Especially for solar energy, which is generated as direct current, it is an obvious alternative that the energy collection inside the park could be done on a DC medium voltage level. This requires DC-DC converters connecting the low voltage DC output of the solar cells to medium voltage DC.

Therefore, medium voltage DC-DC converters needed to be researched and analysed for possible use in DC distribution and collection grids.

1.2. Application Cases

Before going into possible medium voltage DC-DC converter topologies, it is useful to analyse typical examples for applications where such a converter could be used. In regards of renewable energies and new grid structures, that are being developed, two main applications are considered here.

The first one is a microgrid application since nowadays a lot of thought is put into self-supplying industry complexes. Big industries are investing more and more money into solar energy generation on their facilities to generate some of their energy on their own. To use this energy efficiently it is also considered to include an energy storage system into their facility energy management system. Realizing such structure will result in new requirements for the converters on such a facility and is opening opportunities for new technologies.

A special type of microgrid, but probably a niche application, could be in the field of ship grids that are proposed to distribute the energy using a DC-distribution grid. For small vessels a low voltage DC-distribution has already been realized [1], [2]. Within large ships, medium voltage DC distribution has been discussed. Although the medium voltage DC-DC converters evaluated in this thesis might find application also in ship grids, the special requirements for this application are not considered here.

The second application considered is the regenerative energy generation where a lot of research is invested into the question of how to integrate them into the grid [3]. Especially solar power plants might prove quite suitable since the electrical power generated by the solar cells is already DC and would not need to be transformed. This means it is expected to be advantageous to replace existing AC inverters and transformers with a DC-DC converter, which could also at the same time increase the voltage level to a medium voltage range, reducing the transmission losses. Of course replacing existing structures might have too high costs, but for newly planned solar parks this could improve the energy efficiency of the power plant, especially if it is a high power plant using a considerable amount of surface. There also might be some applications for wind power systems if the energy will be transported through HVDC, lines which would make a transformation needed beforehand. Although energy collection in a wind farm might be done using a medium voltage DC grid, an additional DC-DC conversion were required connecting medium voltage DC to high voltage DC, which is not in the scope of this thesis.

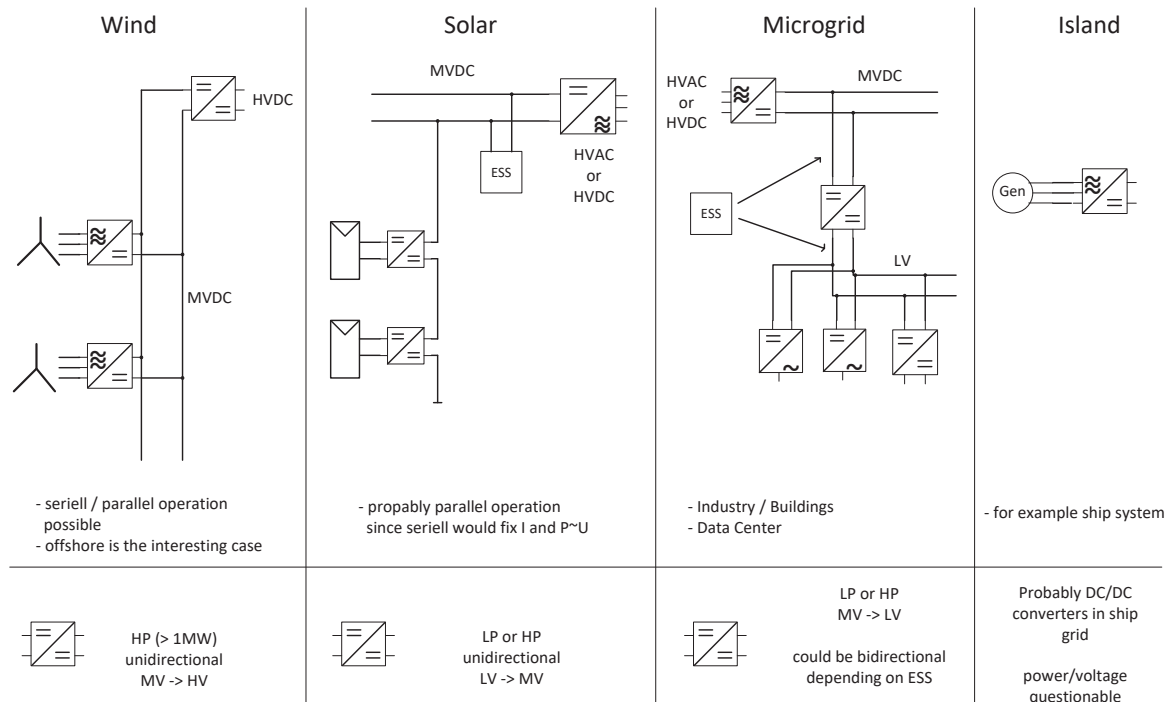


Figure 1: Possible applications for a medium voltage DC-DC converter

It is obvious that these different applications (Figure 1) would have different requirements for a DC-DC converter. The energy flow could be uni- or bidirectional, the converter could be isolated or not, the power level could differ from low to high power and the transformation could be on different levels, meaning for example from medium voltage to high voltage or from low voltage to medium voltage etc. As mentioned before the wind and ship grid application will not be considered more deeply instead concentrating on a possible industrial microgrid or solar park application. For a solar park the requirements for a medium voltage DC-DC converter would be a conversion from low voltage to medium voltage and it would be sufficient for the converter to be unidirectional.

1.3. Example for an Industrial Microgrid

To get a better picture of which kind of converters could be needed in a microgrid application an example for a microgrid is introduced. This possible microgrid application is done for a small industry complex, which while could appear like this in real situations. For connecting the industry complex to the grid a 50MVA transformer will be used as connection to the transmission line. This microgrid also includes several 5MW drives, some smaller drives, some small consumers, cooling units and an air condition system. It is important to consider that some of the drives might have a fixed speed or a variable speed since this changes the requirements for the connected converters. There will also be some energy production by a small solar plant as well as an energy storage system to use the generated energy most efficiently. This microgrid structure is reproduced three times in this section for comparison

purposes; first with a conventional AC distribution, second with a pure DC distribution and last with a hybrid distribution since it could be beneficial for some parts to be distributed with ac while others would run more efficiently with dc. For the AC distribution it might be needed to include a STATCOM so this will also be taken into consideration.

The first microgrid variation, the AC microgrid, can be seen in Figure 2.

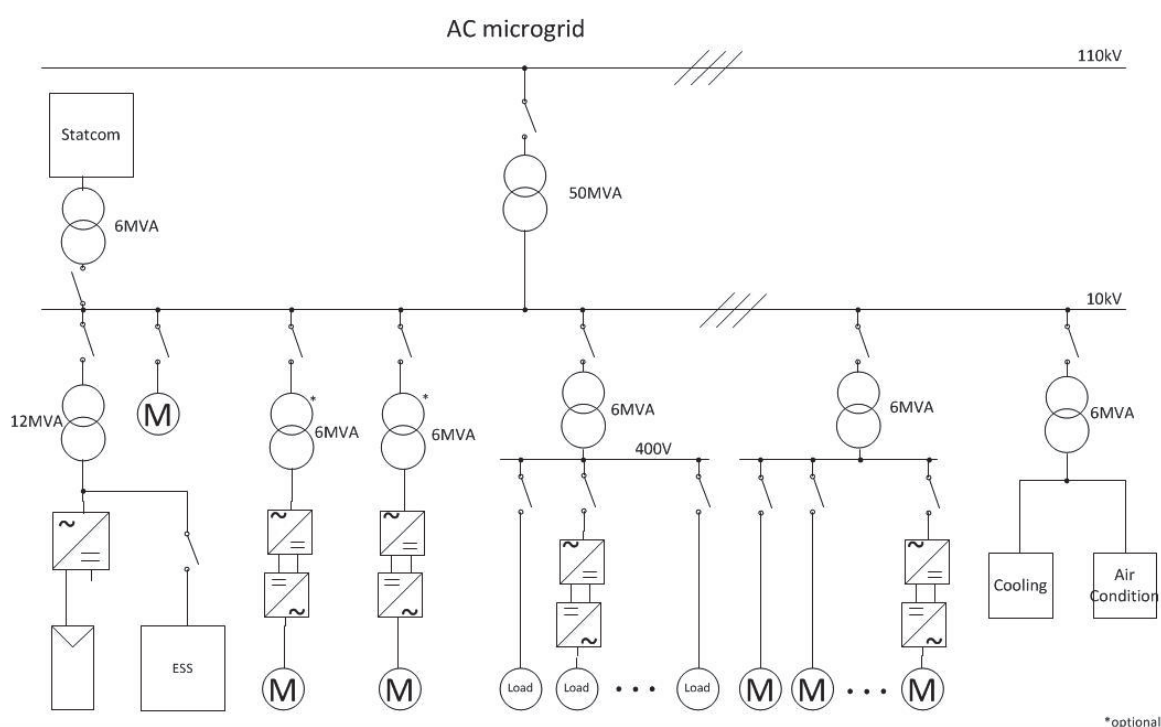


Figure 2: Possible AC microgrid structure for a small industry complex

As can be seen a microgrid based on AC transmission will include AC-AC converters to regulate the output of the drives with variable speed as well as provide the required voltage for loads that can vary in their needed voltage supply. There will also be many transformers to bring the voltage from a medium voltage level to a low voltage level. It is important to consider that these transformers will surely be needed for small loads and drives but they can be optional for the main drives if the AC-AC converters can operate at the medium voltage distribution voltage line directly. It is also required to include a DC-AC converter to connect the solar plant to the industry complex distribution grid.

All in all, for this example there would be 4 AC-AC converters, one DC-AC converter as well as 5 fixed transformers to connect the different components to the medium voltage bus bar with two possibly additional transformers for the main drives depending on the converters used. But it has to be kept in mind that an AC-AC converter is actually a combination of an AC-DC converter and a DC-AC converter, so the actual number of converters is higher than it seems at a first glance. And finally there is one big transformer to connect the medium voltage line to the AC distribution grid outside of the industry complex.

In comparison, the DC microgrid shown in Figure 3 will need only one transformer. All the components can be connected to the medium voltage line by using either DC-DC or AC-DC converters. Of course instead of the transformers mentioned before there are additional DC-DC converters required for the low voltage consumers to bring the voltage to an acceptable level. And in the end there also needs to be one final DC-AC converter as well as one large transformer to connect the DC microgrid of the industry complex to the AC distribution grid which is in place nowadays. All in all, such a microgrid would need 5 DC-DC converters, 6 AC-DC converters and the DC-AC converter and transformer combination for the grid connection. In a pure DC-distribution grid, even loads that only require a fixed frequency AC supply need to be fed by power electronic converters.

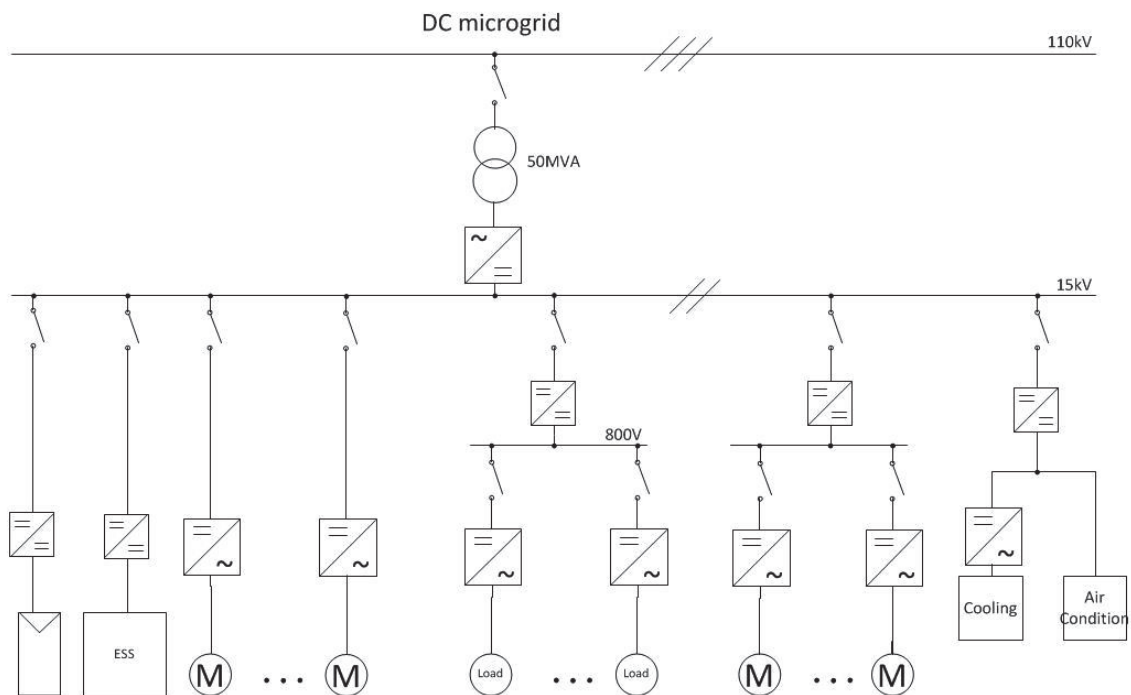


Figure 3: Possible DC microgrid structure for a small industry complex

So the best solution could probably be a Hybrid microgrid (Figure 4) where part of the distribution is done in AC and part in DC. This leads to the lowest number of converters and transformers to be used in order to keep the losses at a minimal level. Such a hybrid microgrid would connect the drives, which do not need any converter and just a transformer to an AC medium voltage line, while the other components would be connected to a DC medium voltage line reducing the numbers of converters that would be needed with an AC distribution. The DC medium voltage could then be transformed to the AC medium voltage level before going with a transformer to the grid distribution line. To conclude this microgrid would be made up of 4 DC-DC converters, 4 AC-DC converters, one smaller transformer, one DC-AC converter as well as the large transformer for the grid connection.

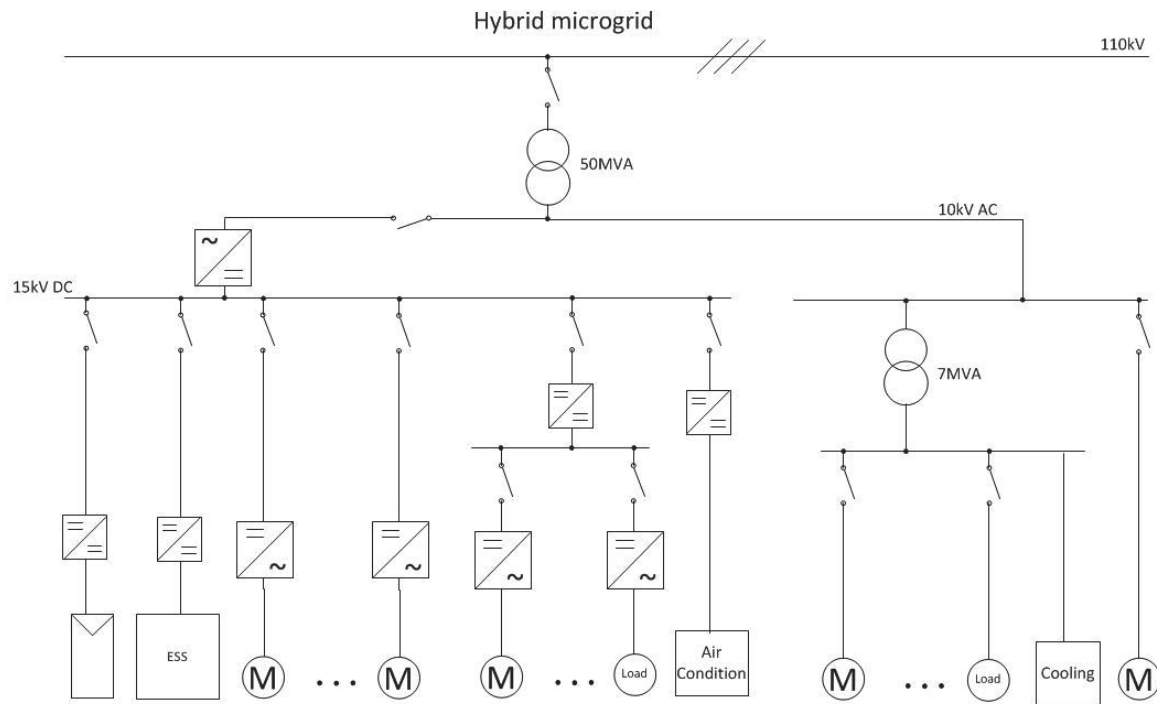


Figure 4: Possible Hybrid microgrid structure for a small industry complex

After qualitatively comparing the possible configurations for an industry microgrid, it is important to make a comparison between the different solutions in regards of components and possible efficiency. Therefore, the following typical efficiencies according to the industry for the components will be used for a general comparison.

Table 1: Losses of components inside the microgrids

Component	Losses
Transformer > 10MVA	0.4%
Transformer > 1MVA	0.5%
Transformer < 1MVA	0.6%
DC-DC converter <5MVA	1%
DC-DC converter >5MVA	0.8%
DC-DC converter (controlled) <5MVA	1.5%
DC-DC converter (controlled) >5MVA	1.2%
AC-DC or DC-AC converter 5 to 20MVA	0.8%
AC-DC or DC-AC converter 1 to 5MVA	0.9%
AC-DC or DC-AC converter ≤ 1MVA	1.2%
STATCOM	0.9%

If these values are used to compare the efficiency of the possible microgrids, the following results are obtained:

AC microgrid: 98.1%

DC microgrid: 97.5%

Hybrid microgrid: 98.4%

This look at the microgrid application leads to the conclusion that for a smart implementation of a microgrid a hybrid solution would be the best and there would be a need for several different kinds of medium voltage DC-DC converters. For example, for the energy storage system the converter needs to be bidirectional while the converter for the solar energy generation is only unidirectional. In regards of voltage levels these would all be for low to medium voltage elevation or for raising the voltage to the medium voltage range.

However, since the microgrid application is not the only case of interest the solar energy generation will be considered next. Such a converter would be unidirectional and would need some control for the varying input voltage and would raise the voltage from low to medium voltage level. To get a better view at the requirements of such a converter, a case study is done based on the power plant “Agua Caliente” which is one of the biggest solar plants realized at the moment. In addition, requirements considering the safety of the converter and the plant can be found in Appendix A.

1.4. Agua Caliente

While there are many general reports about the Agua Caliente solar plant ([4]-[6]) because of its impressive size and the huge amount of power that can be generated, technological facts are sparse. Thus the described structure of the power plant is only a possible structure, based on the publicly known facts and the most logically layout in accordance with other solar plants. Facts are that the solar plant will produce 250MW (AC peak), is connected to a 500kV transmission line, is using 400 central converters (type SMA Sunny Central 720 [7]) and every solar string is made of 15 FirstSolar solar modules [8] in series and that several of these strings are connected in parallel to raise the current level. These connected strings are called a solar-array and each array is connected to one of the central converters. After that there are several possible ways for the distribution to be implemented. According to an SMA datasheet [9] it would be possible to connect two of these converters to a transformer to raise the power, but it is not clear if this is used in the Agua Caliente solar plant or if it is just one converter per transformer. So even if these facts and the datasheets give a good indication about the project some questions remain (see Figure 5), like for example what the medium voltage level is and how the energy distribution inside the park is actually done. Due to the fact that the plant is in the United States, most probably the medium voltage distribution voltage is 34.5 kV. The other standardized medium voltage of 13.8 kV would be quite low for a 250 MW installation. The arising question now is if for example the DC-AC converters and the transformers could be replaced by DC-DC converters. Or more clearly could

something like that be competitive in regards of efficiency and costs. It has also to be taken into consideration that it would make a difference if the solar plant would be connected to a high voltage AC or DC transmission line.

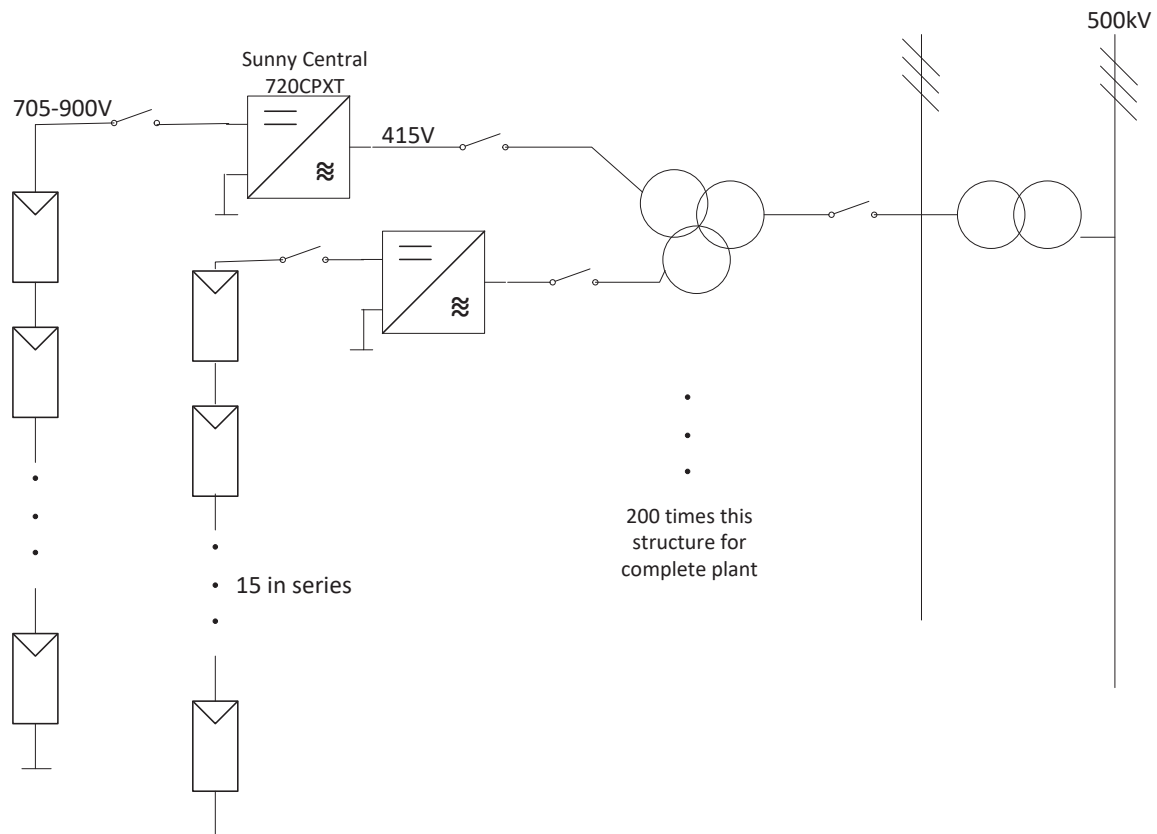


Figure 5: Structure of Agua Caliente Solar Plant

The next step would be to have a look at another important facet of the solar plant and that is the length of the transmission lines inside a solar power plant and the losses introduced by them in regards to the size of the solar power plant and if these issues could be improved.

1.5. Transmission Losses in Regards to Solar Plant Size

For considering if a change from an AC converter and a transformer to a DC-DC converter would be competitive it is important to take into account the size of such a power plant and the energy collection system inside the plant. Nowadays photovoltaic plants have become an important contributor in generation of electrical energy, generating hundreds of MWs, and a lot of research is therefore invested into studying such systems [10], [11]. To achieve these power levels, a huge number of solar panels need to be installed, using a large surface area. Covering such a large area, where the energy is generated, means that the power must be collected over long distances, which leads to a low efficiency if the energy

transmission is done under low voltage conditions. A better efficiency could be expected by increasing the voltage to a medium voltage level using a DC-DC converter, resulting into an interest into the research of possible DC-DC configurations for the photovoltaic plant grid [12], [13]. To illustrate the sizing of large photovoltaic plants, which is related to the efficiency problem of the farm internal energy transmission system [14], Figure 6 shows the power density; the relation of generated energy to covered area which are values that are publicly available for realized large photovoltaic plants. As can be seen the resulting numbers for energy to surface area are not very impressive and are stuck around 30 W/m^2 or even lower for the large power plants that were realized not long ago.

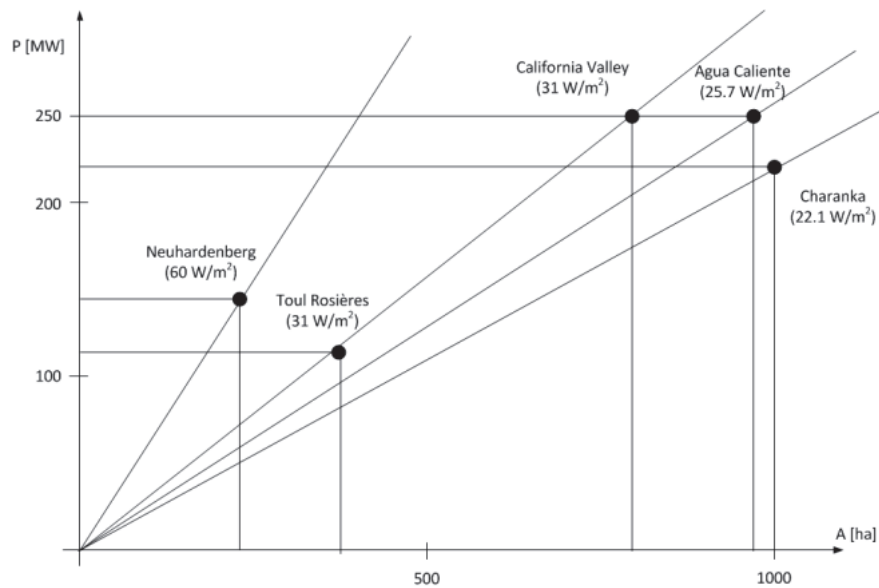


Figure 6: Examples of power to area relation for actual PV plants

To better analyse the problem of low energy generation to surface area as well as considering problems this causes in the energy transmission inside the power plant it is important to understand how such a power plant functions. Normally a photovoltaic plant is divided into several subareas (Figure 7) and in each subarea the energy is collected through low voltage DC lines and then converted to low voltage AC. Each subarea additionally has an inverter transformer, which elevates the voltage to medium level. These voltages are then collected and finally elevated to a high voltage range for better transmission over long distances.

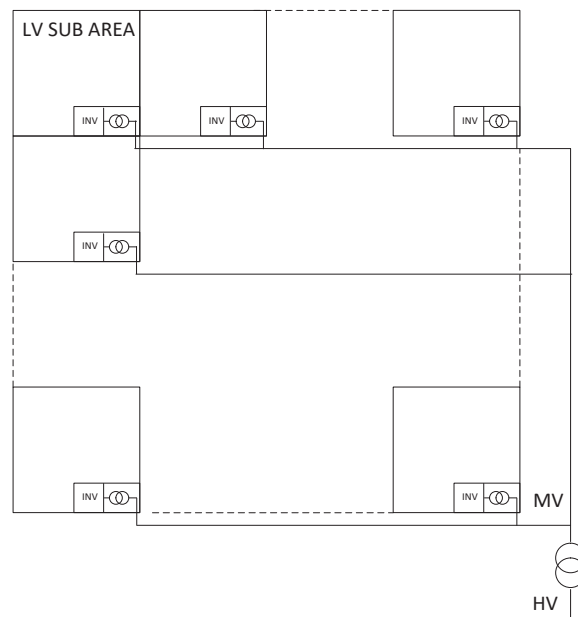


Figure 7: Scheme of subarea divisions in a PV plant

The subareas (Figure 8a) consist of several solar cell arrays (Figure 8b) which normally have an inverter input attached to convert the low DC voltage (~1KV with modern solar modules) to a low voltage AC (normally around 400-600V depending on the converter that is used) [15]. The low voltage is elevated to medium voltage by a transformer.

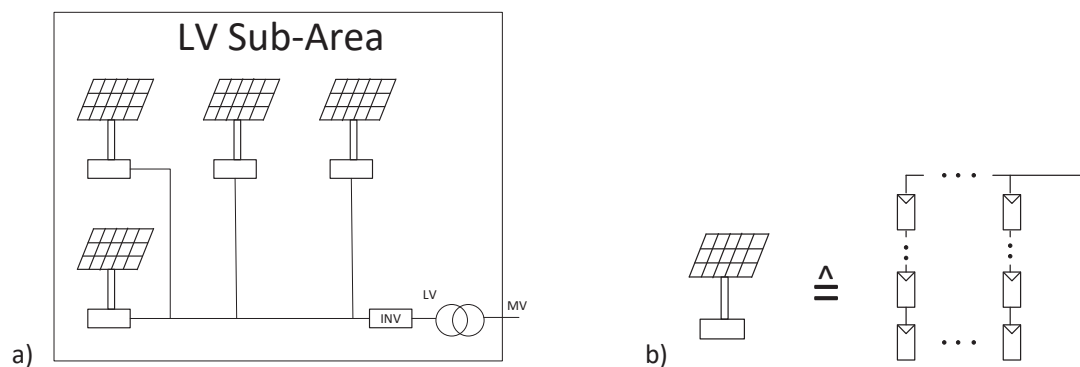


Figure 8: a) Interconnections in a PV plant subarea, b) Structure of a solar array

A different solution (Figure 9) could be a system where the power collection inside one subarea is realized by using a DC-DC converter allowing the elevation of the voltage of the collection-lines inside of one subarea. This voltage rise will result in an increase of the energy efficiency of the internal transportation lines, but the effects of one additional power electronic conversion must be taken into account, influencing the overall efficiency. Of course if the whole power plant is connected to an HVDC transmission line the additional conversion to AC could be omitted while increasing the efficiency of the whole structure.

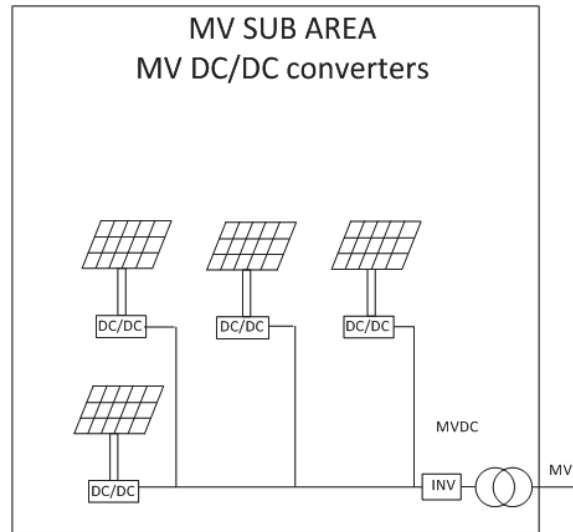


Figure 9: Alternative PV plant subarea configuration with use of DC-DC converters

To further analyse the possibilities of a change from low voltage to medium voltage the next section will define the needed formulas to characterize the advantages of the voltage elevation and the drawbacks of an additional conversion.

Photovoltaic plants, having a large surface area, show long distances from the solar modules up to the point where the power level reaches the area of hundreds of kW or even MWs. Therefore, the transmission efficiency is of great importance and will be calculated in the following part. To simplify this calculation only the line ohmic resistance will be used.

While there are some considerations of how to connect the solar arrays in regards of thermal aging and life time of connection cables [16], in relation to the electrical efficiency the rule “the shorter the cables the better” is obvious. It is assumed that every subarea (Figure 10) has an inverter and one transformer collecting the power of several solar cell arrays, which is placed at the corner of the subarea. Connecting the solar cell arrays to the inverter along the x- and y-axis means that the current is transported through a line with the length of $L_{xSA} + L_{ySA}$.

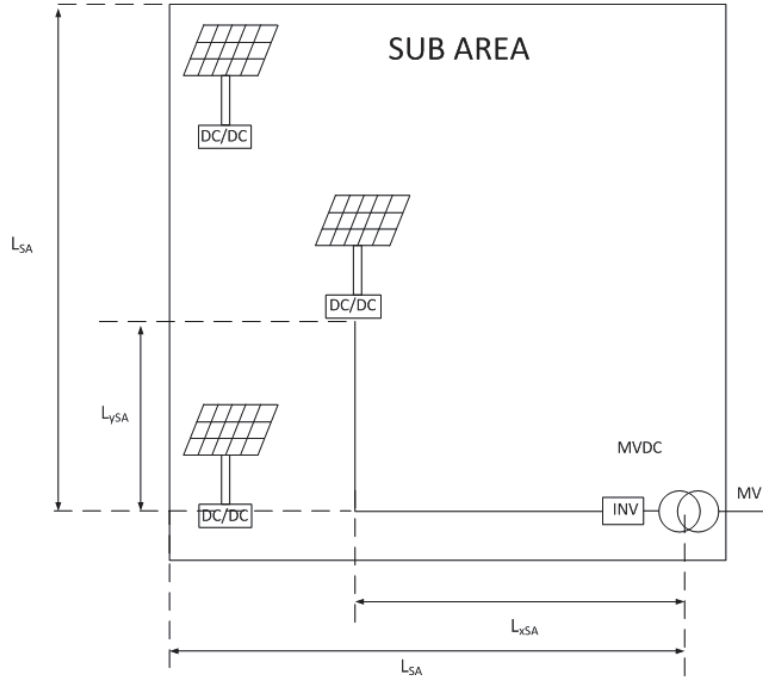


Figure 10: Wiring in a subarea

This means the total current that is transported in the subarea (using one equivalent line) can be calculated by using the mean-value of the sum of the x and y lengths in [m]:

$$L_{totSAmean} = L_{xSAmean} + L_{ySAmean} = \frac{0 + L_{SA}}{2} + \frac{0 + L_{SA}}{2} = L_{SA} \quad (1)$$

The resistance of these lines, which is also depending on the conductor section A_{cu} , is

$$R_{SA} = \frac{\rho \cdot L_{SA}}{A_{cu}} \quad (2)$$

with ρ being the copper resistivity of $17 \cdot 10^{-9} \Omega m$.

Now the voltage drop ΔU introduced by the line current can be calculated by

$$\Delta U = 2 R_{SA} \cdot I = 2 \frac{\rho \cdot L_{SA}}{A_{cu}} \cdot I \quad (3)$$

For the following calculations a current density in the copper lines of $D_j = 10 \text{ A/mm}^2$ will be used, of course this value might differ from case to case. The factor 2 considers 2 wires of one interconnection.

The relation of current, conductor section and current density can be described as

$$I = A_{cu} \cdot D_j \quad (4)$$

If this is now inserted into the voltage drop calculation, the formula will change to

$$\Delta U = 2R_{SA} \cdot I = 2 \frac{\rho \cdot L_{SA}}{A_{cu}} \cdot A_{cu} D_j \cdot 10^6 = 2\rho L_{SA} D_j \cdot 10^6 \quad (5)$$

including the before mentioned copper resistivity this leads to

$$\Delta U = 2\rho L_{SA} D_j \cdot 10^6 = 34 \cdot 10^{-3} \cdot L_{SA} \cdot D_j \quad (6)$$

Now the line efficiency can be calculated by

$$\eta = \frac{U - \Delta U}{U} = \frac{U - 34 \cdot 10^{-3} \cdot L_{SA} \cdot D_j}{U} \quad (7)$$

with U being the line voltage in [V]

For power plants, the power density D_p can be expressed in $[W/m^2]$. Taking into account that the power density of the complete plant is identical to the power density of one subarea, the dimension of one subarea can be calculated by

$$L_{SA} = \sqrt{\frac{P[W]}{D_p[W/m^2]}} \quad (8)$$

It has to be paid attention to the fact that the power for this calculation is the power in one subarea. So either a variable calculation for different L_{SA} can be done based on common converter power levels used in photovoltaic plants or for realized power plants the actual values can be calculated by knowledge about the used converters. Table 2 shows the estimated line lengths of the subareas of the photovoltaic plans shown in Figure 6 based on converters used.

Table 2: Estimated L_{SA} of actual PV plants

Photovoltaic plant	L_{SA}	Total Power
Agua Caliente	155m	250MW
California Valley	130m	250MW
Charanka	150m	221MW
Neuhardenberg	100m	145MW
Toul Rousières	125m	110MW

In Figure 11 a more general approach is taken and the length of one subarea L_{SA} is represented as function of its chosen power level. On the horizontal axis, power levels between 200kW and 3MW, which correspond to power values of industrial converters, are represented. This representation is calculated on the base of a power density of the subarea equal to 30 W/m^2 .

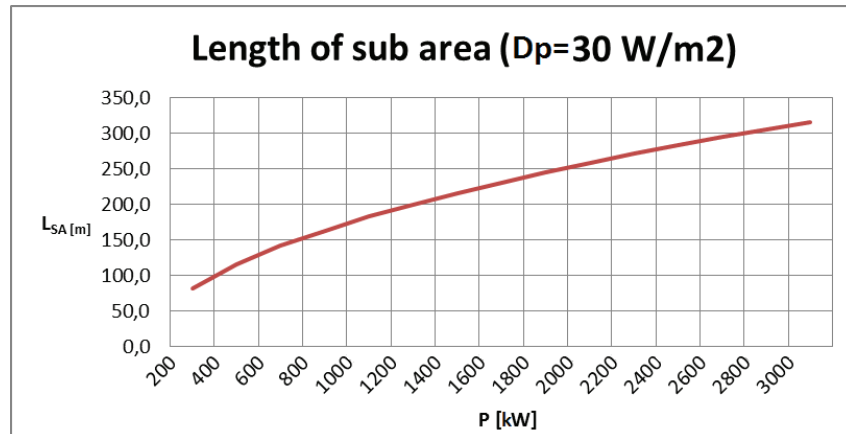


Figure 11: Dimensions of a subarea depending on the power level

For a comparison of the energy efficiency of a line depending on the subarea length L_{SA} three values of the line voltage U were considered, 800V, 1600 V and 3200V. The first value corresponds to the value of a DC voltage at the DC-link side of one inverter that is connected to one 400 AC line. The values of 1600 and 3200 V correspond to the voltage at the output of one DC/DC converter where the voltage is doubled, respectively quadrupled. These voltages would also correspond to the DC voltage of a large MV inverter to be used for one large sub-area. As can be seen in Figure 12 the efficiency starts to decrease notably with low voltage levels and long lines.

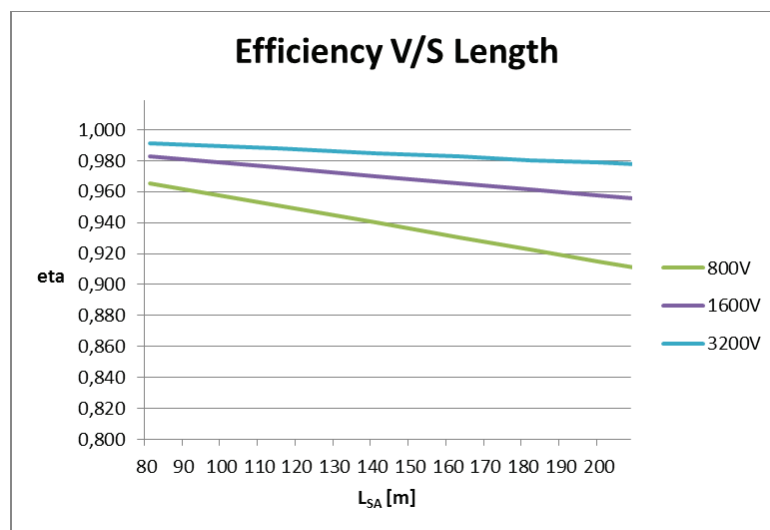


Figure 12: Energy efficiency of the collection lines in a subarea

So to improve the efficiency the addition of a DC-DC converter directly at each solar cell array could prove to be useful.

For a photovoltaic plant a non-isolated step-up topology could be reasonable in terms of efficiency. To get an impression on how such a converter could improve the energy transmission in a solar plant it is assumed that such a converter would have an efficiency of at least 97%. Using this number an efficiency

comparison between a normal 800V subarea transmission and variants including a DC-DC converter can be done. The first case uses a simple two stage topology where the input voltage is doubled and the second quadruples the input voltage. Figure 13 shows that this becomes more efficient after a mere hundred meters.

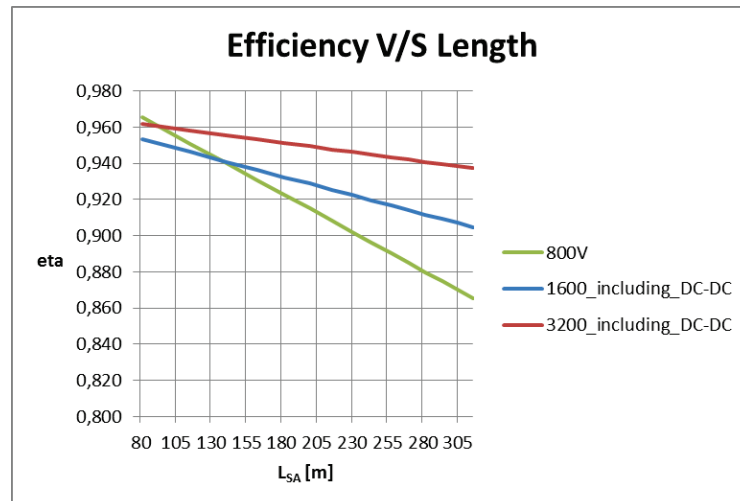


Figure 13: Comparison of the efficiency with included DC-Converter

Comparing these results to the subarea line lengths of actual power plants (Table 2) it becomes apparent that the use of a DC-DC converter is a realistic way to increase the electrical energy production for large photovoltaic plants like realized nowadays. The comparison shows that using a DC-DC converter would become more efficient than the conventional method after a mere hundred meters, which is realistic in regards of the subarea transmission line length of realized large photovoltaic plants. Of course the addition of a DC-DC converter will increase the costs of a photovoltaic plant, but considering the increase of efficiency leading to an increased electrical energy production it might prove cost-efficient especially if one keeps in mind that medium voltage converters normally have a higher efficiency than low voltage converters.

For comparing the solutions for large solar plants, not only the efficiency has to be considered but many other features that are listed in the following table as advantages and disadvantages, not further quantified in the research.

Table 3: Advantages and disadvantages of using low voltage AC converters

Advantages:	Disadvantages:
High modularity	Many components
High redundancy	High failure rate
High standardisation	Low power density
Easy expandability	Mediocre efficiency <98%
Good costs	Complex control
	Energetic break-even quite late?

Table 4: Advantages and disadvantages of using medium voltage DC converters

Advantages:	Disadvantages:
Good modularity	Many components
Good redundancy	Probably higher costs
Good standardisation	Needed efficiency of 99% to compete
Easy expandability	Might only prove more efficient if connected to HVDC
Cascading structures	Complex control
Useable for DC microgrids	Energetic break-even quite late?
Easy connection to energy storage systems	
Lower transmission losses	

This comparison shows that both methods, the nowadays used low voltage AC distribution as well as the medium voltage DC distribution, have advantages. And with an increasing size of the solar power plants the medium voltage distribution could become more efficient and even cheaper as the AC distribution. Therefore, a suitable DC-DC converter topology and the photovoltaic plant configuration are worth more research in the near future.

1.6. DC-DC Converters

Since it has become quite apparent that medium voltage DC-DC converters can prove useful in the future it is important to research what topologies already exist or are researched at the moment [17]. In the field of regenerative energies converters for wind energy regeneration as well as photovoltaic plants could be considered. At the moment there are no MV DC-DC converters for wind energy or photovoltaic systems in commercial use but different topologies have been studied recently. These converter topologies can be separated into isolated and non-isolated. For isolated converters the advantage is the use of low voltage semiconductors at the input and lower isolation requirements for drivers, but transformers for this are difficult to design at high voltage and high power levels. Problems are poor coupling, dielectric losses in insulation as well as core losses. As an alternative non-isolated converter topologies are proposed. Of course, differences in safety requirements have to be considered too, which are different for equipment connected to low voltage installations or to medium voltage installations. But in large plants it could be assumed that the electrical installation components are not accessible for public, i.e. safety considerations are similar to industrial installations, where only trained and instructed personal have access. The required measures to achieve the appropriate insulation coordination are not discussed in detail here, but due to the fact that functional safety can also be achieved by active protection devices (which could be redundant to guarantee a very low risk of major damage), this problem isn't seen as a major hurdle for using non-isolated DC-DC converters.

1.6.1. Non-Isolated DC-DC Converters

One direction the research of converters is taking is to use well known topologies like the boost converter (Figure 14) and replace the switches with silicon carbide devices to increase the efficiency of converters and use them directly for medium voltage distribution [18].

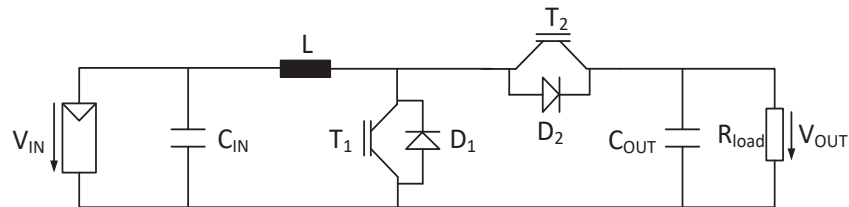


Figure 14: Boost-converter

First simulation and test results showed that it is possible to reach an efficiency of 98.5% for a ~30kW converter if the standard switching devices are replaced by silicon carbide MOSFETs. But while these results are quite encouraging the problem is that while these devices can handle a voltage of up to 10kV the current rating is today only 10A, which would mean that the normal functionality of connecting several solar strings in parallel to increase the current would not work. And this means it is also questionable if a change from the nowadays used system structure to a solar farm relating on such converters would improve better in terms of efficiency, component number and costs. Even these SiC MOSFETs are not commercially available yet and when they go into production there is also the question if they would be cost efficient for use in a converter. Larger SiC MOSFET modules might become available in future, but for 10 kV devices experts agree that those might not become commercially of interest within the coming 10 years.

Another topology, based on the basic buck and boost converters, that is introduced in [19], is a hybrid boost and buck/boost converter which aims to achieve a high step-up conversion ratio (Figure 15). In the paper the approach is to connect a boost converter and a buck/boost converter in series to achieve high-voltage gain in order to achieve the overall goal of replacing common converter technologies with multiple modules of single-switch single-inductor transformerless converters.

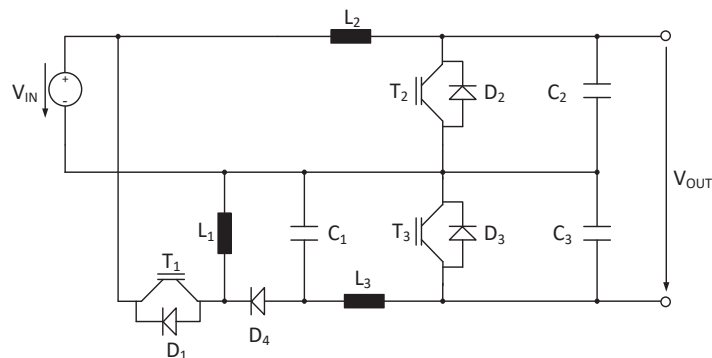


Figure 15: Hybrid boost and buck/boost converter

The paper also compares the use of this converter in a DC collection grid of a wind farm with a typical AC collection grid for offshore wind farms. The use of this converter and the DC grid would reduce the weight of the cables and the magnetic components, but the losses would be slightly higher than in an AC system. Using a diode bridge rectifier could allow a reduction of losses but there would be issues with harmonics. In general, the author sees good opportunities for this approach to become more efficient than the used AC systems especially when SiC devices are broadly available.

In [20] a resonant step-up (RS) converter is proposed, in which a capacitor and one inductor are used to achieve the step-up ratio. Main feature of this converter is that it can achieve soft switching for all switches and diodes, reducing losses. This converter (Figure 16) lets the capacitor voltage C_r change between positive and negative by alternatively firing the switch pairs T_1/T_4 and T_2/T_3 . This change of polarity within the capacitor is controlled with a converter bridge and the defined positive current working region. The commutation of the capacitor current from one converter leg to another is therefore assured and as consequence it is possible to use switches without turn off ability.

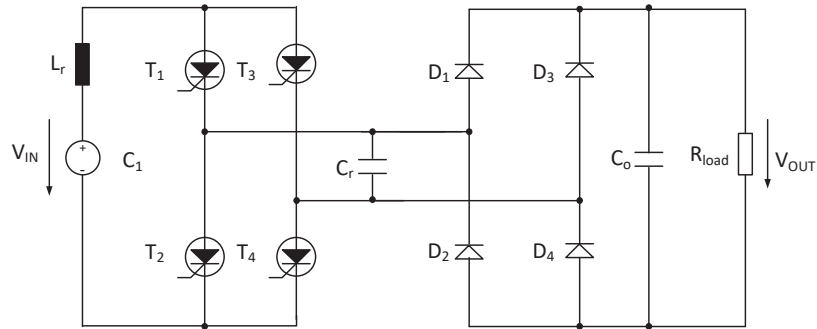


Figure 16: Resonant step-up converter (RS)

A bidirectional version of this RS converter is proposed in [21]. It is based on two resonant circuits, which share a common energy storage capacitor. The topology is simple and utilizes thyristors, which can all soft switch (Figure 17).

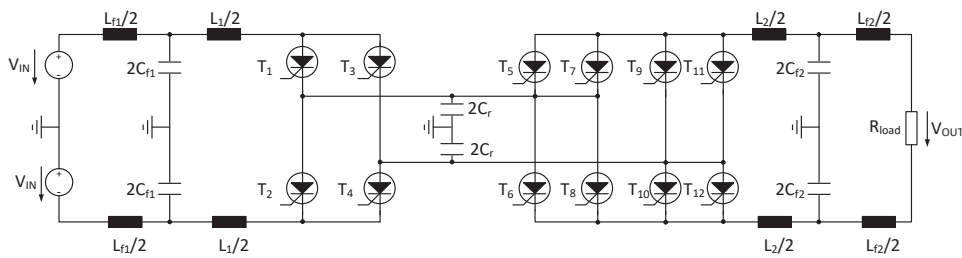


Figure 17: Bidirectional resonant step-up converter with ZCS

This topology can for example be connected to voltage source converters or to a HVDC grid. The interesting part about this topology is that both converter sides operate as resonant converter, so that a resonant (soft) turnoff can be achieved. What makes this converter bidirectional is the fact that it is possible to change the current direction on the high-voltage side and the voltage polarity on the low-

voltage side by choosing the firing angle in the high-voltage circuit. To control this system, the frequency regulation principle is used. This means that the firing frequency is synchronized with the capacitor voltage C_r by using a phase-locked loop (PLL). All in all, the advantages of this converter are a very high gain, zero current switching (ZCS) in the high-voltage circuit, reducing switching losses and it is not vulnerable to commutation failure. On the other side, the cost for the high voltage switches may be considerable and there is a problem with harmonics at lower powers.

Although the use of transformers is avoided in these topologies, high power inductors are needed, which can resist a peak-to-peak voltage across the inductor almost twice the output voltage. Another disadvantage is that the voltage stress of the active switches is equal to the output voltage which increases the conduction losses.

Another approach is a high-efficiency non-isolated resonant switched-capacitor (RSC) step-up converter (Figure 18), which can achieve soft switching for all switches and diodes and has no magnetic component since due to a small value of resonant inductance either a small air-core inductor or the parasitic inductance existing in the circuit can be used [22].

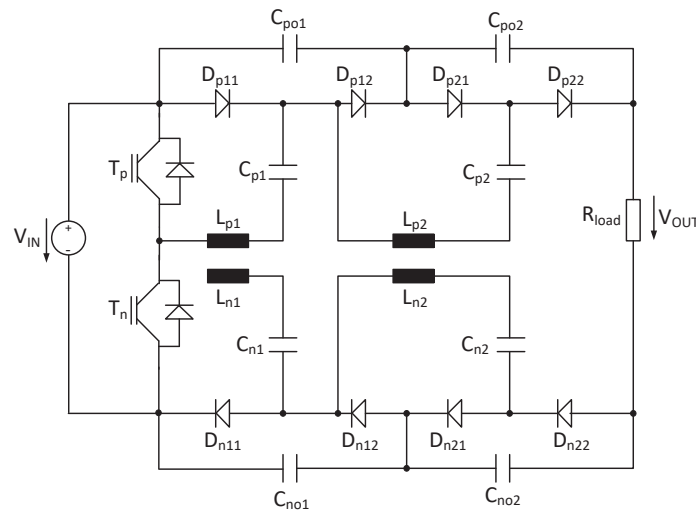


Figure 18: Resonant switched-capacitor step-up converter (RSC)

The switches T_p and T_n are controlled complementary with 0.5 duty cycle. When T_p is turned on, all the negative resonant capacitors (C_n) are charged by the input voltage source or the capacitors (C_{no}) through the resonant inductors (L_n). When the switch T_n is turned instead all the positive resonant capacitors C_p are charged in the same way as the before mentioned negative resonant capacitors. After half of the switching period - when the switching frequency is the same as the resonant frequency - all the currents of the resonant inductors reach zero therefore achieving soft switching. According to the author of this paper this topology significantly reduces the switching losses, increases switching frequency and minimizes the overall system volume in comparison to a hybrid boost and buck/boost or RS converter. But like the topology before this will only be useful once SiC semiconductors become widespread.

Another combination of common topologies is discussed in [23]. Here a boost converter and a LCC resonant converter are combined to achieve a transformerless large voltage ratio converter (Figure 19). This converter is controlled by the duty cycle and the switching frequency to achieve good results for a wide range of line and load conditions. It also offers the advantage of being modular meaning that it is easy to add more units in series or parallel to achieve the desired voltage ratings. The research on this topology indicates that soft switching is achieved and that a high efficiency (96%) is possible.

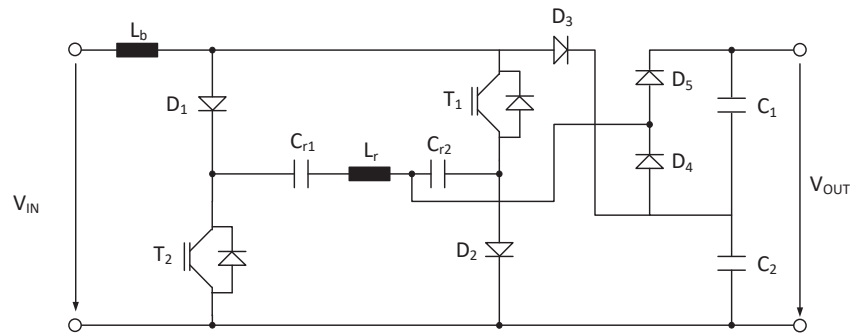


Figure 19: Combined boost and LCC resonant converter

1.6.2. Isolated DC-DC Converters

Of course, there are also common converters depending on electromagnetic transformation. A promising example of these is the LLC resonant converter (Figure 20: LLC resonant converter) with the inductors being elements from the transformer's principle circuit diagram. This converter has many advantages: a wide output load range with reduction of switching losses on the primary side through zero voltage switching (ZVS) and low turn-off current, low voltage stress and zero current switching (ZCS) on the secondary side diode rectifier, as well as the possibility to integrate resonant elements within a transformer. While most publications describe low power MOSFET based designs, with switching frequencies in the range of hundreds of kHz including variable frequency control a realized prototype converter for a high power application is based on a medium frequency transformer (MFT) to provide isolation and increase power density and uses IGBTs ([24] - [26]).

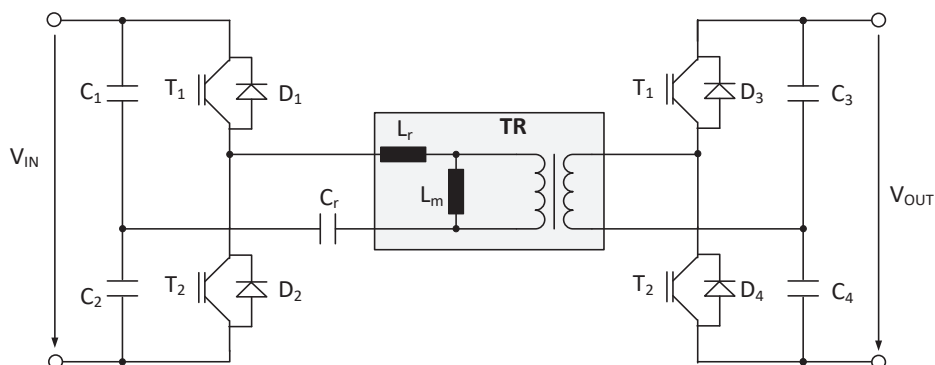


Figure 20: LLC resonant converter

Since the idea of zero voltage switching is very attractive there are also other converters being proposed right now that use it like in [27]. This converter consists of 8 switches at the input that are arranged into two pairs of 4 switches, which are then connected to two modular asymmetrical pulse-width modulated resonant circuits (Figure 21). To step-up the voltage the converter is operated close to the resonant point. Since this leads to the output voltage being sensitive to the switching frequency a constant frequency with duty ratio control is needed. ZVS is then achieved by having the resonant current slightly lagging behind the input voltage. While this topology is certainly interesting the efficiency is not optimized yet (94.2%) and more research has to be done in this field.

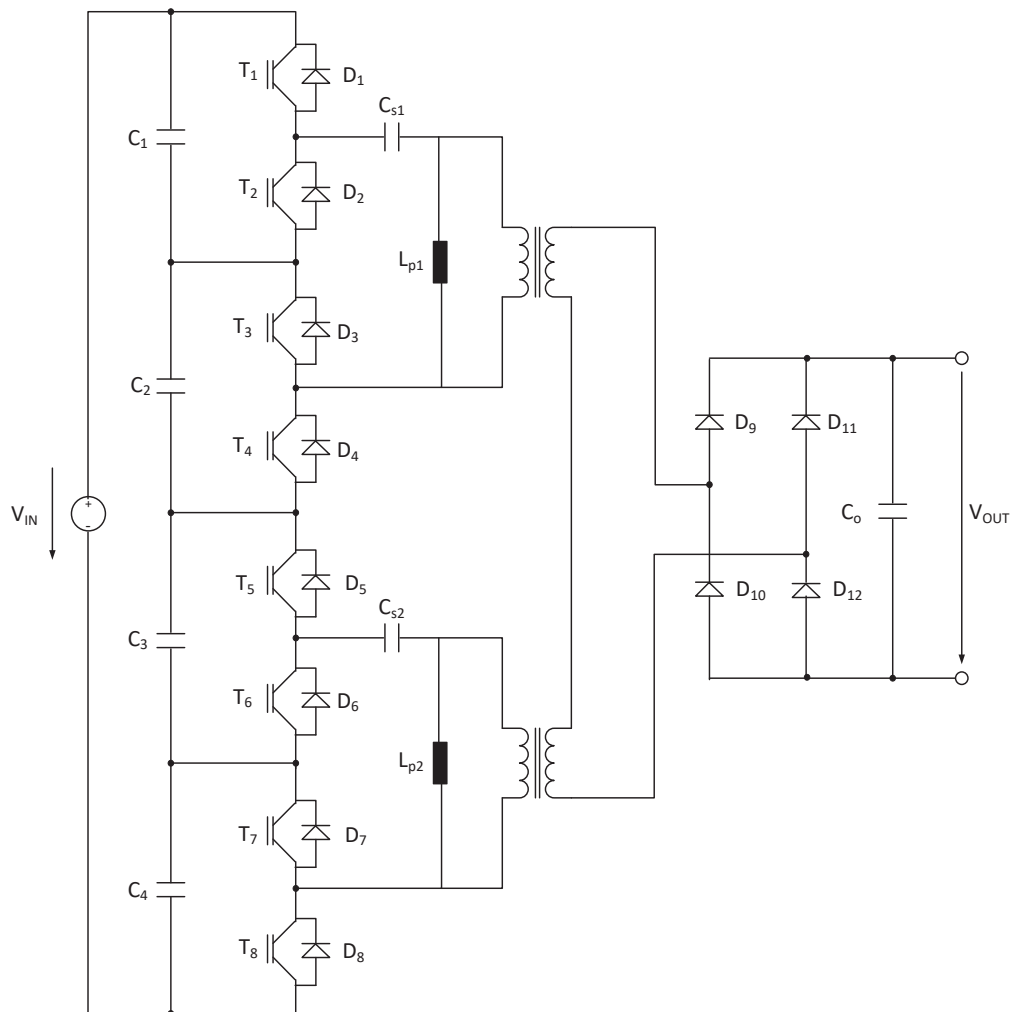


Figure 21: 8-Switch converter with ZVS

There are also converters called Dual Active Bridge (DAB) converters, which are being proposed since the 1990's and can be seen in Figure 22.

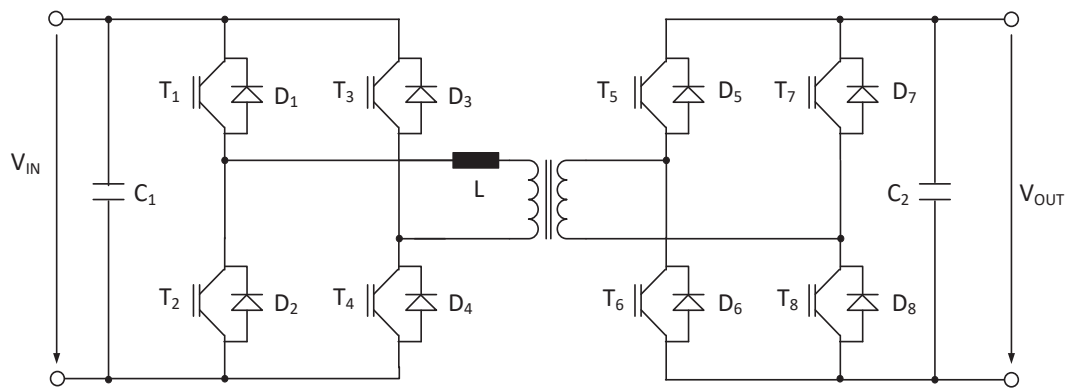


Figure 22: Dual Active Bridge

Another example is a DAB based on an H-bridge on the low voltage side and an NPC converter on the high voltage side (Figure 23) [28]. To increase the output voltage of such a converter often many cells are connected in series-parallel, where the power flow and output voltage are shared between the different levels.

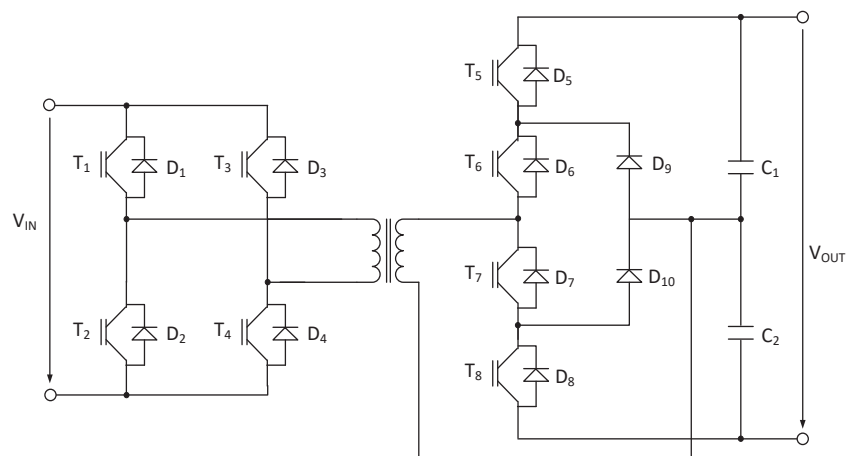


Figure 23: Dual Active Bridge converter with H-bridge and NPC

The main advantage of this topology is that semiconductors with low blocking capability can be used even for medium voltage applications, but it also has an increased short circuit power due to the capacitors. So in case of a short circuit the energy in the capacitors will be consumed resulting in a high short circuit current if no careful protection steps are taken.

As can be seen there is a lot of research going on in the field of medium voltage DC-DC converters. Many of these converters are dedicated to wind energy generation but there is also research for solar power or distribution and smart grids.

2. The Multistage Stacked Boost Architecture

2.1. Current diverter

High power DC-DC converters are not yet in broad use and the optimal topology has not yet been identified. Thus it is still very interesting to research a new topology. This new topology is based on the current diverter topology. The current diverter principle ([29], [30], [31]) has first been proposed and is used to equalize the voltage between different cells, especially balancing series connected supercapacitors. By loading the series connected capacitors but only feeding power into one cell and thus causing a kind of virtual unbalance between the cells, the diverter will distribute this energy to all cells equally and thus can also be used as a DC-DC step-up converter. By loading only one cell and feeding power into the outer terminals of the series connected capacitors, the diverter can be used as a DC-DC step-down converter

A current diverter consists of cells/stages with each stage containing two active switches, a capacitor and an inductor (Figure 24). The principle operation of this topology might be explained by looking at just two neighboured cells, e.g. the cells including C_1 and C_2 and sharing the common inductor L_1 . In case the cell with C_1 has a higher voltage than C_2 , switch T_1 can be turned-on and some energy is transferred into the inductor L_1 . Next T_1 would be turned-off, which results in the current commutating into the free-wheeling diode D_2 and now charging C_2 . In case an energy transfer from C_2 to C_1 is required, T_2 would be turned-on instead in order to transfer energy from C_2 into L_1 and through D_1 , after turn-off of T_2 C_1 is charged. For the energy transfer between the cells including C_2 and C_3 and sharing inductor L_2 , switches T_2'/D_2' and T_3'/D_3' are used, for the energy transfer between the cells with C_3 and C_4 sharing the inductor L_3 switches T_3/D_3 and T_4/D_4 , etc.

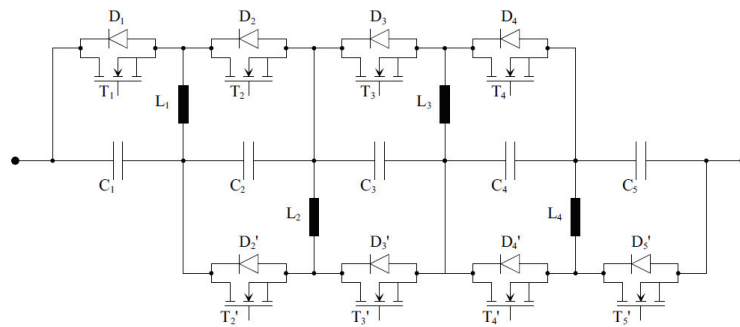


Figure 24: Balancing capacitor voltages with a current diverter topology

The next chapter will explain this topology in more detail, introduce the MSBA family by showing interesting variations based on the idea, give some formulas about the current and voltage levels in the converter and show efficiency calculations as well as simulation results.

2.2. The Elementary MSBA Cell

The elementary MSBA cell is build out of one capacitor, one inductor and two switches with freewheeling diodes. The principle operation of the MSBA topology can be explained by looking at just one cell and a voltage source (Figure 25). When the switch T_2 is turned on energy is transferred into the inductor L_2 . Next the switch T_2 would be turned-off, which results in the current commutating into the free-wheeling diode D_2 and charging the capacitor C_2 .

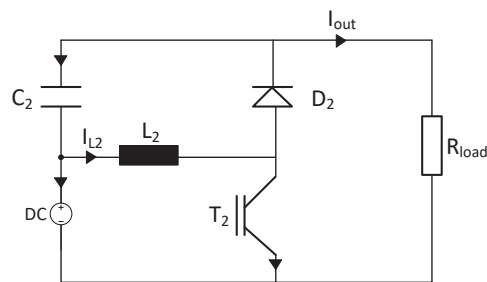


Figure 25: Elementary MSBA cell

If the duty cycle d of the switch is set to 0.5 the capacitor would in steady state be charged equally to the input voltage and the output voltage would be two times the input voltage. This can also be seen in the waveforms shown in Figure 26. This simulation considered the typical design of such a stage with the energy content of the capacitor much higher than the peak stored energy in the inductor. Background for this way of design is the requirement to have on one hand an almost ripple-free dc-voltage output and on the other hand only small inductors. In the simulation the voltage ripple on C_2 is such a small value that it cannot be seen in the scale required to show the full output voltage.

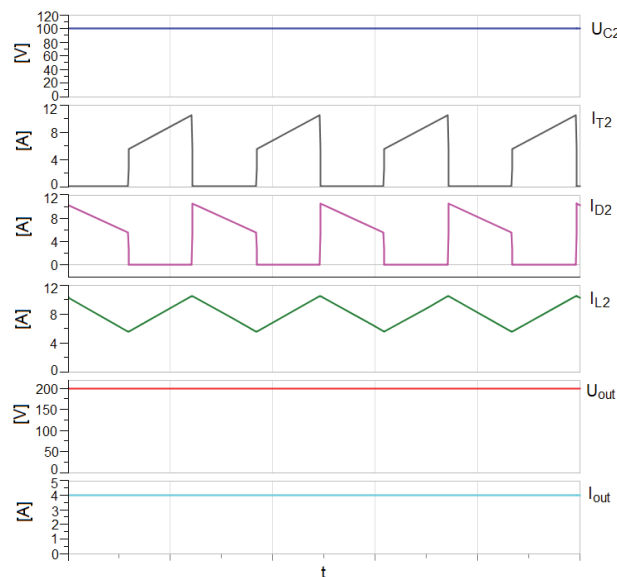


Figure 26: Waveforms of the elementary MSBA stage

To use this topology as converter with constant output voltage even for an open loop control, an input boost stage will be added to provide a constant input voltage for the MSBA cell even for a varying voltage from the primary energy source, which could e.g. be a solar array leading to the Multistage Stacked *Boost* architecture (MSBA). An advantage of this topology is the capability to increase the step-up ratio simply by adding more cells.

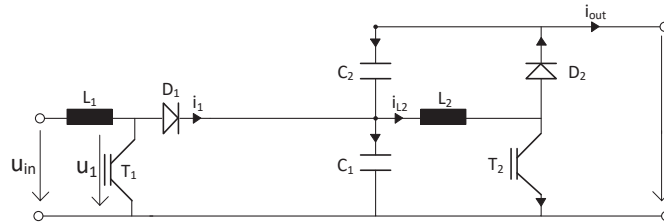


Figure 27: Elementary stage for the Multistage Stacked Boost Architecture

Figure 27 shows the simplest version of this topology with a 1-to-2 ratio, meaning that the output voltage of the circuit has the doubled value of the stabilized input voltage (output of the boost stage). This can be achieved with a simple control of the duty cycle of the switches (fixed 50%). Therefore, the duty cycle d needs to be defined.

2.3. Duty Cycle Definition

The definitions of the duty cycles of the classical buck and boost converters are generally based on the turn-on duration of the used transistors. Figure 28 gives the standard definitions of the respective duty cycles, together with the relations between input and output voltages.

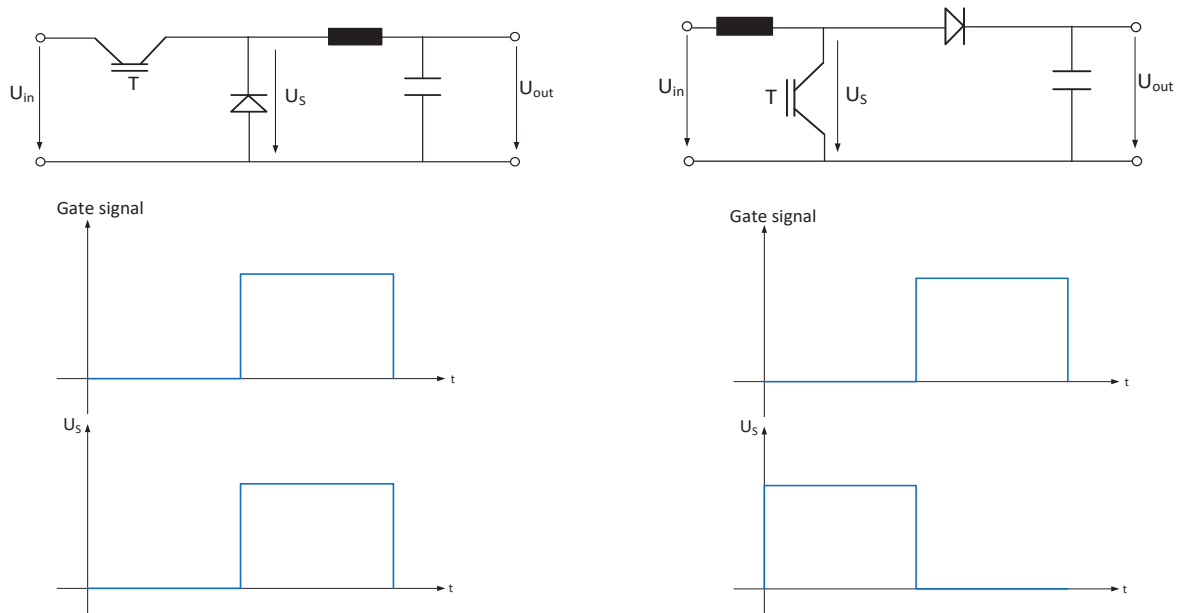


Figure 28: Buck converter (left) and boost converter (right)

Using these characterizations, but defining the duty cycle as the conduction time of the series switch (the transistor for the buck converter, but the diode for the boost converter) the following equations result:

Buck converter

$$d = \frac{T_{on}}{T_p}$$

Voltage ratio:

$$U_{out} = d \cdot U_{in}$$

Boost converter

$$d = \frac{T_{off}}{T_p} \quad (9)$$

$$U_{out} = \frac{1}{d} \cdot U_{in} \quad (10)$$

Redrawing the basic scheme of the elementary MSBA cell (Figure 29) it becomes obvious that the scheme between input and output is that of a boost converter, just supplemented with an additional capacitor C_2 between the positive input voltage terminal and the positive output terminal.

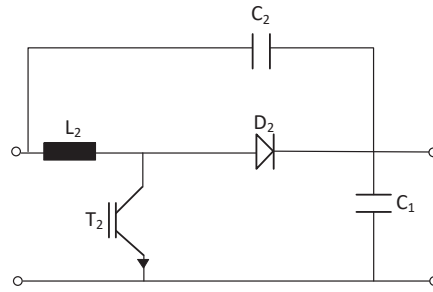


Figure 29: Redrawn scheme for the MSBA cell

Using the definition of the duty cycle like in equation (9), the conduction time of T_2/D_2 is determining the duty cycle. The output voltage related to input voltage would be $1/d$ and the capacitor voltage at C_2 would be $1/(d-1)$. With a duty cycle of 0.5, the output voltage is double of the input voltage, while the capacitor voltage becomes equal to the input voltage. Therefore, the duty cycle is chosen as the ratio of the turn-off time of the switch to the switching period T_p .

$$d = \frac{T_{off}}{T_p} \quad (11)$$

2.4. Specific Resonance Properties

2.4.1. General Description of the Resonance Phenomenon

After these definitions, it is important to have a closer look at the open-loop behaviour of the elementary MSBA cell. This will be done open-loop with one PWM modulator to operate the switches at a fixed duty cycle (Figure 30).

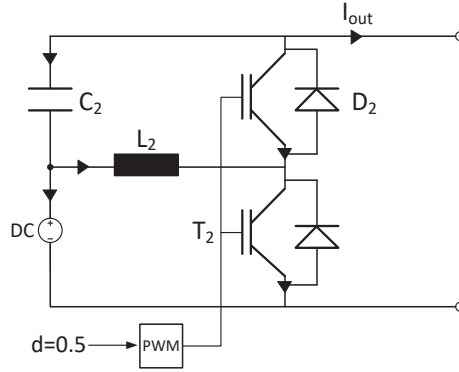


Figure 30: Block diagram of open-loop elementary MSBA

The input voltage is constant and for the first simulation the duty cycle is a constant value equal to 0.5. Therefore, the capacitor voltage must reach a steady-state value equal to the value of the input voltage source.

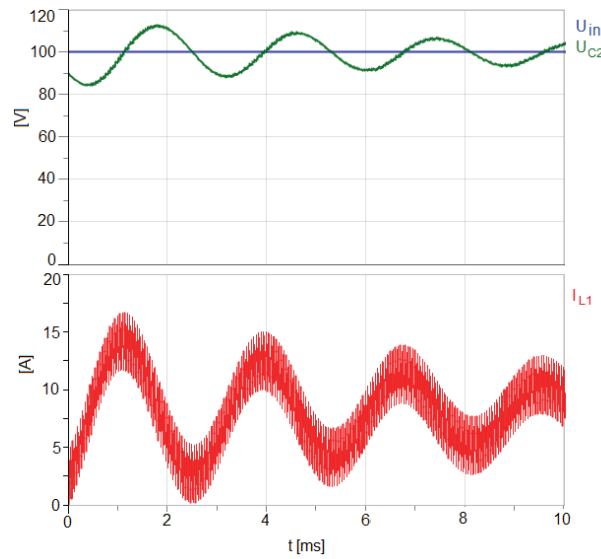


Figure 31: The typical resonance of the MSBA stage with constant duty cycle

As can be seen in Figure 31 the elementary MSBA cell shows resonant phenomena. For calculating the resonance frequency this stage can be described with the formulas for the state variables of the system; the capacitor voltage U_{C2} and the inductor current I_{L1} . Hereby the capacitor voltage is determined by the current contribution coming from the inductor I_{L1} and the contribution of the output current I_{out} . The inductor current is determined by the contributions of the capacitor voltage U_{C2} and the input voltage U_{in} .

$$u_{C2} = \frac{1}{C_2} \int (d_1 \cdot i_{L1} - i_{out}) dt \quad (12)$$

$$i_{L1} = \frac{1}{L_1} \int (-d_1 \cdot u_{C2} + (1-d_1) \cdot u_{in}) dt \quad (13)$$

It is now possible to use these formulas to generate a state space representation using the expression

$$\dot{x} = A \cdot x + B \cdot u \quad (14)$$

In this equation u is the input vector, while x is the state vector. There are also two matrices, the state matrix A and the input matrix B . A detailed explanation of the state space representation and how the MSBA converter can be represented by it will be given in 0. So for the elementary MSBA stage it results in:

$$x = \begin{bmatrix} u_{C2} \\ i_{L1} \end{bmatrix}, \quad u = \begin{bmatrix} u_{in} \\ 0 \end{bmatrix} \quad \text{and} \quad A = \begin{bmatrix} 0 & \frac{d_1}{C_2} \\ -\frac{d_1}{L_1} & 0 \end{bmatrix} \quad (15)$$

The fastest way to now get the resonant frequency of the system is to determine the eigenvalues of the state matrix.

$$\det(sI - A) = \det \begin{bmatrix} s & -\frac{d_1}{C_2} \\ \frac{d_1}{L_1} & s \end{bmatrix} = s^2 + \frac{d_1^2}{L_1 C_2} = 0 \quad (16)$$

This will result in the Eigenvalues of

$$\lambda_{1,2} = \pm j \cdot \frac{d_1}{\sqrt{L_1 C_2}} \quad (17)$$

The resonance frequency can now be calculated with the help of the formula

$$\omega = \sqrt{\alpha^2 + \beta^2} \quad (18)$$

if the eigenvalues are considered in the general form

$$\lambda = \alpha + j\beta \quad (19)$$

Therefore, the resonance frequency of the elementary MSBA stage results in

$$f_{res} = \frac{d}{2\pi\sqrt{LC}} \quad (20)$$

From the curves of Figure 31, it is possible to verify the oscillation frequency: The measured period is equal to 2.81ms, leading to a resonance frequency of 355 Hz. The calculated value of the resonance frequency on the base of the L and C parameters as well as the value of the duty cycle (d) accords to

$$f_{res} = \frac{d}{2\pi\sqrt{LC}} = \frac{0.5}{2\pi\sqrt{500 \cdot 10^{-6} \cdot 100 \cdot 10^{-6}}} = 355.8Hz \quad (21)$$

The transient phenomenon shown in Figure 31 is the result of a only 90% pre-charged capacitor. In this first test the input voltage was set to 100V and the fixed duty cycle of 0.5 keeps the capacitor voltage to the same value of 100V.

In the following figures (Figure 33, Figure 34) the behaviour of the MSBA cell for different duty cycles is shown. The initial conditions of the capacitor voltage and inductor current (the state variables of the MSBA) are set accurately in order to have a non-oscillating system at the beginning. After a delay an additional load is connected as perturbation (Figure 32). This perturbation excites the resonant circuit.

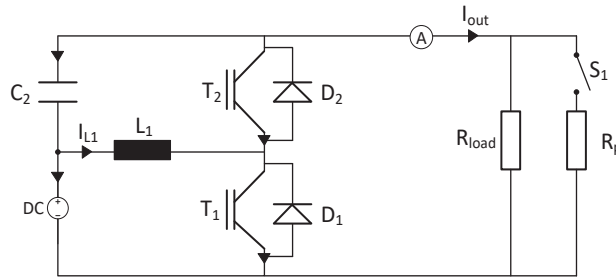


Figure 32: The MSBA stage with output load step as perturbation

Figure 33 shows the behaviour of the circuit when the duty-cycle is set to 2/3, meaning that the output voltage of the converter will now be 3/2 times the input voltage, namely 150V. According to the formula used before the resonance frequency will now change to:

$$f_{res} = \frac{d}{2\pi\sqrt{LC}} = \frac{2/3}{2\pi\sqrt{500 \cdot 10^{-6} \cdot 100 \cdot 10^{-6}}} = 474.5Hz \quad (22)$$

Compared to the simulation results shown in Figure 31 it can be seen that the period of the represented oscillations is $T_{res}=8.44/4ms=2.11ms$, resulting in the resonance frequency of $f_{res}= 473,9Hz$, almost same as the calculated one and the difference is a result of the imprecise period measurement.

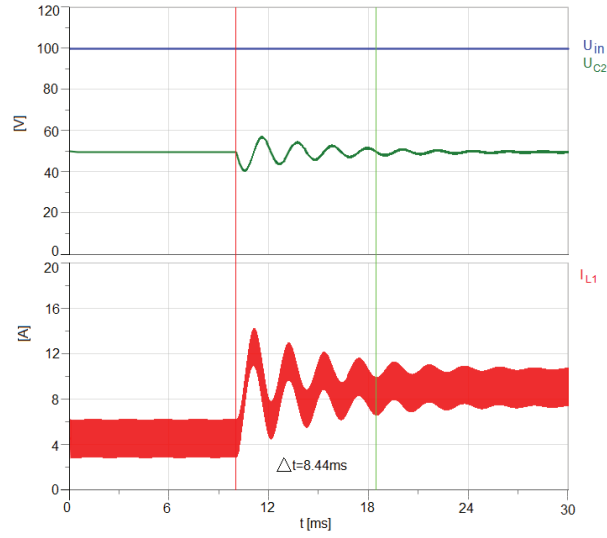


Figure 33: Oscillation of the MSBA stage with a fixed duty cycle of $d=2/3$

Figure 34 shows the behaviour of the circuit when the duty-cycle is set to $1/3$, meaning that the output voltage of the converter will now be 3 times the input voltage, namely 300V. According to the formula used before the resonance frequency will now change to:

$$f_{res} = \frac{d}{2\pi\sqrt{LC}} = \frac{1/3}{2\pi\sqrt{500 \cdot 10^{-6} \cdot 100 \cdot 10^{-6}}} = 237 \text{ Hz} \quad (23)$$

This is again compared to the simulation results shown in Figure 31. It can be seen that the period of the represented oscillations is $T_{res}=12.68/3 \text{ ms}= 4.23\text{ms}$, resulting in the resonance frequency of $f_{res}= 236.6\text{Hz}$, almost the same as the calculated one.

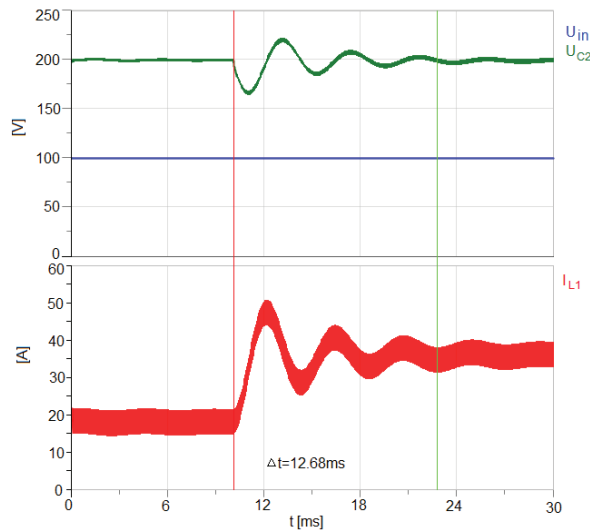


Figure 34: Oscillation of the MSBA stage with a fixed duty cycle of $d=1/3$

2.4.2. Resonance Excitation of the MSBA Cell due to a Load Change

To avoid the initial resonance in the simulation of the MSBA cell discussed before, the initial conditions have to be set properly. These initial conditions refer to the capacitor voltage U_{C2} as well as the inductor current I_{L1} . It is important to take into account the ripple due to the switching of the converter to calculate the initial conditions correctly. Therefore, the input voltage was again fixed to 100V and the starting value of the capacitor was set to 100.25V. And for the inductor the starting value was set to 5.5A.

This fully non oscillating state of the elementary MSBA cell is represented in the left part of Figure 35. The upper plot represents the capacitor voltage as well as the input voltage while the lower plot shows the inductor current. After 2.5ms an additional load resistor is switched on and the corresponding perturbation excites the inherent resonance of the circuit which can be seen in the right part of Figure 35.

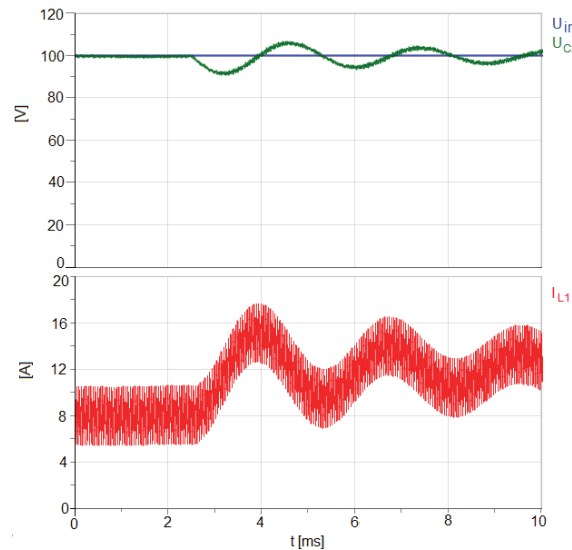


Figure 35: Excitation of the circuit resonance by a fast perturbation

The reason for this behaviour is that the step waveform of the additional load covers a wide frequency domain that includes the components which excites the resonance of the circuit.

2.4.3. The Non-Excited Regime for Load Variation

A simple method to filter the exciting frequency is to introduce a time constant for the load current, which is equivalent to a limitation of the bandwidth. Therefore, an inductor L_2 is inserted into the load circuit which can be seen in Figure 36.

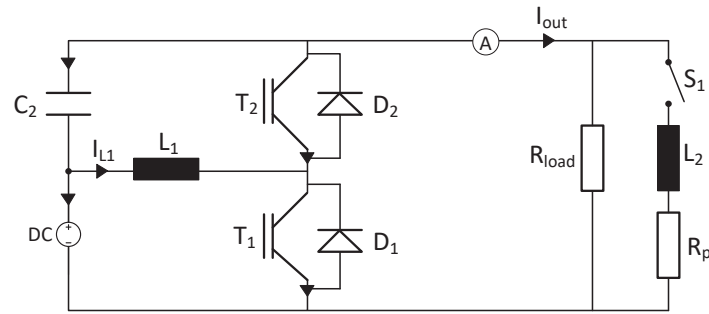


Figure 36: MSBA stage with filtered load circuit

The result of filtering the additional load step is represented in Figure 37. As expected the oscillation of the capacitor voltage has disappeared and the inductor currents presents an increase according to one first order circuit.

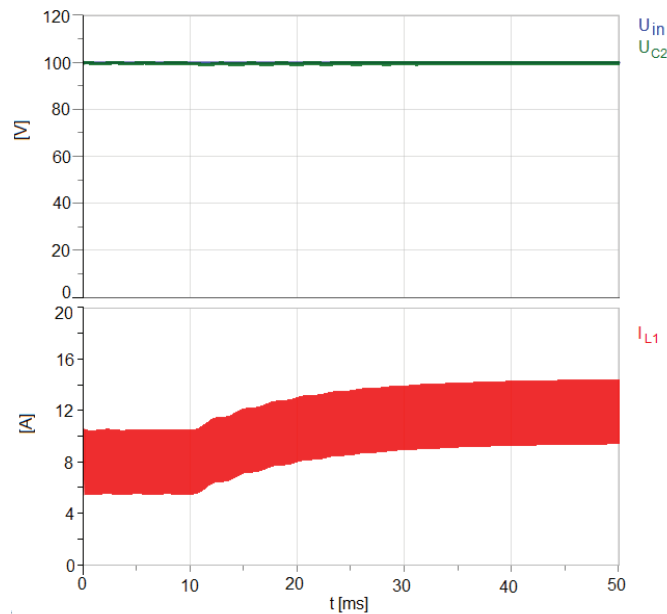


Figure 37: The non-excited resonance due to the filtered load-step

A detailed observation shows a small residual oscillation of the current at the beginning of the increase (between 10 and 20ms mainly). This is probably due to the presence of a strong current ripple because of the switching nature of the converter.

2.4.4. The Non-Excited Regime for an Input Voltage Variation

The resonance phenomenon can be excited either by fast changes of the load or also by fast changes of the input voltage. The goal of this simulation is to show that the resonance of the MSBA cell can only be avoided by elimination of the exciting frequency-components at the circuit input. For this purpose, the input voltage of the converter is provided by a controlled voltage source (Figure 38), where the control

variable is filtered by one PT1 element. The time constant in this verification is chosen at an identical value as for the filtered load step (10ms), which corresponds to a cutting frequency at 100Hz, which is around one third of the natural resonant frequency of the uncontrolled MSBA stage.

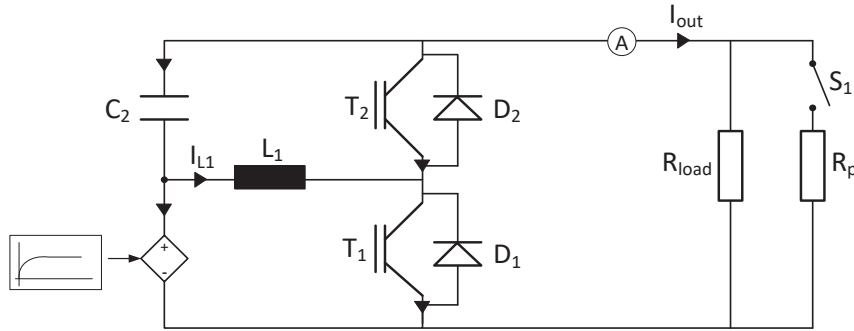


Figure 38: The MSBA cell with filtered input voltage source

The simulated phenomenon of a variation of the input voltage with limited dynamics is represented through Figure 39. The upper plot shows again the input voltage as well as the capacitor voltage, two curves which are clearly superposed. The current rise is shown in the lower plot and a dominant current rise with first order time constant can be observed. However, there is also a superposed residual resonant current due to the not synchronized transient related to the superposed switching phenomenon.

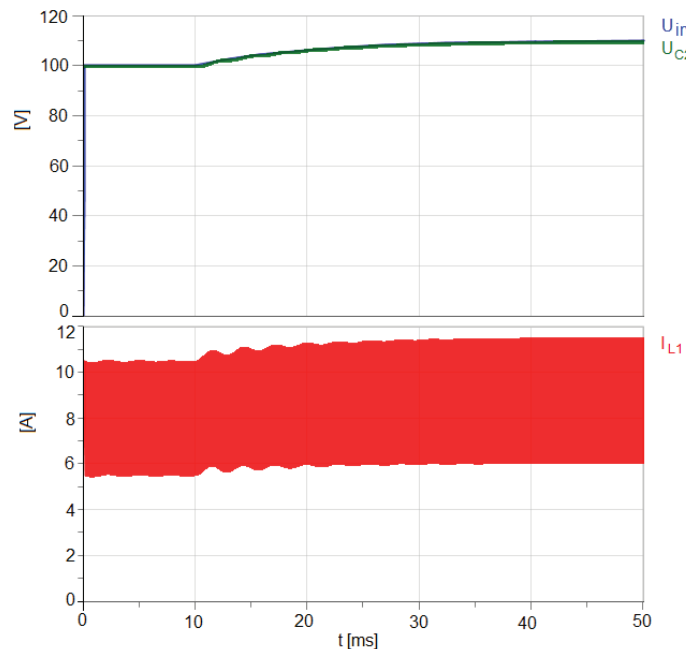


Figure 39: Transient response of the voltage increase at the converter input with limited dynamics

Now that the elementary MSBA cell has been examined an excerpt of the MSBA family is shown.

2.5. The Multistage Stacked Boost Architecture Family

2.5.1. The Symmetric Step-Up MSBA

The symmetric step-up MSBA converter is built out of MSBA cells and an input boost stage which is not connected at the top or bottom of the MSBA cells but in the middle. Figure 40 shows the scheme of a one-to-plus-and-minus-two step-up converter; meaning there are three MSBA cells connected to the boost stage. Of course the step-up ratio can easily be extended by adding more stages. This symmetric Multistage Stacked Boost Architecture [32] could be advantageous for applications where a \pm voltage output is required in comparison to the asymmetric MSBA (Chapter 3) where the output voltage is not split and goes from zero to maximum.

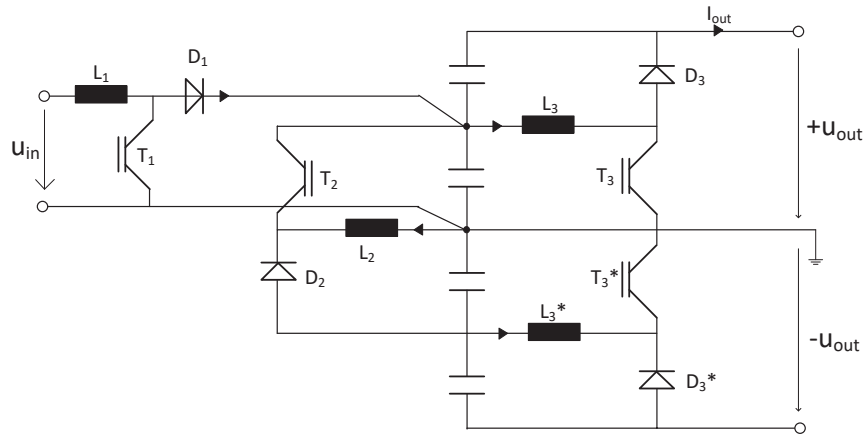


Figure 40: 4-stage symmetric MSBA

To better understand this topology having a look at the equations defining the circuit is advantageous. The boost stage will not be considered for this since it is a well-known and well researched topology. Figure 41 shows a symmetric MSBA in a uni-directional version with five stages, with the numbering here going from 1 for the first stage to 3 and 3* for the top and bottom.

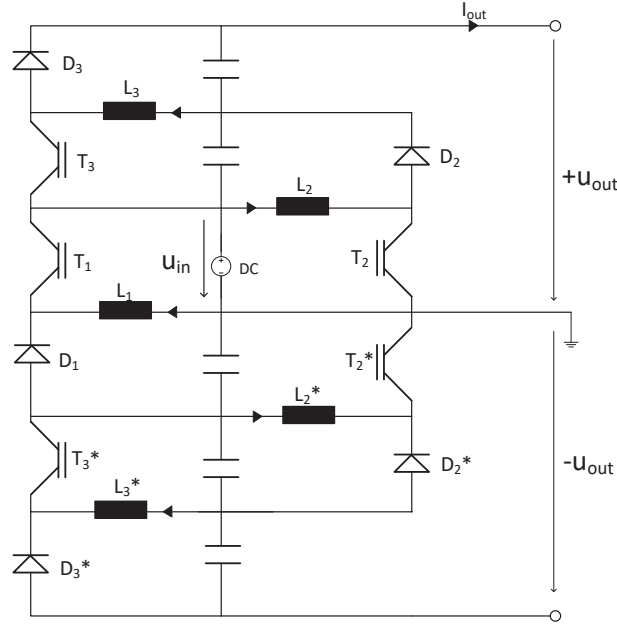


Figure 41: Component-Numbering for the 6-stage MSBA with a +/- output

The reason why the stages, which are away from the input the same number of stages, are numbered with x and x^* becomes apparent when regarding the currents, since the current value for these is the same. It is important to notice that the current formulas are for a fixed duty cycle of 0.5 since this would be the normal application case, because otherwise there can occur problems, which will be explained later on. So this results in the following equations for the currents in each stage:

$$I_1 = \frac{I_{in}}{2} \quad (24)$$

$$I_n = I_n^* = \frac{I_{in}}{2 \cdot n} \quad (25)$$

The reason why this topology is only useful with a duty cycle of 0.5 is that having a different duty cycle would unbalance the whole system (Figure 42), since the $+$ and $-$ output voltage would not have the same value anymore. The reason for this is that the constant input voltage is only added to the $+$ output.

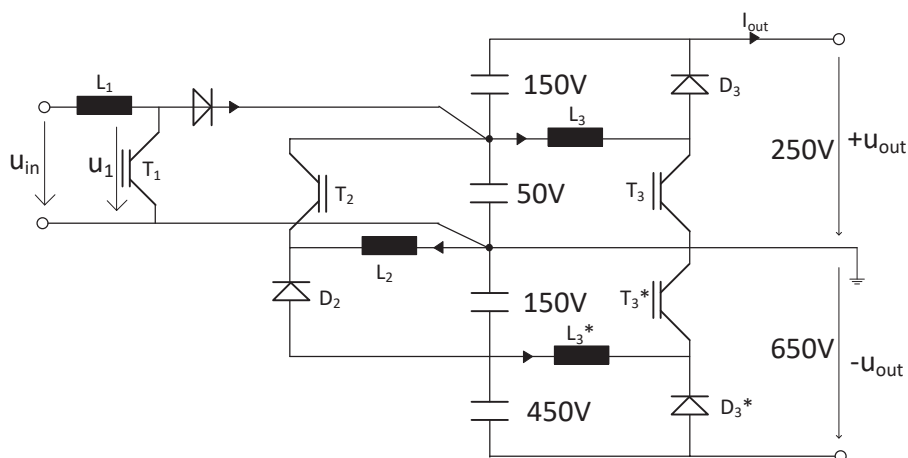


Figure 42: Showing the unbalance of a +/- MSBA with a duty cycle of $d=0.75$

A low voltage prototype was built to experimentally verify the formulas and simulation results, which can be seen in Figure 43.

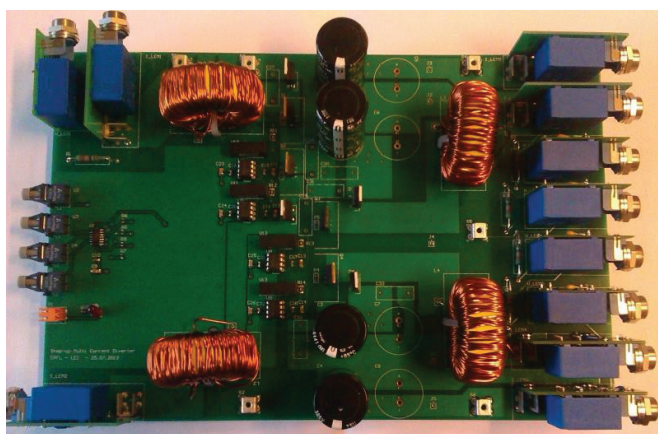


Figure 43: Symmetric 4-stage MSBA prototype

The electric scheme is identical to the scheme shown in Figure 40 and the converter is built with optical receivers and LEM transducers in order to have a fully compatible interface concept for the numeric controller. Table 5 shows the nominal data of the prototype.

Table 5: Nominal values of the prototype

U_{in}	100 V
U_{out+}	200 V
U_{out-}	200 V
I_{load}	5A

A fixed duty cycle of 0.5 for open-loop tests was used. For first tests the input voltage was set to $U_{in}=10V$ and the input current to $I_{in}=0.75A$. Figure 44 shows the currents in the four inductors, clearly confirming the earlier formulas.

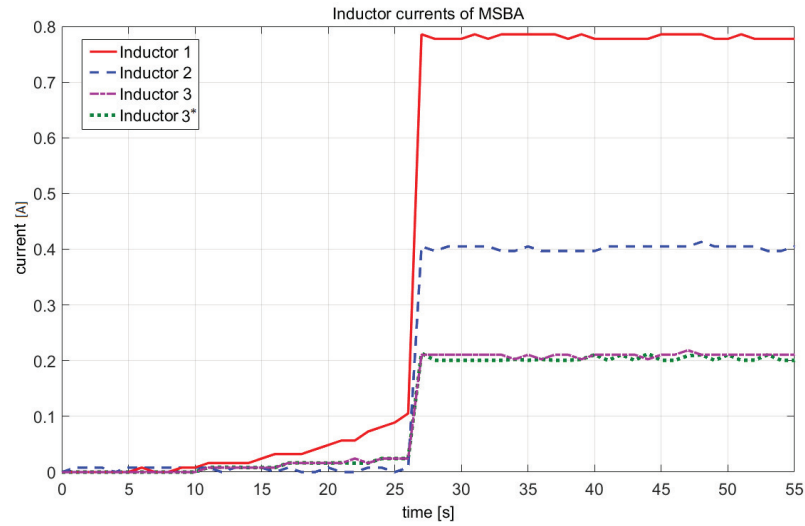


Figure 44: Inductor currents received with a prototype

2.5.2. The Asymmetric Step-Down MSBA

Figure 45 shows a MSBA topology as a step-down converter with a step-down factor equal to 5. A topology like this could for example be used for variable speed drives where the power electronic applications are connected to supply voltages higher than the standard level.

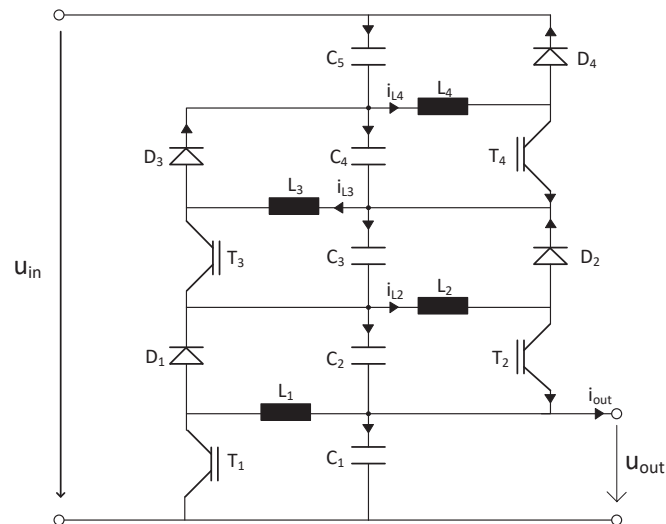


Figure 45: Asymmetric Step-down MSBA converter with 5 levels

This variation of the MSBA topology works well with a current control strategy relying on feed-forward of the measured output current, where each stage of the asymmetric step-down MSBA balances one capacitor pair. This kind of control allows the converter to reach good dynamics in case of perturbations. More details and more applications for such a converter topology are described in [33]. Additionally this kind of step-down converter can be also realized as symmetric converter topology.

2.5.3. The Symmetric MSBA with NPC Inverter

A more specific application of the Multistage Stacked Boost Architecture is the multilevel photovoltaic inverter as shown in Figure 46. The first stage of the converter is a classical boost converter while a symmetric +2 and -2 MSBA is used as second stage to elevate the input voltage to its double value. The complex application from the point of view of the number of active switches is realized by adding a 5-Level NPC inverter to this. The interconnection of the two units is realized with direct lines between all intermediary levels of the MSBA stack and the 5-Level inverter [34]. Since this application is intended for a PV plant the unidirectional power flow of the PV application allows the use of one transistor and one diode in each stage, but in the shown topology two power MOSFETs were chosen instead.

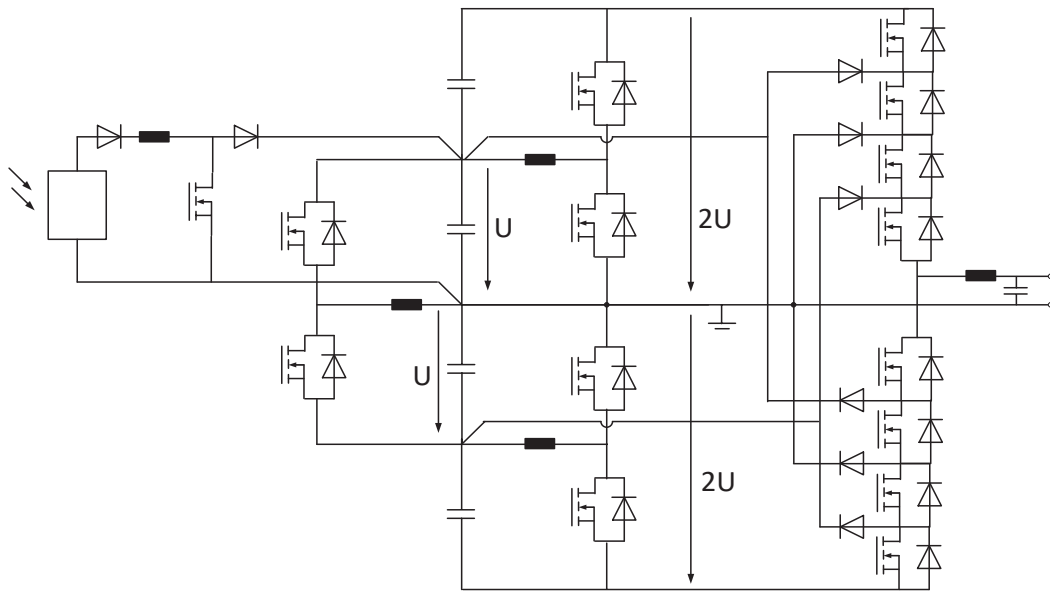


Figure 46: Symmetric step-up MSBA followed by a 5-Level NPC inverter

In the shown case the MSBA converter is realized with a +2 and -2 ratio, followed by a 5 level NPC inverter but a higher elevation factor can be reached by adding positive and negative stages to the MSBA converter and by increasing the number of steps of the multilevel inverter.

2.5.4. NPC Balanced Capacitive Divider

The NPC Balanced Capacitive Divider [35] is based on the series connection of NPC inverter cells, using semiconductor devices with lower voltage blocking capability than the total input voltage Figure 47. A

galvanic isolation is realized by using several MF transformers, each designed for a fraction of the total power. The output uses multiple diode rectifiers connected in series. The circuit also uses a capacitive voltage divider at its input, allowing an active balancing of the intermediate levels according the principle of the current divider. The balancing half bridges allow an N-1 mode of operation in case of a fault or disconnection of one of the series connected cells. The shown 3-Level NPC topology for the half bridges allows in addition the continuous variability of the total voltage transformation ratio.

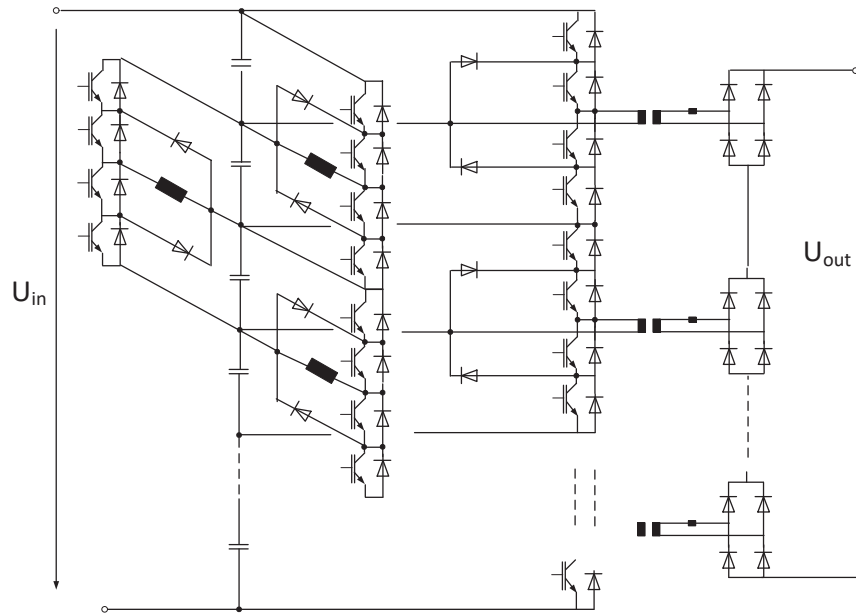


Figure 47: High-voltage converter with separated balancing circuits

A simplified two-cell version of this converter was used for building a prototype and measurement results, which can be found in [35].



3. The Asymmetric Multistage Stacked Boost Architecture

3.1. MSBA Characteristic Equations

The following chapter will show that the duty cycle d has a great influence on the behaviour of the MSBA converter since it is part of all the equations that define the circuit. For a clear understanding the following picture (Figure 48) shows the numbering used for the components of the topology:

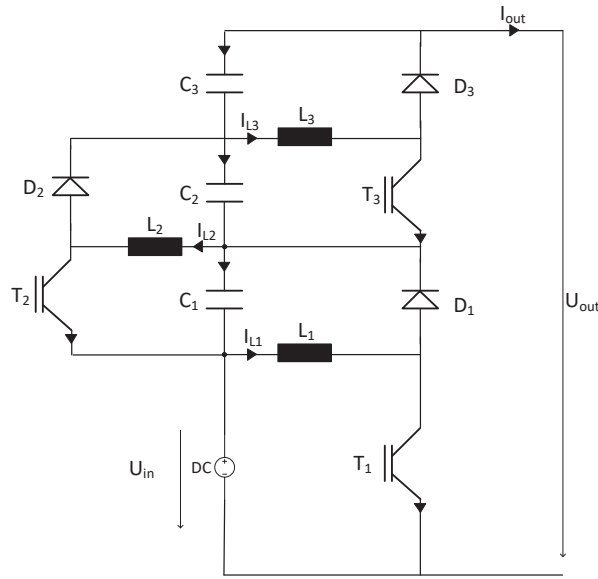


Figure 48: Numbering of MSBA from bottom to top

So the bottom component is numbered with one and the top will be numbered with n . Since this thesis concentrates on a 4-stage MSBA converter, this analysis will first concentrate on describing three connected MSBA cells.

In general, this converter can be described by the following equations for the capacitor voltages:

$$V_{C_{n+1}} = V_{C_n} \cdot \frac{1-d}{d} \quad (26)$$

with

$$V_{C_1} = V_{in} \cdot \frac{1-d}{d} \quad (27)$$

The maximum voltage the switches and diodes see is:

$$V_{\text{Switch}_n} = V_{C_{n-1}} \cdot \frac{1}{d} \quad (28)$$

with

$$V_{\text{Switch}_1} = V_{in} \cdot \frac{1}{d} \quad (29)$$

Changing the duty cycle to a lower value increases the stress on the switches while having a higher duty cycle will result in having a lower voltage than the input voltage on all switches except the first one.

So in general the ratio from output to input voltage (Figure 49) can be described as:

$$\frac{V_{\text{out}}}{V_{in}} = 1 + \frac{1-d}{d} + \left(\frac{1-d}{d}\right)^2 + \dots + \left(\frac{1-d}{d}\right)^n \quad (30)$$

where n is the number of MSBA cells. The stage number of the converter would be $n+1$ since the boost input stage will be added.

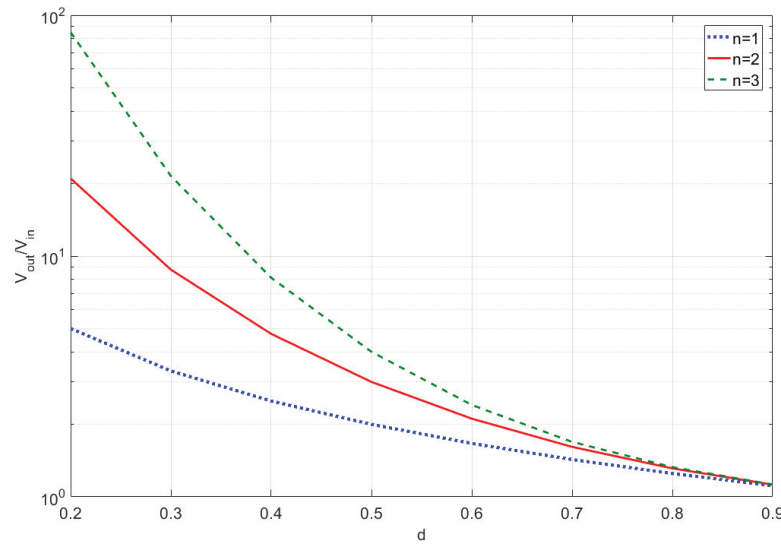


Figure 49: Relation of output and input voltage for different duty cycles d and number of MSBA cells n

The next step is to understand the currents flowing through the components and determine a formula, which can be applied to for a variable number of stages in the architecture. Therefore, it was practical to go through the circuit and having a look into only one duty cycle (Figure 50).

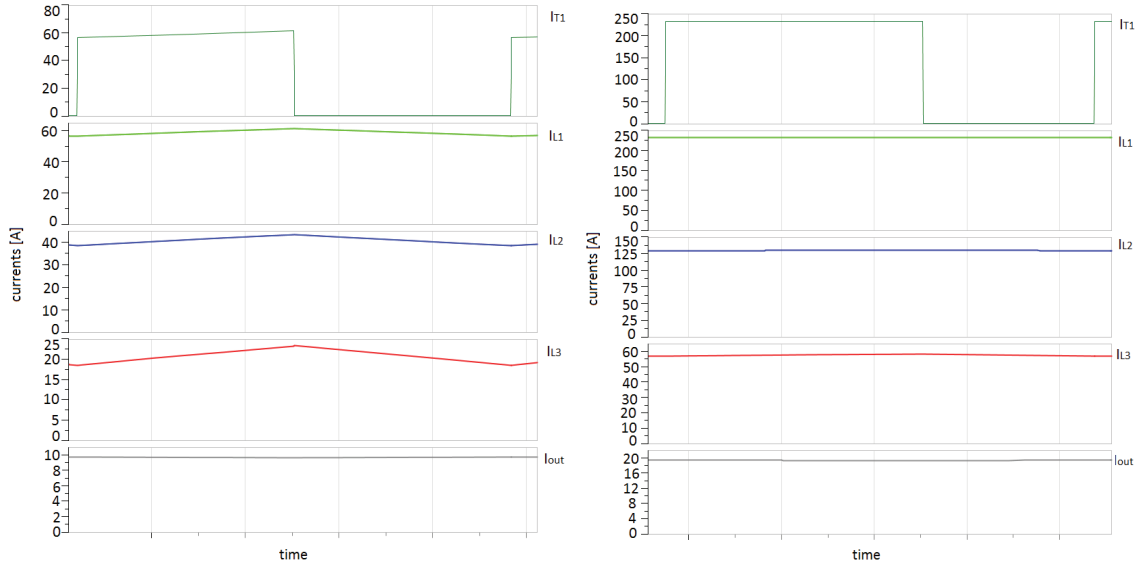


Figure 50: Simulation results for the inductor currents with $d=0.5$ (left) and $d=0.4$ (right)

These insights as well as thinking about how the circuit functions led to the formulas for the currents through the circuit components. Starting at the top, the charge extracted by the load from the connection point of diode and capacitor per switching cycle is $I_{out} \cdot T_p$. During the time: $d \cdot T_p$, while the diode is conducting, this charge has to be delivered through it, partly going directly into the load, partly re-charging the capacitor, which has to deliver the portion going to the load while the diode is blocking. The charge delivered during diode conduction is $d \cdot T_p \cdot I_{nmax}$. This results in:

$$I_{nmax} = \frac{I_{out}}{d} \quad (31)$$

The capacitor of the cell n is not only loaded by the resulting charge drawn from the output terminal through all the cells ($I_{out} \cdot T_p$), but also during the conduction time of the transistor by the inductor current $(1-d) \cdot T_p \cdot I_{n+1}$. Again this charge has to be delivered through the diode path during the turn-on time of the diode, resulting in the formula for the cells with $n < n_{max}$:

$$I_n = \frac{I_{out} + (1-d) \cdot I_{n+1}}{d} \quad (32)$$

The input current can finally be calculated from the current going through the lower transistor path ($d \cdot I_1$) and the output current, which has its return path in common with the input voltage source.

$$I_{in} = (1-d) \cdot I_1 + I_{out} \quad (33)$$

The alternative is to start calculating at the input, using the average current through the paths.

All capacitors have to have an average current of zero in steady state in order to stay at a constant dc-voltage level. I.e. the only paths that deliver average currents not equal to zero are the ones connected to the switches and to the input source and the load.

These current values are also the maximum current the switches and diodes see. In addition, the current ripple is not considered in the formulas, they are valid for the average values within a switching cycle T_p .

After this general analysis the equations could be completely simplified by having a duty cycle of $d=0.5$. This duty cycle is chosen because it nicely balances a good step-up ratio with the maximum voltage across the components. In addition, when using this duty cycle all capacitors will be charged to the same value, so only the currents will be different in each stage.

$$V_{in} = V_{C1} = V_{Cn} \quad (34)$$

$$V_{Switch} = V_{Diode} = 2 \cdot V_{in} \quad (35)$$

This means that for a duty cycle of 0.5 the switches and diodes always see double the input voltage, which is a positive aspect of this topology since, despite how many stages there are, the switches only need to have the blocking ability of the doubled input voltage.

Of course, in a voltage controlled operation, the duty cycle will deviate in dynamic situation from the steady state design value of 0.5, which has to be considered for a real circuit design. By including reasonable duty cycle limitations within the control the margins for higher dynamic loads could be kept small.

Figure 51 shows the currents through the switches for a three stage topology, where red is switch 3, blue is switch 2 and green is switch 1. The current for the diodes look the same, of course reversed in regard of conducting.

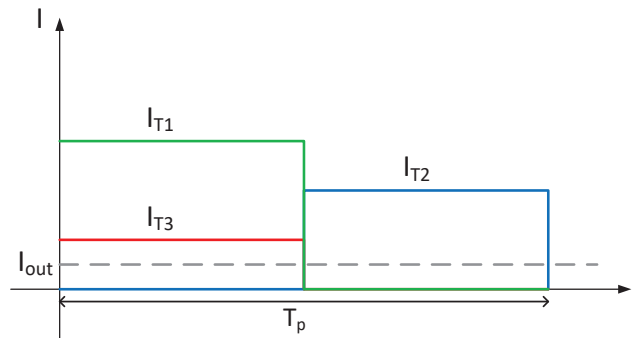


Figure 51: Stage currents of the switches in a MSBA

So the currents can be calculated quite easily with the following equation of the duty cycle is 0.5.

$$I_n = 2 \cdot I_{out} + I_{n+1} \quad (36)$$

The current value here is the same for every component in one stage, so I_1 applies to the Switch 1, the Diode 1 and the Inductor 1. This means the output current can be calculated by:

$$I_{out} = \frac{1}{n+1} \cdot I_{in} \quad (37)$$

After defining the equations that describe the circuit, the 4-stage MSBA will be investigated for its resonant phenomena.

3.2. Specific Resonance Phenomena

3.2.1. The 4-Stage Asymmetric MSBA

The elementary MSBA stage showed resonant phenomena; therefore, it is necessary to also have a look at the 4-stage MSBA converter and its resonant properties. Figure 52 shows the setup-used for these simulations. The MSBA converter runs in steady-state with an input voltage of 100V and after a time delay an additional load ($R_{load}=R_p=40\Omega$) is connected as perturbation.

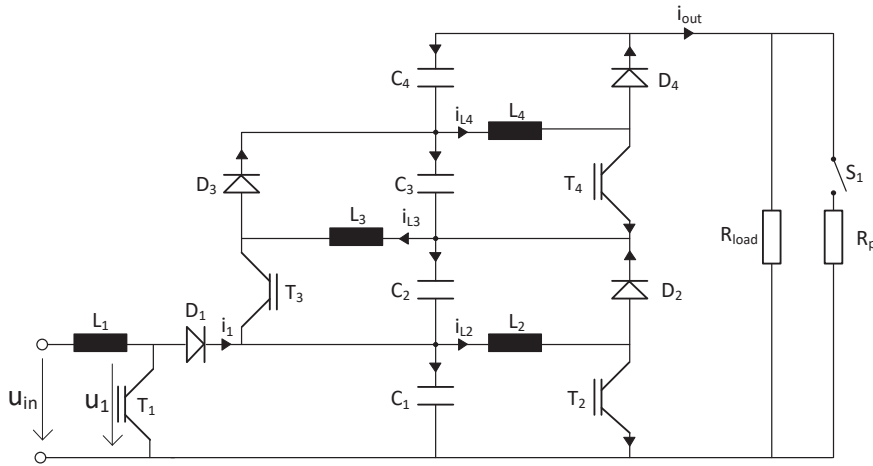


Figure 52: The 4-stage MSBA stage with output load step as perturbation

Figure 53 shows the output voltage in the first plot, the capacitor voltages in the second plot and the currents in the inductors as well as the output current in the third plot for the 4-stage MSBA converter. The simulation shows that the perturbation at 5ms results in the resonance phenomena.

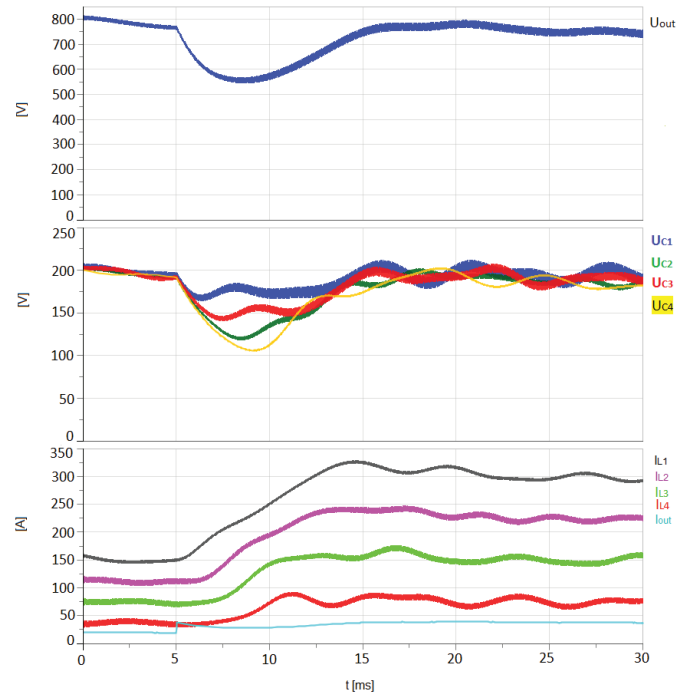


Figure 53: Resonant phenomena in the 4-stage MSBA with a fixed duty cycle of $d=0.5$

It is clear that the Multistage Stacked Boost Architecture needs a control that can handle these resonant properties, so that perturbations do not become a problem when running the converter.

3.2.2. The MSBA Connected to an Inverter

It is also interesting to see how the Multistage Stacked Boost converter behaves when connected to a DC/AC converter. It is of interest here if the resonance phenomena of the MSBA converter would be triggered by the switching or by perturbations from the DC/AC converter. Figure 54 shows how such a set-up could look like.

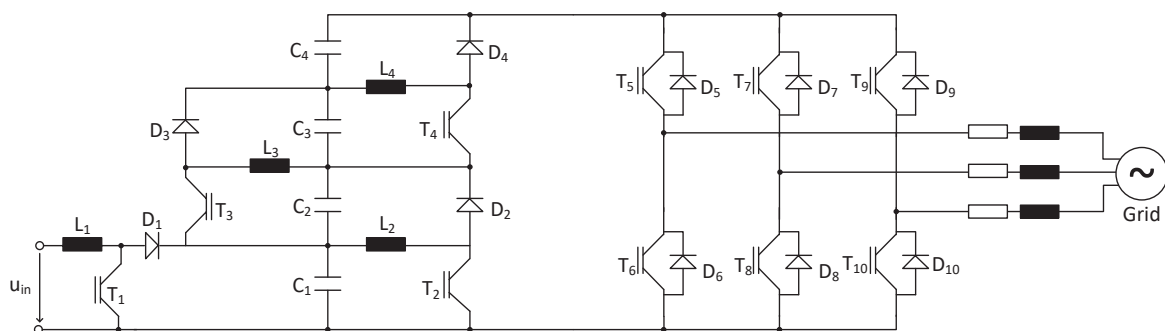


Figure 54: Connection of MSBA and DC/AC converter

To simulate this case a vector control of three-phase quantities will be used while the MSBA converter runs in open loop. Vector control has been used for many years often in drive applications and is also

applied for voltage source converters connecting to the grid. The three-phase quantities of a system are represented by space vectors using a rotating frame reference. Figure 54 shows a three-phase PWM where the output is connected through passive R-L components to the 50Hz grid. The control in this case needs to impose the magnitude and phase of the current fed into the grid. Therefore, the space-vector theory is used to transform the instantaneous values of the three phases into one complex variable. To achieve ideal conditions for the space-vector components in steady-state, the space-vector is calculated in the stationary reference-frame and is then transformed into a rotating reference frame, where its components become continuous values [36]. Figure 55 shows how this setup looks like when implemented in PLECS.

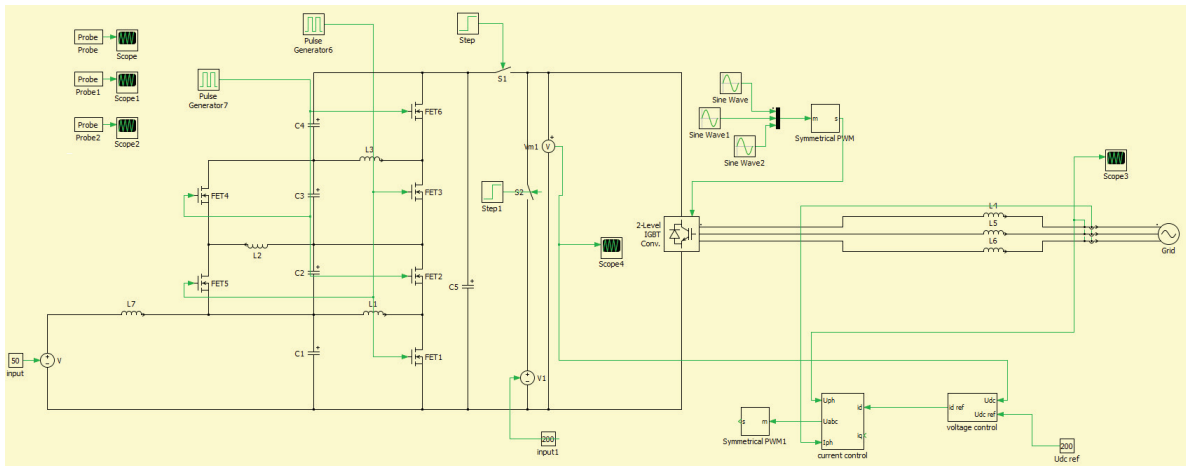


Figure 55: Connection of MSBA and DC/AC converter with control

For this simulation (done with PLECS) the DC/AC converter is controlled with two control loops. For the current control loop of the DC/AC converter connected to the grid, the structural diagram shown in Figure 56 used.

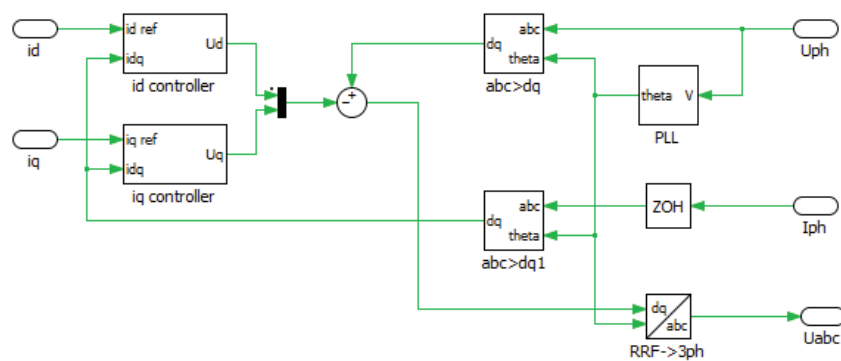


Figure 56: Current control of the DC/AC converter

This control loop ensures the correct transmission of energy to the grid without causing perturbations in the grid voltage or frequency. It is important that the current control system is designed so that the real

and imaginary part of the current space vector can be changed individually, without generating transient phenomena. The second control loop is the voltage control loop shown in Figure 57.

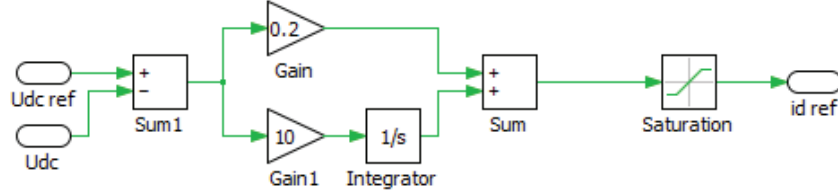


Figure 57: Voltage control of the DC/AC converter

This control loop ensures that the voltage input of the DC/AC converter, meaning the output of the MSBA converter is kept at a fixed voltage. To see if the resonant properties of the MSBA converter are influenced by the DC/AC converter, the MSBA converter is run open-loop with a fixed duty cycle of 0.5 and a switching frequency of 10kHz, while the inverter switched with 1000Hz. In the beginning, the two converters are run separately and after a time delay they are connected. Figure 58 shows the capacitor voltages of the MSBA stages.

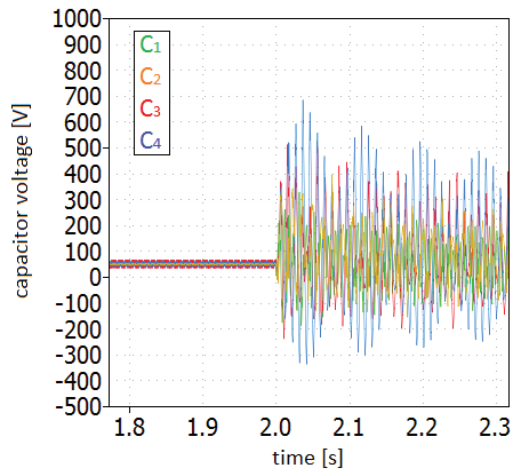


Figure 58: Connection of MSBA and DC/AC converter

It is apparent that the MSBA converter shows its resonant properties if it is run open-loop and connected to a DC/AC converter. Therefore, a good control dealing with these oscillations will be needed regardless if the MSBA converter is used to feed a DC-load or if it is connected to another converter.

3.3. Efficiency and Loss Calculation

After having a look at the resonance phenomena and after having defined this circuit by its currents and voltages a loss analysis regarding the number of stages can be done. To do this the number of stages that will be used has to be set. Since it would be interesting to have a comparison between a setup with a

symmetric and an asymmetric MSBA converter as well as a case where the duty cycle is not 0.5, the setups shown in Table 6 will be investigated.

Table 6: Cases for efficiency analysis

	d	V_{in}	I_{in}	V_{out}	I_{out}	MSBA cells
Asym.	0.5	1000V	300A	6kV	50A	5
Sym.	0.5	1000V	300A	+/-3kV	50A	5
Asym.	0.439	1000V	300A	6kV	50A	3

3.3.1. Asymmetric MSBA with d= 0.5

To consider which kind of switches should be used, it is helpful to list the values that are defining the safe operating area in each stage (Table 7). These are the maximum voltages (V_{Tmax}), as well as the maximum currents (I_{max}). To ensure that the switches are safe against small oscillations and overshoots it is good to add a 20% margin to this resulting in I_{safe} . Since these values are just the maximum currents while the switches are conducting the rating for the collector current (I_C) of the switches is half of this value since a duty cycle of 0.5 is used.

Table 7: Ratings for the switches

	V_{Tmax}	I_{max}	I_{safe}	I_C
T_1	2000V	500A	600A	300A
T_2	2000V	400A	480A	240A
T_3	2000V	300A	360A	180A
T_4	2000V	200A	240A	120A
T_5	2000V	100A	120A	60A

Normally the usable voltage of a switch is about 2/3 of the maximum voltage rating. Since in this case there will be a voltage of 2000V it is clear that the switch needs to have at least a voltage rating of 3000V. Since for this calculation the switches in every stage should be the same, the current rating is at least 300A. Since the commonly available switches have a current rating of $I_C=400A$ this will be used and an IGBT from Infineon [37] is chosen for the calculation.

The conduction losses of the switch can be calculated by:

$$P_{cond} = 0.5 \cdot U_{CE} \cdot I_{max} \quad (38)$$

The switching losses on the other hand can be calculated by:

$$P_{sw} = (E_{on} + E_{off}) \cdot f \quad (39)$$

The values for E_{on} and E_{off} can be found in one of the graphs in the data sheet:

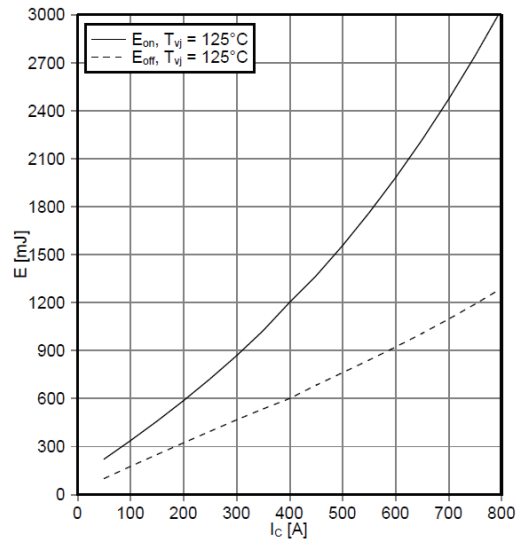


Figure 59: Switching loss characteristics [37]

For the calculations a switching frequency of 1kHz will be used and the results of the calculation can be found in

Table 8: Losses in the switches with $f=1\text{kHz}$

	P_{cond}	E_{on}	E_{off}	E_{sw}	P_{sw}	P_{total}
T_1	1050W	1600mJ	800mJ	2400mJ	2400W	3450W
T_2	740W	1200mJ	600mJ	1800mJ	1800W	2540W
T_3	480W	850mJ	450mJ	1200mJ	1200W	1680W
T_4	270W	600mJ	350mJ	950mJ	950W	1220W
T_5	100W	350mJ	200mJ	550mJ	550W	650W

The total losses are quite high so it needs to be verified that the chosen IGBT can handle the thermal stress these losses cause. The module has a thermal resistance R_{thCH} of 16K/kW. And the cooling will probably have about the same thermal resistance as well, resulting in an R_{TU} of 32K/KW. Considering that the application is intended for large solar plants, the location might be similar to a desert so it is realistic to consider an air temperature of 55°C so it can be assumed that the water of the cooling will not fall under 65°C. The IGBT is designed to have a maximum operating temperature of 125°C, but it would be safer to leave some margin so for the calculation a maximum of 115°C will be used. This will result in a possible temperature difference of $\Delta T_{max} = 115^\circ\text{C} - 65^\circ\text{C} = 50\text{K}$. Therefore, the maximum losses that the switch can handle can be calculated by:

$$P_{th\ max} = \frac{\Delta T_{max}}{R_{TU}} = 1.56\text{kW} \quad (40)$$

It is apparent that these switches can't be used under the before mentioned conditions. A possibility would be to reduce the switching frequency to 500Hz. Table 9 shows the results of this calculation.

Table 9: Losses in the switches with $f=500\text{Hz}$

	P_{cond}	E_{on}	E_{off}	E_{sw}	P_{sw}	P_{total}
T_1	1050W	1600mJ	800mJ	2400mJ	1200W	2250W
T_2	740W	1200mJ	600mJ	1800mJ	900W	1640W
T_3	480W	850mJ	450mJ	1200mJ	650W	1130W
T_4	270W	600mJ	350mJ	950mJ	475W	745W
T_5	100W	350mJ	200mJ	550mJ	275W	375W

So with a reduced switching frequency it would be possible to use the IGBTs at least for the stages containing T_3 - T_5 , but the first two stages will need different switches. The next sizing of IGBTs has a current rating of 800V and an ABB device is chosen this time [38]. Table 10 shows the results of this calculation.

Table 10: Losses in the switches with $f=500\text{Hz}$

	P_{cond}	E_{on}	E_{off}	E_{sw}	P_{sw}	P_{total}
T_1	775W	750mJ	850mJ	1600mJ	800W	1550W
T_2	560W	600mJ	750mJ	1350mJ	675W	1275W

Calculating the maximal possible losses in regards of the thermal stress results in $P_{\text{thmax}}=2.08\text{KW}$ because this module has a larger base plate and accordingly a lower R_{th} . This device can thus be used for the first two stages. So the total losses in the switches are:

$$P_{\text{switches}} = 1550W + 1275W + 1130W + 745W + 375W = 5070W \quad (41)$$

This means that for an output of 300kW the input power needs to be 305.07kW, which results in an efficiency of:

$$\eta = \frac{300}{305.07} = 98.3\% \quad (42)$$

Of course this efficiency only includes the switches at the moment and not the diodes and the inductors. The capacitor losses are negligible.

Therefore the diodes need to be considered next. The losses of a diode are divided into the conduction and the reverse-recovery losses. The conduction losses can be calculated with

$$P_{\text{cond}} = 0.5 \cdot U_f \cdot I_{\text{max}} \quad (43)$$

The reverse-recovery losses can be calculated with

$$P_{\text{rr}} = f \cdot E_{\text{rec}} \quad (44)$$

The values for U_f and E_{rec} can be found in the datasheets of the components. Since there is normally no separate diode device, which would be useful for a power converter the same IGBTs as before will be

used instead. So this means the 3.3kV / 800A IGBT from ABB for the two lower diodes and the 3.3kV / 400A from Infineon for the three top diodes. Table 11 shows the result of the loss calculations.

Table 11: Losses in the diodes with $f=500\text{Hz}$

	P_{cond}	E_{rec}	P_{rr}	P_{total}
T_1	500W	900mJ	450W	950W
T_2	360W	800mJ	400W	760W
T_3	337.5W	450mJ	225W	562.5W
T_4	180W	370mJ	185W	365W
T_5	75W	270mJ	135W	210W

So the total losses in the diodes are:

$$P_{\text{diodes}} = 950W + 760W + 562.5W + 365W + 210W = 2847.5W \quad (45)$$

If these losses are added to the losses of the switches it means that for an output of 300kW the input power needs to be 307.9175kW, which results in an efficiency of:

$$\eta = \frac{300}{307.9175} = 97.4\% \quad (46)$$

Now only the inductor losses need to be included so these will be considered in chapter 3.3.4.

3.3.2. Symmetric MSBA with $d=0.5$

As for the asymmetric MSBA it is helpful to list the values that are defining the safe operating area of the switch in each stage (Table 12). The naming of the switches is done according to Figure 41. These are the maximum voltages (V_{Tmax}), as well as the maximum currents (I_{max}). To ensure that the switches are safe against small oscillations and overshoots it is good to add a 20% margin to this resulting in I_{safe} . Since these values are just the maximum currents while the switches are conducting the rating for the collector current (I_c) of the switches is half of this value since a duty cycle of 0.5 is used.

Table 12: Ratings for the switches

	V_{Tmax}	I_{max}	I_{safe}	I_c
T_1	2000V	300A	360A	180A
T_2	2000V	200A	240A	120A
T_2^*	2000V	200A	240A	120A
T_3	2000V	100A	120A	60A
T_3^*	2000V	100A	120A	60A

Normally the usable voltage of a switch is about 2/3 of the maximum voltage rating. Since in this case there will be a voltage of 2000V, it is clear that the switch needs to have at least a voltage rating of 3000V. Since for this calculation the switches in every stage should be the same, the current rating is at least 180A. Since the commonly available switches have a current rating of $I_c=400\text{A}$ this will be used and

the IGBT from Infineon [37] was again chosen for the calculation and the switching frequency was directly set to 500Hz. The results for the loss calculation are shown in Table 13.

Table 13: Losses in the switches with $f=500\text{Hz}$

	P_{cond}	E_{on}	E_{off}	E_{sw}	P_{sw}	P_{total}
T_1	480W	850mJ	450mJ	1200mJ	600W	1080W
T_2	270W	600mJ	350mJ	950mJ	475W	745W
T_2^*	270W	600mJ	350mJ	950mJ	475W	745W
T_3	100W	350mJ	200mJ	550mJ	275W	375W
T_3^*	100W	350mJ	200mJ	550mJ	275W	375W

So the total losses in the switches are:

$$P_{\text{switches}} = 1080W + 745W + 745W + 375W + 375W = 3320W \quad (47)$$

This means that for an output of 300kW the input power needs to be 303.32kW, which results in an efficiency of:

$$\eta = \frac{300}{303.32} = 98.91\% \quad (48)$$

The diodes will be considered next. Since there is normally no separate diode device, which would be useful for a power converter the same IGBTs as before will be used instead. So this means the 3.3kV / 400A IGBTs from Infineon will be used. Table 14 shows the result of the loss calculations.

Table 14: Losses in the diodes with $f=500\text{Hz}$

	P_{cond}	E_{rec}	P_{rr}	P_{total}
T_1	337.5W	450mJ	225W	562.5W
T_2	180W	370mJ	185W	365W
T_2^*	180W	370mJ	185W	365W
T_3	75W	270mJ	135W	210W
T_3^*	75W	270mJ	135W	210W

So the total losses in the diodes are:

$$P_{\text{diodes}} = 562.5W + 365W + 365W + 210W + 210W = 1712.5W \quad (49)$$

If these losses are added to the losses of the switches it means that for an output of 300kW the input power needs to be 305.032kW, which results in an efficiency of:

$$\eta = \frac{300}{305.032} = 98.35\% \quad (50)$$

Now only the inductor losses need to be included so these will be considered in chapter 3.3.4.

3.3.3. Asymmetric MSBA with $d=0.439$

Again it is helpful to list the values that are defining the safe operating area of the switch in each stage (Table 12). These are the maximum voltages (V_{Tmax}), as well as the maximum currents (I_{max}). To ensure that the switches are safe against small oscillations and overshoots it is good to add a 20% margin to this resulting in I_{safe} . Since these values are just the maximum currents while the switches are conducting the rating for the collector current (I_c) of the switches has to be adjusted according to the duty cycle.

Table 15: Ratings for the switches

	V_{Tmax}	I_{max}	I_{safe}	I_c
T_1	2556V	446A	535A	300A
T_2	3268V	260A	312A	175A
T_3	4176V	114A	137A	77A

Normally the usable voltage of a switch is about 2/3 of the maximum voltage rating. Since in this case there will be a voltage of 4176V, it is clear that the switch needs to have at least a voltage rating of 6265V. Since for this calculation the switches in every stage should be the same, the current rating is at least 300A. Since the commonly available switches have a current rating of $I_c=400A$ this will be used and the IGBT from ABB [39] was chosen for the calculation and the switching frequency was directly set to 500Hz. The results for the loss calculation are shown in Table 13.

Table 16: Losses in the switches with $f=500Hz$

	P_{cond}	E_{on}	E_{off}	E_{sw}	P_{sw}	P_{total}
T_1	1076mJ	2000mJ	1500mJ	3500mJ	1750mJ	2826W
T_2	514mJ	1250mJ	750mJ	2000mJ	1000mJ	1514W
T_3	163mJ	750mJ	500mJ	1250mJ	625mJ	788W

The total losses are quite high so it needs to be verified that the chosen IGBT can handle the thermal stress these losses cause. The module has a thermal resistance R_{thCH} of 16K/kW. And the cooling will probably have about the same thermal resistance as well, resulting in an R_{TU} of 32K/kW. Considering that the application is intended for large solar plants, the location might be similar to in a desert so it is realistic to consider an air temperature of 55°C so it can be assumed that the water of the cooling will not fall under 65°C. The IGBT is designed to have a maximum operating temperature of 125°C, but it would be safer to leave some margin so for the calculation a maximum of 115°C will be used. This will result in a possible temperature difference of $\Delta T_{max}=115^\circ C-65^\circ C=50K$. Therefore the maximum losses that the switch can handle can be calculated by:

$$P_{th\ max} = \frac{\Delta T_{max}}{R_{TU}} = 1.56kW \quad (51)$$

It is apparent that these switches can't be used under the before mentioned conditions. Since there are no semiconductors available with a higher rating the solution used before can't be applied, so in this case for the first stage two IGBTs will be put in parallel to half the current. This results in the losses shown in Table 17.

Table 17: Losses in the switches with two parallel IGBTs

	P_{cond}	E_{on}	E_{off}	E_{sw}	P_{sw}	P_{total}
T_1	2.463mJ	2.1100mJ	2.750mJ	2.1850mJ	2.925mJ	2776W
T_2	514mJ	1250mJ	750mJ	2000mJ	1000mJ	1514W
T_3	163mJ	750mJ	500mJ	1250mJ	625mJ	788W

So the total losses in the switches are:

$$P_{switches} = 2776W + 1514W + 788W = 5078W \quad (52)$$

This means that for an output of 300kW the input power needs to be 305.078kW, which results in an efficiency of:

$$\eta = \frac{300}{305.078} = 98.34\% \quad (53)$$

The diodes will be considered next. Since there is normally no separate diode device, which would be useful for a power converter the same IGBTs as before will be used instead. Table 14 shows the result of the loss calculations.

Table 18: Losses in the diodes with $f=500\text{Hz}$

	P_{cond}	E_{rec}	P_{rr}	P_{total}
T_1	2.288W	2.800mJ	2.400W	1376W
T_2	350W	825mJ	412.5W	762.5W
T_3	122W	600mJ	300W	422W

So the total losses in the diodes are:

$$P_{diodes} = 1376W + 762.5W + 422W = 2560.5W \quad (54)$$

If these losses are added to the losses of the switches it means that for an output of 300kW the input power needs to be 307.6365kW, which results in an efficiency of:

$$\eta = \frac{300}{307.6365} = 97.52\% \quad (55)$$

Now only the inductor losses need to be included so these will be considered in chapter 3.3.4.

3.3.4. Inductor Losses

Of course, the losses of the inductors also need to be included, but here it has to be decided how to size these components. This question arises since one needs to weight the losses and the possible oscillations and ripples of voltages and currents. It is recommended to operate the circuit with a ripple current of less than 20-30% of the average inductor current to avoid increased losses.

The inductor losses are mainly losses inside the core, which can be calculated with the core material k_1 and the volume V_e :

$$P_{core} = k_1 \cdot f^a \cdot B^b \cdot V_e \quad (56)$$

Therefore, it is important to select the right core material to keep the losses small. Of course, this is also a question of the cost and the size of the inductor, but for a laboratory research these factors don't have a high priority. Table 19 shows different core types and their application limits.

Table 19: Overview of criteria to choose an inductor core type [40]

Min. L	Max. L	Type of Core	Adjustable?	High current?	Frequency limit
20 nH	1 μ H	Air cored, self-supporting	Y	Y	1 GHz
20 nH	100 μ H	Air cored, on former	N	Y	500 MHz
100 nH	1 mH	'Slug' tuned open winding	Y	N	500 MHz
10 μ H	20 mH	Ferrite ring	N	N	500 MHz
20 μ H	0.3 H	RM Ferrite Core	Y	N	1 MHz
50 μ H	1 H	EC or ETD Ferrite Core	N	Y	1 MHz
1 H	50 H	Iron	N	Y	10 kHz

The additional components that create noticeable losses inside the inductor are the windings. The copper losses of the windings depend on the average turn length, the number of turns and the resistance R_W . So the winding losses can be calculated by

$$P_{winding} = I_L^2 \cdot R_W \quad (57)$$

These equations showed how inductor losses can be calculated. But sizing and optimizing an inductor takes time and experience and would be outside of the time limit for this thesis in regards of just using it for an efficiency and loss calculation. Commonly the inductor losses in a power electronic application are around 1-1.5%. So for the following chapter it will be assumed that for the 5-stage symmetric and asymmetric MSBA as well as the three-stage asymmetric MSBA the total losses of the inductors will be 1%.

3.3.5. Comparison of the Losses and the Efficiency

Comparing the losses with of the asymmetric and the symmetric MSBA, it becomes apparent that the symmetric MSBA is more advantageous since the losses are recognizable smaller (Figure 60). This is a result of having lower currents in the stages, which can be seen in a comparison of the losses for each stage separately when having a 5-stage converter.

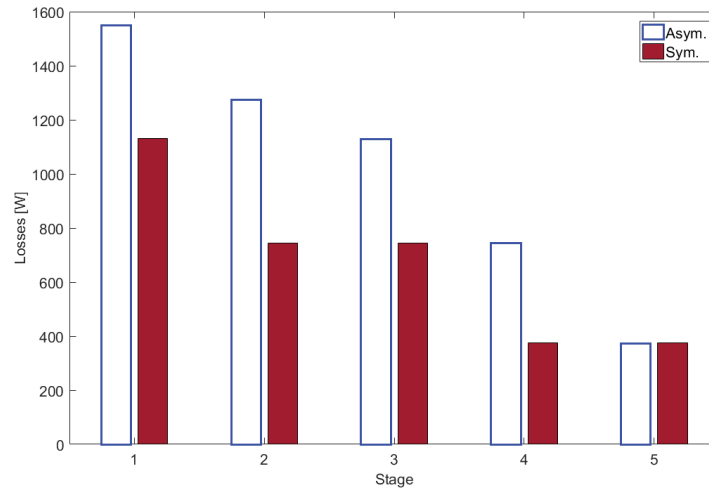


Figure 60: Loss comparison for the asymmetric MSBA (blue) and the symmetric MSBA (red)

Adding all the losses from the previous chapters together results in an efficiency of

$$\eta_{asym} = \frac{300}{307.9175} = 96.4\% \quad \eta_{sym} = \frac{300}{304.7825} = 97.35\% \quad (58)$$

Table 20 offers a quick overview of this and the settings for the calculations; the input power and the output voltage and current ratings while applying a switching frequency of 500Hz.

Table 20: Comparison of efficiency for the MSBA for f=500Hz

	d	η	V_{in}	I_{in}	V_{out}	I_{out}	Stages
Asym.	0.5	96.4%	1000V	300A	6kV	50A	5
Sym.	0.5	97.35%	1000V	300A	+/-3kV	50A	5
Asym.	0.439	96.52%	1000V	300A	6kV	50A	3

The first one is an asymmetric MSBA with five stages and a duty cycle of 0.5 having the input at the bottom while the second one has the same number of stages and the same duty cycle but the input is in the middle (symmetric MSBA). The third configuration that had been considered had only three stages, since this is the number needed to reach an output voltage of 6kV with a duty cycle of 0.439; of course, the input here was at the bottom. For these three MSBA types, it became quite apparent, that a higher duty cycle results in high stage currents and voltages making it more difficult to find suitable switches but it can be advantageous in regards of the efficiency if suitable components are found. In regards of the two MSBA configurations using a 0.5 duty cycle it is reasonable that the symmetric one has a better efficiency since the currents are also symmetric and therefore not as high in the top/bottom stages as with the asymmetric approach. But it has to be kept in mind that these two have a different potential regarding ground and therefore it depends on the application which one would be suited better.

Another advantage of the symmetric topology compared to the asymmetric is that the design ratings for the switches are closer to each other, which resulted at using only the 400A IGBT for all stages of the

symmetric MSBA, while for the asymmetric 800A IGBTs had to be used for two of the stages. But since the main functioning of both the symmetric and the asymmetric MSBA are the same the investigation will continue with the asymmetric topology.

It is also interesting to examine the losses in regards of the switching devices. The calculations show that most of the losses in an a MSBA converter are a result of the switching and conducting losses, which could be further be reduced in the future with the use of silicon carbide devices.

3.4. Energetic Macroscopic Representation

The Energetic Macroscopic Representation (EMR) is a graphical as well as functional description of an energetic system based on the physical causality. The EMR highlights the energetic properties of the subsystems of a whole system in order to deduce its control scheme in a systematic way [41], [42].

It has to be kept in mind that the EMR is a description and not a modelling method of a system. Therefore, a modelling step is required before building the EMR of a system. Such modelling could for example be done by using mathematical equations. One important principle is the physical causality, which indicates that the output of a dynamical system can only be an integral function of its inputs. Another important principle used in the EMR technique is the inversion principle, which considers the control as just an inversion of the system model. Some inversions can be directly achieved while other inversions require a closed loop. But of course other control schemes can also be implemented together with an EMR model of the system.

Systems can be represented by the EMR using the 4 basic EMR elements (Table 21) and the interactions in a circuit:

- Energy sources (green ovals, terminals of the systems)
- Accumulation elements (orange rectangles with diagonal line, energy storage)
- Conversion element without energy accumulation (various orange pictograms, energy conversion)
- Coupling elements for energy distribution (orange overlapped pictograms, energy distribution)

Of course, other elements can be added for specific use. All the elements are interconnected according to the action and reaction principle using exchange variables (arrows). The product of action and reaction variables between two elements leads to the instantaneous power exchanged [43], [44].

Table 21: Elements of the Energetic Macroscopic Representation

	source element (energy source)		accumulation element (energy storage)		Indirect inversion (closed-loop control)
	mono-physical conversion element		mono-physical coupling element (energy distribution)		Direct inversion (open-loop control)
	multi-physical conversion element		multi-physical coupling element (energy distribution)		coupling inversion (energy criteria)
	amplification element		switching element		Inversion of a switching element

3.4.1. Elementary MSBA Cell

Since the structure of the asymmetric MSBA with four stages is quite complex, the approach is to do one step after the other, representing one stage first and then by using the superposition theorem adding the other stages one by one. The addition order for the stages will start with the top stage, go down to the bottom MSBA stage, and then add the load and last the boost input stage.

The elementary stage of a MSBA is represented in Figure 61. Since this representation is done from top to bottom of a complete 4-stage converter the numbering starts with the fourth stage.

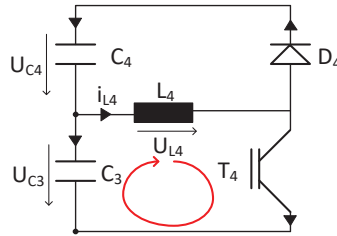


Figure 61: Elementary MSBA stage

Considering the picture above the equation of the lower loop can be represented as:

$$\begin{aligned}
 u_{L4} &= -d_4 \cdot u_{C4} - d_4 \cdot u_{C3} + u_{C3} \\
 &= -d_4 \cdot u_{C4} + (1 - d_4) \cdot u_{C3}
 \end{aligned}
 \tag{59}$$

This source for this formula can also be seen in Figure 62, which highlights the contribution from the different capacitors:

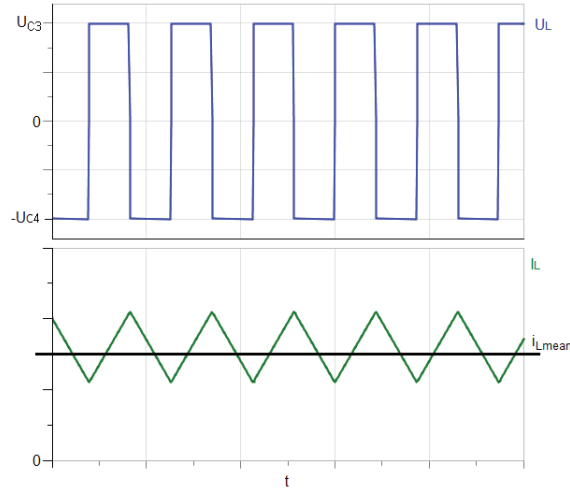


Figure 62: waveform of current and voltage in the inductor of the MSBA stage

The equation can now be split into two parts

$$u_{Lmean}^- = -d_4 \cdot u_{C4} \quad (60)$$

where u_{Lmean}^- is the contribution of the voltage mean value coming from the upper capacitor C_4 , which decreases the inductor current and

$$u_{Lmean}^+ = (1 - d_4) \cdot u_{C3} \quad (61)$$

which is the contribution of the voltage mean value coming from the lower capacitor C_3 , that increases the inductor current.

According to the aforementioned formulas the system can also be represented as shown in Figure 63.

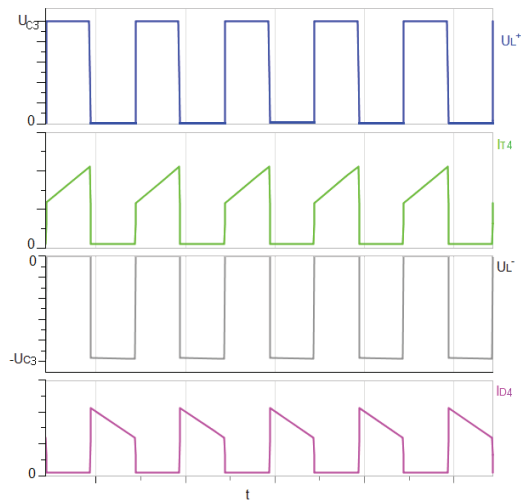


Figure 63: Waveform representation of the MSBA structure

So the mean values of the currents can further be defined as:

$$i_{Lmean}^{D4} = i_{D4} = d_4 \cdot i_{L4} \quad (62)$$

$$i_{Lmean}^{T4} = i_{T4} = (1 - d_4) \cdot i_{L4} \quad (63)$$

This leads to the following formulas for the accumulation elements. The capacitor C_4 is represented by the contribution from the inductor current i_{L4} :

$$\begin{aligned} u_{C4} &= \frac{1}{C_4} \int d_4 \cdot i_{L4} dt \\ &= \frac{1}{C_4} \int i_{D4} dt \end{aligned} \quad (64)$$

The inductor L_4 is represented by the contributions of the capacitor voltages U_{C3} and U_{C4} :

$$\begin{aligned} i_{L4} &= \frac{1}{L_4} \int (-d_4 \cdot u_{C4} + (1 - d_4) \cdot u_{C3}) dt \\ &= \frac{1}{L_4} \int (u_{D4} - u_{T4}) dt \end{aligned} \quad (65)$$

And finally the capacitor C_3 is represented by the current contribution coming from the switch T_4 :

$$u_{C3} = \frac{1}{C_3} \int -i_{T4} dt \quad (66)$$

It is important to keep in mind that the diodes and switches act complementary to each other and for this representation the value d corresponds to a control variable that can be varied continuously between 0 and 100%. Further, the inductor current and the capacitor voltage are average values in this representation. In the expression (67) the variables u_{D4} , u_{T4} , i_{D4} and i_{T4} correspondent to the average voltage and current contributions of the diode and the transistor when these components are in their conduction modes. They should not be confused with any instantaneous voltages or currents across the elements.

$$u_{T4} = d_4 \cdot u_{C4} \quad (68)$$

$$u_{D4} = (1 - d_4) \cdot u_{C3} \quad (69)$$

Using this definition and the formulas above results in the EMR of the elementary stage shown in Figure 64:

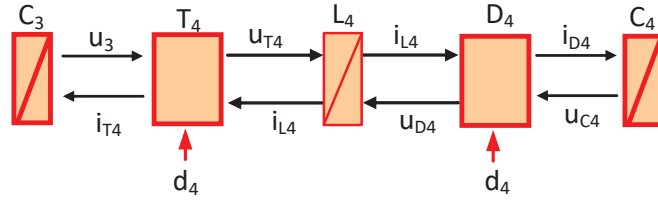


Figure 64: EMR of the elementary MSBA stage

In this figure, the three blocks with a diagonal bar depict the two main causal functions associated with the inductor L_4 and the capacitors C_3 and C_4 . These blocks are the accumulation elements of the elementary MSBA stage. The blocks between the accumulation elements are the conversion elements and combine the “feedback” variables i_{L4} and u_{C4} in order to be fully compatible with the real behaviour of the converter topology.

In the next step, the EMR will be expanded to two and then three MSBA stages.

3.4.2. Two and Three MSBA Stages

The schematic of two connected MSBA stages is shown in Figure 65.

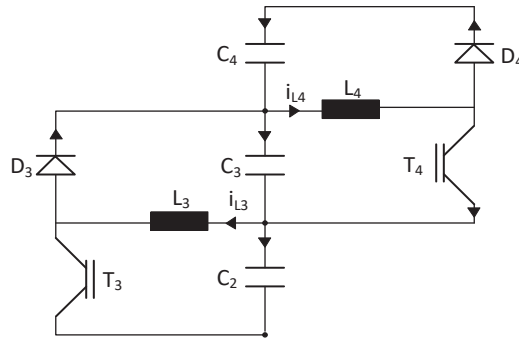


Figure 65: Two MSBA stages

The formula representing Capacitor C_3 has to be adapted in comparison to the elementary stage since there is now also a component coming from the inductor L_3 in addition to the component coming from the diode D_4 :

$$\begin{aligned}
 u_{C3} &= \frac{1}{C_3} \int (d_3 \cdot i_{L3} - i_{T4}) dt \\
 &= \frac{1}{C_3} \int (i_{D3} - i_{T4}) dt
 \end{aligned} \tag{70}$$

The inductor L_3 can be described by the components coming from the capacitors C_3 and C_2 . These can then be represented by the variables U_{D3}^* and U_{T3}^* which correspond to the average voltage contributions from the diode and the transistor when these components are in their conduction modes.

$$\begin{aligned} i_{L3} &= \frac{1}{L_3} \int (-d_3 \cdot u_{C3} + (1-d_3) \cdot u_2) dt \\ &= \frac{1}{L_3} \int (u_{D3} - u_{T3}) dt \end{aligned} \quad (71)$$

At this stage of the representation the capacitor C_2 only sees a contribution from the Diode D_3 :

$$u_{C2} = \frac{1}{C_2} \int -i_{T3} dt \quad (72)$$

This results in the EMR shown in Figure 66, where the capacitors C_2 , C_3 and C_4 as well as the inductors L_3 and L_4 are shown as accumulation blocks. The blocks between the accumulation elements are again the conversion elements and combine the “feedback” variables of the inductors and the capacitors in order to be fully compatible with the real behaviour of the converter topology.

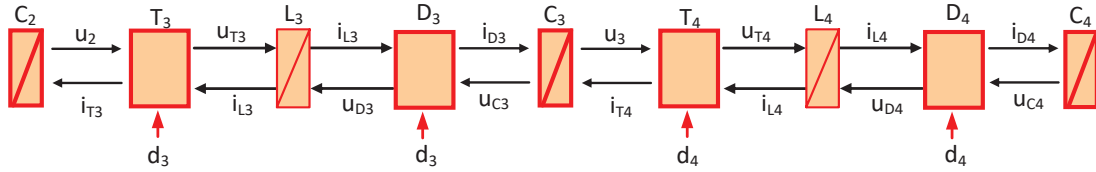


Figure 66: EMR for 2-stage MSBA

Now a third MSBA stage can be added to the converter; the corresponding scheme of the topology can be seen in Figure 67.

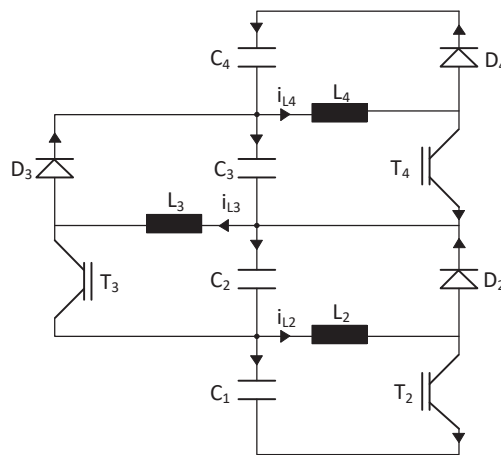


Figure 67: 3-stage MSBA converter

In contrast to the equations used for the 2-stage MSBA, the representation of the capacitor C_2 has to be adjusted to include the component coming from the inductor L_2 :

$$\begin{aligned} u_{C2} &= \frac{1}{C_2} \int (d_2 \cdot i_{L2} - i_{r3}) dt \\ &= \frac{1}{C_3} \int (i_{D2} - i_{r3}) dt \end{aligned} \quad (73)$$

The inductor L_2 is described by the components coming from the capacitors C_3 and C_1 . These components can then be represented by the variables U_{D2}^* and U_{T2}^* which correspond to the average voltage contributions from the diode and the transistor when these components are in their conduction modes.

$$\begin{aligned} i_{L2} &= \frac{1}{L_2} \int (-d_2 \cdot u_{C2} + (1 - d_2) \cdot u_1) dt \\ &= \frac{1}{L_2} \int (u_{D2} - u_{r2}) dt \end{aligned} \quad (74)$$

The capacitor C_1 only sees a contribution from the Diode D_2 at this stage of the Energetic Macroscopic Representation:

$$u_{C1} = \frac{1}{C_1} \int -i_{r2} dt \quad (75)$$

This results in the EMR shown in Figure 68, where the capacitors C_1 , C_2 , C_3 and C_4 as well as the inductors L_2 , L_3 and L_4 are shown as accumulation blocks. The blocks between the accumulation elements are again the conversion elements and combine the “feedback” variables of the inductors and the capacitors in order to be fully compatible with the real behaviour of the converter topology.

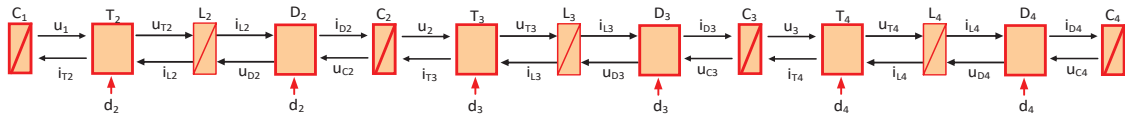


Figure 68: EMR for 3-stage MSBA converter

Now that the Energetic Macroscopic Representation of the MSBA stages is done, the load/output can be added to the converter in the next step.

3.4.3. Three MSBA Stages with Output Stage

The schematic of the 3-stage MSBA converter with an added output stage is shown in Figure 69.

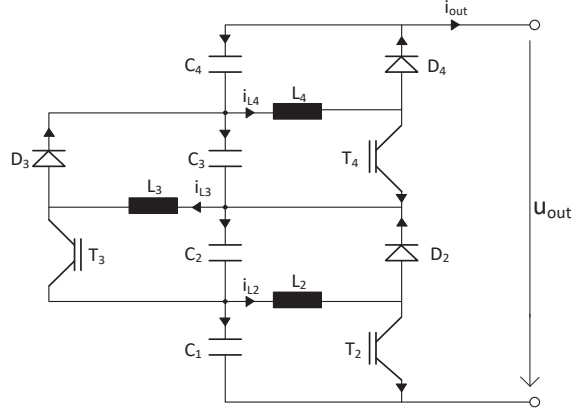


Figure 69: Three stage MSBA with output

The added output changes the currents of the structure since the output current is a component of the capacitor representation. This results in the following representation of capacitor C_4 :

$$\begin{aligned} u_{C4} &= \frac{1}{C_4} \int (i_{L4} - i_{out}) dt \\ &= \frac{1}{C_4} \int (i_{D4} - i_{out}) dt \end{aligned} \quad (76)$$

Comparing this to the other MSBA stages it becomes clear that all other capacitor values are based on C_4 so the load current will now also be in the representation of the other capacitors:

$$u_{C3} = \frac{1}{C_3} \int (i_{D3} - i_{T4} - i_{out}) dt \quad (77)$$

$$u_{C2} = \frac{1}{C_2} \int (i_{D2} - i_{T3} - i_{out}) dt \quad (78)$$

$$u_{C1} = \frac{1}{C_1} \int (-i_{T2} - i_{out}) dt \quad (79)$$

This can be represented in the EMR by using coupling elements (Figure 70). In addition there is now an output voltage represented by

$$u_{out} = u_{C1} + u_{C2} + u_{C3} + u_{C4} \quad (80)$$

which also needs to be represented by a coupling element.

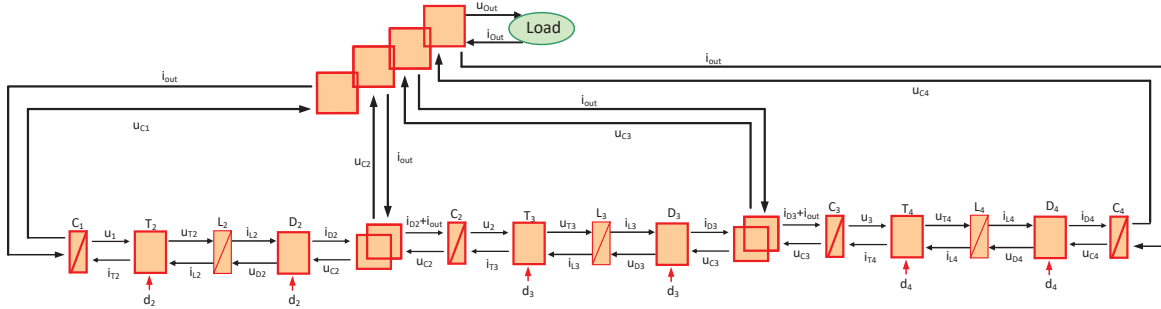


Figure 70: EMR representation of 3-stage MSBA with load

In the final step the boost input stage will be represented with the Energetic Macroscopic Representation and then be added to the converter.

3.4.4. Boost stage

For representing the input converter the diode and switch of this stage are summarized into C_{V1} using the current I_1 and the voltage U_1 to represent it (Figure 71).

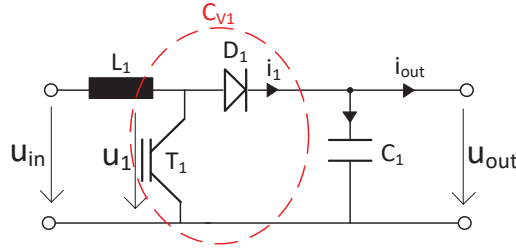


Figure 71: Input boost stage

The Inductor L_1 can be represented with the help of the components related to the converter input voltage and the voltage U_1 :

$$i_{L1} = \frac{1}{L_1} \int (u_{in} - u_1) dt \quad (81)$$

The capacitor C_1 sees a contribution from the current I_1 and the output current:

$$u_{C1} = \frac{1}{C_1} \int (i_1 - i_{out}) dt \quad (82)$$

The block C_{V1} which includes the switch T_1 and the Diode D_1 , is represented solely by the duty cycle d and the capacitor voltage from C_1 and the inductor current from L_1 :

$$\begin{aligned} u_1 &= d_1 \cdot u_{C1} \\ i_1 &= d_1 \cdot i_{L1} \end{aligned} \quad (83)$$

The EMR of the boost converter is shown in Figure 72 where L_1 and C_1 are represented by accumulation blocks while C_{V1} is the conversion block connecting them. The representation is completed by two source elements, the converter source and the load.

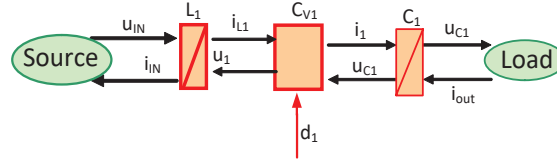


Figure 72: EMR representation of the boost stage

Now that the representation of the boost stage is complete, it can be added to the three-stage MSBA converter, resulting in the four-stage asymmetric Multistage Stacked Boost Architecture.

3.4.5. Four Stage MSBA Converter

The schematic of the four-stage MSBA converter, which consists of three elementary MSBA stages and an input boost stage, can be seen in Figure 73.

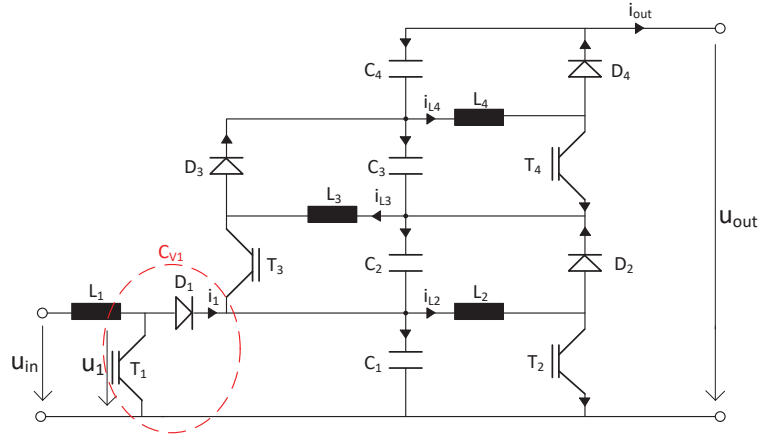


Figure 73: 4-stage MSBA converter

When connecting the boost stage to the three MSBA stages the capacitor description of first stage (C_1) needs to take into account the following stage. This means that now in addition to the already know components, there is a component coming from the diode D_2 .

$$u_{C1} = \frac{1}{C_1} \int (i_1 - i_{T2} - i_{out}) dt \quad (84)$$

Keeping this change in the first capacitor in mind, the representations of the boost stage and the three MSBA stages can now be put together. This results in the EMR of the asymmetric MSBA shown in Figure 74, which contains conversion elements for the inductors L_1 - L_4 as well as the capacitors C_1 - C_4 . There are also several conversion elements, which combine the “feedback” variables of the inductors and the capacitors in order to be fully compatible with the real behaviour of the converter topology. In addition, several coupling elements can be seen which represent the “feedback” component of the output current in the different elements as well as the combination of the capacitor voltages at the output. Last but not least the two source elements, the input source and the load are represented.

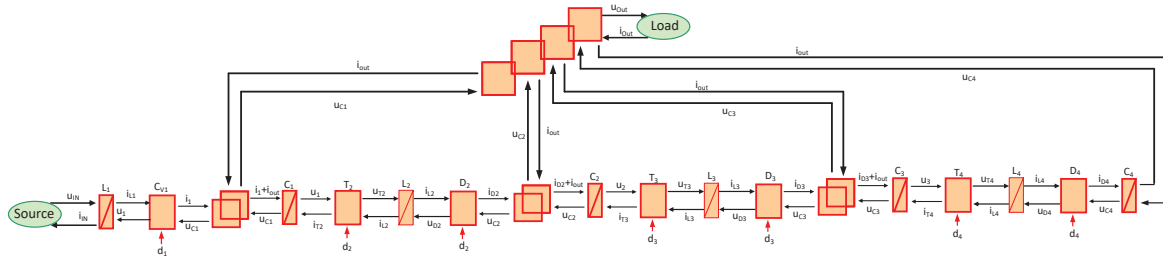


Figure 74: EMR for the 4-stage MSBA

Since the representation of the four-stage asymmetric Multistage Stacked Boost Architecture is now complete, it is time to verify the concept with the help of a simulation. Therefore, this representation of the MSBA converter will be implemented with MATLAB/Simulink.

3.4.6. Simulation

The elements of the simulation are the implementation of the equations shown before. The inductors are represented by the formula

$$i_{L,n} = \frac{1}{L_n} \int (u_{Dn} - u_{Tn}) dt \quad (85)$$

which contains the variables U_{Dn} and U_{Tn} which correspond to the average voltage contributions from the diode and the transistor of the respective stage when these components are in their conduction modes. This is exactly represented in the inductor block in the simulation (Figure 75).

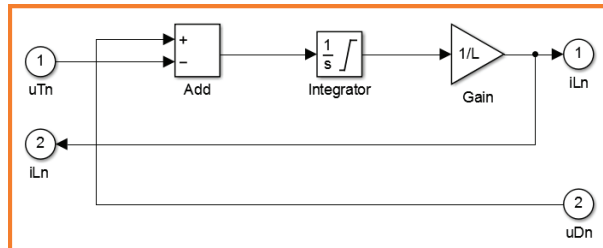


Figure 75: Inductor block for the MSBA stage of the EMR simulation

The capacitors are represented by the equation that contains the contribution coming from the output current, the switch of the respective stage and the diode of the stage before.

$$u_{Cn} = \frac{1}{C_n} \int (i_{Dn} - i_{T(n+1)} - i_{out}) dt \quad (86)$$

Therefore the capacitor implementation results in the block shown in Figure 76.

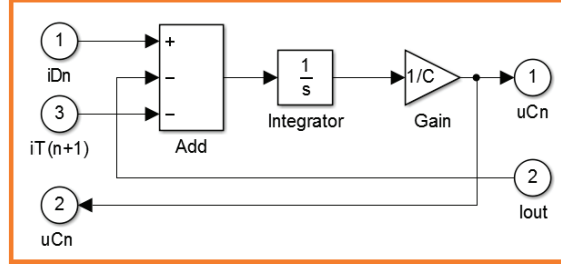


Figure 76: Adapted capacitor block for the MSBA stage of the EMR simulation

The diode blocks (Figure 77) use the following formula, showing the “feedback” variable of the capacitor voltage:

$$u_{Dn} = (1 - d_n) \cdot u_{C(n-1)} \quad (87)$$

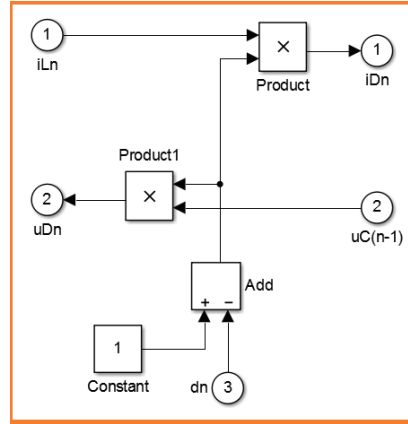


Figure 77: Diode block for the MSBA stage of the EMR simulation

In the same manner the blocks for switches (Figure 78) show the “feedback” variable of the capacitor voltage and are represented by

$$u_{Tn} = d_n \cdot u_{Cn} \quad (88)$$

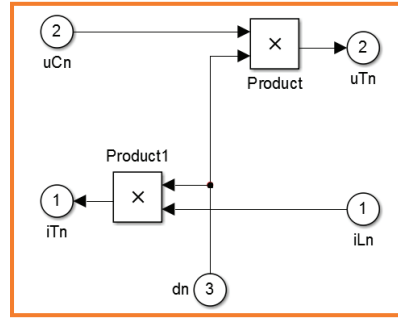


Figure 78: Switch block for the MSBA stage of the EMR simulation

The load relies on a load resistor, which is implemented by a variable in the step block. A step block is used to have the possibility of changing the load during the simulation for testing how the converter works with perturbations at the output (Figure 79).

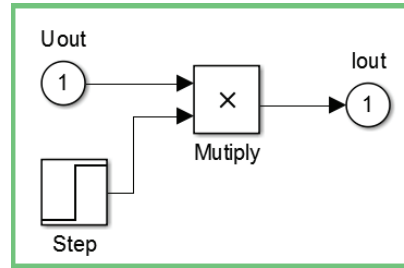


Figure 79: Load block of the EMR simulation

A source block for soft start-up was implemented as shown in Figure 80. The ramp and saturation blocks are used for the start-up of the converter, increasing the voltage slowly to the desired input voltage level and avoiding potential problems during the start-up. In addition, the input current is feed to a Terminator since in the Energetic Macroscopic Representation of the MSBA it is a component coming from the inductor L_1 and needs to be connected to the source.

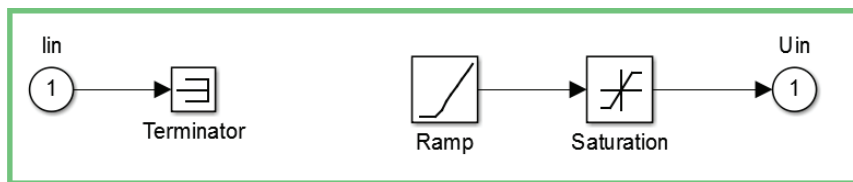


Figure 80: Source block of the EMR simulation

For the boost stage the inductor L_1 is again represented by the equation containing the contribution of the components related to the converter input voltage U_{in} and the voltage U_1 :

$$i_{L1} = \frac{1}{L_1} \int (u_{in} - u_1) dt \quad (89)$$

And as can be seen this is exactly represented in the inductor block in the simulation (Figure 81).

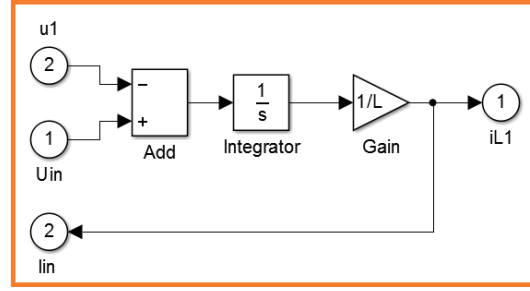


Figure 81: Inductor block for the boost stage of the EMR simulation

Same is true for the capacitor C_1 which is represented by the formula containing the contribution coming from the output current and the current of I_1 :

$$u_{C1} = \frac{1}{C_1} \int (i_1 - i_{out}) dt \quad (90)$$

Using this equation for the simulation results in the capacitor block that is shown in Figure 82:

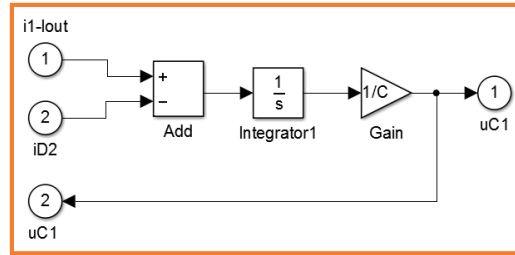
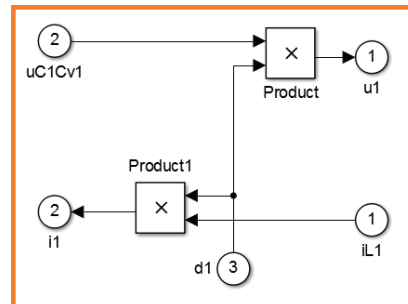


Figure 82: Capacitor block for the boost stage of the EMR simulation

The converter C_{v1} block (Figure 83) which includes the switch T_1 and the Diode D_1 , is represented solely by the duty cycle d and the capacitor voltage from C_1 and the inductor current from L_1 and uses the following formulas:

$$\begin{aligned} u_1 &= d_1 \cdot u_{C1} \\ i_1 &= d_1 \cdot i_{L1} \end{aligned} \quad (91)$$


Figure 83: C_{v1} block for the boost stage of the EMR simulation

In addition to these blocks for the elements of the MSBA converter there are also coupling elements needed. In the simulation there is no need for the coupling elements shown before that represent the “feedback” of the output current, since this was directly done by adding a third connection port to the affected blocks. This means that only two coupling elements need to have separate blocks. One is the coupling block for the load, which adds the capacitor voltages to calculate the output voltage. This block can be seen in Figure 84.

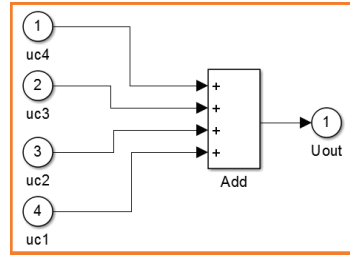


Figure 84: Coupling block for the voltage output

The second coupling block that is needed connects the capacitor C_1 with the conversion element C_{v1} and the output current I_{out} and can be seen in Figure 85.

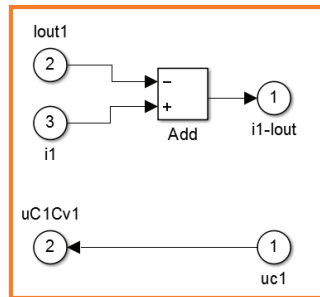


Figure 85: Coupling block for the boost stage

After defining all the elements of the boost and MSBA stages, the 4-stage MSBA converter can be implemented (Figure 86). This results in a simulation containing two source blocks (source and load), eight accumulation elements (the capacitors and inductors), seven conversion elements (representing “feedback” variables) and two coupling elements (output voltage and boost stage).

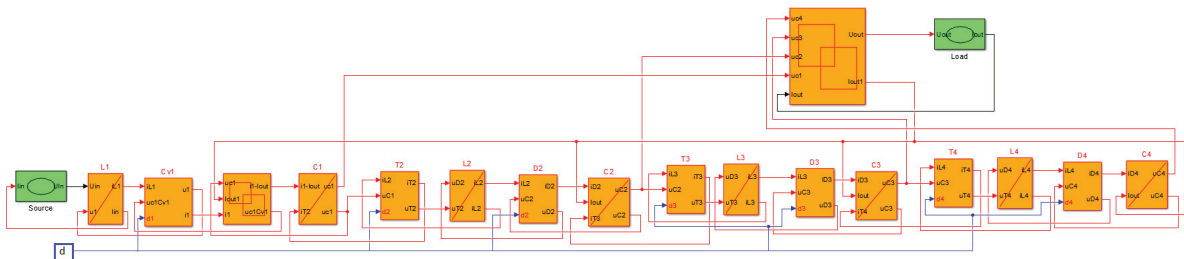


Figure 86: Matlab/Simulink implementation of the 4-stage MSBA

For testing purpose the simulation is run in open loop with a fixed duty cycle of 0.5, using an input voltage of 100V and a load of 40Ω. Figure 87 shows the capacitor voltages on the left and the inductor currents on the right. It is apparent that the Energetic Macroscopic representation works quite well, since the capacitor voltages are all at the same level and the inductor currents show the expected behaviour. Meaning they get smaller in in each stage. Figure 88 show the output voltage on the left and the output current on the right. Both are at the expected levels, the output voltage is eight times the input voltage and the output current is accordingly an eighth of the input current.

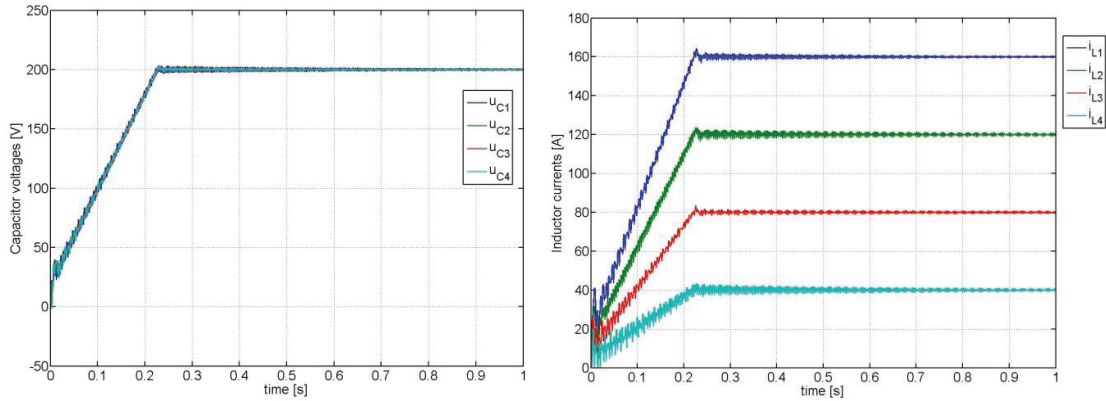


Figure 87: Capacitor voltages (left) and inductor currents (right) of the 4-stage MSBA

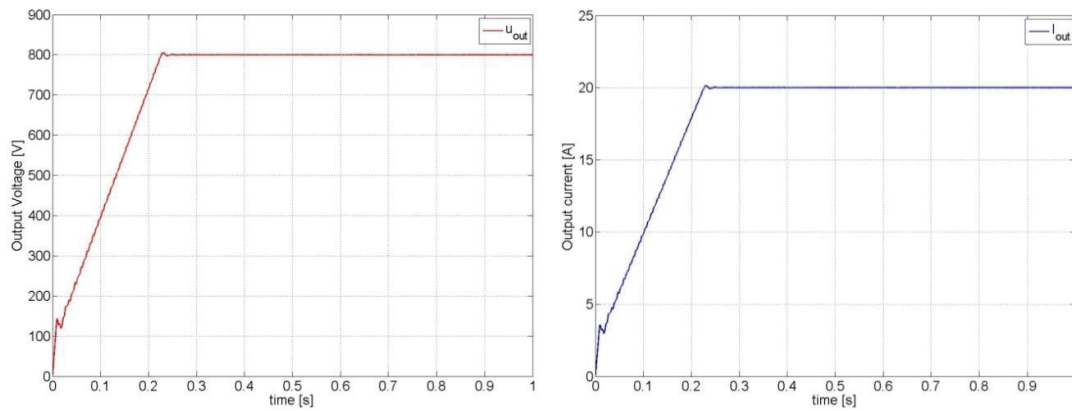


Figure 88: Output voltage (left) and output current (right) of the 4-stage MSBA

It is apparent that the Energetic Macroscopic Representation of the four-stage asymmetric Multistage Stacked Boost Architecture is correct and that the simulation is working without a problem. Therefore, it is now time to stop running the converter in open-loop and research possibly control methods and implement and simulate them.



4. Control

4.1. Linearized Fast Feed-Forward

4.1.1. Introduction

The idea is the use a cascaded control system; a current controller for the inductor currents relying on the feedback of the load current as well as a superimposed voltage controller for the capacitor voltages. Cascaded controls have the following advantages:

- easy limitation of the internal variables;
- simplification of the control circuit stabilisation
- small subsystems, which makes it easier to dimension the controllers
- reduced influence of the disturbance variables
- easier implementation by adjusting one control loop after another

It is important to realise that normally the inner control has to operate faster than the superimposed controls, which can be done for example with different sampling intervals [36].

4.1.2. The Boost Stage

The scheme of the boost input stage is shown in Figure 89. The main quantity that needs to be controlled is the output of the stage, in this case the capacitor voltage. For the actual control a PWM modulation is used, where the duty cycle d defines the ratio of the input voltage to the output voltage. For the closed-loop control the two state variables of the converter (the capacitor voltage and the inductor current) need to be controlled.

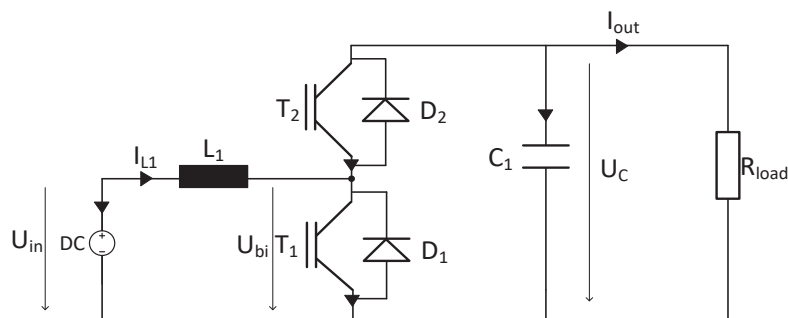


Figure 89: Input boost-stage of the MSBA converter

4.1.2.1. Linearization and Feed-Forward (LFF)

Many control strategies for a classical boost converter are given in the literature ([45]-[46][47][48][49]). Independently of the nature of such controller, the main characteristic is that they are generally able to maintain the output voltage in any conditions regarding the load.

In the case of the cascade of the boost topology with an MSBA stage, the output current of the boost converter appears as a state variable of the next stage, the MSBA converter. This state variable is intended to be measured, according the condition of such a variable to be safely controlled, avoiding overload of the semiconductor devices. As a consequence, the control structure of the boost input stage can be developed based on the available information of its load current. A dedicated control structure using the principle of Feed-Forward will be studied (Figure 90).

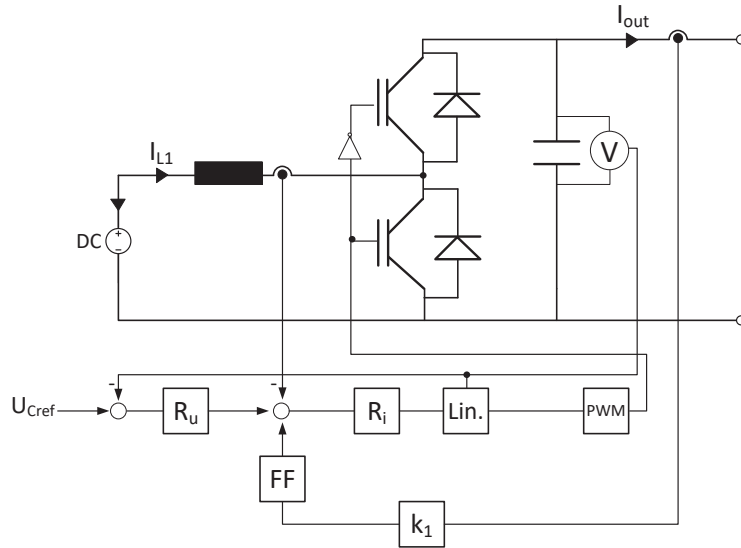


Figure 90: Block diagram of the boost stage with LFF control structure

4.1.2.2. Linearized Command of the Boost Converter

The PWM modulator is controlling the ratio between the input and the output voltage (which is the capacitor voltage) of the boost scheme according relation:

$$U_{bi} = \frac{U'_{cm}}{\hat{U}_h} U_c \quad (92)$$

U_{bi} and U_c are the input and output voltage of the boost stage according the indication in Figure 89, while U'_{cm} is the control variable applied to a classical PWM modulator and \hat{U}_h is the maximum value of the triangular carrier (Figure 91).

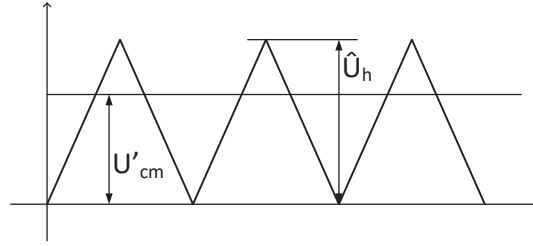


Figure 91: PWM modulation and according references

The voltage across the inductor can be defined as

$$U_L = U_{in} - U_{bi} = U_{in} - \frac{U'_{cm}}{\hat{U}_h} U_C \quad (93)$$

The linear control of the inductor voltage is obtained through a bias control quantity

$$U'_{cm0} = \frac{U_{in}}{U_C} \hat{U}_h \quad (94)$$

which is added to the control variable U_{cm} delivered by the current controller.

$$U'_{cm} = U'_{cm0} + U_{cm} \quad (95)$$

The bias control quantity is depending on both the converter input U_{in} and the converter output U_C .

Finally, the voltage at the terminals of the inductor can be linearly controlled (-1 factor) as

$$\begin{aligned} U_L &= U_{in} - U_{bi} = U_{in} - \frac{U'_{cm}}{\hat{U}_h} U_C = \\ &= U_{in} - \frac{U_{cm0} + U_{cm}}{\hat{U}_h} U_C = U_{in} - \frac{\frac{U_{in}}{U_C} \cdot \hat{U}_h + U_{cm}}{\hat{U}_h} U_C \\ &= -\frac{U_{cm}}{\hat{U}_h} U_C \end{aligned} \quad (96)$$

A structural diagram of the current control of the inductor is given in Figure 92, including the superimposed voltage control of the capacitor.

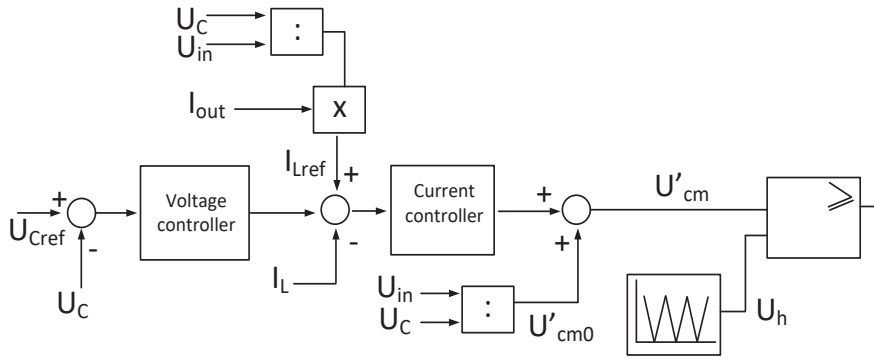


Figure 92: Control structure of the boost stage

The dynamic performance of the control of the boost stage is illustrated in the simulations in Figure 93 which were done with Gecko Circuits. The input voltage was set to 100V, the capacitor was pre-charged to 200V and the load to 10Ω. All parameters for the P controllers used in this and all the following simulations were initially set with the help of the Magnitude Optimum Criterion [36] to reach good dynamics. They were then refined based on the simulation results. The final parameter for the p-voltage controller was 1 and the parameter for the p-current controller was 0.5. In the first subplot the voltage reference and the actual capacitor voltage are shown. The second plot corresponds to the output quantity of the voltage controller. The plot line illustrates the current at the output (load current). The fourth plot corresponds to the inductor current, while the last (fifth) curve represents the feed-forward quantity for the inductor current reference. This quantity is calculated from the load current (measured) and takes into account the ratio between the input and output voltages of the converter.

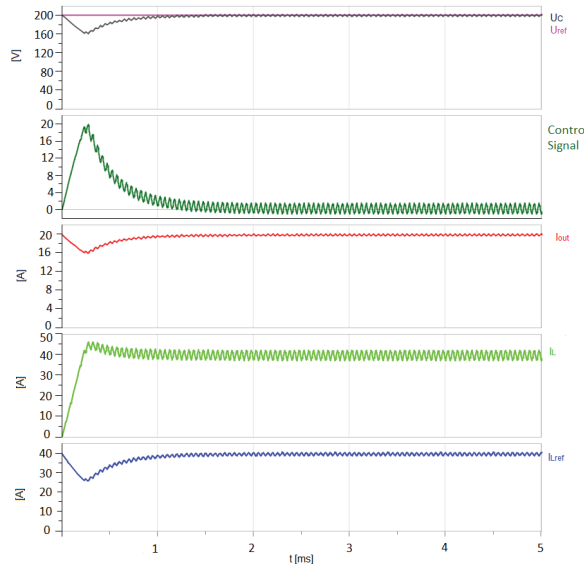
Figure 93: transient response of the boost stage with $U_{in}=100V$

Figure 93 showed that this control structure works fine when the duty cycle is 0.5. To validate that it will also work for other input to output voltage relations, simulations with an input voltage of 50V and 150V

were done, while the output voltage remained fixed at 200V. As can be seen in Figure 94 the control handles the changed input conditions without any problem.

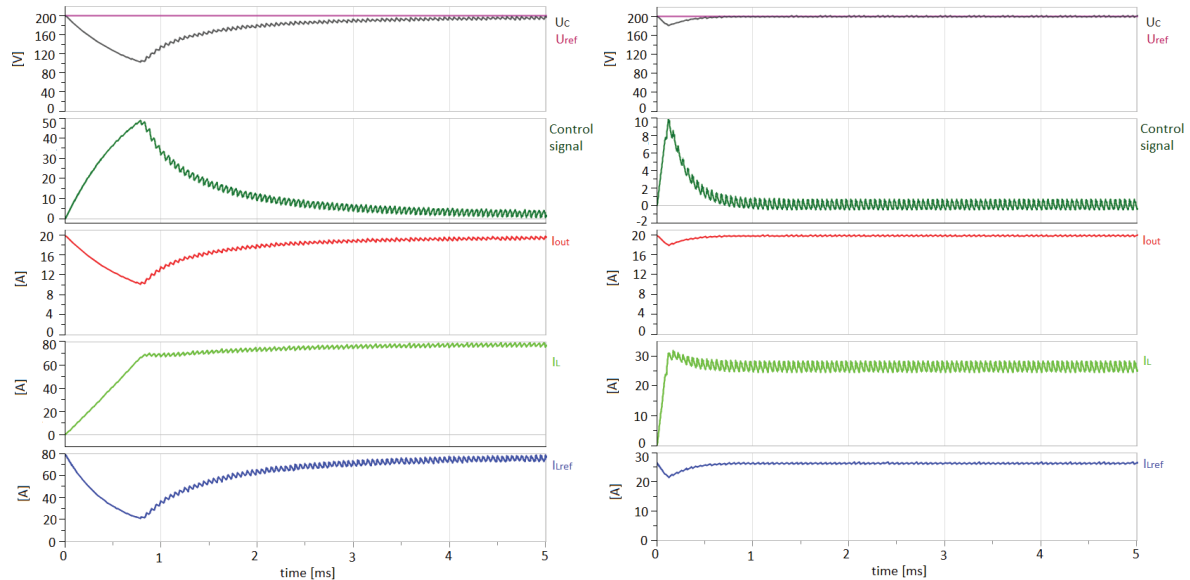


Figure 94: transient response of the boost stage with $U_{in}=50V$ (left) and $U_{in}=150V$ (right)

4.1.2.3. Dynamic Response of the Boost Stage against Perturbation

To verify the dynamic performance of the boost stage against perturbations, a switched load resistor is added. The scheme for this verification is shown in Figure 95. The additional resistor is connected at $t=2.5ms$, while the control structure stays the same as indicated in Figure 92. For both resistors the value of 20Ω was used.

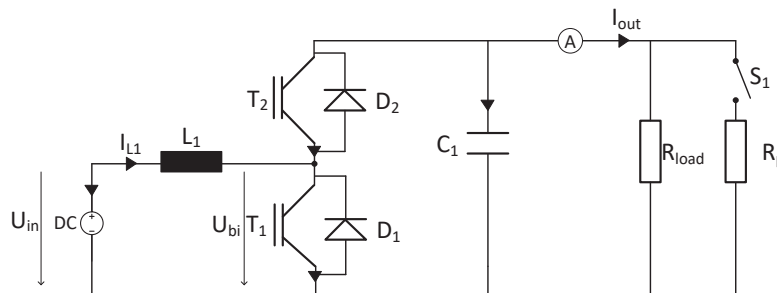


Figure 95: The boost stage with load step

Figure 96 shows that the addition of a load step causes a drop in the capacitor voltage but the control brings it quickly (under 0.5ms) back to the desired level with only minimal oscillations.

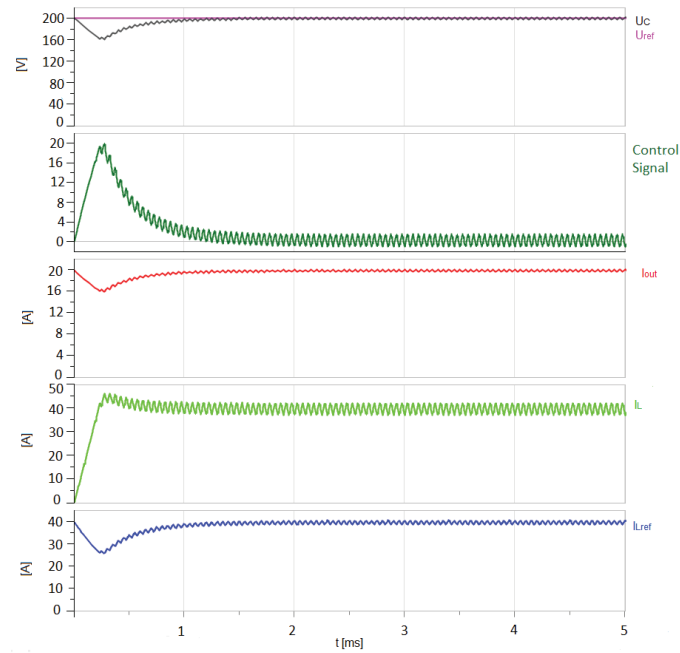


Figure 96: Dynamic response of the boost stage with load step

Since the control for the input boost stage is clearly working fine, the single MSBA stage will be looked at next.

4.1.3. The MSBA cell

The single MSBA cell converter can also be controlled in order to avoid the resonant phenomena described before. Like the control structure for the boost stage, the chosen MSBA control structure uses two cascaded controllers with feedback of the load current (Figure 97) to generate the PWM.

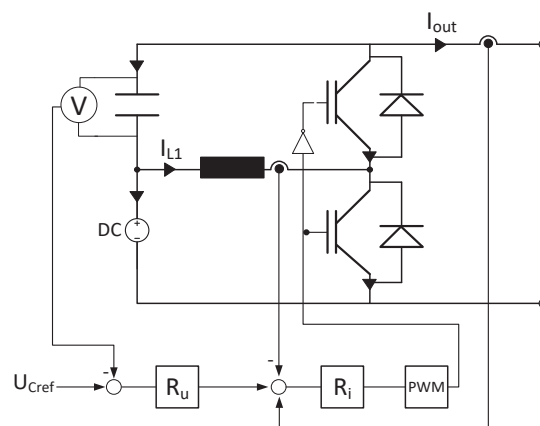


Figure 97: Block diagram of a MSBA cell and control structure

4.1.3.1. The Control Structure

The control structure used for the MSBA cell is represented in Figure 98. The current in the inductor is controlled with a simple proportional controller and the converter-part itself is commanded through a PWM modulator. Due to the presence of a pure integral component for the system to be controlled, the current controller doesn't need any integral component.

The superimposed voltage balancing controller is also a single proportional controller. Even if the output load represents a perturbation for the voltage control loop, the need of an integral component in the controller itself can be avoided through feed-forward of the perturbation current that is measured. The feedforward signal must of course represent an anticipation quantity for the inductor current. This signal will be calculated from the measured output current through the factor(s) k . These factors are based on the relation of the output current to the inductor current in each stage, based on the equation:

$$I_n = 2 \cdot I_{out} + I_{n+1} \quad (97)$$

In order to properly protect the current solicitation of the power semiconductor devices and the passive components, the control structure must present the possibility to limit the current during transient operation. Therefore, between the voltage balancing controller with its feedforward signal and the current controller, a limitation element has been inserted.

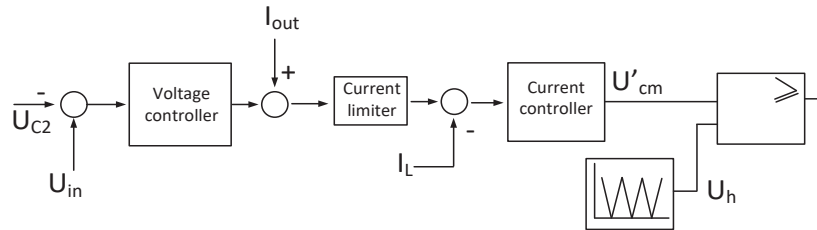


Figure 98: Control circuits of the MSBA cell

4.1.3.2. Dynamic Response of the Controlled MSBA Cell

The dynamic response of the controlled MSBA cell is verified by simulation. The initial conditions are a pre-charged capacitor with a voltage level of 90V and again the input voltage of 100V. The circuit is loaded from the beginning with a resistor of 50Ω. The load current is therefore equal to 4A under steady state conditions and the value of the inductor current is equal to double the output current if the duty cycle of the MSBA cell is equal to 0.5. The parameter for the p-voltage controller was 0.2 and the parameter for the p-current controller was 1; in addition the current limiter was set to 12A. The curves represented in Figure 99 and Figure 100 show the results of the controlled MSBA stage under such conditions. Figure 99 shows the transient without any limitation of the current reference and Figure 100 shows the same transient with the limited current reference.

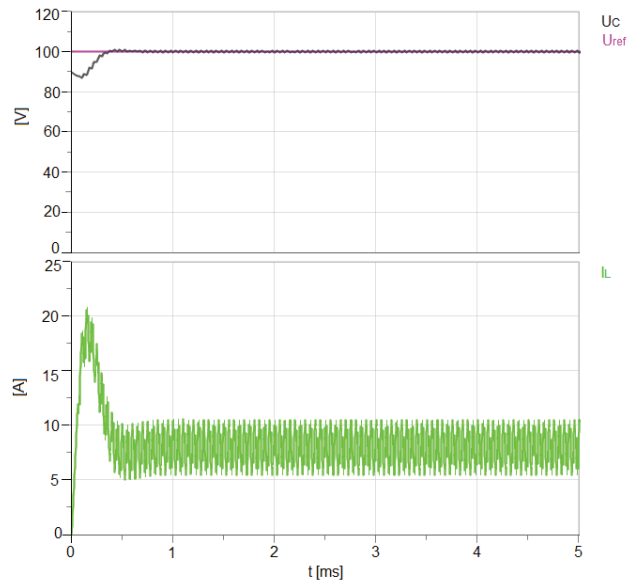


Figure 99: Dynamic response of the controlled MSBA cell without current limitation

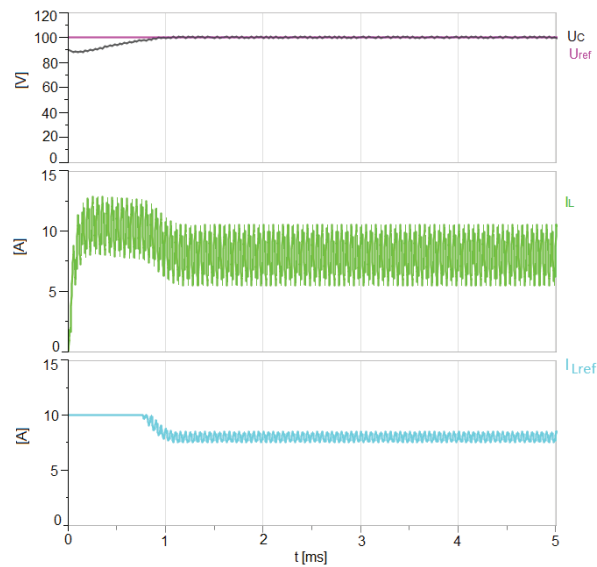


Figure 100: Dynamic response of the controlled MSBA cell with current limitation

4.1.3.3. Dynamic Performance with Perturbations

The same control as used in the previous simulation is now tested in case of a perturbation, only change was setting the current limiter to 20A. The perturbation is introduced at the level of the output load of the converter, with an additional resistor connected in parallel and switched on at the simulation time of 2.5ms. The topology scheme used is represented Figure 101.

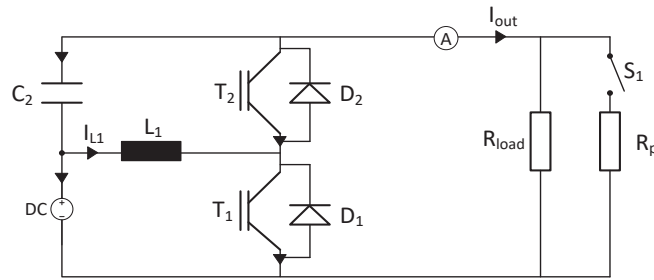


Figure 101: The MSBA cell with output load step

The simulation results are given through the curves in Figure 102. The plot shows the output voltage with the superposed reference value. The second plot of Figure 102 shows the current in the inductor and the last (third) one the inductor reference value.

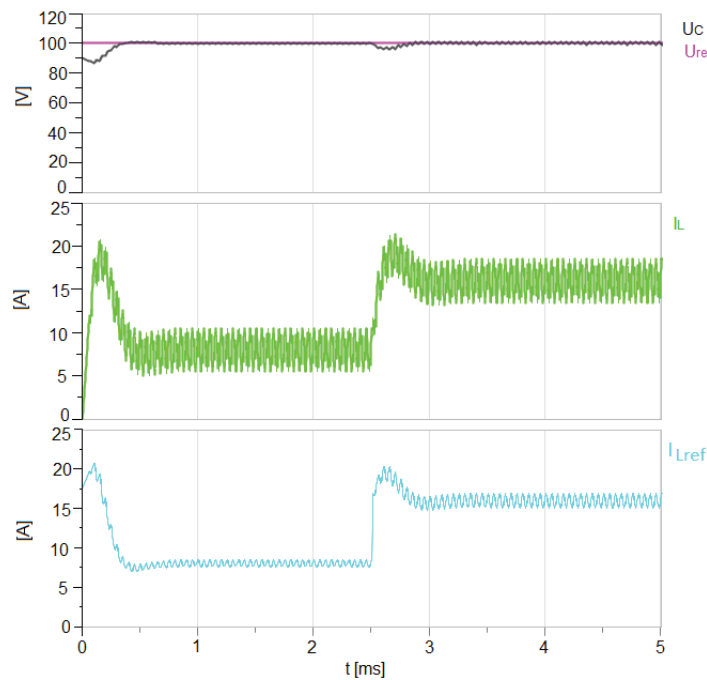


Figure 102: Dynamic response of the MSBA cell control in the case of a load step

The next step is now to add the MSBA cell to the boost input stage first as load and then as controlled stage.

4.1.4. Controlled Boost Stage with MSBA Cell as “Load”

4.1.4.1. Input Boost Stage Combined with MSBA Cell

In the first step, the MSBA cell will be added to the input boost stage as load, meaning that it will run with a PWM and a fixed 0.5 duty cycle. This is done to check if it would be enough to control the boost stage and run the MSBA cells open-loop or if a more sophisticated control is needed.

Figure 103 shows the boost stage connected with MSBA cell; the 2-stage MSBA converter. In the first approach the MSBA cell will be considered as load, meaning that it will be controlled by a fixed duty cycle of 0.5 while the boost stage is controlled with the LFF control implementation (Figure 104). The input voltage is still set to 100V and the load resistance has a value of 40Ω.

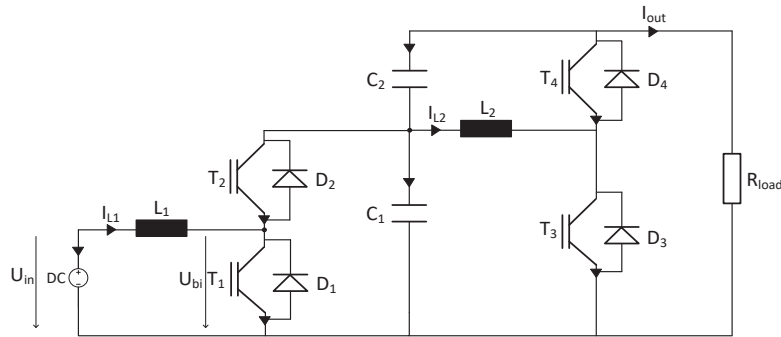


Figure 103: 2-stage MSBA converter

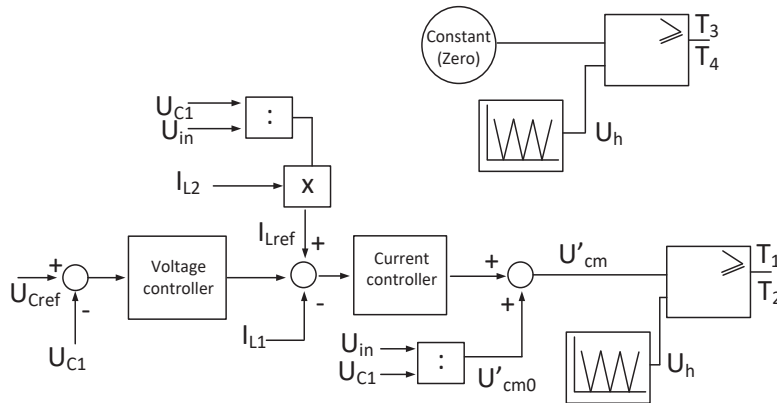


Figure 104: Control circuits of the boost stage with MSBA cell as load

The dynamic performance of the boost control of this system is illustrated in Figure 105 and the parameter for the p-voltage controller was 1 and the parameter for the p-current controller was 0.5. In the first subplot the voltage reference and the actual capacitor voltage of the boost stage output are shown again. The second plot corresponds to the output quantity of the voltage controller. The third plot illustrates the current at the output of the boost stage (current of inductor L_2). The fourth plot

corresponds to the inductor current of the boost stage (L_1), while the last (fifth) curve represents the feedforward quantity for the inductor current reference. This quantity is calculated from the load current (measured) and takes into account the ratio between the input and output voltages of the converter.

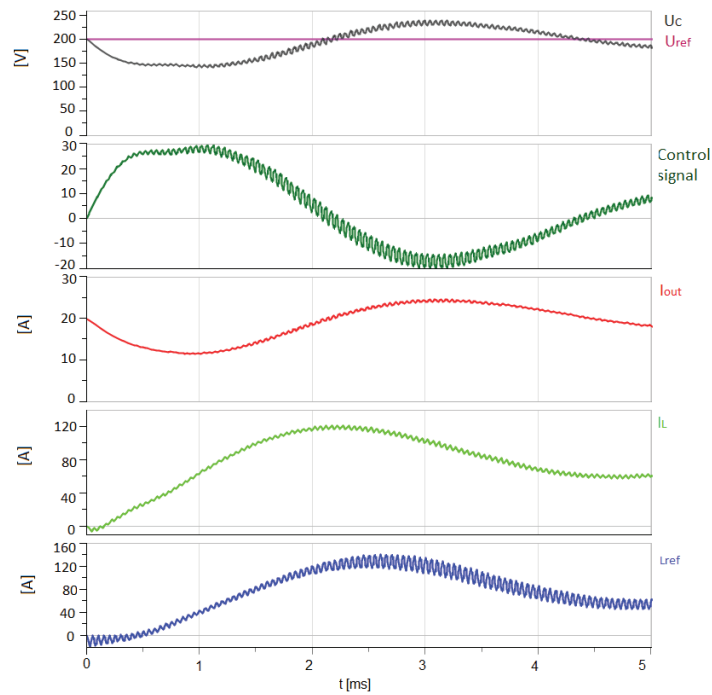


Figure 105: Dynamic performance of the boost stage with an MSBA cell as load

To get a complete impression of the system behaviour Figure 106 shows the output voltage of the converter in the first subplot and the output current in the second subplot. In addition, the capacitor voltage of C_2 is shown in the last plot.

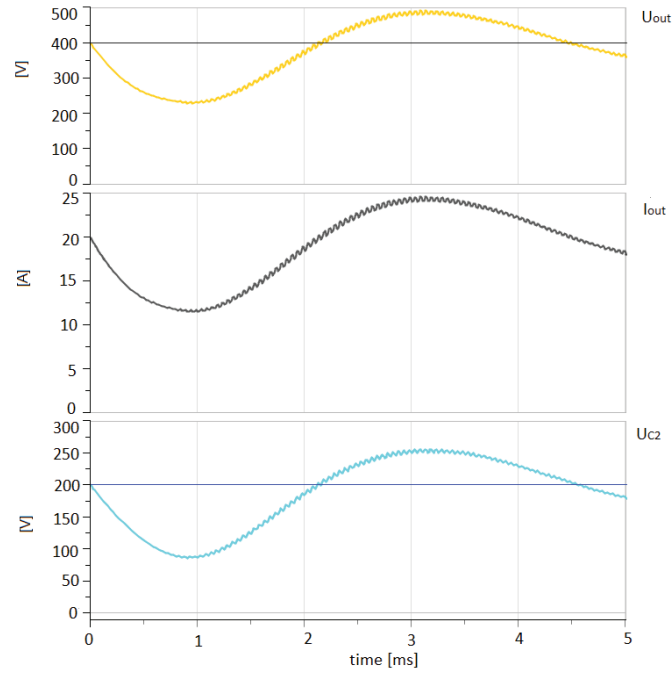


Figure 106: Output waveforms of the boost with MSBA cell as load converter

As can be seen in these figures, the system shows the resonance phenomena related to the open-loop approach of the MSBA cell. This resonance phenomenon affects the whole converter and the LFF control of the boost stage cannot damp or negate them. Another still quite simple approach could be using the output current as feed-forward signal for the boost stage control.

4.1.4.2. Controlled Boost Stage with Single Open-Loop MSBA Cell Relying on Output Current

Figure 107 shows the boost stage connected with the MSBA cell. In this configuration, the boost stage is relying on the output current of the converter to control the whole structure (Figure 108) in contrast to before relying on the output current of the boost stage. The input voltage is still set to 100V and the load resistance has a value of 40Ω and all parameters were the same as before.

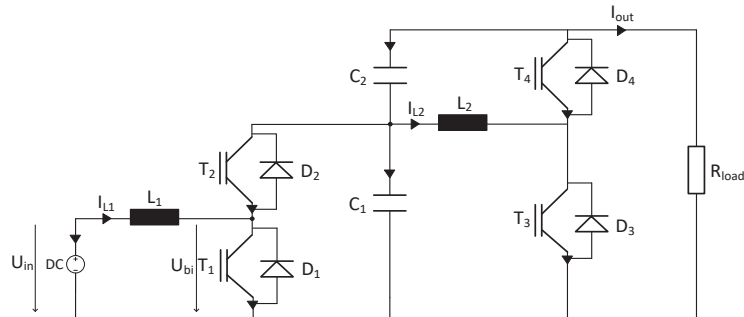


Figure 107: The boost stage with one MSBA stage

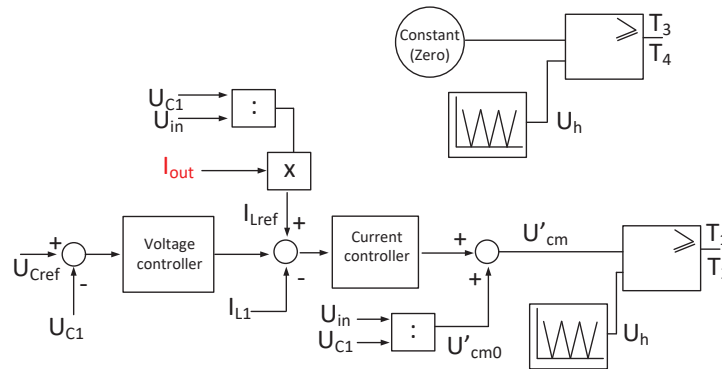


Figure 108: Control circuits of the boost stage with MSBA cell in open-loop

The dynamic performance of the boost control of this system is illustrated in Figure 109. In the first subplot the voltage reference and the actual capacitor voltage of the boost stage output are shown again. The second plot corresponds to the output quantity of the voltage controller. The third plot illustrates the current at the output of the converter (I_{out}). The fourth plot corresponds to the inductor current of the boost stage (I_L), while the last (fifth) curve represents the feedforward quantity for the inductor current reference. This quantity is calculated from the load current (measured) and takes into account the ratio between the input and output voltages of the converter. For the first 10ms the load of the converter is the before mentioned 40Ω resistance, after that a perturbation is simulated by adding a resistor of the same value to the load.

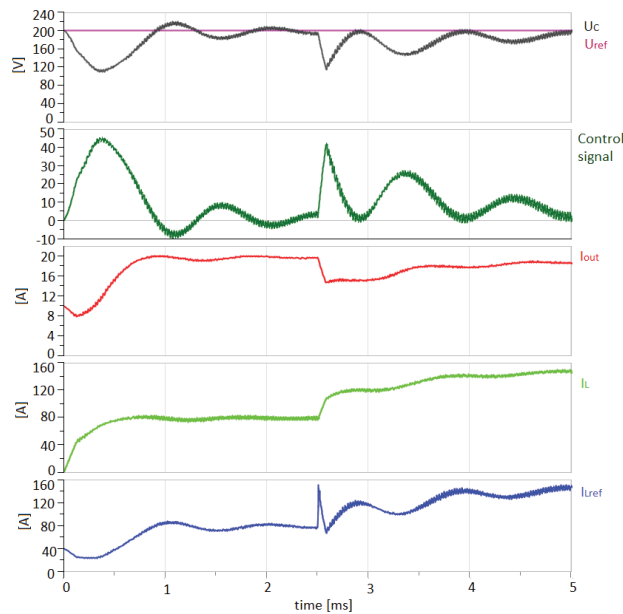


Figure 109: Dynamic performance of the boost stage with an MSBA cell in open-loop

To get a complete impression of the system behaviour Figure 110 shows the output voltage of the converter in the first subplot and the output current in the second subplot. In addition, the capacitor voltage of C_2 is shown in the last plot.

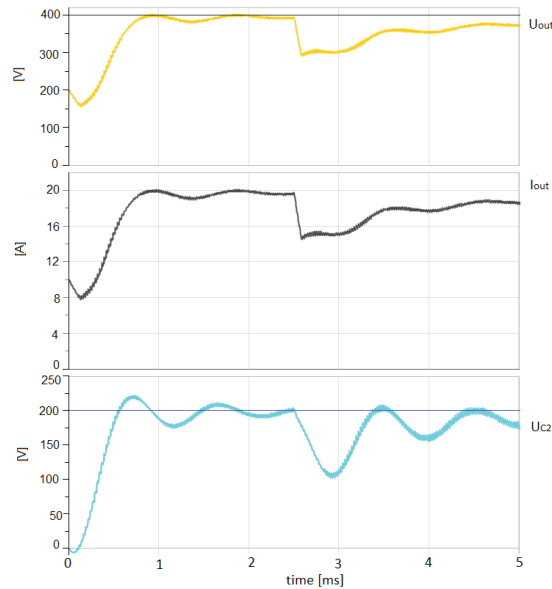


Figure 110: Output waveforms of the boost with MSBA cell in open-loop

As can be seen in these figures, the system shows the resonant phenomena related to the open-loop approach to the MSBA cell at the start and after a perturbation. But after some time the control is able to dampen these oscillations. What becomes apparent is that the output voltage and the voltage of the second capacitor C_2 are not at the desired level. They are 5-10V below, since the voltage of the second capacitor is not controlled in this approach. Therefore, the MSBA stage of the converter also needs to be controlled.

4.1.5. Multilevel MSBA Converter

4.1.5.1. Controlled Boost Stage with Controlled MSBA Cell

In the next simulation, the control method for the MSBA that had previously been successfully tested has been implemented in addition to the control of the boost stage and the whole control structure can be seen in Figure 111.

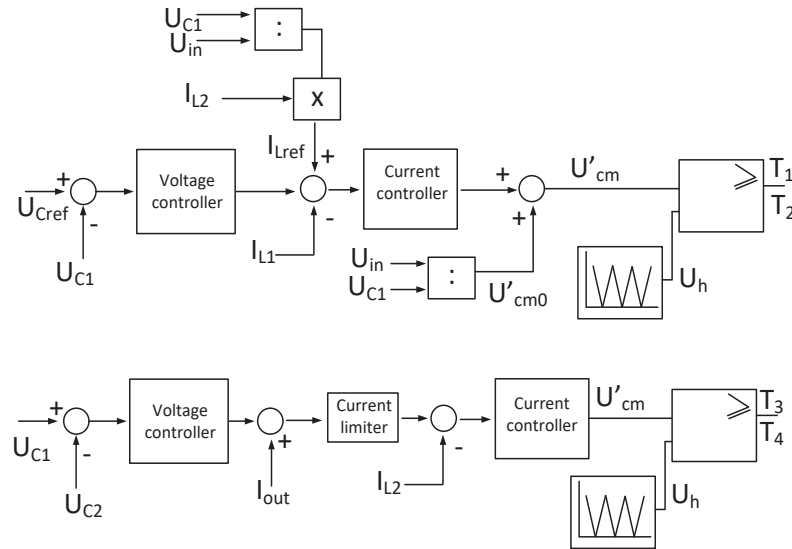


Figure 111: Control structure for the controlled boost stage and MSBA cell

For this simulation, the parameter for the p-voltage controller was 0.2 and the parameter for the p-current controller was 1 for the MSBA cell; in addition the current limiter was set to 12A. For the boost stage the parameter for the p-voltage controller was 1 and the parameter for the p-current controller was 0.5. The dynamic performance of the boost control of this system is again simulated and is illustrated in Figure 112. Again, in the first subplot the voltage reference and the capacitor voltage of C_1 are shown. The second plot corresponds to the output quantity of the voltage controller. The third plot line illustrates the current at the output of the boost stage (current of inductor L_2). The fourth plot corresponds to the inductor current of the boost stage (L_1), while the last (fifth) curve represents the feed-forward quantity for the inductor current reference.

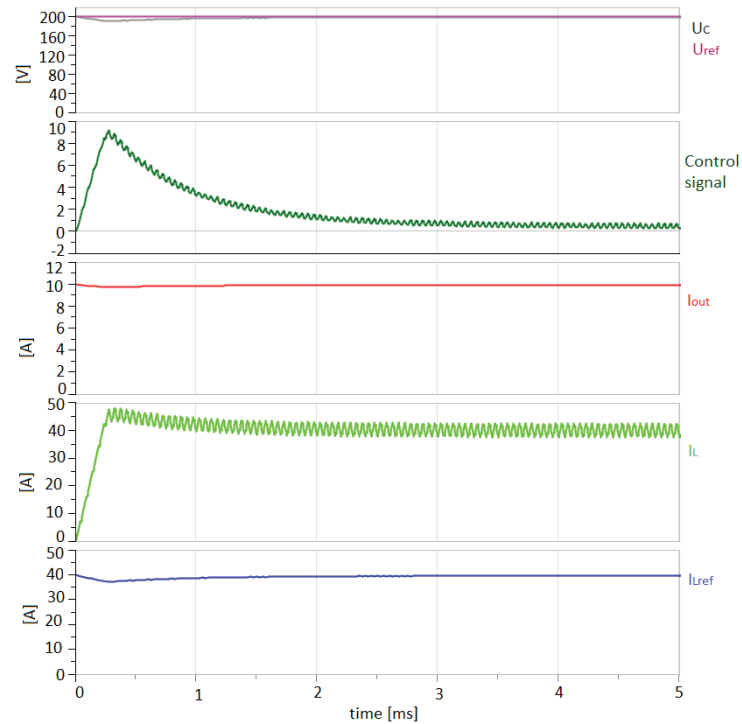


Figure 112: Dynamic performance of the controlled boost and MSBA stage

In addition, Figure 113 shows the output voltage of the converter (first plot) as well as the output current in the second plot. For reference the voltage at the second capacitor is also shown.

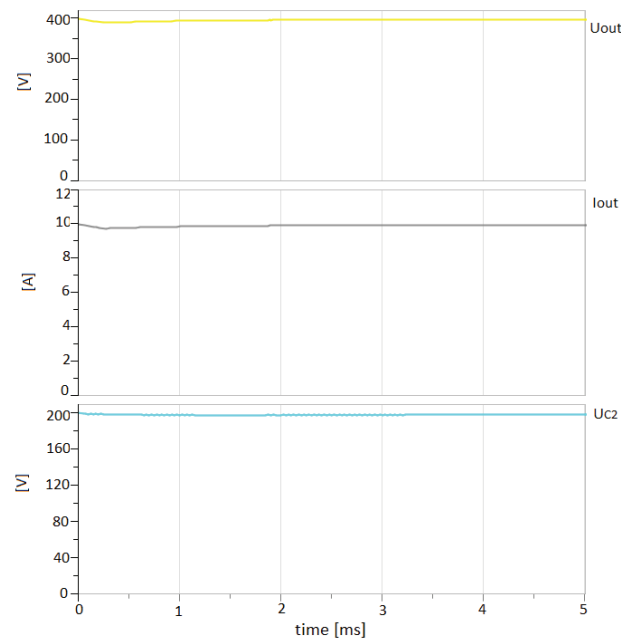


Figure 113: Output waveforms of the controlled boost and MSBA stage

It becomes apparent that with the implementation of such a control there is no longer a problem with resonant oscillations from the MSBA cell. The voltages of the capacitors are stabilized after a time of 4ms, leading to the desired stable output quantities.

4.1.5.2. Controlled Boost Stage with Controlled MSBA Cell relying on Reference

In the control strategy before, the control of the MSBA stage relies on the comparison of the capacitor voltages. But it should also be possible to control the MSBA stage if the MSBA voltage controller relies instead on the reference voltage that is used for the boost stage. Since the capacitors should be charged equally the reference voltage for both is the same. Figure 114 shows how the adjusted control structure of the system looks like.

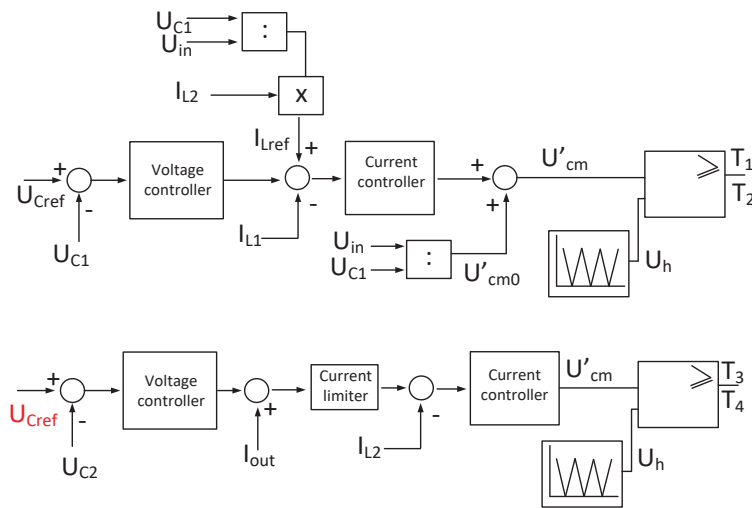


Figure 114: Control structure where the MSBA cell is relying on the capacitor reference voltage

All parameters were the same as in the simulations before and the dynamic performance of the boost control of this system is simulated and is illustrated in Figure 115. Again, in the first subplot the voltage reference and the capacitor voltage of C_1 are shown. The second plot corresponds to the output quantity of the voltage controller. The third plot line illustrates the current at the output of the boost stage (current of inductor L_2). The fourth plot corresponds to the inductor current of the boost stage (L_1), while the last (fifth) curve represents the feed-forward quantity for the inductor current reference.

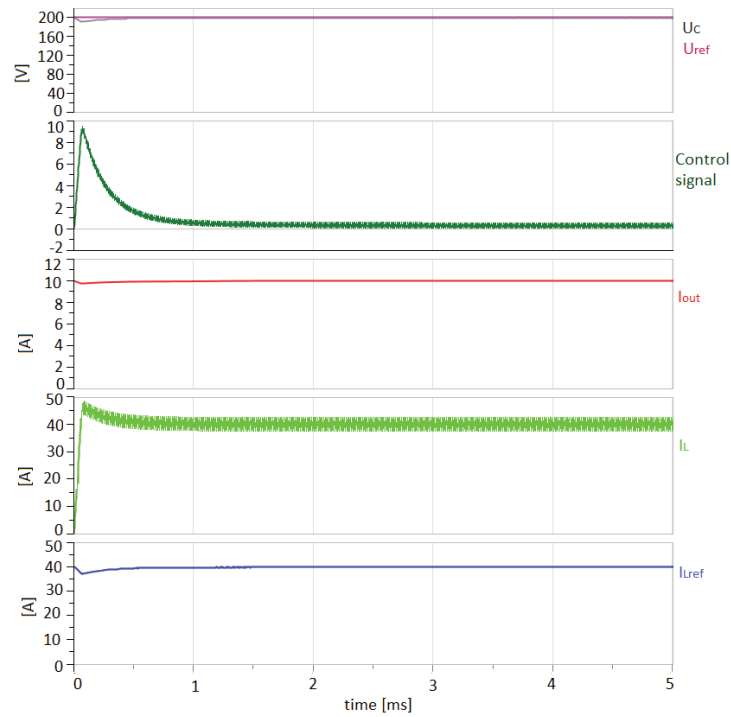


Figure 115: Dynamic behaviour for boost and MSBA stage with adjusted reference

In addition, Figure 116 shows the output voltage of the converter (first plot) as well as the output current in the second plot. Again the voltage at the second capacitor is also shown (third plot).

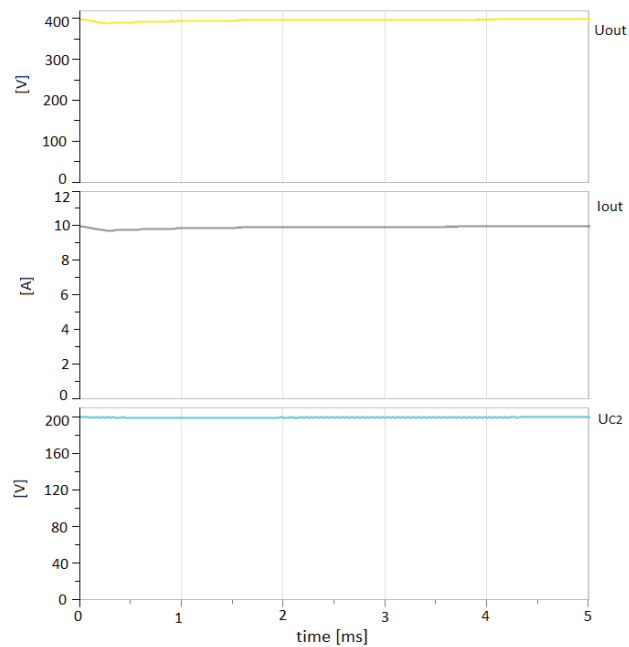


Figure 116: Output waveforms of the controlled boost and MSBA stage with adjusted reference

By comparing the results of this approach to the one used before it becomes clear, that both are able to provide stable output quantities without resonant oscillations. But since this approach is probably going to have slower reaction times it would be only useful for cases where the duty cycle differs from 0.5 so that the previous capacitor voltages could not be used as reference.

4.1.5.3. Controlled Boost Stage with Controlled MSBA Cell with Perturbation

As in the control simulations done before a perturbation is now added to the system by switching on an additional load (also 40Ω) after 2.5ms. The dynamic performance of the boost control of this system is simulated and is illustrated in Figure 117 on the left side. Again, in the first subplot the voltage reference and the capacitor voltage of C_1 are shown. The second plot corresponds to the output quantity of the voltage controller. The third plot line illustrates the current at the output of the boost stage (current of inductor L_2). The fourth plot corresponds to the inductor current of the boost stage (L_1), while the last (fifth) curve represents the feedforward quantity for the inductor current reference. The curves in the left picture show the dynamic responses of the MSBA stage, where the first plot shows the voltages in the two capacitors. The second and third plots show the inductor current of the MSBA stage as well as the limited current reference.

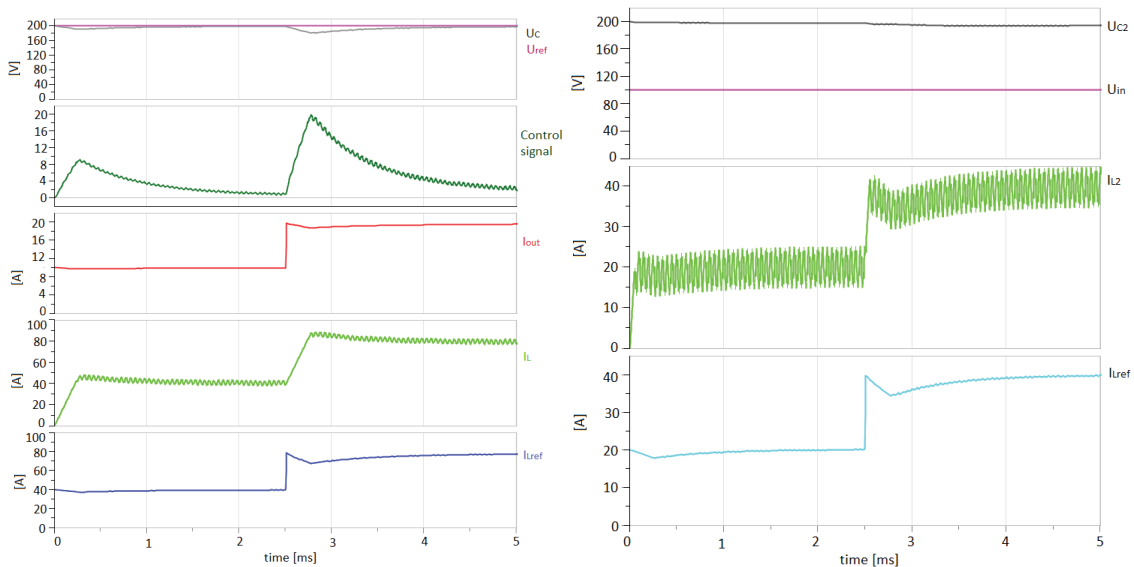


Figure 117: Dynamic behaviour for the boost (left) and the MSBA (right) cell with perturbation

In addition, Figure 118 shows the output voltage of the converter (first plot) as well as the output current in the second plot.

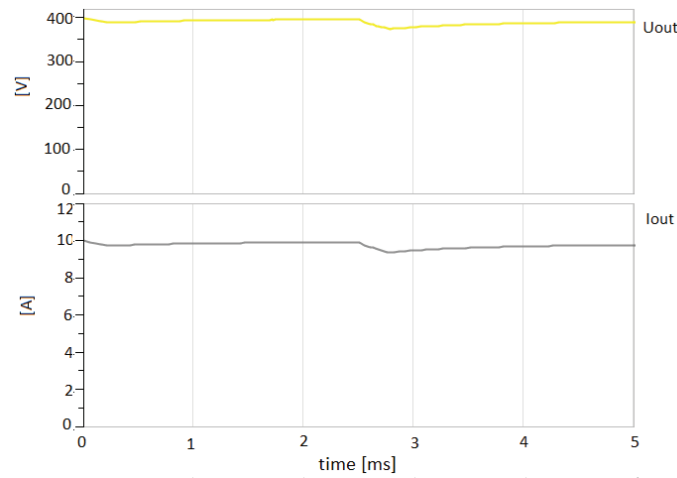


Figure 118: Output waveforms of the controlled boost and MSBA cell with perturbation

It is apparent that the control can adjust to perturbations at the output without any problems.

4.1.5.4. The 4-Stage MSBA

Finally, a boost stage, controlled with the LFF control scheme in combination with three MSBA cells, also called a 4-stage MSBA converter, will be investigated. Therefore, a feed-forward control based on the output current will be implemented for the MSBA stages. Figure 119 shows how such a 4-stage Multistage Stacked Boost converter looks like.

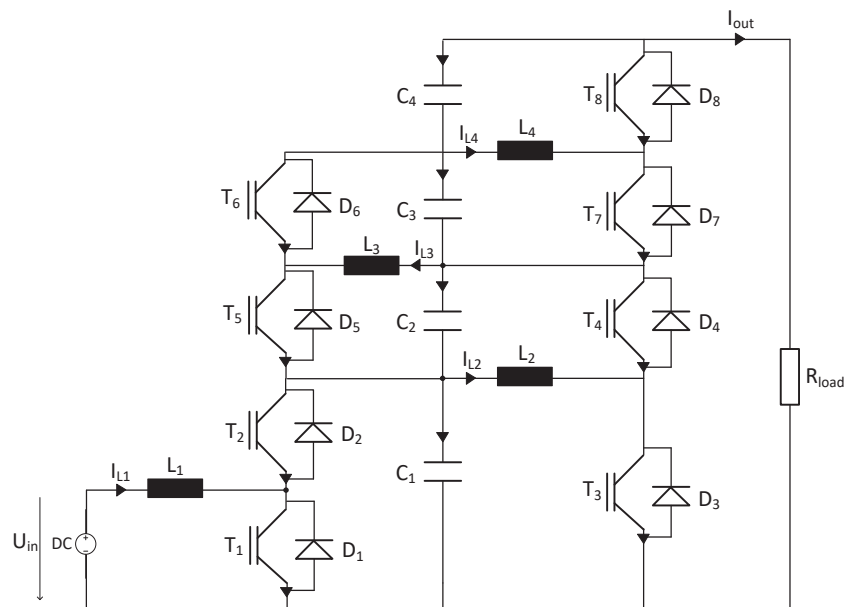


Figure 119: The 4-stage MSBA converter

As mentioned before the simulations for this case are only done for controlled MSBA stages since the previous results showed that running the MSBA stages in open-loop is not reliable. The input voltage for the simulations is set to 100V and the load resistance has a value of 40Ω . In addition, the capacitors and inductors will have pre-charged values.

In this section the boost stage is relying again on the LFF control (Figure 120 left) and the MSBA stages are controlled by two cascaded controllers with feedback of the load current (Figure 120 right) to generate the PWM.

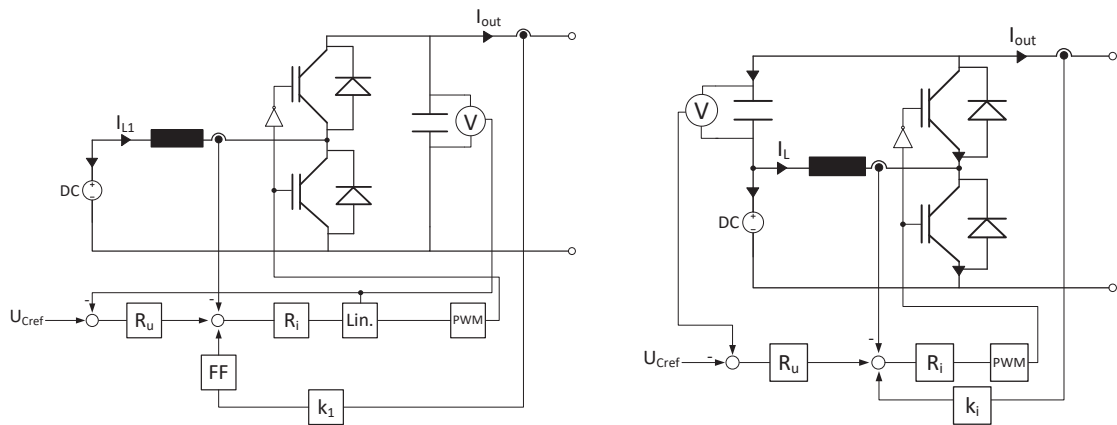


Figure 120: Block diagram of control structure for boost stage (left) and for a MSBA cell (right)

The detailed control system can be seen in Figure 121.

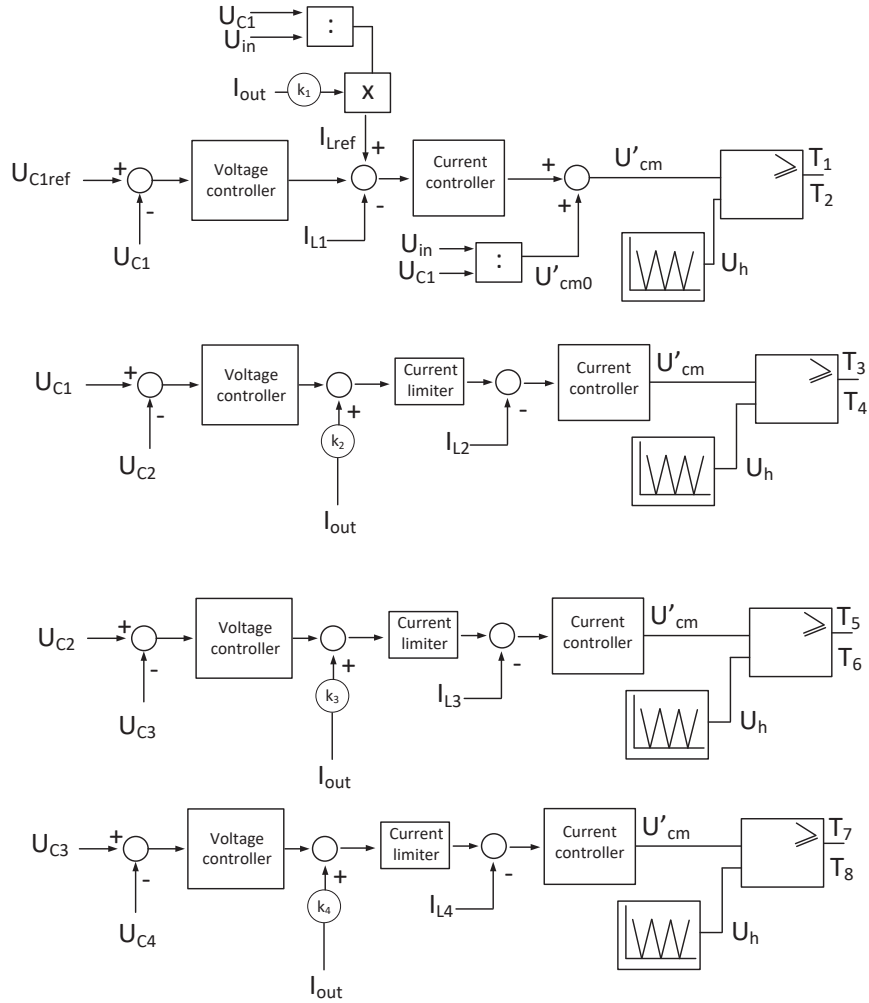


Figure 121: Control structure for the controlled boost and three MSBA stages

For this simulation, the parameter for the p-voltage controller was 1 and the parameter for the p-current controller was 0.5 for the boost stage. For the first MSBA stage the parameter for the p-voltage controller was 0.2 and the parameter for the p-current controller was 1 for the MSBA cell; in addition the current limiter was set to 220A with regards to the expected currents in the load change simulation. For the second MSBA stage the parameter for the p-voltage controller was 0.2 and the parameter for the p-current controller was 1 for the MSBA cell; in addition the current limiter was set to 150A. For the last MSBA stage the parameter for the p-voltage controller was 0.2 and the parameter for the p-current controller was 1 for the MSBA cell; in addition the current limiter was set to 75A. The dynamic performance of the boost control of this system is illustrated in Figure 122. In the first subplot the voltage reference and the actual capacitor voltage of the boost stage output are shown. The second plot corresponds to the output quantity of the voltage controller. The third plot illustrates the current at the output of the converter (I_{out}). The fourth plot corresponds to the inductor current of the boost stage (I_{L1}), while the last (fifth) curve represents the feedforward quantity for the inductor current reference.

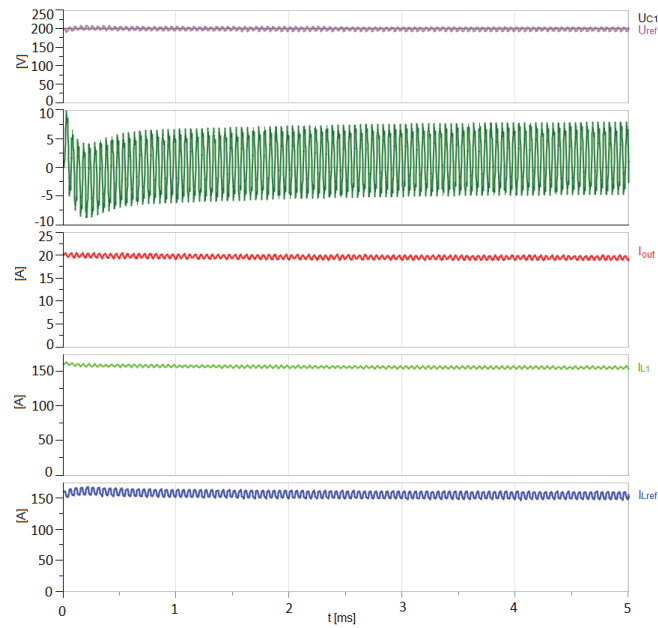


Figure 122: Dynamic performance of the boost stage

In addition, Figure 123 shows the output voltage in the first plot while the second plot shows the voltages of the capacitors. The last plot represents the inductor currents as well as the output current.

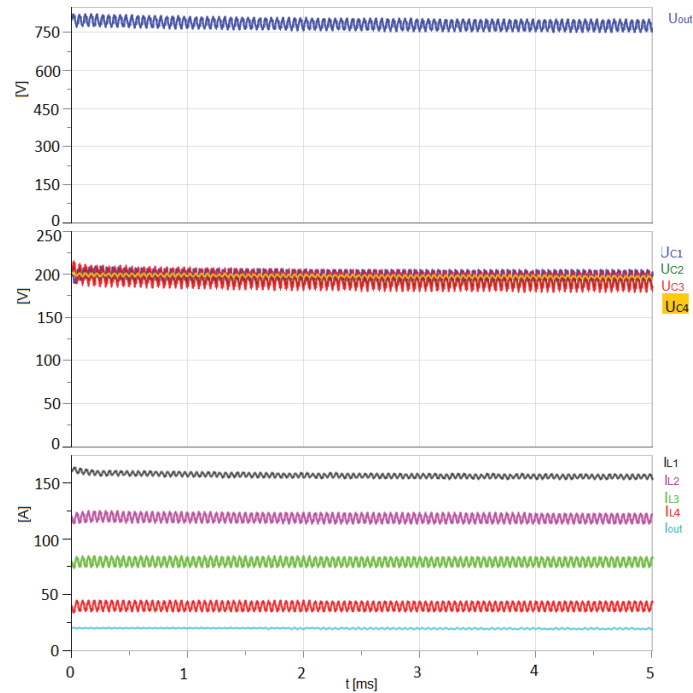


Figure 123: Output waveforms of the boost and three MSBA stages

Looking at these simulation results it becomes clear, that the control is able to provide stable output quantities without resonant oscillations for a four stage MSBA topology.

4.1.5.5. The LFF Controlled Boost Stage with Three Controlled MSBA Cells with Perturbation

The same control as used in the previous simulation is now tested in case of a perturbation. The perturbation is introduced at the level of the output load of the converter, with an additional resistor (also 40Ω) connected in parallel and switched on at the simulation time of 5ms. The topology scheme used is represented in Figure 124.

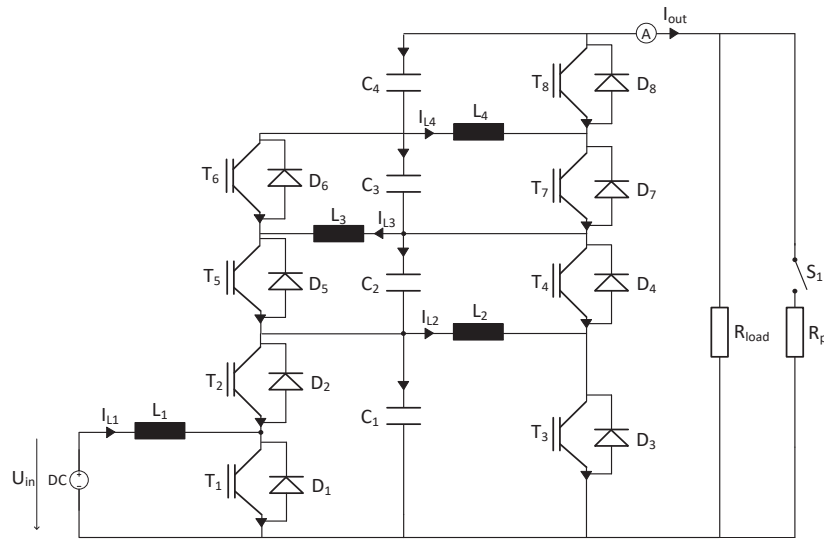


Figure 124: Boost stage with three controlled MSBA cells with output load step

The dynamic performance of the boost control of this system is illustrated in Figure 125. The first subplot shows the voltage reference and the capacitor voltage of the boost stage. The second plot corresponds to the output quantity of the voltage controller. The third plot illustrates the current at the output of the converter (I_{out}). The fourth plot corresponds to the inductor current of the boost stage (I_{L1}), while the last (fifth) curve represents the feedforward quantity for the inductor current reference.

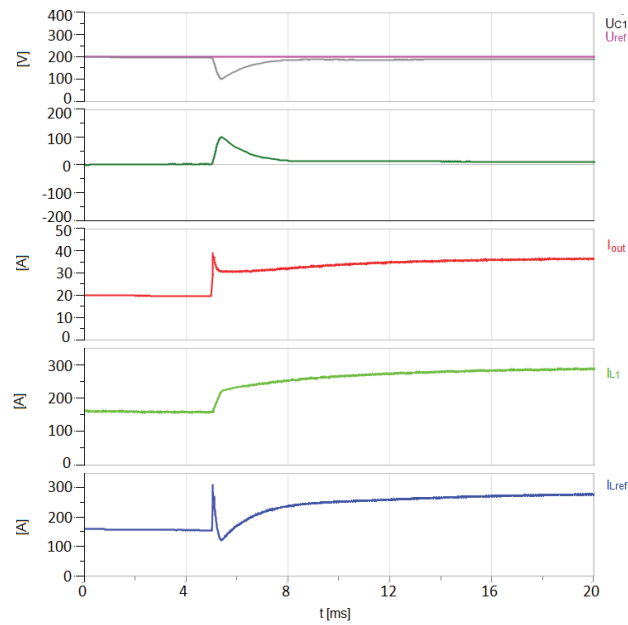


Figure 125: Dynamic performance of the boost stage with perturbation

Finally, Figure 126 shows the output voltage in the first plot while the second plot shows the voltages of the capacitors. The last plot represents again the inductor currents as well as the output current.

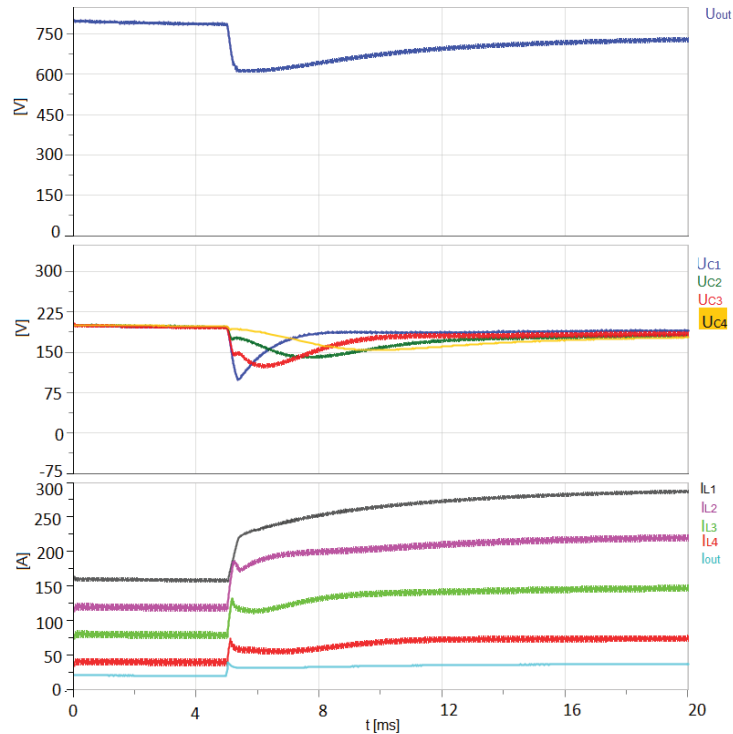


Figure 126: Output waveforms of the boost and three MSBA cells with perturbation

The simulations showed that the control can handle the perturbation at the output, but it is not that fast (10-15ms) anymore and there is quite a voltage drop until the voltages are adjusted to the correct levels again.

4.1.6. Start-Up of the 4-Stage MSBA Converter

For avoiding problems at the start-up of the converter, a slow increase of the input voltage up to the intended level of 100V is implemented as shown in Figure 127. This means that now the capacitors and inductors have no pre-charged voltages and currents anymore.

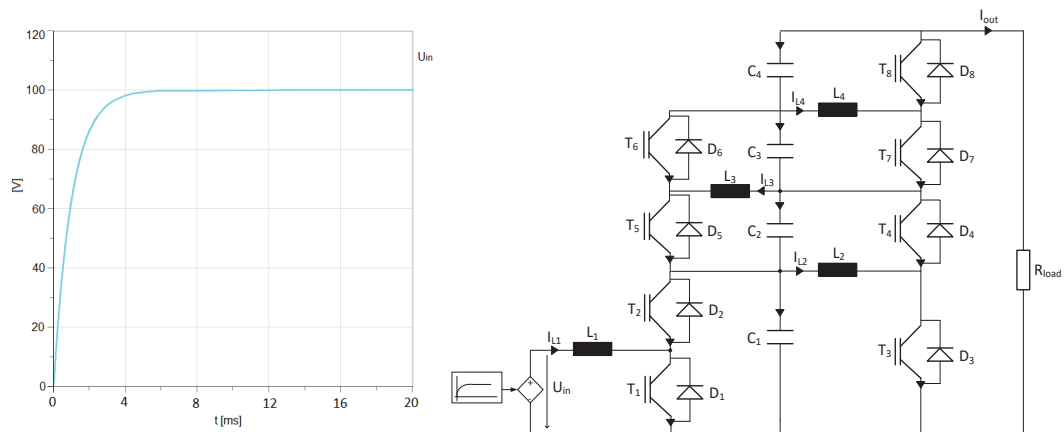


Figure 127: Start-up behaviour of the input voltage for the four-stage MSBA (left) and the according topology scheme (right)

The dynamic performance of the boost control of this system is illustrated in Figure 128. The first subplot shows the voltage reference and the capacitor voltage of the boost stage. The second plot corresponds to the output quantity of the voltage controller. The third plot illustrates the current at the output of the converter (I_{out}). The fourth plot corresponds to the inductor current of the boost stage (L_1), while the last (fifth) curve represents the feedforward quantity for the inductor current reference.

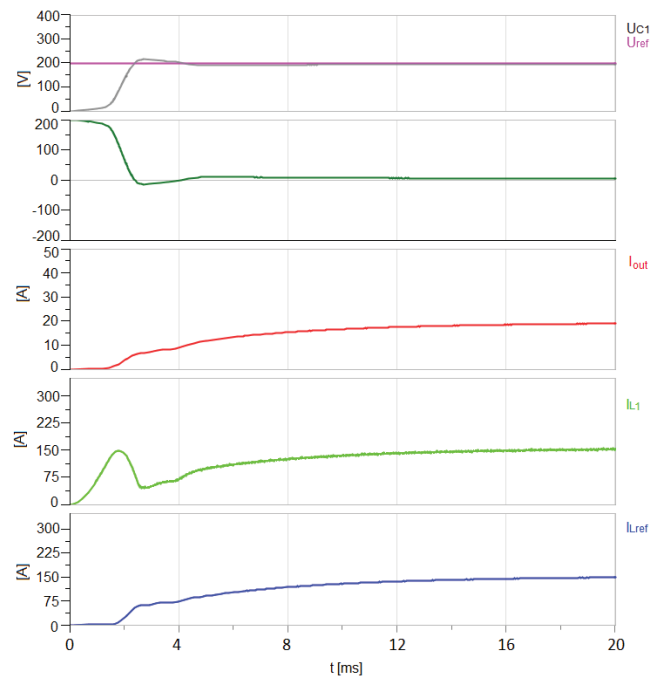


Figure 128: Dynamic performance of the boost stage during start-up

Finally Figure 129 shows the output voltage in the first plot while the second plot shows the voltages of the capacitors. The last plot represents again the inductor currents as well as the output current.

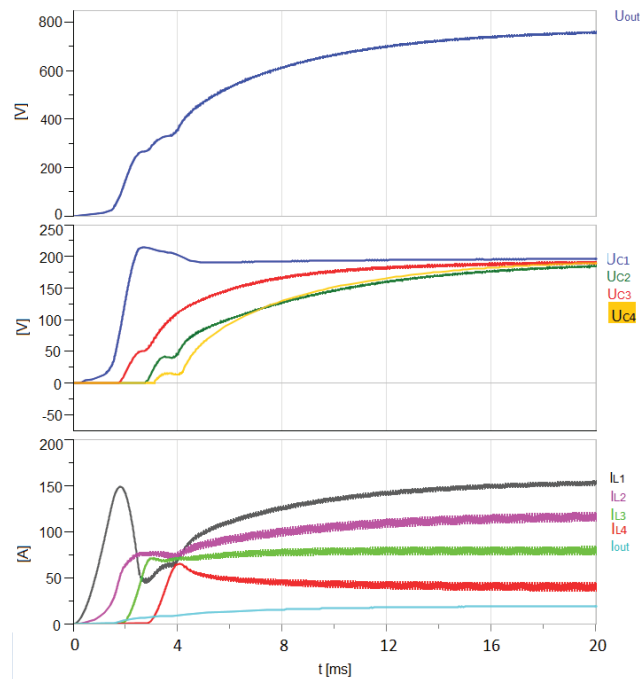


Figure 129: Output waveforms of 4-stage MSBA converter during start-up

These simulations show that using this start-up method works. No resonant oscillations are occurring, there are no overshoots of the currents over their maximum and only the voltage in the first capacitor overshoots by around 25V.

4.1.7. Energetic Macroscopic Representation and the LFF Control

It became apparent that the simulation program used before might not be optimal for executions that are more complex since it became very slow and unstable. Therefore, the LFF control was also implemented the Energetic Macroscopic Representation that had been done before. A picture of the control for the four-stage MSBA is shown in Figure 130.

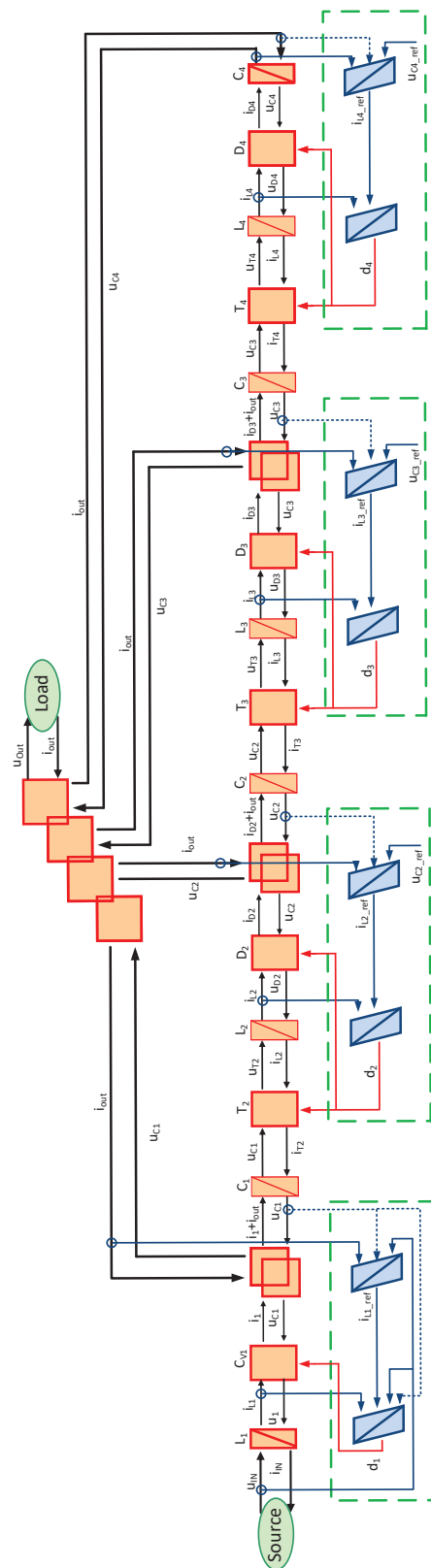


Figure 130: Control for the 4-stage MSBA converter

Since the control structure is made of two control schemes, one for the boost stage and one that is used for each MSBA stage, these two controls will be shown separately in the following sections.

4.1.7.1. Control of the MSBA Stages

The control structure used for the single MSBA stage is represented in Figure 131. The current in the inductor is controlled with a simple proportional controller and the converter-part itself is commanded through a PWM modulator. The superimposed voltage balancing controller is also a single proportional controller. In order to properly protect the current solicitation of the power semiconductor devices and the passive components, the control structure must present the possibility to limit the current during transient operation. Therefore, between the voltage balancing controller with its feedforward signal and the current controller, a limitation element has been inserted.

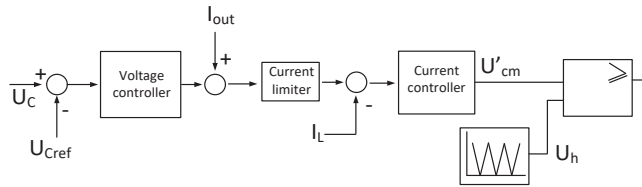


Figure 131: Control circuits of the MSBA cell

Figure 132 shows how this control looks when combined with the Energetic Macroscopic Representation of the MSBA cell.

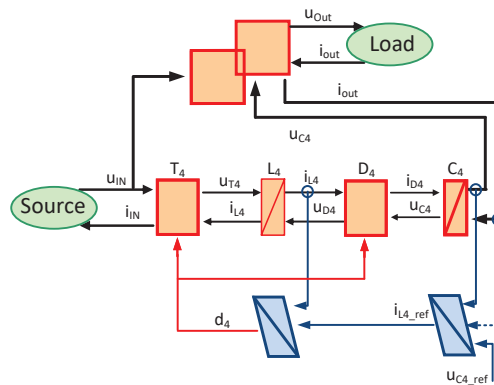


Figure 132: Control structure for the elementary MSBA stage

Shown in blue are the two control blocks that are used. The first block (Figure 133) includes the voltage controller and the current limiter and gives out the inductor current reference voltage.

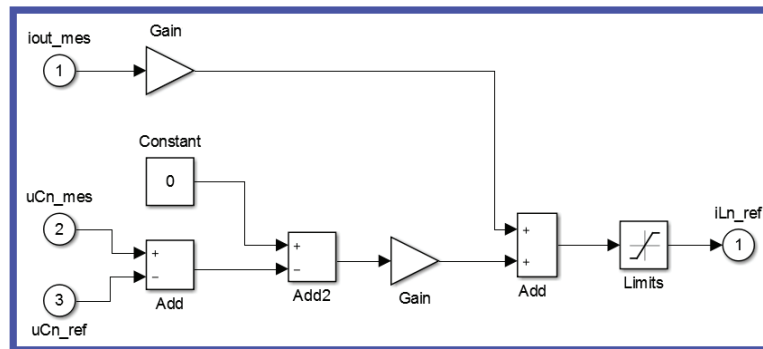


Figure 133: Voltage control block

The second block includes the current controller and is shown in Figure 134.

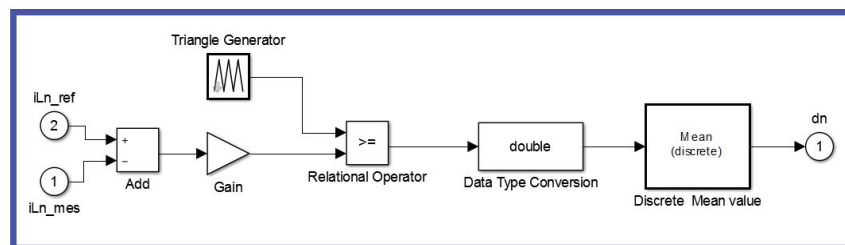


Figure 134: Current control block

If this was implemented as control of a prototype the relational operator output of 0 or 1 that could be used to directly control a switch. Since the EMR is based on a variable duty cycle a block to evaluate the mean value of the relational operator output during a switching period is used, since this is exactly the needed value d .

4.1.7.2. Control of the Boost Stage

In the case of the cascade of the boost topology with an MSBA stage, the output current of the boost converter appears as a state variable of the next stage, the MSBA converter. This state variable is measured, according the condition of such a variable to be safely controlled, avoiding overload of the semiconductor devices. As a consequence, the control structure of the boost input stage can be developed based on the available information of its load current. A dedicated control structure using the principle of Feed-Forward was used and is shown in Figure 92.

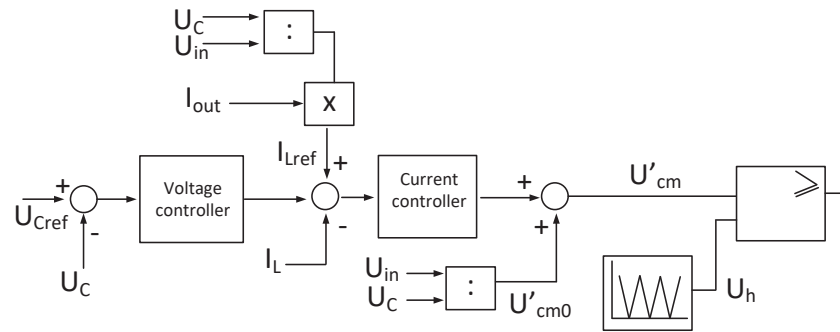


Figure 135: Control structure of the boost stage

Figure 136 shows how this control looks when combined with the Energetic Macroscopic Representation of the boost stage.

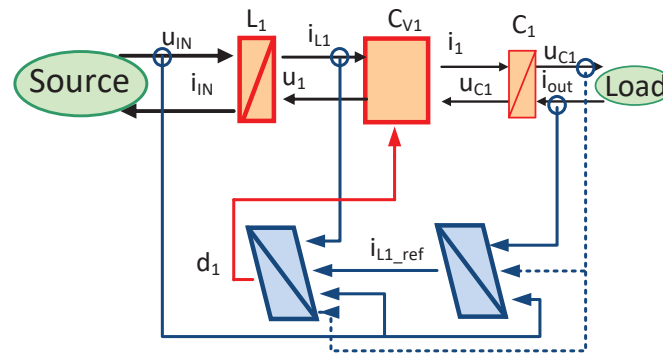


Figure 136: Control structure for the boost stage

Shown in blue are the two control blocks that are used. The first block (Figure 137) includes the voltage controller and gives out the inductor current reference voltage.

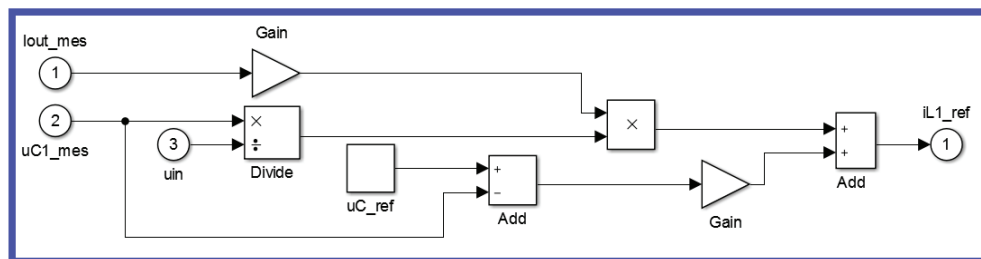


Figure 137: Voltage control block

The second block includes the current controller and is shown in Figure 138.

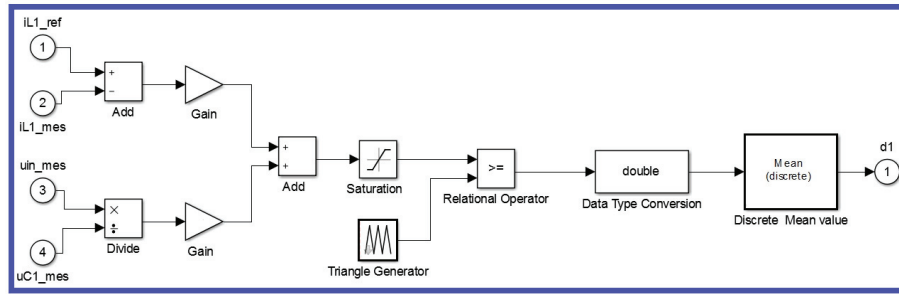


Figure 138: Current control block

Same as for the MSBA cell, if this was implemented as control of a prototype the relational operator output of 0 or 1 that could be used to directly control a switch. Since the EMR is based on a variable duty cycle a block to evaluate the mean value of the relational operator output during a switching period is used again, since this is exactly the needed value d .

Since the detailed functioning of the control blocks for the boost stage and the MSBA cells has been explained, the next paragraph will show the simulation results for the 4-stage MSBA converter.

4.1.7.3. Simulation of the Controlled 4-stage MSBA Converter

For the simulation of the controlled system the load is set to 40Ω . At the start of the simulation all values are set to 0 and then the input voltage starts to increase up to 100V. For the switches, a switching frequency of 20kHz is chosen and a duty cycle of 0.5 for the first period is applied as starting value. For the boost stage the parameter for the p-voltage controller was 1.2 and the parameter for the p-current controller was 10. For the first MSBA stage the parameter for the p-voltage controller was 0.5 and the parameter for the p-current controller was 1 for the MSBA cell; in addition the current limiter was set to 250A with regards to the expected currents in the load change simulation. For the second MSBA stage the parameter for the p-voltage controller was 0.2 and the parameter for the p-current controller was 1 for the MSBA cell; in addition the current limiter was set to 175A. For the last MSBA stage the parameter for the p-voltage controller was 0.2 and the parameter for the p-current controller was 1 for the MSBA cell; in addition the current limiter was set to 80A.

Figure 139 shows the output voltage and the output current of the EMR simulation of the boost stage with implemented LFF control.

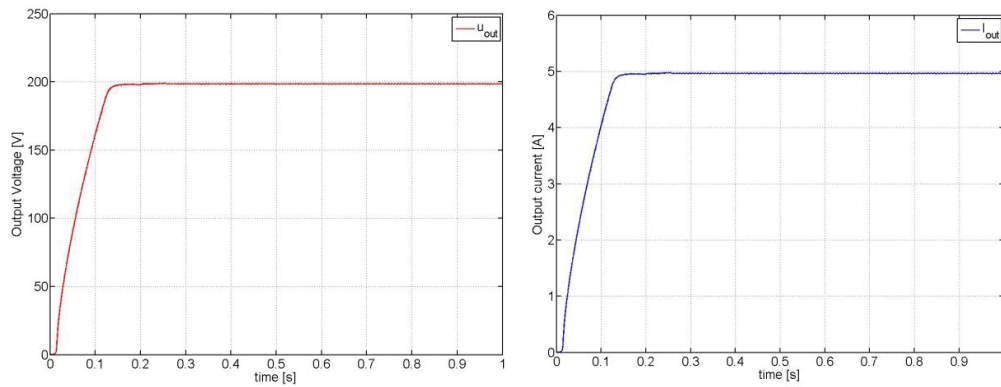


Figure 139: Output voltage (left) and output current (right) of the boost stage

As can be seen the voltage and current are at the desired levels and there are no problems, so the control is working fine. Therefore, the elementary MSBA stage will be simulated next.

Figure 140 shows the output voltage and the output current of the EMR simulation of the elementary MSBA stage with implemented control.

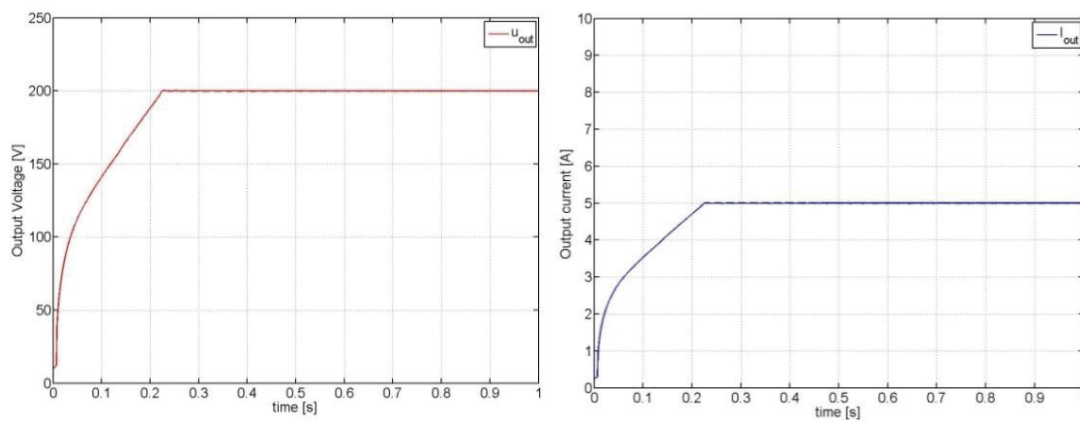


Figure 140: Output voltage (left) and output current (right) of elementary MSBA stage

The simulation results show that the output voltage reaches the desired level and there are no problems with oscillations. Therefore, the 4-stage MSBA converter can be simulated as next step.

Figure 141 shows the capacitor voltages and the inductor currents of the EMR simulation of the 4-stage MSBA converter with implemented control and Figure 142 shows the output voltage and the output current.

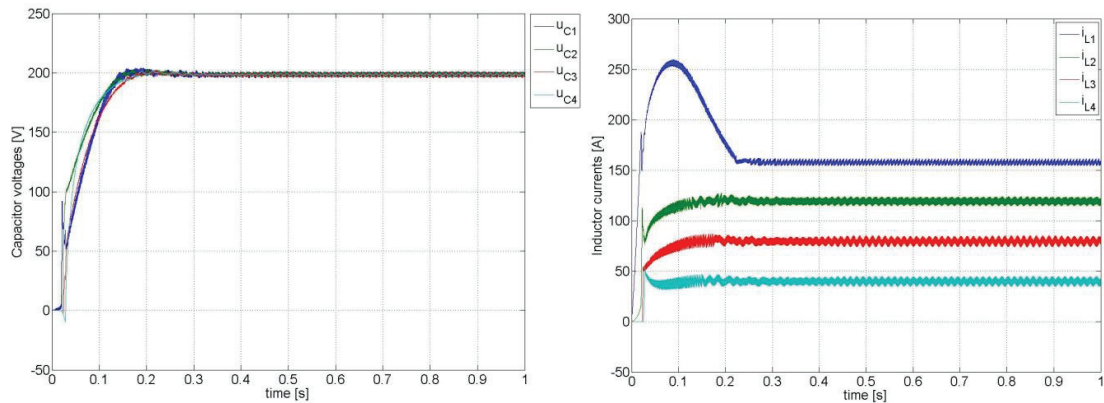


Figure 141: Capacitor voltages (left) and inductor currents (right) of the 4-stage MSBA

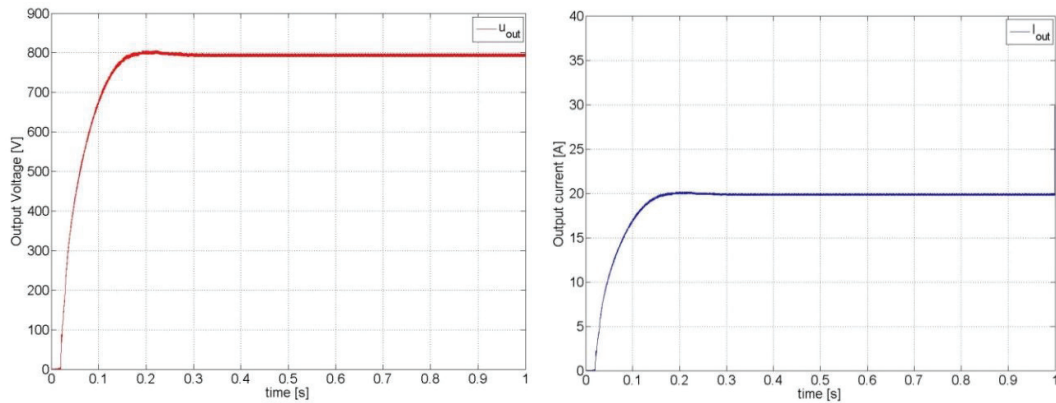


Figure 142: Output voltage (left) and output current (right) of the 4-stage MSBA

The simulations show that the desired output voltage is reached without a problem and without oscillations. The current of the first inductor shows a high spike during the start-up, but this can be handled by implementing a current limiter into the control of the boost stage.

The same simulation is now done with a step of the load at the time 0.6s. Figure 143 shows the capacitor voltages and the inductor currents of the EMR simulation of the 4-stage MSBA converter with implemented control during a perturbation at the output and Figure 144 shows the output voltage and the output current.

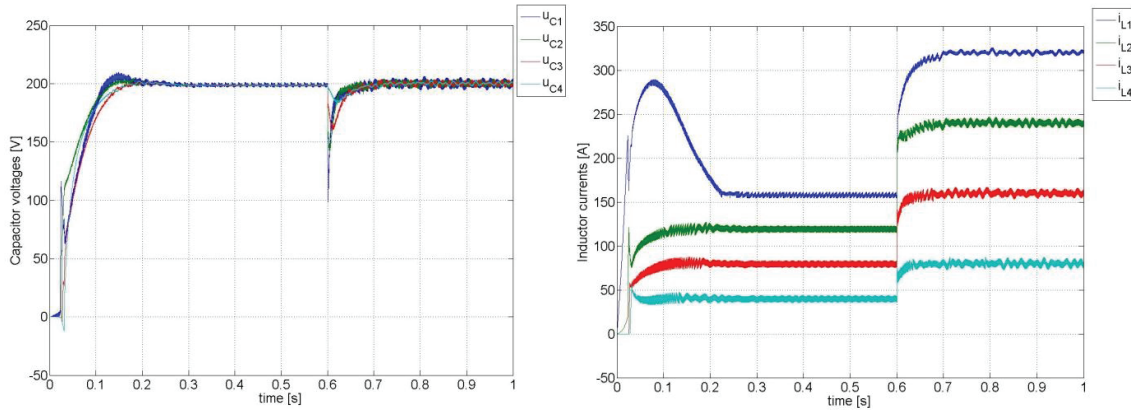


Figure 143: Capacitor voltages (left) and inductor currents (right) of the 4-stage MSBA

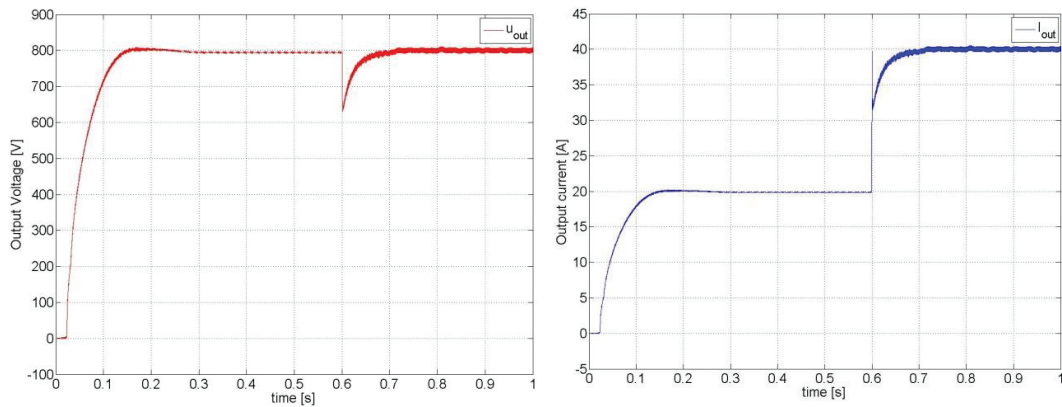


Figure 144: Output voltage (left) and output current (right) of the 4-stage MSBA

The simulations showed that the EMR works fine and that the control can handle the perturbation at the output. But there is quite a voltage drop until the voltages are adjusted to the correct levels again.

The previous simulations showed that the control method based on feed-forward of the output current for the MSBA stages works well even for more than one MSBA stage. The simulations of the dynamic responses showed that this control can get rid of the resonance oscillations of the MSBA stages and also handle perturbations. Next simulations of the boost stage combined with two MSBA stages were shown. First only the boost stage was controlled with the LFF control method and the MSBA stages were run open-loop. The simulations showed that this method is not suitable for converters with a higher number of MSBA stages since it can't get rid of all the oscillations and cannot keep the voltage levels at the desired values. After that a feed forward control was implemented and it worked very well in this case, even if it had to be slightly adjusted in regards of the current reference for the boost stage compared to the method shown in the first report. Two alternative ways for controlling the MSBA stages in this situation, one relying on the comparison of the capacitor voltages and the other one on the reference voltage that is used for the boost stage, showed that both work very well and therefore later on only one was considered. Finally, simulations with three MSBA stages, resulting in the desired 4-stage MSBA converter, were done to verify that the control structure of the boost and MSBA stages together can



handle normal operation and perturbations. Last, the start-up of the four-stage MSBA converter was considered. Simulations showed that by slowly increasing the input voltage from zero to the desired level the resonant oscillations can be avoided.

4.2. State Space

4.2.1. Description

To analyse complex systems - especially if they have many inputs and outputs - it is important to reduce the complexity of the mathematical model, as well as to use compute programs for most of the necessary computations to save time since calculating all the needed matrix operations by hand would be very inefficient. The state space approach is one possible solution. This control theory is based on the description of system with n first-order differential equations. These equations are then combined into a vector-matrix differential equation. The use of this matrix simplifies the mathematical representation of the system. The main advantage of this approach is the fact that an increase in the number of state variables or the number of inputs / outputs does not increase the complexity of the equations [50]. Since the Multistage Stacked Boost architecture (MSBA) can be considered a complex system the state space approach will be used in the following paragraphs.

4.2.2. Mathematical Equations

Figure 145 shows three connected MSBA stages with an input voltage source. The boost stage is not considered in this case, since it would be assumed that the boost stage would most likely be handling the maximum power point tracking to optimize the output from the solar cells. So the MSBA stages would be used to just elevate the voltages and can therefore have a different control.

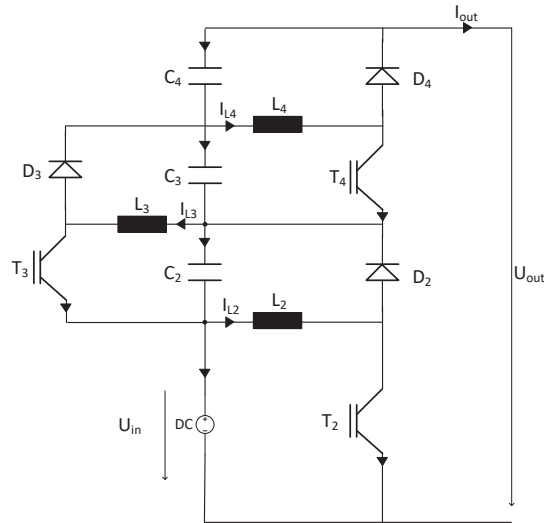


Figure 145: 4-stage MSBA converter representation for State Space

For describing the system, the equations for the capacitor voltages are introduced:

$$u_{C4} = \frac{1}{C_4} \int (i_{D4} - i_{out}) dt \quad (98)$$

$$i_{d4} = d_4 \cdot i_{L4} \quad (99)$$

$$\begin{aligned}
 u_{C4} &= \frac{1}{C_4} \int (i_{D4} - i_{out}) dt \\
 &= \frac{1}{C_4} \int [d_4 \cdot i_{L4} - i_{out}] dt
 \end{aligned} \tag{100}$$

$$\begin{aligned}
 u_{C3} &= \frac{1}{C_3} \int (i_{D3} - i_{L4} + i_{C4}) dt \\
 &= \frac{1}{C_3} \int [d_3 \cdot i_{L3} - (1 - d_4) \cdot i_{L4} - i_{out}] dt
 \end{aligned} \tag{101}$$

$$u_{C2} = \frac{1}{C_2} \int (i_{D2} + i_{T4} - i_{L3} + i_{C3}) dt \tag{102}$$

$$i_{T4} = (1 - d_4) \cdot i_{L4} \tag{103}$$

$$\begin{aligned}
 u_{C2} &= \frac{1}{C_2} \int [d_2 \cdot i_{L2} + (1 - d_4) \cdot i_{L4} - i_{L3} + d_3 \cdot i_{L3} - (1 - d_4) \cdot i_{L4} - i_{out}] dt \\
 &= \frac{1}{C_2} \int [d_2 \cdot i_{L2} - i_{L3} + d_3 \cdot i_{L3} - i_{out}] dt \\
 &= \frac{1}{C_2} \int [d_2 \cdot i_{L2} - (1 - d_3) \cdot i_{L3} - i_{out}] dt
 \end{aligned} \tag{104}$$

The other formulas that are needed are the inductor currents:

$$i_{L4} = \frac{1}{L_4} \int ((1 - d_4) \cdot u_{C3} - d_4 \cdot u_{C4}) dt \tag{105}$$

$$i_{L3} = \frac{1}{L_3} \int ((1 - d_3) \cdot u_{C2} - d_3 \cdot u_{C3}) dt \tag{106}$$

$$i_{L2} = \frac{1}{L_2} \int ((1 - d_2) \cdot u_{in} - d_2 \cdot u_{C2}) dt \tag{107}$$

4.2.3. State Space Approach

When using the state space representation, a system is normally depicted as shown in Figure 146.

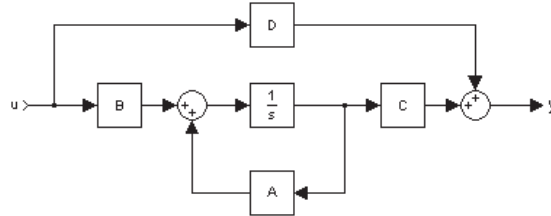


Figure 146: State Space representation

and is therefore defined by

$$\dot{x} = A \cdot x + B \cdot u \quad (108)$$

In this equation u is the input vector, while x is the state vector. There are also two matrixes, the state matrix A and the input matrix B . Of course the output has to be defined as well:

$$y = C \cdot x + D \cdot u \quad (109)$$

where C is the output matrix. There is another matrix added called the feedthrough matrix D , but this represents a direct relationship of the input and output and in a real system this can physically almost never happen. So for the three-stage MSBA the before mentioned equations lead to the following definition of vectors:

$$x = \begin{bmatrix} i_{L2} \\ u_{C2} \\ i_{L3} \\ u_{C3} \\ i_{L4} \\ u_{C4} \end{bmatrix} \quad u = \begin{bmatrix} u_{in} \\ 0 \\ 0 \\ 0 \\ 0 \\ 0 \end{bmatrix} \quad (110)$$

These definitions lead to the following differential equations:

$$\begin{aligned}
 \frac{di_{L2}}{dt} = \dot{x}_1 &= \frac{1}{L_2} \cdot ((1-d_2) \cdot u_{in} - d_2) \cdot u_{C2} \\
 \frac{du_{C2}}{dt} = \dot{x}_2 &= \frac{1}{C_2} \cdot (d_2 \cdot i_{L2} - (1-d_3) \cdot i_{L3} - i_{out}) \\
 \frac{di_{L3}}{dt} = \dot{x}_3 &= \frac{1}{L_3} \cdot ((1-d_3) \cdot u_{C2} - d_3 \cdot u_{C3}) \\
 \frac{du_{C3}}{dt} = \dot{x}_4 &= \frac{1}{C_3} \cdot (d_3 \cdot i_{L3} - (1-d_4) \cdot i_{L4} - i_{out}) \\
 \frac{di_{L4}}{dt} = \dot{x}_5 &= \frac{1}{L_4} \cdot ((1-d_4) \cdot u_{C3} - d_4 \cdot u_{C4}) \\
 \frac{du_{C4}}{dt} = \dot{x}_6 &= \frac{1}{C_4} \cdot (d_4 \cdot i_{L4} - i_{out})
 \end{aligned} \tag{111}$$

which result in

$$\begin{aligned}
 \dot{x}_1 &= 0 \cdot i_{L2} + \frac{-d_2}{L_2} \cdot u_{C2} + 0 \cdot i_{L3} + 0 \cdot u_{C3} + 0 \cdot i_{L4} + 0 \cdot u_{C4} + \frac{(1-d_2)}{L_2} \cdot u_{in} \\
 \dot{x}_2 &= \frac{d_2}{C_2} \cdot i_{L2} + 0 \cdot u_{C2} + \frac{-(1-d_3)}{C_2} \cdot i_{L3} + 0 \cdot u_{C3} + 0 \cdot i_{L4} + 0 \cdot u_{C4} - i_{out} \\
 \dot{x}_3 &= 0 \cdot i_{L2} + \frac{(1-d_3)}{L_3} \cdot u_{C2} + 0 \cdot i_{L3} + \frac{-d_3}{L_3} \cdot u_{C3} + 0 \cdot i_{L4} + 0 \cdot u_{C4} \\
 \dot{x}_4 &= 0 \cdot i_{L2} + 0 \cdot u_{C2} + \frac{d_3}{C_3} \cdot i_{L3} + 0 \cdot u_{C3} + \frac{-(1-d_4)}{C_3} \cdot i_{L4} + 0 \cdot u_{C4} - i_{out} \\
 \dot{x}_5 &= 0 \cdot i_{L2} + 0 \cdot u_{C2} + 0 \cdot i_{L3} + \frac{(1-d_4)}{L_4} \cdot u_{C3} + 0 \cdot i_{L4} + \frac{-d_4}{L_4} \cdot u_{C4} \\
 \dot{x}_6 &= 0 \cdot i_{L2} + 0 \cdot u_{C2} + 0 \cdot i_{L3} + 0 \cdot u_{C3} + \frac{d_4}{C_4} \cdot i_{L4} + 0 \cdot u_{C4} - i_{out}
 \end{aligned} \tag{112}$$

Since all equations describing the system are defined they can be transformed into the state matrix:

$$A = \begin{bmatrix} 0 & \frac{-d_2}{L_2} & 0 & 0 & 0 & 0 \\ \frac{d_2}{C_2} & 0 & \frac{-(1-d_3)}{C_2} & 0 & 0 & 0 \\ 0 & \frac{(1-d_3)}{L_3} & 0 & \frac{-d_3}{L_3} & 0 & 0 \\ 0 & 0 & \frac{d_3}{C_3} & 0 & \frac{-(1-d_4)}{C_3} & 0 \\ 0 & 0 & 0 & \frac{(1-d_4)}{L_4} & 0 & \frac{-d_4}{L_4} \\ 0 & 0 & 0 & 0 & \frac{d_4}{C_4} & 0 \end{bmatrix} \tag{113}$$

and the input matrix.

$$B = \begin{bmatrix} \frac{(1-d_2)}{L_2} \\ 0 \\ 0 \\ 0 \\ 0 \\ 0 \end{bmatrix} \quad (114)$$

Finally the components describing the output need to be defined:

$$y = u_{out} \quad (115)$$

$$\begin{aligned} u_{out} &= (u_{in} + u_{C2} + u_{C3} + u_{C4}) \\ &= u_{in} + 0 \cdot i_{L2} + u_{C2} + 0 \cdot i_{L3} + u_{C3} + 0 \cdot i_{L4} + u_{C4} \end{aligned} \quad (116)$$

$$C = [0; 1; 0; 0; 1; 1] \quad (117)$$

In addition, for this type of converter there is also a direct feedback of the input to the output, which does not happen very often. Therefore, the feedthrough matrix results in:

$$D = [1; 0; 0; 0; 0; 0] \quad (118)$$

4.2.4. State Space Computing with MATLAB

Now that the state space description is defined they can be used for computing with MATLAB. The whole system is therefore defined with the command

```
RE=ss(A,B,C,D);
```

All the equations the state space representation is based on contain values for the capacitors and inductors. Therefore, in the following research the values that will be used in the low voltage prototype (chapter 5.1) were implemented. This means all the inductors have a value of 1.7mH and the capacitors a value of 1.5mF.

Now the characteristic polynomial can be calculated using the command

```
poly_car=poly(A);
```

which results in:

$$P = p^6 + 4.9 \cdot 10^5 p^4 - 2.12 \cdot 10^{-9} p^3 + 5.77 \cdot 10^{10} p^2 - 3.24 \cdot 10^{-4} p + 9.42 \cdot 10^{14} \quad (119)$$

To get an insight of the system it is important to calculate the eigenvalues of the state matrix since this represents the pole of the system (i.e., the singularities where the transfer function's magnitude is unbounded), therefore the identity matrix I is needed as well as a transfer to the Laplace domain (s):

$$P(s) = \det(s \cdot I - A) = 0 \quad (120)$$

$$s \cdot I = \begin{bmatrix} s & 0 & 0 & 0 & 0 & 0 \\ 0 & s & 0 & 0 & 0 & 0 \\ 0 & 0 & s & 0 & 0 & 0 \\ 0 & 0 & 0 & s & 0 & 0 \\ 0 & 0 & 0 & 0 & s & 0 \\ 0 & 0 & 0 & 0 & 0 & s \end{bmatrix} \quad (121)$$

For a first analysis the duty cycle is fixed to a constant value of $d_1=d_2=d_3=d_4=0.5$

Using the command

`eigenvalues=eig(A);`

results in

$$\begin{aligned} \lambda_{1,2} &= -3.55 \cdot 10^{-15} \pm 5.64 \cdot 10^2 i \\ \lambda_{3,4} &= 3.55 \cdot 10^{-15} \pm 1.39 \cdot 10^2 i \\ \lambda_{5,6} &= \pm 3.9 \cdot 10^2 i \end{aligned} \quad (122)$$

and Figure 147 shows a plot with these values.

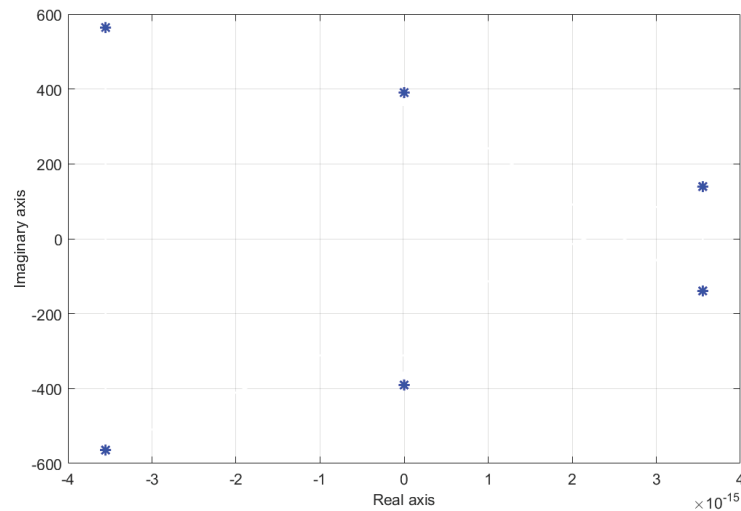


Figure 147: Eigenvalues of the system

Now the state space representation the transfer function of the system can also be calculated:

`tf_delta_com=tf(RE)`

which results in:

$$G(s) = \frac{s^6 - 5.68 \cdot 10^{-14} s^5 + 5.88 \cdot 10^5 s^4 + 6.18 \cdot 10^{-10} s^3 + 9.62 \cdot 10^{10} s^2 + 0.94 \cdot 10^{-3} s + 3.77 \cdot 10^{15}}{s^6 - 4.9 \cdot 10^5 s^4 - 2.12 \cdot 10^{-9} s^3 + 5.77 \cdot 10^{10} s^2 + 0.32 \cdot 10^{-1} s + 9.42 \cdot 10^{14}} \quad (123)$$

It is also now possible to transform the function into the form where it is easy to see the zeros, the poles and the gain with the command:

`Ta=zpk(tf_delta_com(1))`

This results in:

$$T_a = \frac{(s^2 + 5.74 \cdot 10^4) \cdot (s^2 + 1.96 \cdot 10^5) \cdot (s^2 - 3.35 \cdot 10^5)}{(s^2 + 1.94 \cdot 10^4) \cdot (s^2 + 1.52 \cdot 10^5) \cdot (s^2 - 3.18 \cdot 10^5)} \quad (124)$$

Before a control can be implemented it is important to check if the system is controllable. A system is controllable if it is possible to use an unconstrained control vector to transfer the system from any initial state x to any other state in a finite interval of time. If a system is completely controllable, then the following equation must be true:

$$\begin{aligned} x(0) &= -\sum_{k=0}^{n-1} A^k B \beta_k \\ &= -\begin{bmatrix} B & AB & \cdots & A^{n-1}B \end{bmatrix} \begin{bmatrix} \beta_0 \\ \beta_1 \\ \vdots \\ \beta_{n-1} \end{bmatrix} \end{aligned} \quad (125)$$

with

$$\beta_k = \int_0^{t_1} \alpha_k(\tau) u(\tau) d\tau \quad (126)$$

This requires that the rank of the $n \times n$ matrix $\begin{bmatrix} B & AB & \cdots & A^{n-1}B \end{bmatrix}$ is n .

The checks for controllability and observability can also be calculated with MATLAB using the following commands:

`G=ctrb(A,B);`

This results in:

$$G = \begin{bmatrix} 294.12 & 0 & -2.88 \cdot 10^7 & 0 & 5.65 \cdot 10^{12} & 0 \\ 0 & 9.8 \cdot 10^4 & 0 & -1.92 \cdot 10^{10} & 0 & 4.71 \cdot 10^{15} \\ 0 & 0 & 2.88 \cdot 10^7 & 0 & -8.48 \cdot 10^{12} & 0 \\ 0 & 0 & 0 & 9.61 \cdot 10^9 & 0 & -3 - 77 \cdot 10^{15} \\ 0 & 0 & 0 & 0 & 2.83 \cdot 10^{12} & 0 \\ 0 & 0 & 0 & 0 & 0 & 9.42 \cdot 10^{14} \end{bmatrix} \quad (127)$$

$$Rang_G = rank(G) = 6$$

This shows that the system is controllable. Another method to verify this would be to calculate if the determinant is not equal to zero. Since G is a quadratic matrix this would mean it also has full rank. The reason why a control for the system is needed is shown in Figure 148, which shows that the actual system suffers from huge ringing.

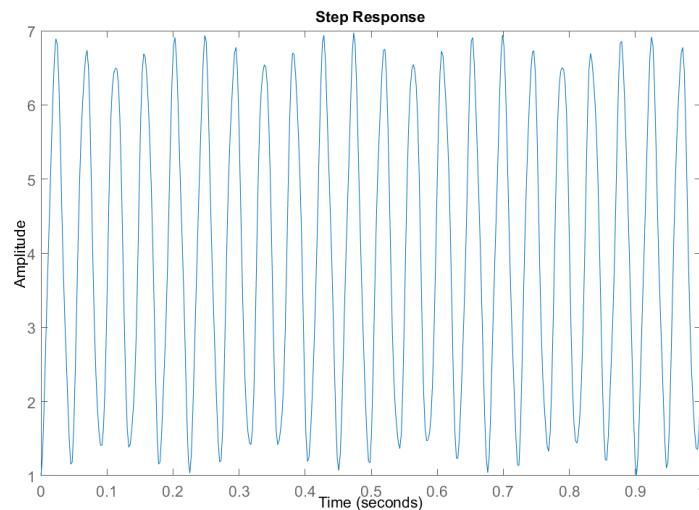


Figure 148: Step response of the uncontrolled system

This calculation can be verified with a Simulink simulation, which is shown in Figure 149.

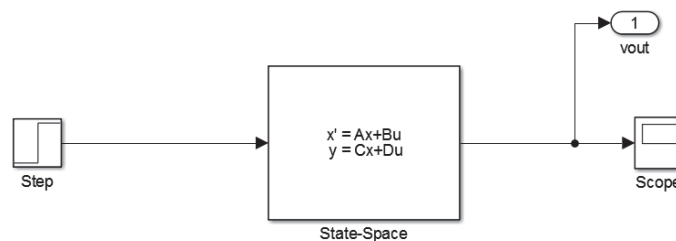


Figure 149: Implementation of the state space system in Simulink

For the following steps it is needed to place the desired closed-loop poles. So it will be assumed that all state variables are available for feedback, meaning all can be measured. Therefore, the closed-loop poles that would be good for the system will be determined based on control speed, damping ratio, bandwidth and/or steady-state requirements. For a fast response of the system, the poles are placed far from the $j\omega$ axis, but this may result in the system becoming nonlinear which should be avoided. In general, a fast response will increase the needed energy of the control structure as well as the costs. In general, systems will use a controller with a damping ratio ζ and the natural frequency ω_n . So for a system like

$$\dot{x} = A \cdot x + B \cdot u \quad (128)$$

$$y = C \cdot x + D \cdot u \quad (129)$$

u can be chosen as the following control signal:

$$u = -K \cdot x \quad (130)$$

with K being the state feedback gain matrix, which will interact with the system as shown in Figure 150.

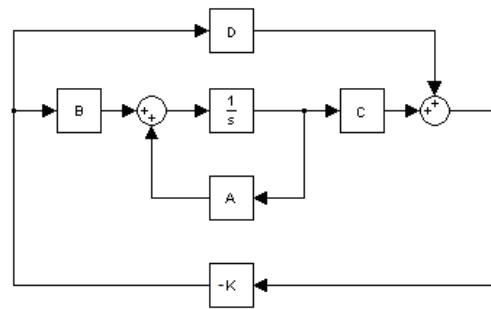


Figure 150: State space representation with feedback

The stability and transient-response characteristics of the system can be determined by the eigenvalues of $A-BK$ matrix (regulator poles).

For calculating a K matrix which forces the poles of the $A-BK$ matrix to be the desired poles ($\mu_1 \dots \mu_n$), several methods are possible. One is using the transformation matrix T , with the following steps [50]:

1. Check if the system is completely controllable
2. Determine the factors $a_1 \dots a_n$ of the characteristic polynomial of the matrix A by using $\det(sI-A) = s^n + a_1 s^{n-1} + \dots + a_{n-1} s + a_n$
3. Determine the transformation Matrix T which will transform the system into the controllable canonical form. This is done using $T = MW$. M is the controllability matrix $= [B \mid AB \mid \dots \mid A^{n-1}B]$ and W is the matrix made from $a_1 \dots a_n$

$$W = \begin{bmatrix} a_{n-1} & a_{n-2} & \dots & a_1 & 1 \\ a_{n-2} & a_{n-3} & \dots & 1 & 0 \\ \dots & \dots & \dots & \dots & \dots \\ a_{n-1} & 1 & \dots & 0 & 0 \\ 1 & 0 & \dots & 0 & 0 \end{bmatrix} \quad (131)$$

4. Use the desired poles / eigenvalues to write the characteristic polynomial

$$(s - \mu_1) \cdot (s - \mu_2) \cdot \dots \cdot (s - \mu_n) = s^n + \alpha_1 \cdot s^{n-1} + \dots + \alpha_{n-1} \cdot s + \alpha_n \quad (132)$$

and determine the values $\alpha_1 \dots \alpha_n$.

5. Now matrix K can be acquired by

$$K = [\alpha_n - a_n \mid \alpha_{n-1} - a_{n-1} \mid \dots \mid \alpha_1 - a_1] \cdot T^{-1} \quad (133)$$

Another common method to determine the Matrix K is using the Ackermann's formula. The desired closed-loop poles are again $\mu_1 \dots \mu_n$.

1. The first step is to introduce the Matrix $\tilde{A} = A - BK$.
2. Therefore, the desired characteristic equation will be

$$\det(sI - \tilde{A}) = (s - \mu_1) \cdot (s - \mu_2) \cdot \dots \cdot (s - \mu_n) = s^n + \alpha_1 \cdot s^{n-1} + \dots + \alpha_{n-1} \cdot s + \alpha_n = 0 \quad (134)$$

3. Using the formula above and the Cayley-Hamilton theorem the Ackermann formula can be derived as

$$K = [0 \ 0 \ \dots \ 0 \ 1] [B^T A B^T \dots^T A^{n-1} B]^T q(A) \quad (135)$$

Where

$$q(A) = B(\alpha_2 K + \alpha_1 B K \tilde{A} + K \tilde{A}^2) + A B(\alpha_1 K + K \tilde{A}) + A^2 B K \quad (136)$$

What has not yet been discussed is how to acquire the desired closed-loop poles. It has to be kept in mind that if these poles are placed too far from the $j\omega$ axis the system becomes very fast but also may become nonlinear. It is also important to balance the response time and the amount of control energy (higher speed needing more energy, leading to more costs). One possibility to achieve this is applying one functionality of the Root-locus method.

4.2.5. Root-Locus Method

The method gets its name from the locus of roots of the characteristic equation of the closed-loop system when a specific parameter (normally the gain K) is varied from 0 to ∞ . This shows the contributions of all poles and zeros to the locations of the closed-loop poles. The basic idea of this method is that the values s of the transfer function must satisfy the characteristic equation of the system (keeping in mind that s makes the transfer function around the loop equal to -1). Figure 151 shows the root-locus of the MSBA converter.

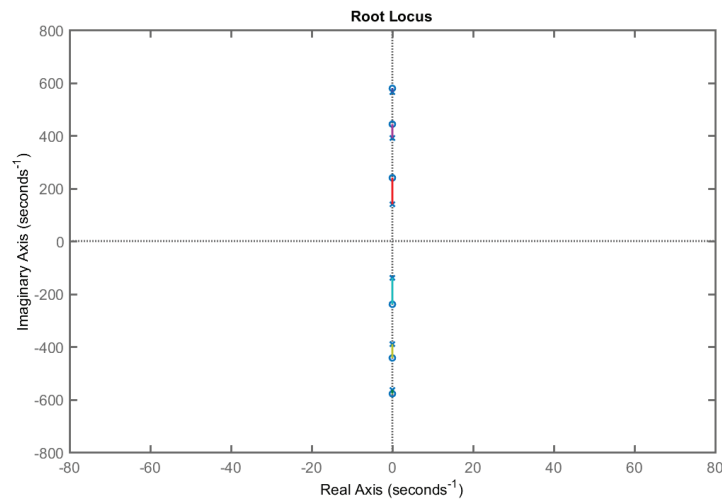


Figure 151: Root-locus of the MSBA

Since the poles and zeros of an open-loop system are always located symmetrically about the real axis the root loci are also always symmetrical to this axis. Therefore, only the upper half needs to be constructed and can then be mirrored to the lower-half s plane.

For a control design by the root-locus method the idea is to add poles and zeros to the systems open loop transfer function therefore forcing the root loci to pass through desired closed-loop poles. Adding a pole to the open-loop transfer function has the effect of pulling the root locus to the right, lowering the systems stability and slowing the settling of the response. Otherwise, adding zeros to the transfer function will pull the root locus to the left, making the system more stable and faster. The placement of additional poles or zeros is influenced by the desired damping ratio and the undamped natural frequency of the systems dominant closed-loop poles. So how to pick the desired closed-loop poles now? Figure 152 shows the pole placement area and its limiting reasons.

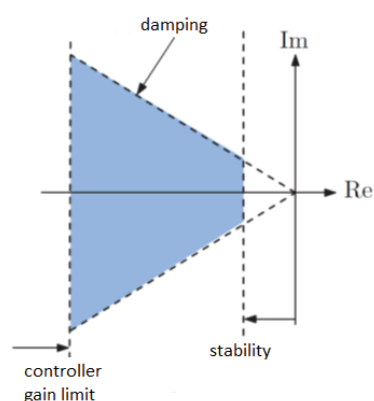


Figure 152: Pole placement area [51]

A good start for placing poles is the Linear Quadratic Regulation (LQR) [52]. The LQR command returns the optimal controller gain assuming a linear system, a quadratic cost function and a reference equal to

zero. Two parameters can be chosen for this method (R and Q), which balance the control effort and the error. To place equal importance on the control and the output state variables it is best to choose $R=1$ and $Q=C'C$. Using this method results in the values for K:

$$K = -[1.4928 \quad 0.9832 \quad 0.4899 \quad 1.1620 \quad 0.1900 \quad 1.2137] \quad (137)$$

The new step response of the system is shown in Figure 153.

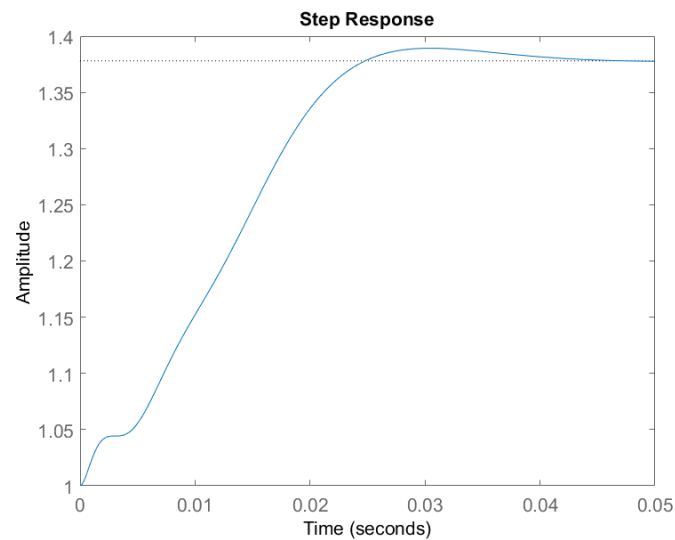


Figure 153: Step response of the controlled system

It is apparent that the step response has a steady state error that needs to be adjusted and it might also be helpful to adjust the poles to achieve a better response. This can be done with a precompensation with a gain of 2.89:

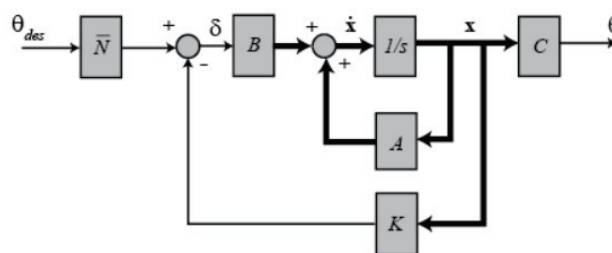


Figure 154: Precompensation in a state space system

The result of adding such a precompensation can be seen in Figure 155.

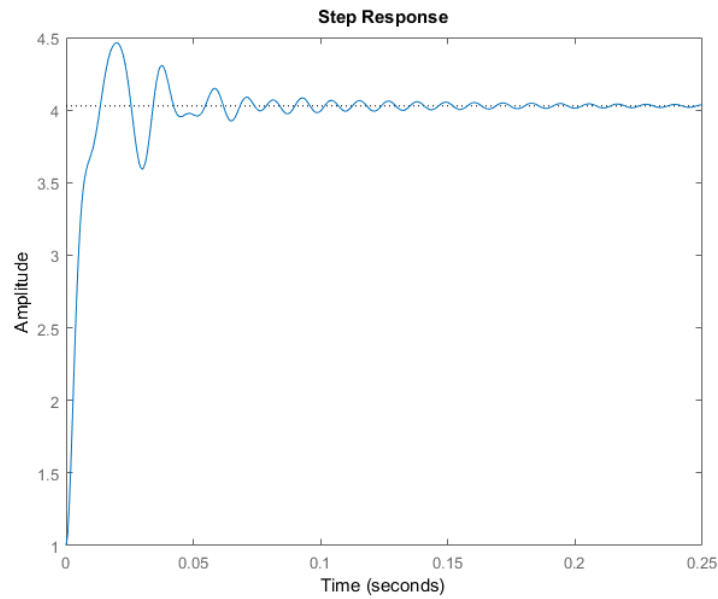


Figure 155: Step response with precompensation

Since this figure shows that the response is not damped in a satisfactory way the values of Q can be adjusted slightly to receive a better response which is shown in

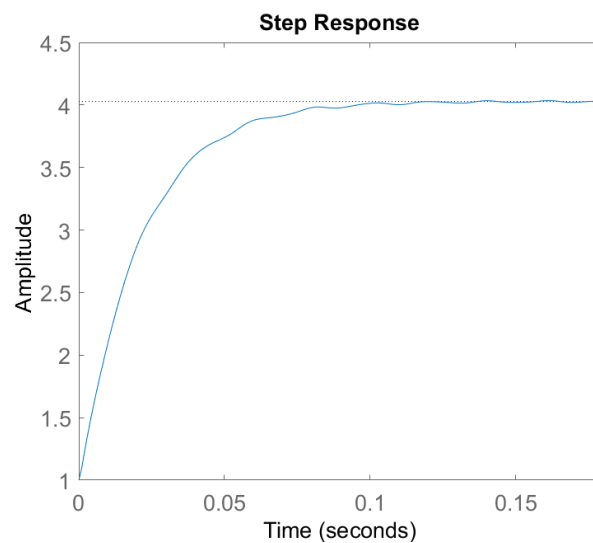


Figure 156: Step response with adjusted Q

This calculation can also be verified in Simulink where the input is not zero but instead 50, like it would be for prototyping. The result of this simulation is shown in Figure 157.

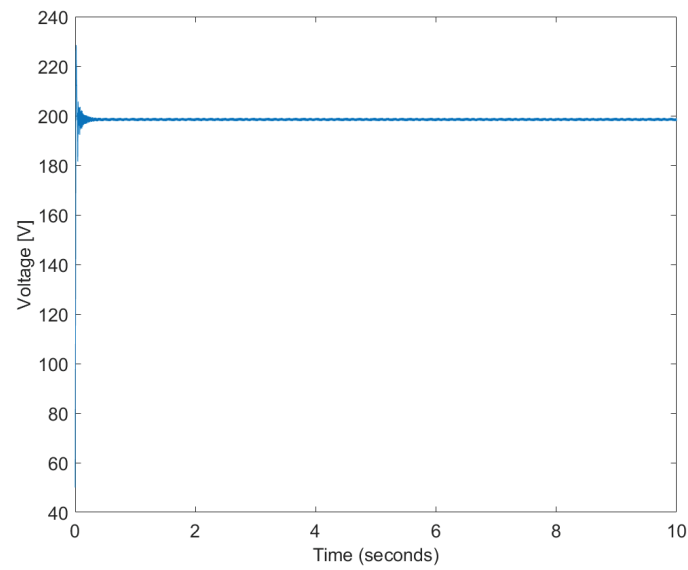


Figure 157: Simulation of the state space system

Since this is working very well, it was also investigated how the control behaves when a change at the input occurs (Figure 158).

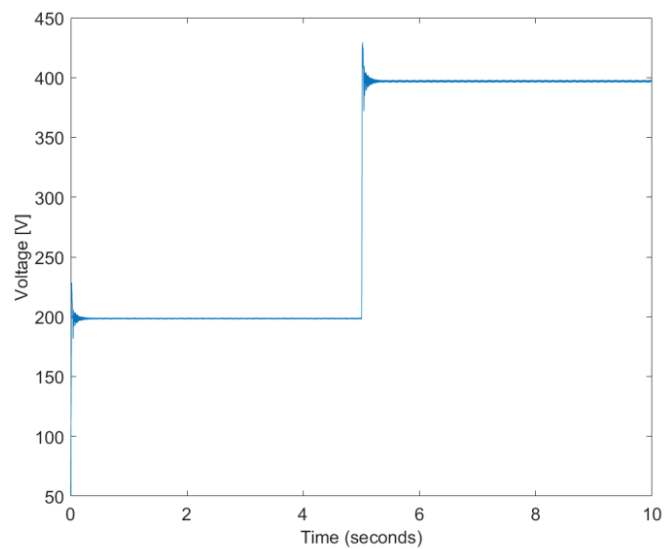


Figure 158: Simulation of the state space system with input change

Finally shows how the control handles a change add the output (load increase).

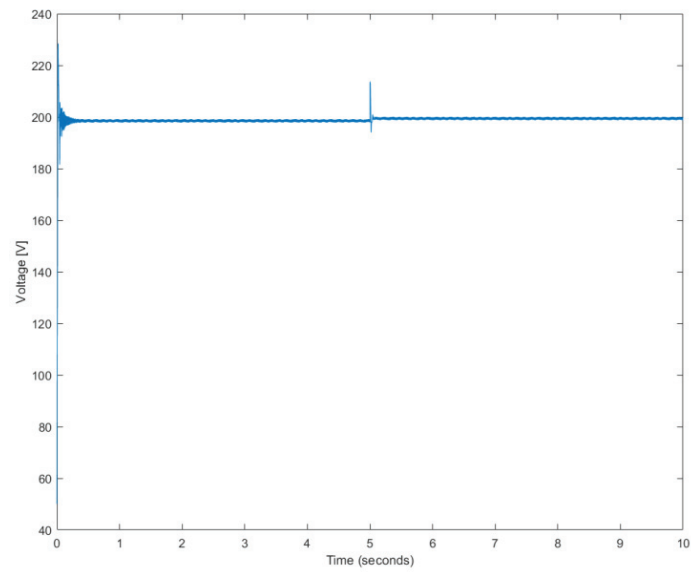


Figure 159: Simulation of the state space system with input change

The control can handle these perturbations well and therefore an observer-based control will be researched next, to reduce the needed number of state variables.

4.3. Observer Control

The state space control shown before relies on measuring the state variables of the system. In a converter it is normally not feasible and also not cost efficient to conduct this many measurements. Therefore, a control strategy using an observer would be advantageous. Such a state observer provides an estimation of the internal state of the converter by just measuring the input and output of the real system. Figure 160 shows how a system with an observer can look like.

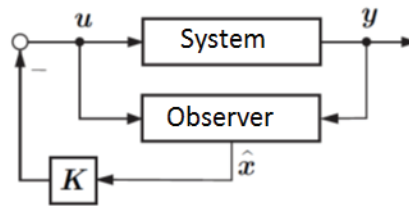


Figure 160: System with observer

Normally the observer model of a system is derived from the state-space equations. Sometimes additional terms need to be included to ensure that the model proves correct results according to the real system, meaning it needs to adjust for errors. The observer is used to obtain an estimated value $\hat{x}(t)$ for the state vector $x(t)$ of the system. In contrast to the state space control before the control signal will now be:

$$u = -K \cdot \hat{x} \quad (138)$$

A system is said to be observable if it is possible to determine the state of the system from the observation of the output over a finite time interval.

The conditions of controllability and observability may govern the existence of a complete solution to the control system design problem. Although most physical systems are controllable and observable, corresponding mathematical models may not possess the property of controllability and observability [50].

If the system is completely observable, then, given the output $y(t)$ is uniquely determined from the following equation:

$$y(t) = \alpha_0(t) \cdot Cx(0) + \alpha_1(t) \cdot CAx(0) + \dots + \alpha_{n-1}(t) \cdot CA^{n-1}x(0) \quad (139)$$

To prove this the rank of the $n \times n$ matrix $\begin{bmatrix} C^* & A^*C^* & \dots & (A^*)^{n-1}C^* \end{bmatrix}$ must be n (The asterisk used as a superscript of a matrix, such as A^* , implies that it is a conjugate transpose of matrix A).

$Ob=obsv(A,C);$

$$Ob = \begin{bmatrix} 0 & 1 & 0 & 1 & 0 & 1 \\ 333.33 & 0 & 0 & 0 & 0 & 0 \\ 0 & -9.8 \cdot 10^4 & 0 & 0 & 0 & 0 \\ -3.27 \cdot 10^7 & 0 & 3.27 \cdot 10^7 & 0 & 0 & 0 \\ 0 & 1.92 \cdot 10^{10} & 0 & -9.61 \cdot 10^9 & 0 & 0 \\ 6.41 \cdot 10^{12} & 0 & -9.61 \cdot 10^{12} & 0 & 3.2 \cdot 10^{12} & 0 \end{bmatrix} \quad (140)$$

$$Rang_Ob = rank(Ob) = 6$$

This means that the system is observable. A Luenberger-Observer will be used in this case and the schematic of that observer is shown in Figure 161.

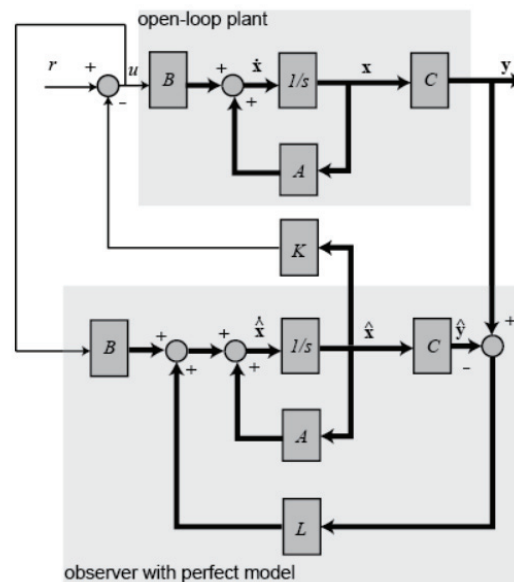


Figure 161: Observer model

The observer is basically a copy of the state space system; it has the same input and almost the same differential equations. An extra term compares the actual measured output y to the estimated output \hat{y} ; this will cause the estimated states \hat{x} to approach the values of the actual states x . The error dynamics of the observer are given by the poles of $(A-LC)$.

First, the observer gain L needs to be chosen. It would make sense to have the dynamics of the observer to be much faster than the system itself; therefore, it is reasonable to place the poles at much farther to the left than the dominant poles of the system. To use the “*place*”, six observer poles need to be placed at different locations.

$$op1 = -100; op2 = -101; op3 = -102;$$

$$op4 = -103; op5 = -104; op6 = -105;$$

Because of the duality between controllability and observability, the same technique used to find the control matrix can be used again with replacing the matrix B by the matrix C and taking the transposes of each matrix

$$L = \text{place}(A', C', [op1 \ op2 \ op3 \ op4 \ op5 \ op6])';$$

The equations in the block diagram above are given for \hat{x} . It is conventional to write the combined equations for the system plus observer using the original state x plus the error state: $e = x - \hat{x}$. Which can then be used as state feedback $u = -K \hat{x}$. This then results in the combined state and error equations with the full-state feedback and an observer.

$$At = \begin{bmatrix} A - B \cdot K & B \cdot K \\ \text{zeros}(\text{size}(A)) & A - L \cdot C \end{bmatrix} \quad (141)$$

$$Bt = \begin{bmatrix} B \cdot \bar{N} \\ \text{zeros}(\text{size}(B)) \end{bmatrix} \quad (142)$$

$$Ct = [C \ \text{zeros}(\text{size}(C))] \quad (143)$$

The step response of the system with observer is shown in Figure 162.

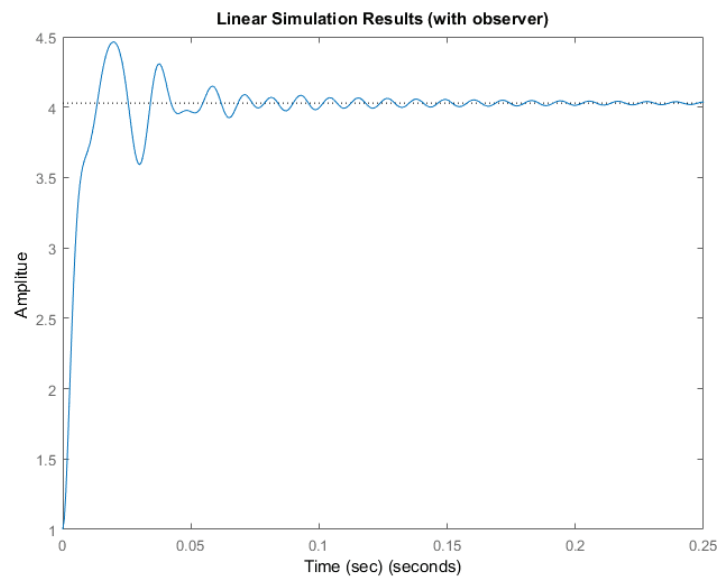


Figure 162: Step response with observer

Once again the system is not damped very well so the parameters are slightly adjusted resulting in the step response shown in Figure 163.

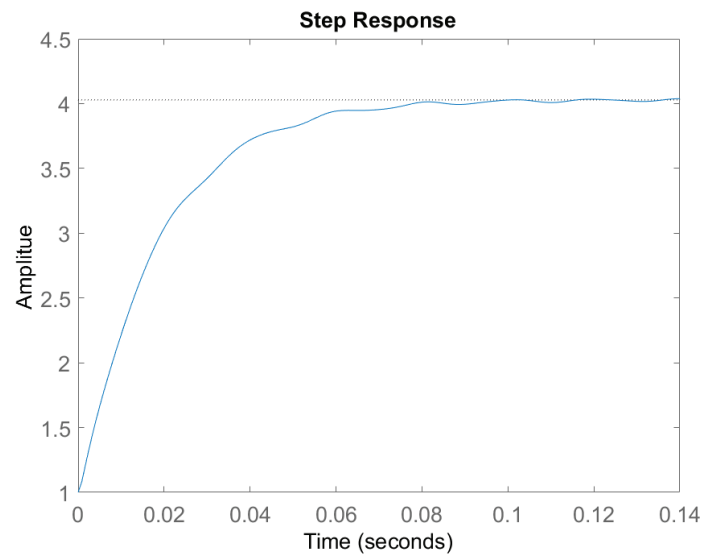


Figure 163: Dampened step response with observer

This calculation can also be verified in Simulink where the input is not zero but instead 50, like it would be for prototyping. The implementation of this is shown in Figure 164 and the result of this simulation is shown in Figure 165.

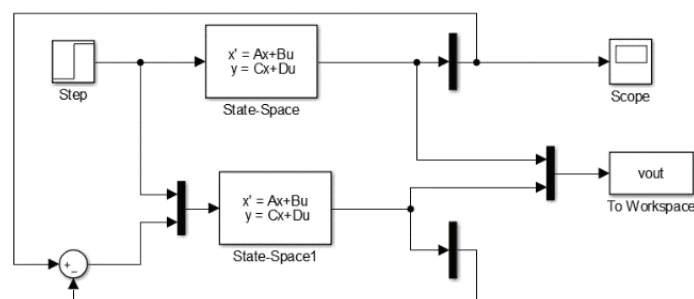


Figure 164: Simulink Observer Implementation

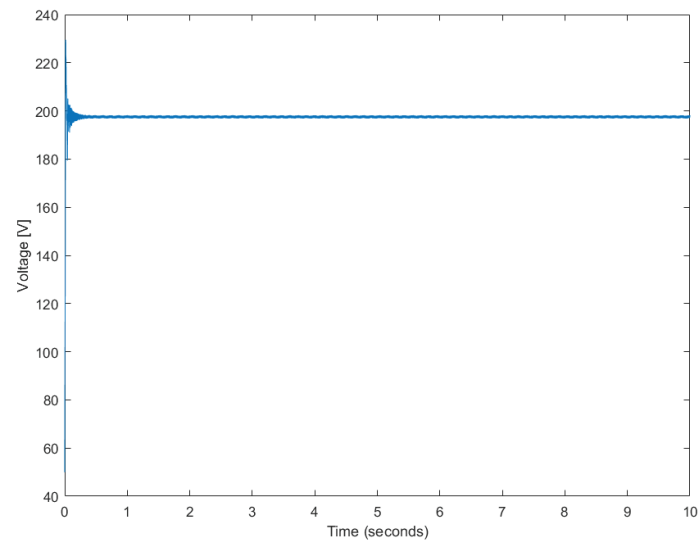


Figure 165: Step response in Simulink

This result is almost identical to the results of the state space simulation without the observer. This shows that the observer is working reliably and fast.



5. Prototype and experimental results

5.1. The Prototype

To verify the simulation results and the working of the proposed controls a low voltage prototype was built in the Industrial Electronics Laboratory (LEI) at EPFL, which is shown in Figure 166.

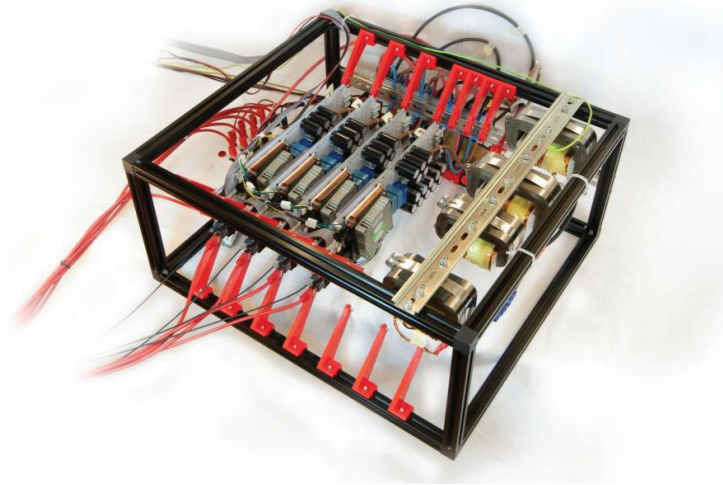


Figure 166: 4-stage asymmetric MSBA prototype

The prototype is using optical receivers and LEM transducers as a compatible interface concept for the numeric controller. The converter is built to work with an input voltage of 100V using a step up ratio of 1:8. More details about the prototype ratings can be found in Table 22.

Table 22: Prototype ratings

	Converter		IGBT
V_{in}	100V	V_{max}	600V
V_{out}	800V	I_c	72A
P_{out}	1.5kW	E_{on}	4.4mJ
C_{1-4}	1.5mF	E_{off}	3.45mJ
L_{1-4}	1.7mH	V_{CE0}	1.7V
f_s	20kHz	R_{Gate}	1 Ω

The prototype has been built using a fast prototyping modular system [53]. The Printed Circuit Boards (PCBs) from this modular system contain two power switches and the interface connections to the control unit. The switches in this case are 600V/50A IGBTs which are used for the actual switch in the MSBA converter as well as the diode. In regards of controlling the IGBTs there is an included control unit that generates the PWM gate signals. In addition, these boards include the possibility for adding

capacitors in two banks (maximal eleven in parallel in each bank). Another useful addition of the PCB is an implemented current sensor, which in this case was used to measure the inductor current in each stage. A schematic of the PCB is shown in Figure 167.

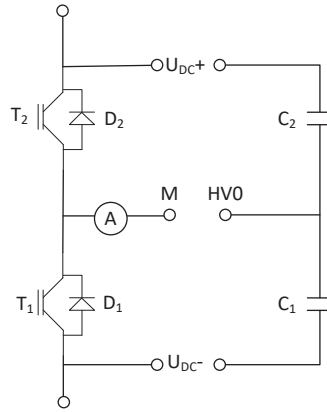


Figure 167: PCB schematic

For each stage of the four-stage MSBA converter one PCB is used. The capacitor banks are filled with several capacitors to reach $150\ \mu\text{F}$ in each stage. Since the PCBs are made up of two capacitor banks each, the connections between the boards have to be considered carefully to reach the desired design of the MSBA converter. Figure 168 shows how this is handled.

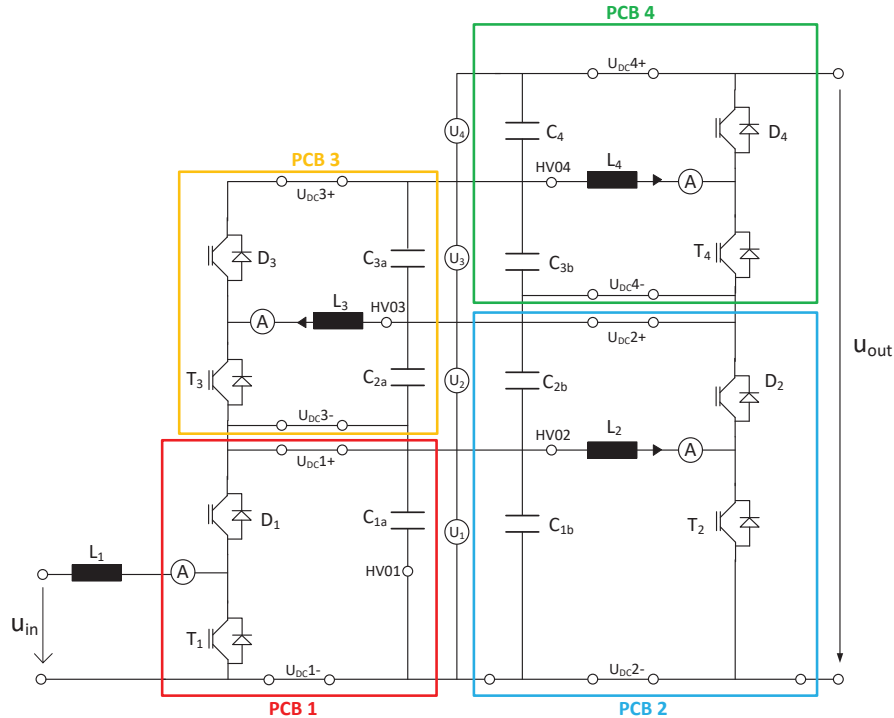


Figure 168: Connections of the four PCBs into the prototype

Additionally, each PCB includes the following components in addition to the capacitor banks:

- 1 current sensor to measure the current that flows through the middle-point of the two power switches; LEM LAH 50-P
- 2 DC-DC converters to generate the 15 V gate voltages for the IGBTs; R05P215S/P
- 2 IGBT Gate Driver Opto-couplers to isolate the gates of the IGBTs; ACPL-333J
- 2 Metallized Polypropylene Film Capacitors for fast commutation of the IGBTs; Epcos B32794
- Heatsink & Fan Cooler; Dynatron DB127015BU
- 1 CPLD to ensure the operation of the control unit on the PCB; Altera EPM7064SLC44-10N
- 2 fibre optics-receivers to receive the PWM signals from the BoomBox; HFBR-2521
- 1 Ethernet Pulse transformer; Bel Fuse S558

Figure 169 shows the 4th stage PCB of the MSBA prototype including the before mentioned components.

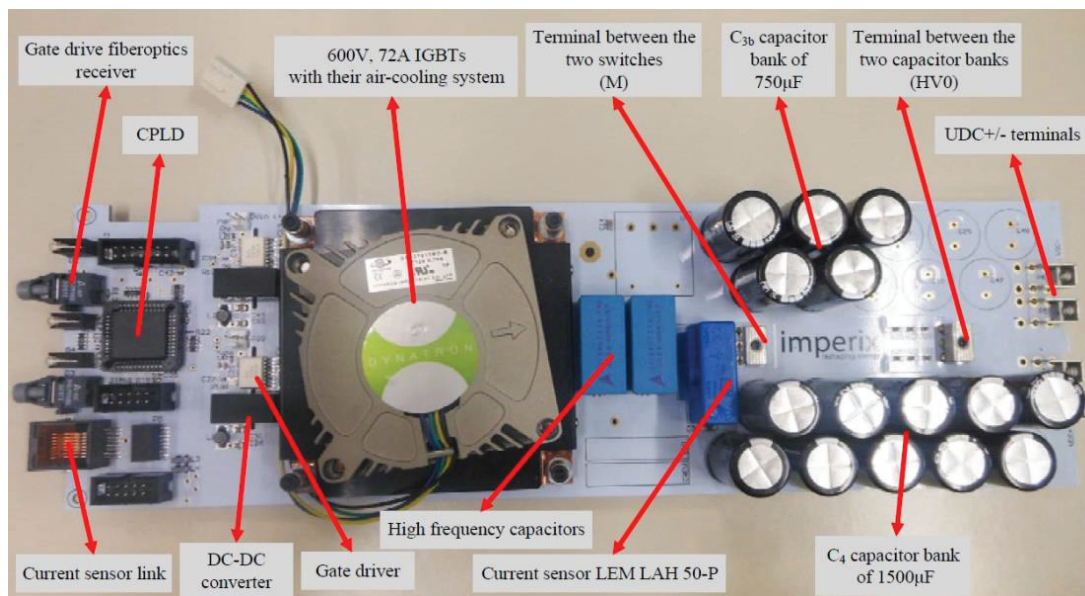


Figure 169: Photo of the PCB [54]

In addition to the before mentioned PCBs for the prototype the control platform from the same company is used; the BoomBox, which is described in the next paragraph.

5.2. Control Platform

The BoomBox is a modular control platform, which is intended for the development of power electronic systems in research environments. Figure 170 shows how the BoomBox looks like.



Figure 170: BoomBox front panel [55]

The BoomBox has 16 analogue inputs for the voltage and current sensors of the converter. This input is then going through an analogue-to-digital converter so that it can be transferred to the microcontroller of the system. These digital signals can then be used in the control software. In addition, the analogue inputs also contain safety mechanisms, which can disable the system if the measured voltages or currents exceed safety limits. The BoomBox also includes eight isolated outputs (fibre optics), so that the PWM signal from the microcontroller transmitted to the fibre optic receivers of the PCB boards, which are connected to the gates of the IGBTs.

This control platform utilizes the programming language C and in the realized measurements the program Code Composer Studio was used for the implementation of the control. To help with the implementation of the control the BoomBox comes packed with several libraries for the BoomBox routines. These include basic functions – like the sensor communication- that can be used in the controller of the power electronic system. Figure 171 shows the parameters that were set for the BoomBox for all the conducted measurements.

Measured Variable	Product Code	Max. Input	Sensitivity s	Hardware gain	a	b
I_{L1}	LEM LAH 50-P	50 A	50 mV/A	4	$-1.53 \cdot 10^{-3}$	0.12
I_{L2}	LEM LAH 50-P	50 A	50 mV/A	4	$-1.53 \cdot 10^{-3}$	-0.07
I_{L3}	LEM LAH 50-P	50 A	50 mV/A	4	$-1.49 \cdot 10^{-3}$	-0.2
I_{L4}	LEM LAH 50-P	50 A	50 mV/A	4	$-1.48 \cdot 10^{-3}$	0.05
I_{out}	IX-LEM LAH 50-P	15 A	105.8 mV/A	4	$7.21 \cdot 10^{-4}$	0.12
U_{C1}	IX-ModuLink400V (Mod. 7)	400 V	4.83 mV/V	8	$7.9 \cdot 10^{-3}$	-0.7
U_{C2}	IX-ModuLink400V (Mod. 6)	400 V	4.84 mV/V	8	$7.88 \cdot 10^{-3}$	-0.4
U_{C3}	IX-ModuLink400V (Mod. 9)	400 V	4.82 mV/V	8	$7.91 \cdot 10^{-3}$	-0.54
U_{C4}	IX-ModuLink400V (Mod. 10)	400 V	4.83 mV/V	8	$7.9 \cdot 10^{-3}$	-0.97
U_m	IX-ModuLink400V (Mod. 8)	400 V	4.9 mV/V	8	$7.79 \cdot 10^{-3}$	-0.6

Figure 171: BoomBox parameters [54]

A sampling frequency of 20kHz was set where each sample is obtained at the first quarter of the switching period when the current or voltage is equal to its respective average value. Therefore, the

sampling was based on the same frequency generator that is used for the generation of the PWM pulses with a phase-shift of 90° . To avoid problems with the electromagnetic interference (EMI) emitted from the power part of the converter the hardware low-pass filter of the BoomBox was enabled in each analogue channel connected to a voltage sensor. Figure 172 shows the complete laboratory setup.

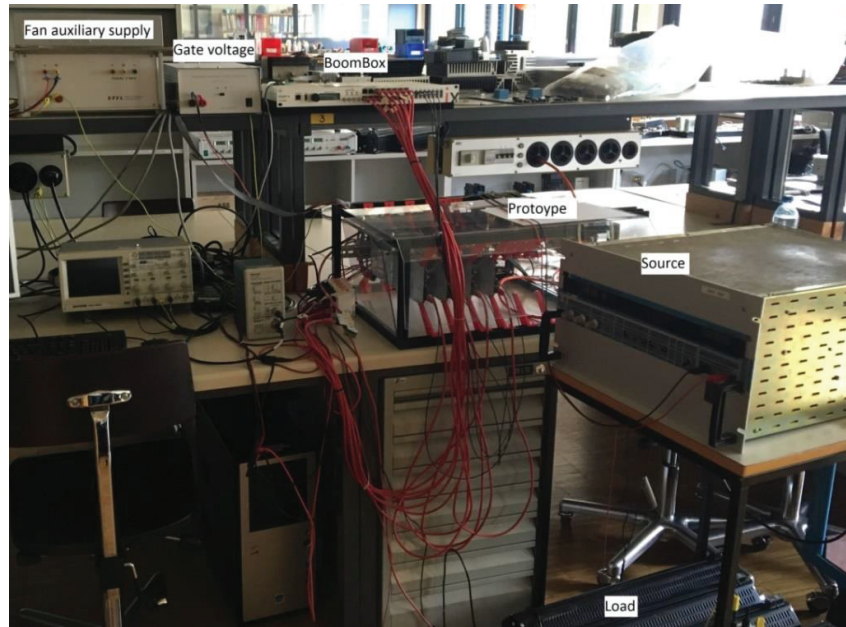


Figure 172: Complete laboratory setup

5.3. Linearized Fast-Feed Forward Measurements

The LFF control (which was shown in 4.1.5.4) is implemented for the before mentioned BoomBox and Figure 173 shows an excerpt how this control file looks like.

```
USER_SAFE UserInit(void)
{
    // Configure a 20 kHz switching frequency on clock source #
    1:
        SetFreqGenPeriod(1, (int)
(SWITCHING_PERIOD/FPGA_CLK_PERIOD));

    // Map PWM channels to clksource #1 with a triangular
    carrier and 0 ns deadtime:
    ConfigPWMChannel(1, 1, TRIANGLE, (int)(0/FPGA_CLK_PERIOD));
    ConfigPWMChannel(2, 1, TRIANGLE, (int)(0/FPGA_CLK_PERIOD));
    ConfigPWMChannel(3, 1, TRIANGLE, (int)(0/FPGA_CLK_PERIOD));
    ConfigPWMChannel(4, 1, TRIANGLE, (int)(0/FPGA_CLK_PERIOD));

    // Channel #1 to #4 is configured with a phase of zero with
    respect to the frequency generator:

    SetPWMPhase(1, 0.0);
    SetPWMPhase(3, 0.0);
    SetPWMPhase(2, 0.0);
    SetPWMPhase(4, 0.0);
}
```

Figure 173: Excerpt of the control file

Figure 174 shows the capacitor voltages during the start-up of the converter. In the beginning, there is an input voltage of 10V, which can be seen at the first capacitor. At around 4.2s the control is turned on and the IGBTs start to switch, bringing the voltages to the expected 20V level because of the 0.5 duty cycle.

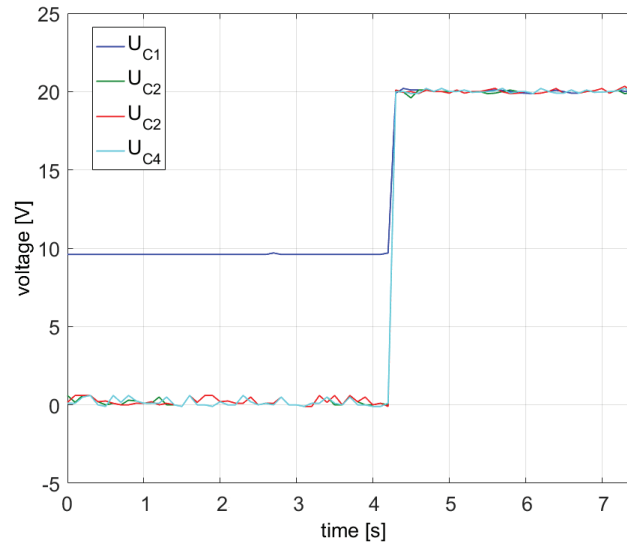


Figure 174: Measured capacitor voltages during start-up

The input voltage for the following measurements was set to 50V using a load of 650 Ω in the beginning and then introducing a perturbation by reducing the load to 330 Ω . The parameters for the controllers were set to the values shown in Table 23.

Table 23: Control parameters for the LFF measurements

	Voltage controller	Current controller	Current limit
Boost stage	0.5	1	25
1. MSBA cell	0.5	1	20
2. MSBA cell	0.5	1	15
3. MSBA cell	0.5	1	10

Figure 175 shows the voltages in the four capacitors of the MSBA converters.

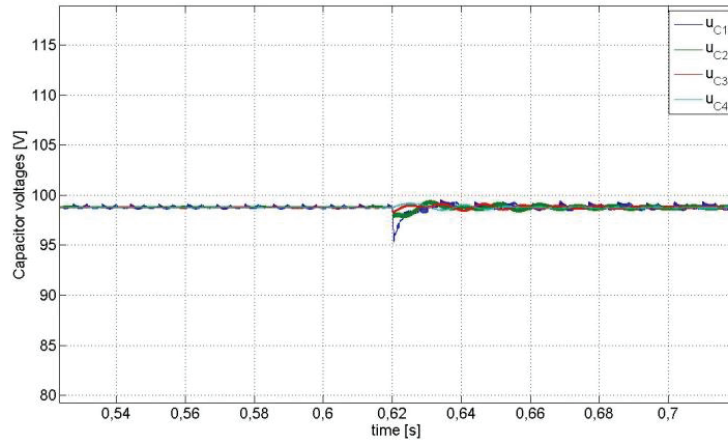


Figure 175: Measured capacitor voltages with a load step at 0.62s

The measurement shows that the control is able to keep all the capacitor voltages at the same level and that it is able to handle the load step with only a small voltage drop between 1-3V in the different capacitors. In addition, there are only very small resonant properties that are of no consequence for the correct functioning of the converter. Figure 176 shows the measured filtered inductor currents for the same test setup as before.

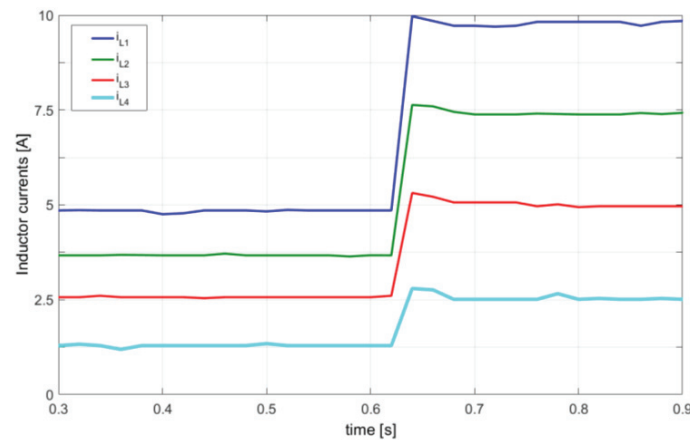


Figure 176: Measured inductor currents with a load step at 0.62s

The measurement of the inductor currents shows the expected behaviour of a small overcurrent when the load is halved, but this is quickly corrected and the currents remain at the correct values. All in all, the measurements showed satisfying results and a good functioning of the implemented control. In addition to the measurements shown before it was also important to measure the efficiency of the converter.

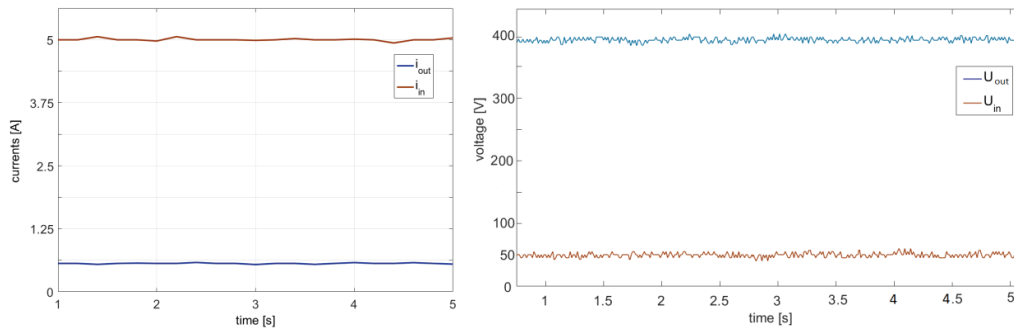


Figure 177: Input and output current (left) as well as input and output voltage (right)

These measurements show that the output current is 0.6A with an input current of 5A. The input voltage is 50V and the output voltage is 394V. This results in an efficiency of

$$\eta = \frac{U_{out} \cdot I_{out}}{U_{in} \cdot I_{in}} \cdot 100\% = 94.56\% \quad (144)$$

which is not a bad result for a prototype that was not optimized at all for efficiency.

5.4. State-Space measurements

The control is again implemented on the BoomBox. The control of the boost stage was handled the same as in the measurements before and in a photovoltaic application, the MPPT could be done in that stage. To implement a state-space control for the MSBA cells it was first necessary to implement all the matrix calculation routines that the BoomBox needs to be able to handle the control. Meaning that functions for matrix and vector additions / subtractions and multiplications had to be implemented as background functions. Programming all these routines by hand takes a lot of time; thankfully, there are reliable resources that can be used. One example is Meschach, which has libraries for computing these mathematical problems [56]. Figure 173 shows an excerpt how doing a simple matrix addition can be done with this:

```
#include "matrix.h"
MAT    *m_add(MAT *A, MAT *B, MAT *C)
MAT    *m_mlt(MAT *A, MAT *B, MAT *C)
MAT    *m_sub(MAT *A, MAT *B, MAT *C)
MAT    *sm_mlt(double s, MAT *A, MAT *OUT)

#include "zmatrix.h"
ZMAT    *zm_add(ZMAT *A, ZMAT *B, ZMAT *C)
ZMAT    *zm_mlt(ZMAT *A, ZMAT *B, ZMAT *C)
ZMAT    *zm_sub(ZMAT *A, ZMAT *B, ZMAT *C)
ZMAT    *zsm_mlt(complex s, ZMAT *A, ZMAT *OUT)
```

Figure 178: Excerpt of the control file

With the help of these routines the state-space control can be implemented on the BoomBox. Figure 179 shows the first measurement results during steady-state.

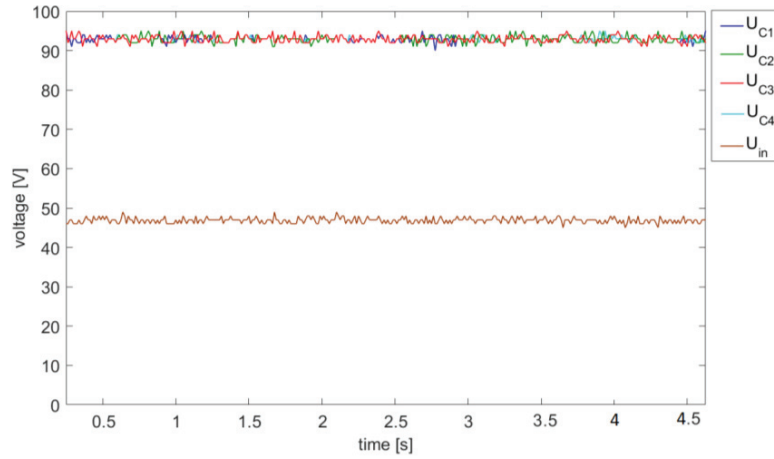


Figure 179: Measured capacitor voltages and input voltage

Figure 180 shows measurement results for the capacitor voltages during a perturbation at around 1.4s at the output; the load changed from $650\ \Omega$ to $330\ \Omega$.

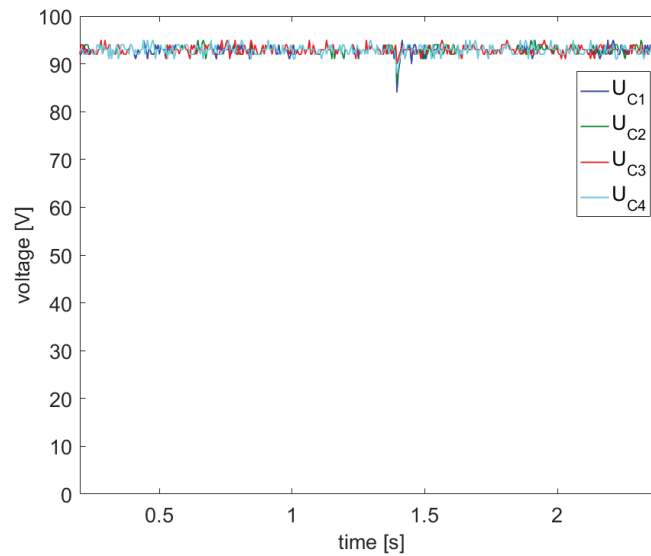


Figure 180: Measured capacitor voltages during perturbation

Figure 181 shows the measured filtered inductor currents for the same test setup as before, this time with a perturbation at around 1.7s.

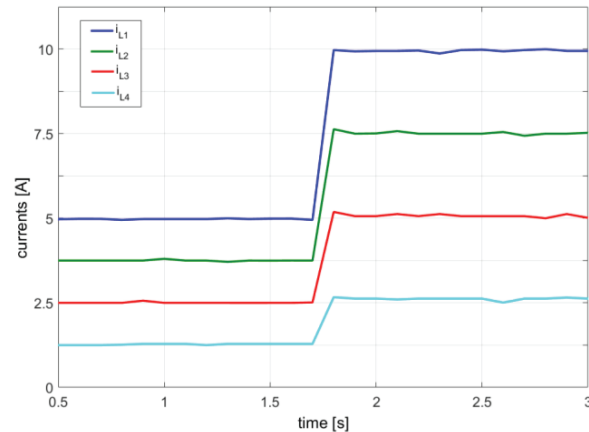


Figure 181: Measured inductor currents with perturbation

The measurement shows clearly that there is only a small voltage drop (less than 10%), most noticeable in the first capacitor. Regarding the currents it is very visible that there is no problems with overshoots during the transition. This means that the control is working reliable and satisfactory.

5.5. Observer measurements

The control is once again implemented on the BoomBox and again the Meschach libraries are used for computing these matrix and vector related calculations. Figure 182 shows the first measurement results for the capacitor voltages during steady-state operation.

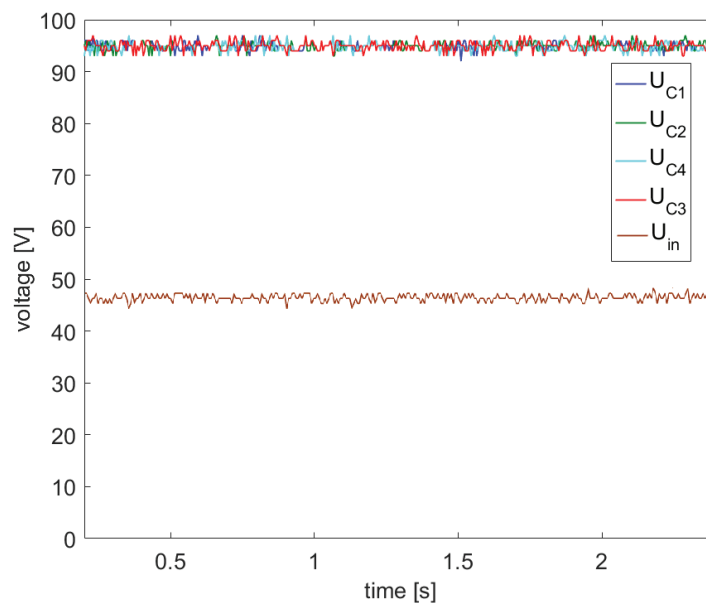


Figure 182: Measured capacitor voltages

Figure 183 shows measurement results for the capacitor voltages during a perturbation at around 2s at the output; the load changed from 650 Ω to 330 Ω .

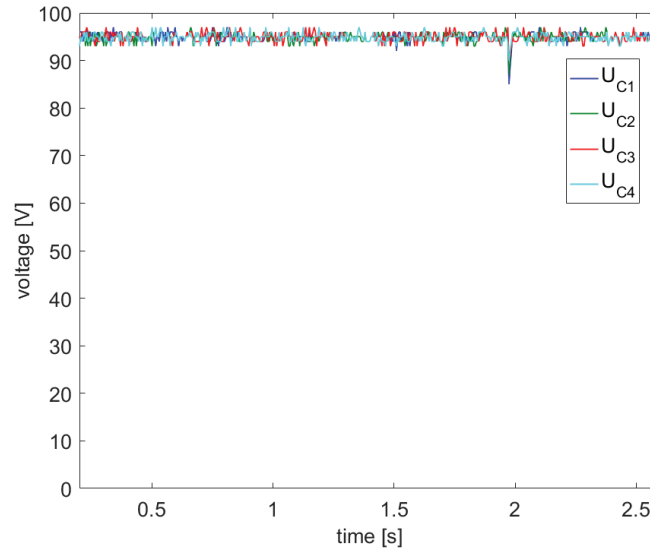


Figure 183: Measured capacitor voltages during perturbation

Figure 184 shows the measured filtered inductor currents for the same test setup as before, this time with a perturbation at around 1.9s.

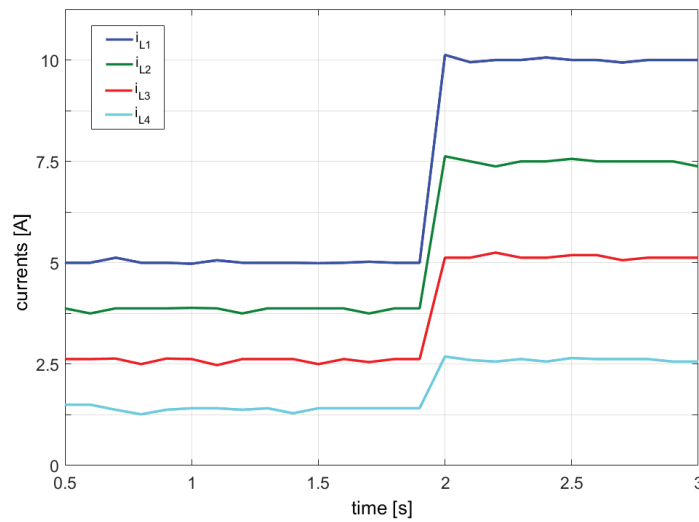


Figure 184: Measured inductor currents with perturbation

Again the measurement shows that there is only a small voltage drop (less than 10%), most noticeable in the first capacitor. In addition the currents have almost no overshoot during the perturbation (less than 2%), making this an excellent control strategy for the Multistage Stacked Boost Architecture.



6. Conclusions and Future Research

6.1. Summary and Conclusion

For this thesis, a medium voltage DC-DC converter topology, the Multistage Stacked Boost Architecture, for photovoltaic power plants was researched. This converter is useful in regards of reducing the transmission losses inside photovoltaic plants by elevating the voltage from low to medium level.

First step was to have a look at possible application cases for a medium voltage DC-DC converter. These application cases included different microgrids for example for an industrial complex. Hereby different configurations of a microgrid with purely AC distribution, purely DC distribution or a hybrid distribution were investigated. The other main application that was considered concerned regenerative energy generation. Photovoltaic plants would here be the main focus since they generate direct current so no additional transformation is needed. In case of wind power generation, it would also be possible to achieve the distribution inside a wind farm on a medium voltage DC level but the voltage would then be needed to be elevated to HVDC level, which was outside the scope of this work. A case study was conducted on the Solar plant “Agua Caliente” and the outlay of the plant was investigated. This lead to a research about the efficiency of the transmission lines inside huge solar plants. An evaluation of this problem together with a comparison of actual power plants as well as an efficiency calculations relied that for power plants that have subareas with a length over a mere hundred meters it becomes inefficient to rely on low voltage distribution. Therefore, a change to a medium voltage distribution with the help of a DC-DC converter would make sense. To decide on a topology different non-isolated and isolated converter topologies were evaluated under the aspects of electrical behaviour, component requirements, potential efficiency, cost and space requirements. In the end, it appeared interesting and promising to investigate a new topology, the Multistage Stacked Boost Architecture.

The introduced converter is based on the current diverter topology, which is used to equalize the voltage between different cells, in this case between different series capacitors. A current diverter consists of several cells/stages with each stage containing two active switches and an inductor. To use this topology as a step-up converter a boost stage was added as input stage forming the Multistage Stacked Boost Architecture. Different converter types forming the MSBA family were shown. In addition to ensure that this topology would be a possible solution for the before mentioned challenges calculations were done to verify a satisfying efficiency of the converter. For these efficiency calculations the performance of the asymmetric MSBA (main focus of this thesis) as well as the symmetric MSBA was compared. A case with a different number of stages and a lower duty cycle to achieve the same output conditions was also included into that comparison.

To understand the elementary properties of Multistage Stacked Boost Architecture the topology was split into its essential stages and an Energetic Macroscopic Representation was done for the separate stages and later on for the complete system. In addition, a control was designed for each stage and also implemented into the EMR. Then the parts were put together for a complete system. The main quantity of the boost input stage that needed to be controlled was the output of the stage, in this case the



capacitor voltage. For the actual control a PWM modulation was used, where the duty cycle d defined the ratio of the input voltage to the output voltage. For the closed-loop control the two state variables of the converter (the capacitor voltage and the inductor current) needed to be controlled. The main characteristic of the controller was that it was able to maintain the output voltage under any conditions regarding the load. In the case of the cascade of the boost topology with an MSBA cell, the output current of the boost converter appears as a state variable of the next stage. This state variable was intended to be measured, according the condition of such a variable to be safely controlled, avoiding overload of the semiconductor devices. As a consequence, the control structure of the boost input stage could be developed based on the available information of its load current. A dedicated control structure using the principle of Feed-Forward was therefore studied.

The elementary MSBA cell in contrast showed resonant phenomenon because of its LC components, and their frequency was calculated with the help of a state-space representation. The cell therefore needed a dedicated control in order to avoid this resonant phenomenon. Like the control structure for the boost stage, the chosen MSBA control structure used two cascaded controllers with feedback of the load current to generate the PWM. The current in the inductor was controlled with a simple proportional controller and due to the presence of a pure integral component for the system the current controller didn't need any integral component. The superimposed voltage balancing controller was also a single proportional controller. Even if the output load represented a perturbation for the voltage control loop, the need of an integral component in the controller itself could be avoided through feedforward of the perturbation current that was measured. The feedforward signal, representing an anticipation quantity for the inductor current, was calculated from the measured output current. In order to properly protect the current solicitation of the power semiconductor devices and the passive components, the control structure included also the possibility to limit the current during transient operation. Therefore, between the voltage balancing controller with its feedforward signal and the current controller, a limitation element was inserted. The dynamic responses of the controlled MSBA cell and the controlled boost stage were verified by simulation and were working well for this case. Finally, the boost stage controlled with the LFF control scheme in combination with three MSBA cells, also called a 4-stage MSBA converter, was researched. Simulation verified that the control was able to provide stable output quantities without resonant oscillations for a four stage MSBA topology.

Since the LFF control relied on the measurement of nine state variables it was considered important to introduce a second control. This control was an observer control. The first step to achieve that was to introduce a State-Space control which is based on the description of system with n first-order differential equations. These equations were then combined into a vector-matrix differential equation. The use of this matrix simplifies the mathematical representation of the system. The eigenvalues of the system were then investigated as well as the controllability and observability of the system. To control the system the desired closed-loop poles needed to be placed. To find out possible locations for the closed-loop poles the Root-Locus method can be used. The placement of additional poles or zeros is influenced by the desired damping ratio and the undamped natural frequency of the systems dominant closed-loop poles. After choosing closed-loop poles simulations of the system showed that the control was working well and that only a small steady state error occurred, which could be adjusted with a precompensation.

But the state space control relies on measuring all the state variables of the system. In a converter it is normally not feasible and also not cost efficient to conduct this many measurements. Therefore, the research continued into a control strategy using an observer. If such an observer is possible it is used to obtain an estimated value for the state vector of the system. The used Luenberger observer is basically a copy of the state space system; it has the same input and almost the same differential equations. An extra term compares the actual measured output to the estimated output; this will cause the estimated states to approach the values of the actual states. Simulation results were almost identical to the results of the state space simulation without the observer. So the observer was working reliably and fast.

To verify the simulation results and the working of the proposed controls a low voltage prototype was built. The prototype was using optical receivers and LEM transducers as a compatible interface concept for the numeric controller. The converter was built to work with an input voltage of 100V using a step up ratio of 1:8 and has been built using a fast prototyping modular system. To implement the control of the system the BoomBox was used to send the digitalized signals to the control software and control signals to the converter. The measurements that were conducted all included normal steady-state operation as well as test to verify the correct functioning during perturbations such as variations of the load. All the measurement showed that the controls were able to keep all the capacitor voltages at the same level and that they were able to handle perturbations with only a small voltage drop different capacitors. In addition, there were only very small resonant properties that are of no consequence for the correct functioning of the converter. Finally a measurement to evaluate the efficiency of the prototype was done, which showed satisfying results.

To conclude, all the research and the simulations as well as the measurement results obtained with the different controls proved satisfactory, showing that the Multistage Stacked Boost Architecture is a reliable and interesting topology.

6.2. Future Prospects

After the end of this thesis work, several challenges and questions arise. On one side this converter should be optimized in regard of efficiency and cost, since during this stage of development it was only optimized for functionality. One point being that it should be possible to further increase the efficiency by finding the optimal components for each stage or in some time maybe switch to SiC devices for the switches to achieve a higher switching frequency, smaller inductors and a higher efficiency.

It would also be interesting to research the symmetric Multistage Stacked Boost Architecture further since the efficiency comparison with the asymmetric MSBA showed promising results and it could be a worthwhile topology for applications where a +/- output voltage is required. Another point that could be worth attention is focusing on the different application cases that are possible for this topology like the use in microgrids or in wind farms and how the converter might be adjusted and optimized for them and what possible safety considerations would include. Finally, it should be considered to study the failure rates and reliability of the converter and check possible fault management techniques and redundancy schemes.



7. Appendix

a) Safety considerations

Before a MSBA converter could be used in a photovoltaic plant it is important to do a FMEA to get an idea which fault and security issues must be covered. Figure 185 shows an excerpt of a solar plant using a DC-DC converter.

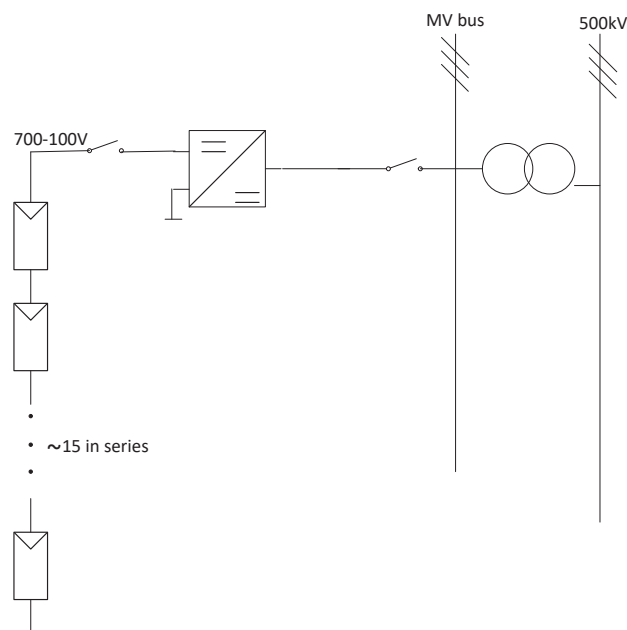


Figure 185: Excerpt of a solar plant

Starting with the transformer used to bring the voltage to high voltage range there can be different problems that need to be considered. On one side, there could be a ground fault on the HV side meaning that there will be a potential shift on the high voltage level, so for protecting the structure there would need to be some protection switch, which can open if a fault like this occurs. On the other side there can also be a ground fault at the converter, which means that a security switch between the converter and the collection bus needs to open and the converter needs to shut down. Another fault that can occur on the transformer is a shortcut in the windings, which would generate an arc in the transformer. And to avoid possible overheating, which would cause for example the isolation to be damaged, a temperature surveillance is needed and the transformer would need to be separated from the lines if a fault like that occurs.

On the solar module level there are mainly two problems that can occur. On one side one of the solar modules can stop working either reducing the generated energy or even taking that array completely out of energy generation depending of the faulty module can be bypassed or if the whole array needs to be shut down. Either way some sort of monitoring system is needed to check the correct working of the



solar arrays and deal with faults. On the other side there could be a ground fault, which would lead to a reduced energy generation a locale overheating in the solar module and probably the complete failure of the solar module string.

For the converter the main problems to consider are a short circuit on the side connected to the MV bus which would lead to a short circuiting the bus therefore a safety switch would need to be implemented that could open during such a fault. Another problem could be a no-load operation meaning that no energy would be delivered which means that the security switch connecting this branch to MV bus should be opened and the branch shut down to find the failure. Of course, there can also be a short circuit on the solar array side of the converter, which would lead to an overvoltage and a safety switch between the solar array and the converter should be opened to protect the solar modules. While there also might occur some kind of no-load operation on the DC side of the converter this only means that no energy will be delivered so there is no security action that would need to be taken.

Another important component that has to be considered when taking the whole solar plant into account is the connection to the grid since there can also be faults that occur at the grid level. If there is an overvoltage at the grid the solar plant should not deliver more energy into the grid therefore all the security switches between the transformer and the converters and the grid should be opened to protect the system. If there is an under voltage at the grid level there is more energy needed from the power plant. It has to be closely monitored if the plant can deliver it and ride-through the fault or reach a critical state at which point the power plant needs to shut down to protect the system. Of course, there could also be a problem with the grid frequency but this is regulated clearly and the power plant needs to follow the mandated actions. If there is a ground fault on the grid, there will be a potential shift and normally the grid safety measurements should disconnect or shut down the power plant to protect it. Also problems like a 3-phase short circuit or an unbalance in the grid will be handled according to the mandated reactions so there is nothing specific for this application that needs to be considered.

Taking into account the problems that can occur in the different components of the solar plant and seeing that a lot of these problems can be handled by safety switches it is important to consider what could happen if faults occur within these switches. If one of the switches triggers falsely it is not a big problem since the only result will be that no energy will come through that branch and this should get an error notification in the system monitoring leading to an easy solving of the problem. The much more severe problem is the probability of one such not triggering when it should which could lead to a partial or complete destruction of components in the circuit so there will be a need for additional safety measures to avoid something like this.

This analysis of the problems that can occur in the solar power plant lead to some requirements that a DC-DC converter would have to fulfil. There should be a decoupling diode to protect the solar arrays as well as a complete removal of short circuits on the medium voltage side by either topology choice or by having a guaranteed possibility to shut down the converter. It would also need to be considered if an isolation of the low voltage and medium voltage side is possible because then a ground fault on the medium voltage side would not lead to a short circuit on the low voltage side anymore.

8. Bibliography

8.1. List of Figures

Figure 1: Possible applications for a medium voltage DC-DC converter	21
Figure 2: Possible AC microgrid structure for a small industry complex.....	22
Figure 3: Possible DC microgrid structure for a small industry complex	23
Figure 4: Possible Hybrid microgrid structure for a small industry complex	24
Figure 5: Structure of Agua Caliente Solar Plant	26
Figure 6: Examples of power to area relation for actual PV plants.....	27
Figure 7: Scheme of subarea divisions in a PV plant	28
Figure 8: a) Interconnections in a PV plant subarea, b) Structure of a solar array	28
Figure 9: Alternative PV plant subarea configuration with use of DC-DC converters.....	29
Figure 10: Wiring in a subarea.....	30
Figure 11: Dimensions of a subarea depending on the power level.....	32
Figure 12: Energy efficiency of the collection lines in a subarea	32
Figure 13: Comparison of the efficiency with included DC-Converter.....	33
Figure 14: Boost-converter.....	35
Figure 15: Hybrid boost and buck/boost converter	35
Figure 16: Resonant step-up converter (RS)	36
Figure 17: Bidirectional resonant step-up converter with ZCS	36
Figure 18: Resonant switched-capacitor step-up converter (RSC).....	37
Figure 19: Combined boost and LCC resonant converter	38
Figure 20: LLC resonant converter	38
Figure 21: 8-Switch converter with ZVS	39
Figure 22: Dual Active Bridge	40
Figure 23: Dual Active Bridge converter with H-bridge and NPC.....	40
Figure 24: Balancing capacitor voltages with a current diverter topology	41
Figure 25: Elementary MSBA cell	42
Figure 26: Waveforms of the elementary MSBA stage.....	42
Figure 27: Elementary stage for the Multistage Stacked Boost Architecture	43
Figure 28: Buck converter (left) and boost converter (right)	43
Figure 29: Redrawn scheme for the MSBA cell	44
Figure 30: Block diagram of open-loop elementary MSBA	45
Figure 31: The typical resonance of the MSBA stage with constant duty cycle.....	45
Figure 32: The MSBA stage with output load step as perturbation.....	47
Figure 33: Oscillation of the MSBA stage with a fixed duty cycle of $d=2/3$	48
Figure 34: Oscillation of the MSBA stage with a fixed duty cycle of $d=1/3$	48
Figure 35: Excitation of the circuit resonance by a fast perturbation.....	49
Figure 36: MSBA stage with filtered load circuit.....	50
Figure 37: The non-excited resonance due to the filtered load-step	50

Figure 38: The MSBA cell with filtered input voltage source	51
Figure 39: Transient response of the voltage increase at the converter input with limited dynamics	51
Figure 40: 4-stage symmetric MSBA	52
Figure 41: Component-Numbering for the 6-stage MSBA with a +/- output	53
Figure 42: Showing the unbalance of a +/- MSBA with a duty cycle of $d=0.75$	54
Figure 43: Symmetric 4-stage MSBA prototype	54
Figure 44: Inductor currents received with a prototype	55
Figure 45: Asymmetric Step-down MSBA converter with 5 levels.....	55
Figure 46: Symmetric step-up MSBA followed by a 5-Level NPC inverter	56
Figure 47: High-voltage converter with separated balancing circuits.....	57
Figure 48: Numbering of MSBA from bottom to top	59
Figure 49: Relation of output and input voltage for different duty cycles d and number of MSBA cells n	60
Figure 50: Simulation results for the inductor currents with $d=0.5$ (left) and $d=0.4$ (right)	61
Figure 51: Stage currents of the switches in a MSBA.....	62
Figure 52: The 4-stage MSBA stage with output load step as perturbation	63
Figure 53: Resonant phenomena in the 4-stage MSBA with a fixed duty cycle of $d=0.5$	64
Figure 54: Connection of MSBA and DC/AC converter	64
Figure 55: Connection of MSBA and DC/AC converter with control	65
Figure 56: Current control of the DC/AC converter	65
Figure 57: Voltage control of the DC/AC converter	66
Figure 58: Connection of MSBA and DC/AC converter	66
Figure 59: Switching loss characteristics [37]	68
Figure 60: Loss comparison for the asymmetric MSBA (blue) and the symmetric MSBA (red).....	75
Figure 61: Elementary MSBA stage	77
Figure 62: waveform of current and voltage in the inductor of the MSBA stage	78
Figure 63: Waveform representation of the MSBA structure	78
Figure 64: EMR of the elementary MSBA stage	80
Figure 65: Two MSBA stages	80
Figure 66: EMR for 2-stage MSBA	81
Figure 67: 3-stage MSBA converter.....	81
Figure 68: EMR for 3-stage MSBA converter.....	82
Figure 69: Three stage MSBA with output	83
Figure 70: EMR representation of 3-stage MSBA with load.....	84
Figure 71: Input boost stage.....	84
Figure 72: EMR representation of the boost stage	85
Figure 73: 4-stage MSBA converter.....	85
Figure 74: EMR for the 4-stage MSBA	86
Figure 75: Inductor block for the MSBA stage of the EMR simulation.....	86
Figure 76: Adapted capacitor block for the MSBA stage of the EMR simulation.....	87
Figure 77: Diode block for the MSBA stage of the EMR simulation.....	87
Figure 78: Switch block for the MSBA stage of the EMR simulation.....	88
Figure 79: Load block of the EMR simulation	88

Figure 80: Source block of the EMR simulation	88
Figure 81: Inductor block for the boost stage of the EMR simulation	89
Figure 82: Capacitor block for the boost stage of the EMR simulation	89
Figure 83: C_{v1} block for the boost stage of the EMR simulation	89
Figure 84: Coupling block for the voltage output	90
Figure 85: Coupling block for the boost stage.....	90
Figure 86: Matlab/Simulink implementation of the 4-stage MSBA	90
Figure 87: Capacitor voltages (left) and inductor currents (right) of the 4-stage MSBA	91
Figure 88: Output voltage (left) and output current (right) of the 4-stage MSBA	91
Figure 89: Input boost-stage of the MSBA converter	93
Figure 90: Block diagram of the boost stage with LFF control structure	94
Figure 91: PWM modulation and according references	95
Figure 92: Control structure of the boost stage.....	96
Figure 93: transient response of the boost stage with $U_{in}=100V$	96
Figure 94: transient response of the boost stage with $U_{in}=50V$ (left) and $U_{in}=150V$ (right)	97
Figure 95: The boost stage with load step	97
Figure 96: Dynamic response of the boost stage with load step	98
Figure 97: Block diagram of a MSBA cell and control structure.....	98
Figure 98: Control circuits of the MSBA cell.....	99
Figure 99: Dynamic response of the controlled MSBA cell without current limitation	100
Figure 100: Dynamic response of the controlled MSBA cell with current limitation.....	100
Figure 101: The MSBA cell with output load step	101
Figure 102: Dynamic response of the MSBA cell control in the case of a load step	101
Figure 103: 2-stage MSBA converter.....	102
Figure 104: Control circuits of the boost stage with MSBA cell as load.....	102
Figure 105: Dynamic performance of the boost stage with an MSBA cell as load	103
Figure 106: Output waveforms of the boost with MSBA cell as load converter.....	104
Figure 107: The boost stage with one MSBA stage	104
Figure 108: Control circuits of the boost stage with MSBA cell in open-loop	105
Figure 109: Dynamic performance of the boost stage with an MSBA cell in open-loop	105
Figure 110: Output waveforms of the boost with MSBA cell in open-loop	106
Figure 111: Control structure for the controlled boost stage and MSBA cell	107
Figure 112: Dynamic performance of the controlled boost and MSBA stage.....	108
Figure 113: Output waveforms of the controlled boost and MSBA stage	108
Figure 114: Control structure where the MSBA cell is relying on the capacitor reference voltage	109
Figure 115: Dynamic behaviour for boost and MSBA stage with adjusted reference	110
Figure 116: Output waveforms of the controlled boost and MSBA stage with adjusted reference	110
Figure 117: Dynamic behaviour for the boost (left) and the MSBA (right) cell with perturbation.....	111
Figure 118: Output waveforms of the controlled boost and MSBA cell with perturbation	112
Figure 119: The 4-stage MSBA converter.....	112
Figure 120: Block diagram of control structure for boost stage (left) and for a MSBA cell (right)	113
Figure 121: Control structure for the controlled boost and three MSBA stages	114

Figure 122: Dynamic performance of the boost stage.....	115
Figure 123: Output waveforms of the boost and three MSBA stages	115
Figure 124: Boost stage with three controlled MSBA cells with output load step	116
Figure 125: Dynamic performance of the boost stage with perturbation	117
Figure 126: Output waveforms of the boost and three MSBA cells with perturbation.....	117
Figure 127: Start-up behaviour of the input voltage for the four-stage MSBA (left) and the according topology scheme (right)	118
Figure 128: Dynamic performance of the boost stage during start-up	119
Figure 129: Output waveforms of 4-stage MSBA converter during start-up.....	119
Figure 130: Control for the 4-stage MSBA converter	121
Figure 131: Control circuits of the MSBA cell.....	122
Figure 132: Control structure for the elementary MSBA stage	122
Figure 133: Voltage control block	123
Figure 134: Current control block	123
Figure 135: Control structure of the boost stage.....	124
Figure 136: Control structure for the boost stage	124
Figure 137: Voltage control block	124
Figure 138: Current control block	125
Figure 139: Output voltage (left) and output current (right) of the boost stage.....	126
Figure 140: Output voltage (left) and output current (right) of elementary MSBA stage	126
Figure 141: Capacitor voltages (left) and inductor currents (right) of the 4-stage MSBA	127
Figure 142: Output voltage (left) and output current (right) of the 4-stage MSBA.....	127
Figure 143: Capacitor voltages (left) and inductor currents (right) of the 4-stage MSBA	128
Figure 144: Output voltage (left) and output current (right) of the 4-stage MSBA.....	128
Figure 145: 4-stage MSBA converter representation for State Space	130
Figure 146: State Space representation	132
Figure 147: Eigenvalues of the system.....	135
Figure 148: Step response of the uncontrolled system	137
Figure 149: Implementation of the state space system in Simulink	137
Figure 150: State space representation with feedback	138
Figure 151: Root-locus of the MSBA	140
Figure 152: Pole placement area [51]	140
Figure 153: Step response of the controlled system.....	141
Figure 154: Precompensation in a state space system	141
Figure 155: Step response with precompensation	142
Figure 156: Step response with adjusted Q	142
Figure 157: Simulation of the state space system.....	143
Figure 158: Simulation of the state space system with input change	143
Figure 159: Simulation of the state space system with input change	144
Figure 160: System with observer.....	145
Figure 161: Observer model.....	146
Figure 162: Step response with observer.....	147



Figure 163: Dampened step response with observer	148
Figure 164: Simulink Observer Implementation	148
Figure 165: Step response in Simulink	149
Figure 166: 4-stage asymmetric MSBA prototype	151
Figure 167: PCB schematic	152
Figure 168: Connections of the four PCBs into the prototype	152
Figure 169: Photo of the PCB [54]	153
Figure 170: BoomBox front panel [55]	154
Figure 171: BoomBox parameters [54]	154
Figure 172: Complete laboratory setup	155
Figure 173: Excerpt of the control file.....	155
Figure 174: Measured capacitor voltages during start-up.....	156
Figure 175: Measured capacitor voltages with a load step at 0.62s.....	157
Figure 176: Measured inductor currents with a load step at 0.62s	157
Figure 177: Input and output current (left) as well as input and output voltage (right)	158
Figure 178: Excerpt of the control file.....	158
Figure 179: Measured capacitor voltages and input voltage.....	159
Figure 180: Measured capacitor voltages during perturbation	159
Figure 181: Measured inductor currents with perturbation.....	160
Figure 182: Measured capacitor voltages	160
Figure 183: Measured capacitor voltages during perturbation	161
Figure 184: Measured inductor currents with perturbation.....	161
Figure 185: Excerpt of a solar plant.....	167



8.2. List of Tables

Table 1: Losses of components inside the microgrids.....	24
Table 2: Estimated L_{SA} of actual PV plants.....	31
Table 3: Advantages and disadvantages of using low voltage AC converters	33
Table 4: Advantages and disadvantages of using medium voltage DC converters	34
Table 5: Nominal values of the prototype.....	54
Table 6: Cases for efficiency analysis	67
Table 7: Ratings for the switches	67
Table 8: Losses in the switches with $f=1\text{kHz}$	68
Table 9: Losses in the switches with $f=500\text{Hz}$	69
Table 10: Losses in the switches with $f=500\text{Hz}$	69
Table 11: Losses in the diodes with $f=500\text{Hz}$	70
Table 12: Ratings for the switches	70
Table 13: Losses in the switches with $f=500\text{Hz}$	71
Table 14: Losses in the diodes with $f=500\text{Hz}$	71
Table 15: Ratings for the switches	72
Table 16: Losses in the switches with $f=500\text{Hz}$	72
Table 17: Losses in the switches with two parallel IGBTs	73
Table 18: Losses in the diodes with $f=500\text{Hz}$	73
Table 19: Overview of criteria to choose an inductor core type [40]	74
Table 20: Comparison of efficiency for the MSBA for $f=500\text{Hz}$	75
Table 21: Elements of the Energetic Macroscopic Representation	77
Table 22: Prototype ratings	151
Table 23: Control parameters for the LFF measurements	156



8.3. References

- [1] ABB, "Onboard DC Grid - The step forward in Power Generation and Propulsion," 2011.
- [2] ABB, "The step forward - Onboard DC Grid," 2014.
- [3] Marco Liserre, Thilo Sauter, and John Y. Hung, "Future Energy Systems: Integrating Renewable Energy Sources into the Smart Power Grid Through Industrial Electronics," *IEEE Industrial Electronics Magazine* Vol. 4, March 2010.
- [4] U.S. Department of Energy, "Final Environmental Assessment - The Agua Caliente Solar Project In Yuma," Nov. 2010.
- [5] FirstSolar. (2016, June) [Online]. <http://www.firstsolar.com/en/About-Us/Projects/Agua-Caliente-Solar-Project>
- [6] PowerMag. (2016, June) [Online]. <http://www.powermag.com/agua-caliente-solar-project-yuma-county-arizona/>
- [7] SMA Solar Technology AG, "SUNNY CENTRAL 500CP XT / 630CP XT / 720CP XT / 760CP XT / 800CP XT / 850CP XT / 900CP XT," *Data-Sheet*.
- [8] FirstSolar, "FS Series 3 Module," *Data-Sheet*, April 2013.
- [9] SMA, "Transformer Requirements," 2012.
- [10] Hafiz Abu Bakar Siddique, Syed Mansoor Ali, and Rik W. De Doncker, "DC Collector Grid Configurations for Large Photovoltaic Parks," *15th European Conference on Power Electronics and Applications (EPE), Lille*, September 2013.
- [11] Woo-Young Choi, Ju-Seung Yoo, and Jae-Yeon Choi, "High efficiency dc-dc converter with high step-up gain for low PV voltage sources," *IEEE 8th International Conference on Power Electronics and ECCE Asia (ICPE & ECCE)*, May 2011.
- [12] J. Komoto and et al., "Study on Very Large Scale Photovoltaic (VLS-PV) Systems," *38th IEEE Photovoltaic Specialists Conference (PVSC), Austin, USA*, June 2012.
- [13] Sheng-Yu Tseng and Hung-Yuan Wang, "A Photovoltaic Power System Using a High Step-up Converter for DC Load Applications," *Energies*, Vol. 6, pp. pp. 1068-1100, 2013.
- [14] Gina K. Steinke and Alfred Rufer, "Use of a DC-DC step up converter in photovoltaic plants for increased electrical energy production and better utilization of covered surface area," *PCIM 2015: International Conference on Power Electronics, Intelligent Motion and Power Quality, Nürnberg*,



Germany, May 2015.

- [15] ABB, "PVS800-57 central inverters," August 2014.
- [16] G. Parise, L. Martirano, and L. Parise, "Life Monitoring Tool of Insulated Cables in Photovoltaic Installations," *IEEE Transaction on Industry Applications*, Vol. 50, May 2014.
- [17] D. Krug, S. Bernet, and S. Dieckerhoff, "Comparison of State-of-the-art voltage source converter topologies for medium voltage applications," *Proceedings of IEEE-IAS*, 2003.
- [18] J. Thoma, D. Chilachava, and D. Kranzer, "A Highly Efficient DC-DC-Converter for Medium-Voltage Applications," *ENERGYCON 2014, Dubrovnik, Croatia*, May 2014.
- [19] N. Denniston, A. Massoud, S. Ahmed, and P. Enjeti, "Multiple module high gain high voltage DC-DC transformers for offshore wind energy systems," *IEEE Transactions on Industrial Electronics*, Vol. 58, No. 5, pp. pp. 1877–1886, May 2011.
- [20] D. Jovcic, "Step-up DC–DC converter for megawatt size applications," *ET Power Electronics.*, Vol. 2, No. 6, pp. pp. 675–685, 2009.
- [21] D. Jovcic, "Bidirectional, high-power DC transformer," *IEEE Transactions on Power Delivery*, Vol. 24, No. 4, pp. pp. 2276–2283, October 2009.
- [22] W. Chen and et al., "Analysis and Comparison of Medium Voltage High Power DC/DC Converters for Offshore Wind Energy Systems," *IEEE Transactions on Power Electronics*, Vol. 28, No. 4, April 2013.
- [23] Hussain Athab, Amirnaser Yazdani, and BinWu, "A Transformerless DC–DC Converter With Large Voltage Ratio for MV DC Grids," *IEEE Transactions on Power Delivery*, Vol. 29, No. 4, August 2014.
- [24] D. Dujic et al., "Soft switching characterization of a 6.5kV IGBT for high power LLC resonant DC/DC converter," *PCIM 2012: International Conference on Power Electronics, Intelligent Motion and Power Quality, Nürnberg, Germany*, May 2012.
- [25] D. Dujic et al., "Characterization of a 6.5kV IGBT for medium-voltage highpower soft-switched resonant DC/DC converter," *APEC 2012: The Applied Power Electronics Conference and Exposition, Long Beach, California*, March 2013.
- [26] Drazen Dujic et al., "Characterization of 6.5 kV IGBTs for High-Power Medium-Frequency Soft-Switched Applications," *IEEE Transactions on Power Electronics*, Vol. 29, No. 2, February 2014.
- [27] John Lam and Praveen K. Jain, "A High Efficient Medium Voltage Step-up DC/DC Converter with Zero Voltage Switching (ZVS) and Low Voltage Stress for Offshore Wind Energy Systems," *16th European Conference on Power Electronics and Applications (EPE'14-ECCE Europe), Lappeenranta*, August

- 2014.
- [28] C. Arrioja, S. Kenzelmann, and A. Rufer, "Reversible DC/DC Converter as interface between Low and Medium Voltage DC Networks," *PCIM 2011: International Conference on Power Electronics, Intelligent Motion and Power Quality, Nürnberg*, May 2011.
- [29] N.H Kutkut, "A modular nondissipative current diverter for EV battery charge equalization," *Applied Thirteenth Annual Power Electronics Conference and Exposition, APEC '98, Vol. 2*, pp. pp. 686 - 690, 1998.
- [30] P. Barrade, S. Pittet, and A. Rufer, "Energy storage system using a series connection of supercapacitors, with an active device for equalizing the voltages," *IPEC 2000: International Power Electronics Conference, Tokyo, Japan*, April 2000.
- [31] P. Barrade, S. Pittet, and A. Rufer, "Series connection of supercapacitors, with an active device for equalizing the voltages," *PCIM 2000: International Conference on Power Electronics, Intelligent Motion and Power Quality, Nürnberg, Germany*, June 2000.
- [32] A. Rufer, P. Barrade, and G. Steinke, "Voltage Step-Up Converter based on Multistage Stacked Boost Architecture (MSBA)," *IPEC 2014: International Power Electronics Conference, Hiroshima, Japan*, May 2014.
- [33] P. Barrade and A. Rufer, "Non-Isolated DC-DC Converters for High Power Applications - Control of the Capacitive Voltage Divider," *PCIM 2014: International Conference on Power Electronics, Intelligent Motion and Power Quality, Nürnberg, Germany*, May 2014.
- [34] A. Rufer, "A Five-Level NPC Photovoltaic Inverter with Active Balanced Capacitive Voltage Divider," *PCIM 2015: International Conference on Power Electronics, Intelligent Motion and Power Quality, Nürnberg, Germany*, May 2015.
- [35] A. Rufer, "High-Power High-Voltage Isolated DC-DC Converters using an NPC Balanced Capacitive Divider," *16th European Conference on Power Electronics and Applications (EPE)*, 2015.
- [36] Hansruedi Bühler, *Réglage de systèmes d'électronique de puissance*, Presses Polytechniques et Universitaires Romandes, Ed., 1997.
- [37] Infineon, "FZ400R33KL2C_B5," *Data Sheet*, 2013.
- [38] ABB, "5SNE 0800E330100," *Data Sheet*, 2007.
- [39] ABB, "5SNA 0400J650100," 2013.
- [40] University of Surrey. (2016, June) [Online]. <http://info.ee.surrey.ac.uk/Workshop/advice/coils/>



- [41] A. Bouscayrol, Guillaud, P. Delarue, and B. Lemaire-Semail, "Energetic Macroscopic Representation and Inversion-Based Control Illustrated on a Wind-Energy-Conversion System Using Hardware-in-the-Loop Simulation," *IEEE Transactions on Industrial Electronics*, Vol. 56, No. 12, 2009.
- [42] A. Bouscayrol et al., "Teaching drive control using Energetic Macroscopic Representation - Summer schools," *14th European Conference on Power Electronics and Applications EPE*, 2011.
- [43] J. P. Hautier and P. J. Barre, "The causal ordering graph - A tool for modelling and control law synthesis," *Studies in Informatics and Control Journal*, Vol. 13, No. 4, pp. pp. 265-283, December 2004.
- [44] (2016, June) [Online]. <http://www.emrwebsite.org>
- [45] Enrico Santi, Antonello Monti, and et al., "Synergetic Control for DC–DC Boost Converter: Implementation Options," *IEEE Transactions on Industry Applications*, Vol. 39, No. 6, November 2003.
- [46] Yuri B. Shtessel, Alan S.I. Zinober, and Ilya A. Shkolnikov, "Sliding mode control of boost and buck-boost power converters using method of stable system centre," *Automatica* 39, 2003.
- [47] Marian K. Kazimierczuk and Antonio Massarini, "Feedforward Control of DC–DC PWM Boost Converter," *IEEE Transactions on Circuits and Systems*, Vol. 44, No. 2, February 1997.
- [48] Marian K. Kazimierczuk and LaVern A. Starman, "Dynamic Performance of PWM DC-DC Boost Converter with Input Voltage Feedforward Control," *IEEE Transactions on Circuits and Systems*, Vol. 46, No. 12, December 1999.
- [49] C. Sreekumar and Vivek Agarwal, "A Hybrid Control Algorithm for Voltage Regulation in DC–DC Boost Converter," *IEEE Transactions on Industrial Electronics*, Vol. 55, No. 6, June 2008.
- [50] Katsuhiko Ogata, *Modern Control Engineering*. Fourth Edition: Pearson Education International, 2002.
- [51] Jan Lunze, *Regelungstechnik 2*, 5th ed.: Springer Verlag, 2008.
- [52] (2016, August) [Online]. https://en.wikipedia.org/wiki/Linear-quadratic_regulator
- [53] imperix. (2016, June) [Online]. <http://imperix.ch/products/power/modules/peb6035-phase-leg>
- [54] Georgios Mademlis, "Control and Design of Multistage Stacked Boost Architecture (MSBA)," EPFL, Diploma Thesis 2015.
- [55] imperix. (2016, June) [Online]. <http://imperix.ch/>



[56] (2016, August) [Online]. <http://homepage.divms.uiowa.edu/~dstewart/meschach/>



8.4. Curriculum Vitae

Name	Steinke
First name	Gina Kristin
Address	Chemin de Boissonnet 77 1010 Lausanne Switzerland
E-mail	ginasteinke@web.de
Nationality	German



PhD research “Medium Voltage DC-DC Converter for DC Distribution Networks – Multistage Stacked Boost Architecture”
École Polytechnique Fédérale de Lausanne (EPFL)

University education Oct. 2005 – July 2012 Electrical Engineering at Karlsruhe Institute of Technology (KIT) for Diploma (eq. to Master)

Jan. – Jul. 2012 Diploma thesis at ABB Corporate Research, Baden-Dättwil, Switzerland

- Design and Simulation of a switch mode power supply (SMPS) for a low voltage power electronic converter
- Transformer and PCB design for the SMPS
- Practical realization and Experimental testing of a 25W prototype of a wide input voltage range SMPS

Jun. – Nov. 2011 Internship at ABB Corporate Research, Baden-Dättwil, Switzerland

- Simulations of resonant DC-DC converters with high voltage IGBTs
- High voltage IGBT characterization under soft switching Conditions
- Characterization of standard 3.3kV and 6.5kV IGBT
- Characterization of modified 6.5kV IGBT with improved switching performances



- Characterization of a prototype 6.5kV BIGT (reverse blocking IGBT)
- Development of a MATLAB based tool for processing of large amount of data obtained during laboratory measurements

Feb. – May 2011 Study research project at Institute of Materials for Electrical and Electronic Engineering at KIT

- Fuel cells (SOFC) characterization
- Impedance measurements with SOFCs at different temperatures and different amount of oxygen
- Analyzing measurements in regard of polarization resistance and efficiency

Sep. and Oct. 2007 Internship at Bombardier Transportation, Mannheim

- Assembling of tram converters
- Soldering of PCBs for measurement equipment of ICEs

School education

2005-06 final school examination

(Abitur, grade point average 1.4; physics award)

Technical Skills

MATLAB, SIMULINK, PLECS, Altium Designer, PExprt, Gecko Circuits, C++, HTML, MS Visio, MS FrontPage

Additional Skills / Activities

- EDV-Co-Tutor
- UNiCert Language Certificate English for Science and Technology
- 2000 - 2006 Voluntary working with kids and teenager in the protestant church
- 2006 - 2014 Responsible for layout and maintenance of the homepages of Judo Club Albruck & Studentinnenwohnheim Rüppurr

Languages

German (native), English (fluent), French (basic)

Publication

[1] D. Dujic, **G. Steinke**, E. Bianda, S. Lewdeni-Schmid, C. Zhao, J. K. Steinke, F. Canales: "Soft switching characterization of a 6.5kV IGBT for high power LLC resonant DC/DC converter"; *Int. Power Conversion and Intelligent Motion Conference – PCIM*; 2012, Nürnberg, Germany, pp: 625-631.

- [2] D. Dujic, **G. Steinke**, E. Bianda, S. Lewdeni-Schmid, C. Zhao, J. K Steinke, F. Canales: "Characterization of a 6.5kV IGBT for medium-voltage highpower soft-switched resonant DC/DC converter"; *The Applied Power Electronics Conference and Exposition – APEC*, March 17–21, 2013, Long Beach, California.
- [3] Drazen Dujic, **Gina K. Steinke**, Marco Bellini, Munaf Rahimo, Liutauras Storasta, and Juergen K. Steinke: "Characterization of 6.5 kV IGBTs for High-Power Medium-Frequency Soft-Switched Applications"; *IEEE Transactions on Power Electronics* Vol.29, February 2014
- [4] A. Rufer, P. Barrade, **G. Steinke**: "Voltage Step-Up Converter based on Multistage Stacked Boost Architecture (MSBA)"; *IPEC 2014: International Power Electronics Conference, Hiroshima, Japan, 18-20 May 2014*
- [5] **Gina K. Steinke**, Alfred Rufer: "Use of a DC-DC step up converter in photovoltaic plants for increased electrical energy production and better utilization of covered surface area"; *PCIM 2015, Nürnberg*
- [6] **Gina K. Steinke**, Alfred Rufer: "Comparison of Multistage Stacked Boost Architecture Topologies in Regards of the Relation between Duty Cycle, Number of Stages and Efficiency", *IECON 2015, Yokohama, Japan - Best session presentation*
- [7] Georgios Mademlis, **Gina K. Steinke**, Alfred Rufer: "Feed-Forward based Control in a DC-DC Converter of Asymmetric Multistage Stacked Boost Architecture", *IEEE Transactions on Power Electronics Issue: 99, 2016*
- [8] Georgios Mademlis, **Gina K. Steinke**, Alfred Rufer: "DC-DC Converter based on the Asymmetric Multistage Stacked Boost Architecture with Feed-Forward Control for Photovoltaic Plan", *PCIM 2016, Nürnberg*
- [9] **Gina K. Steinke**, Alfred Rufer: "Control method for the Multistage Stacked Boost Architecture", *PCIM 2016, Nürnberg*
- [10] **Gina K. Steinke**, Alfred Rufer: "Control Method and Prototyping of the Multistage Stacked Boost Architecture (MSBA)", *EPE 2016, Karlsruhe*